University of Nottingham

UK | CHINA | MALAYSIA

Characteristics, Durability and Degradation Mechanism of CO_2 Electrolysis in Solid Oxide Cells

Anqi Wu, BSc, MSc

Thesis submitted to the University of Nottingham for the degree of Doctor of Philosophy

July, 2024

Abstract

With the development of technology, environmental problems are becoming increasingly serious. It is crucial to use reliable electrochemical technology to treat carbon emissions to achieve the goals of “carbon peak” and “carbon neutrality”. Solid oxide electrolysis cells (SOECs) have become one of the reliable methods for dealing with carbon emissions due to various advantages such as high selectivity, high conversion rate, high efficiency, fast response, controllable reaction and multi fuel adaptability.

Flat-tube SOECs are a novel structure, in which fuel is introduced from the middle of the cells and diffused to the fuel electrode, which may alleviate the diffusion of macromolecules such as CO_2 in the electrode. However, the research on this structure is currently very scarce. In this regard, this study attempted to address this research gap. The innovative points of this paper are as follows:

(i) The utilization of solid oxide electrolysis cells for CO_2 electrolysis may generate by-products such as coke, thereby reducing Faraday efficiency. Therefore, in this thesis, the suitable reaction conditions for long-term operation were first calculated from thermodynamic theory, and then the stability of CO_2 electrolysis operation under high temperature was verified through short-term experiments. The effects of different types and contents of reducing gases on the performance and products of solid oxide electrolysis

cells were also studied. To avoid the impact of sealing on test results, the thesis further explored the types of sealing materials and assembly processes, and determined appropriate process parameters. These exploratory works have laid the foundation for extending the lifespan of flat-tube SOECs.

(ii) Feed gas compositions of 25 vol.% H_2-75 vol.% CO_2 and 23.8 vol.% CO-76.2 vol.% CO_2 with same oxygen partial pressure were selected for long-term durability test under no air conditions for investigating the impact of air, with a focus on analyzing the efficiency changes, impedance changes, and potential degradation mechanisms of SOEC, including degradation of electrodes and electrolyte. The flat-tube SOECs were stable operated for more than 1000 hours under no air conditions, which exceeded that of most current planar SOECs. Through comparative experiments, it was found that strontium segregation at the interface between the air electrode and electrolyte is the main cause of degradation.

(iii) Focusing on the demand for “energy storage”, the durability and degradation mechanism of SOEC under fluctuating currents of -100-300 mA/cm^2 were studied in this paper, after the cells successfully ran for 808 hours. Subsequently, the feasibility of the “power-gas-power” conversion technology was verified using the RSOC (reversible solid oxide cells) system concept in a 50 vol.% CO-50 vol.% CO_2 fuel electrode atmosphere, and over 100 reversible charge-discharge cycles were achieved.

(iv) Consequently, this thesis also conducted research on the

electrolysis stack to verify the durability of constant current electrolysis under different currents, and simultaneously analyzed the degradation of various components. The stack finally successfully achieved stable CO_2 electrolysis operation for over 1200 hours under the high current density of -500 mA/cm^2. Through the analysis of the degradation mechanism under high current density, the influence of interconnects on the overall stability of the stack was discovered, and coating improvements were performed on the interconnects for durability verification of the stack under intermittent pulsed current.

(v) In the assembled two-unit SOEC stack, a manganese-cobalt spinel coating was employed as the protective layer for the interconnects, and lead wire was used to monitor the real-time degradation of various parts in the stack. During over 900 hours of high-temperature CO_2 electrolysis operation, the toxic effect of chromium on the air electrode interconnects seemed to have been alleviated, this work provides ideas for the development of in-situ monitoring technology for stacks.

In summary, this work aims to utilize flat-tube SOECs for CO_2 electrolysis, achieving significant breakthroughs in durability, scalability, and degradation mechanism, which also presented great significance in the development of renewable energy storage. The novel flat-tube cells used in this paper greatly improved the mechanical strength and antioxidant reduction stability of the cells at high temperatures, which provided great

help for long-term CO_2 electrolysis.

Achievements

Publications

[1] **Wu, A.**; Li, C.; Han, B.; Liu, W.; Zhang, Y.; Hanson, S.; Guan, W.; Singhal, S. C. Pulsed electrolysis of carbon dioxide by large-scale solid oxide electrolytic cells for intermittent renewable energy storage. *Carbon Energy* **2023**, *5* (4), e262. https://doi.org/10.1002/cey2.262 (IF: 20.5)

[2] **Wu, A.**; Xiong, M.; Zhang, Y.; Hanson, S.; Wang, J.; Guan, W.; Singhal, S. C. CO_2 utilization by reversible solid oxide cells towards carbon neutralization for long-term energy storage. *Chemical Engineering Journal* **2023**, *466*, 143275. https://doi.org/10.1016/j.cej.2023.143275 (IF: 15.4)

[3] **Wu, A.**; Han, B.; Yao, Y.; Zhang, Y.; Tang, Y.; Hanson, S.; Wang, J.; Guan, W.; Singhal, S. C. Degradation of flat-tube solid oxide electrolytic stack for co-electrolysis of H_2O and CO_2 under pulsed current. *Journal of Power Sources* **2023**, *580*, 233372. https://doi.org/10.1016/j.jpowsour.2023.233372 (IF: 9.2)

[4] **Wu, A.**; Li, C.; Han, B.; Hanson, S.; Guan, W.; Singhal, S. C. Effect of air addition to the air electrode on the stability and efficiency of carbon dioxide electrolysis by solid oxide cells. *International Journal of Hydrogen Energy* **2022**, *47* (58), 24268. https://doi.org/10.1016/j.ijhydene.2022.05.207 (IF: 7.2)

[5] **Wu, A.**; Han, B.; Zhu, L.; Guan, W.; Singhal, S. C. Performance of CO_2 electrolysis using solid oxide electrolysis cell with Ni-YSZ as fuel electrode

under different fuel atmospheres. *International Journal of Green Energy* **2022**, *19* (11), 1209. https://doi.org/10.1080/15435075.2021.1986405 (IF: 3.3)

[6] Pan, H.; **Wu, A.***; Au, S. F.; Yang, Y.; Song, Z.; Liu, Z.; Gong, X.*; Guan, W. Effect of the steam/hydrogen ratio on the performance of flat-tube solid oxide electrolysis cells for seawater. *Sustainable Energy & Fuels* **2023,** *7* (14), 3333. https://doi.org/10.1039/D3SE00351E (IF: 5.6)

[7] Xiong, M.; Han, B.; Yao, Y.; **Wu, A.***; Gao, Y.*; Guan, W. Effect of seawater on the performance of flat-tube solid oxide cell for CO_2/H_2O co-electrolysis. *Fuel* **2024,** *357*, 130039. https://doi.org/10.1016/j.fuel.2023.130039 (IF: 7.4)

[8] Li, C.; **Wu, A.**; Xi, C.; Guan, W.; Chen, L.; Singhal, S. C. High reversible cycling performance of carbon dioxide electrolysis by flat-tube solid oxide cell. *Applied Energy* **2022,** *314*, 118969. https://doi.org/10.1016/j.apenergy.2022.118969 (IF: 11.2)

[9] Luo, X.; **Wu, A.**; Sang, J.; Huang, N.; Han, B.; Wang, C.; Gao, Y.; Guan, W.; Singhal, S. C. The properties of the fuel electrode of solid oxide cells under simulated seawater electrolysis. *International Journal of Hydrogen Energy* **2023,** *48* (28), 10359. https://doi.org/10.1016/j.ijhydene.2022.11.350 (IF: 7.2)

[10] Tang, Y.; **Wu, A.**; Liu, W.; Pei, W.; Guan, W.; Singhal, S. C. Anti-poisoning performance of flat-tube solid oxide fuel cell in high concentration

H_2S environment. *Energy Reports* **2023,** *9*, 5915. https://doi.org/10.1016/j.egyr.2023.05.026 (IF: 5.2)

[11] Tang, Y.; **Wu, A.**; Han, B.; Liu, H.; Bao, S.; Lin, W.; Chen, M.; Guan, W.; Singhal, S. C. Stability of a Solid Oxide Cell Stack under Direct Internal-Reforming of Hydrogen-Blended Methane. *Journal of Electrochemistry*, **2024**, *30* (1), 2314001. https://electrochem.xmu.edu.cn/CN/Y2024/V30/I1/2314001

[12] Yang, H.; **Wu, A.**; Liu, Z.; Su, Y.; Hu, X.; Świerczek, K.; Luo, J.; Meng, A.; Lu, Y.; Lu, Z.et al. A power-to-hydrogen nearby consumption system based on a flat-tube rSOC coupled with local photovoltaics and Yellow River water. *International Journal of Hydrogen Energy* **2024,** *57*, 1111. https://doi.org/10.1016/j.ijhydene.2024.01.113 (IF: 7.2)

[13] Yang, J.; **Wu, A.**; Au, S. F.; Yang, Y.; Huang, X.; Lei, J.; Liu, Z.; Zhang, Y.; Meng, B.; Lu, Z.et al. One-step method to produce feedstock for green ammonia of H_2:N_2≥3:1 by solid oxide cell. *International Journal of Hydrogen Energy* **2024,** *56*, 1132. https://doi.org/10.1016/j.ijhydene.2023.12.264 (IF: 7.2)

[14] Xi, C.; Sang, J.; **Wu, A.**; Yang, J.; Qi, X.; Guan, W.; Wang, J.; Singhal, S. C. Electrochemical performance and durability of flat-tube solid oxide electrolysis cells for H_2O/CO_2 co-electrolysis. *International Journal of Hydrogen Energy* **2022,** *47* (18), 10166. https://doi.org/10.1016/j.ijhydene.2022.01.105 (IF: 7.2)

[15] Yang, G.; Li, Y.; Sang, J.; **Wu, A.**; Yang, J.; Liang, T.; Xu, J.; Guan, W.; Chai, M.; Singhal, S. C. In-situ analysis of anode atmosphere in a flat-tube solid oxide fuel cell operated with dry reforming of methane. *Journal of Power Sources* **2022,** *533*, 231246. https://doi.org/10.1016/j.jpowsour.2022.231246 (IF: 9.2)

[16] Song, Z.; Pan, H.; Wan, G.; **Wu, A.**; Chen, Q.; Guan, W.; Singhal, S. C. Enhancing durability of solid oxide cells for hydrogen production from seawater by designing nano-structured $Sm_{0.5}Sr_{0.5}Co_{3-\delta}$ infiltrated air electrodes. *International Journal of Hydrogen Energy* **2023,** *48* (70), 27095. https://doi.org/10.1016/j.ijhydene.2023.03.366 (IF: 7.2)

[17] Duan, Y.; Cao, B.; Li, S.; **Wu, A.**; Huang, Z.; Wang, J.; Wang, Q.; Yang, J.; Guan, W.; Qi, X. Properties of $CuMn_{1.5}Ni_{0.5}O_4$ spinel as high-performance cathode for solid oxide fuel cells. *Journal of the European Ceramic Society* **2023,** *43* (12), 5298. https://doi.org/10.1016/j.jeurceramsoc.2023.05.003 (IF: 5.7)

[18] Wang, J.; Zhao, Y.; Yang, J.; Sang, J.; **Wu, A.**; Wang, J.; Guan, W.; Jiang, L.; Singhal, S. C. Understanding thermal and redox cycling behaviors of flat-tube solid oxide fuel cells. *International Journal of Hydrogen Energy* **2023,** *48* (57), 21886. https://doi.org/10.1016/j.ijhydene.2023.03.062 (IF: 7.2)

[19] Hu, X.; Yang, Y.; Han, B.; Huang, X.; Lei, J.; Sang, J.; **Wu, A.**; Liu, Z.; Lu, Z.; Guan, W. Efficiency and stability of seawater electrolysis through flat-tube solid oxide cell stack without air. *International Journal of*

Hydrogen Energy **2024,** *55*, 909. https://doi.org/10.1016/j.ijhydene.2023.11.138 (IF: 7.2)

Patents

[20] **Anqi Wu**, Beibei Han, Yan Yao, Meng Xiong, Wanbing Guan, A method for electrolyzing carbon dioxide in a solid oxide electrolytic cell. Application number: 2023106925255. (Chinese)

[21] Meng Xiong, **Anqi Wu**, Beibei Han, Yan Yao, Wanbing Guan, A method for co-electrolysis of seawater and carbon dioxide to synthesize fuel. Application number: 2023105598985. (Chinese)

[22] Meng Xiong, Wanbing Guan, Yan Yao, **Anqi Wu**, Yang Zhang, Beibei Han, An electric energy storage device and system. Application number: 2023107895401. (Chinese)

Acknowledgement

As the years flew by, the intense and fulfilling PhD life is coming to an end. In the past three years and four months, with the support of my supervisors, research teams, friends, and family, I have harvested a lot, both in daily life and scientific research. Before completing my PhD thesis, I would like to express my sincerest gratitude to the supervisors, colleagues, friends, and family who have provided me with help, encouragement, and guidance in scientific research, study, and life over the years.

My heartfelt appreciation goes to my three supervisors: ***Dr. Svenja Hanson***, ***Prof. Wanbing Guan*** and ***Dr. Jing Wang***, and my internal assessor, ***Dr. Mengxia Xu***. Dr. Svenja Hanson not only patiently guided me in research directions, paper writing, and English speaking, but also provided me with care and assistance psychologically and in daily life. She always cares about my safety and the progress of completing thesis or projects. Prof. Wanbing Guan provides me with careful guidance and assistance in the selection of PhD topics, experimental design, and paper writing. During my three-year research life at Ningbo Institute of Materials Technology & Engineering, CAS (Nimte), Prof. Guan provided me with a research platform and gave me a lot of opportunities to visit and make academic presentations, which greatly improved my research ability, stress resistance, and interpersonal communication skills. In these years, Dr. Jing Wang and Dr. Mengxia Xu always points out key issues and propose improvement

suggestions in my reports and speeches.

Needless to say, an experimental PhD cannot be finished in time without the help of everyone in my research team. I would like to thank ***Prof. Jun Yang***, ***Prof. Liangzhu Zhu***, ***Prof. Jianxing Wang***, ***Dr. Wu Liu***, Dr. Beibei Han, Dr. Yang Zhang, Dr. Junkang Sang, Chengtian Wang, Jiawei Yang, Meng Xiong, Yafei Tang, Jiping Wang, Hu Pan, Zihan Song, Xiaogang Hu, Haoliang Tao, Shiqing Li, Zhao Liu, Mingze Gao, Xing Luo, Chaolei Li, Gang Yang, Chengqiao Xi, Shuaifan Li, Yang Wu et al. in Fuel cell technology team at Cnitech. Additionally, I would like to thank Liang Xu, Zihan Wang, Xiaohui Chang at H_2-Bank Co., Ltd. I would like to sincerely thank the faculty at UNNC and graduate office at Nimte.

Last but not the least, I would like to take this opportunity to thank my friends and family who give support and encouragement when I'm feeling down. They always patiently listen to my words and give me advice and comfort.

There are still many people whose names I did not list. Please don't worry, I won't forget the help you have given me. Thanks for all the encounters and assistance. I sincerely wish my supervisors, colleagues, friends, and family to have good health, and a successful career. Wish UNNC and Cnitech become better.

Table of Contents

List of Figures

List of Tables

List of Abbreviations

AEM	anion exchange membrane
ALK	alkaline
ASR	Area specific resistance
BES	Bioelectrochemical systems (BES)
CO_2RR	CO_2 reduction reaction
CRB	CO_2 redox flow battery
D band	Disordered carbon band
DBD	Dielectric barrier discharges
DRT	Distribution of relaxation time
DTU	Technical University of Denmark
ECE	Energy conversion efficiency
EIFER	European Institute for Energy Research
EIS	Electrochemical impedance spectroscopy
GA	Gliding arc
G band	Graphite band
GC	Gas chromatograph
GDC	Gadolinium-doped ceria
IEA	International Energy Agency
INL	Idaho National Laboratory
IRENA	International Renewable Energy Agency
JAERI	Japan Atomic Energy Research Inst
LSC	$La_{1-x}Sr_xCoO_{3-\delta}$
LSCF	$La_{0.6}Sr_{0.4}Co_{0.2}Fe_{0.8}O_{3-\delta}$

LSM	$La_{1-x}Sr_xMnO_3$
MCEC	Molten carbonate electrolysis cells
MEA	Membrane electrode assembly
MEC	Microbial electrolysis cell
MFC	Microbial fuel cell
MW	Microwave
OCV	Open circuit voltage
OER	Oxygen evolution reaction
PEM	proton exchange membrane
PMMA	Polymethyl Methacrylate
PVA	Polyvinyl alcohol
RSOC	Reversible solid oxide cell
RWGS	Reverse water gas shift
ScSZ	Sc_2O_3 stabilized zirconia
SEM	Scanning electron microscope
SLM	Standard litre per minute
SOC	Solid oxide cell
SOEC	Solid oxide electrolysis cell
SOFC	Solid oxide fuel cell
SWPC	Siemens Westinghouse Power Corporation
TCD	Thermal conductivity detector
TEC	Thermal expansion coefficient
TPB	Triple phase boundary
YSZ	yttria-stabilized zirconia

List of Symbols

°C	Degree Celsius
°F	Fahrenheit degree
ppm	Part per million
nm	Nanometer
μm	Micrometer
mm	Millimeter
h	Hour
W	Watt
KJ	Kilojoule
mol	Mole
L/min	Liter per minute
GW	Gigawatt
cm S^{-1}	Centimeter per Siemens
K	Kelvin
A	Ampere
ml/min	Milliliters per minute
Nml/cm^2h	Milliliters per square centimeter per hour
C/mol	Coulomb per mole
J/mol	Joule per mole

Road map of this thesis

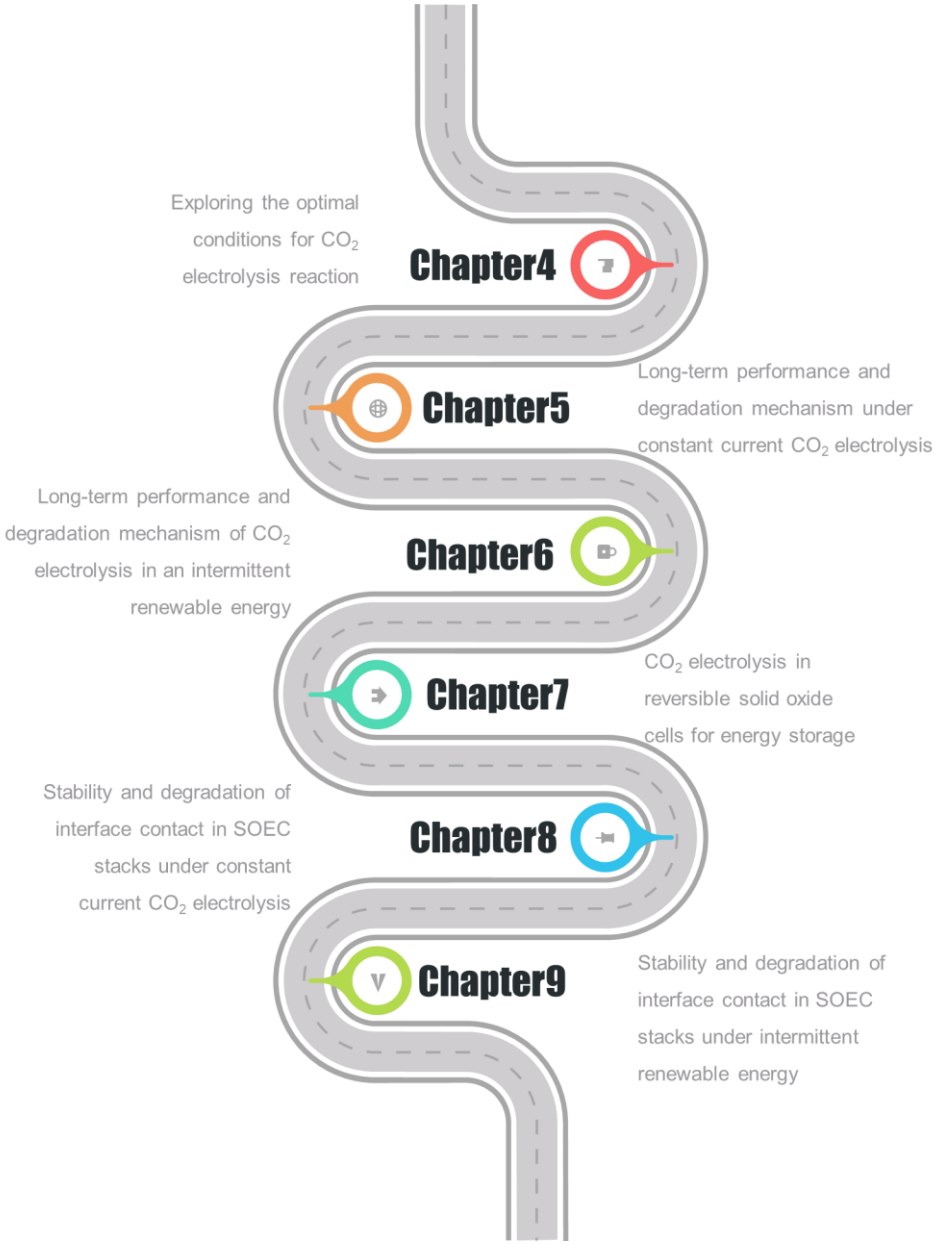

Chapter 1. Research background

1.1 Research background

Since the industrial revolution, with the widespread burning of fossil fuels, CO_2 concentration in the atmosphere has increased year by year, from 280 ppm in 1750 to 424 ppm in 2023. The global heating brought on by the rising CO_2 concentration has greatly threatened the survival of species [1, 2]. Therefore, it is imperative to develop a low-carbon economy and achieve carbon neutrality as soon as possible. The signing of the Paris Agreement in 2015 proposed a long-term goal of maintaining the increase in global average temperature below 2 °C above pre-industrial levels, which further strengthened the determination of countries to strive for the long-term goal of low carbon emissions. Although the spread of COVID-19 reduces people's travel, thereby affecting CO_2 emissions, carbon emissions returned to the previous level once the crisis lifted. Energy transformation and decarbonization remain important measures to alleviate the energy crisis and climate change [3-6].

Solar, wind and tidal energies are common renewable energy sources, however, they all exhibit an “intermittent” operation, with their output power fluctuating in response to changes in external energy [7, 8]. If “intermittent” energy is directly connected to the grid, it may increase the burden on the grid, and affect the normal transmission of electricity [9, 10]. Therefore, it is

necessary to establish an energy consumption and storage system near the power generation system that uses “intermittent” energy, to realize a high proportion of intermittent renewable energy to be integrated [9, 11].

PSP (pumped storage plant) is the largest, most efficient and commercially sustainable form of grid energy storage available in the world [12], but it needs large capital investment, proposes high requirements for geographical location and occupies a large floor area. Recently, the potential for developing new pumped storage sites is declining [7, 13-14]. As a consequence, it is crucial to develop and adopt new energy storage methods to absorb “intermittent” energy. Power-to-Gas (P2G) technology seems to be a promising approach to absorb renewable energy, which involves using electrolysis to split CO_2 into fuel gas and oxygen. The fuel gas can then be stored for later use. This method results in less electricity waste [15]. Lithium-ion, lead-acid and liquid flow batteries are commonly leveraged in electrochemical energy storage technology. These battery systems have a certain installed capacity, but unfortunately, they still expose many shortcomings for large-scale energy storage systems applied to public utilities, and require significant improvements in performance, stability, material life, safety, and efficiency.

A solid oxide electrolysis cell (SOEC) is a device that can directly convert electric energy into chemical energy, which has the advantages of high conversion rate, high efficiency, and fast kinetics. SOECs are a new

energy storage technology with high potential and accuracy for fuel production and energy applications. The electrochemical response of SOECs can be almost completed in an instant [16, 17]. Nowadays, the solid oxide cell (SOC) system has been proven to have great potential to be durable for over 10 years, with a round-trip system efficiency of approximately 60-90%. Compared to other electrochemical energy storage methods, the attraction of SOCs lies in the power-to-gas and gas-to-power storage modes, which can store excess energy through off-peak electricity to produce useful chemicals and fuels such as H_2, CO, O_2 by electrolysis.

The largest obstacle to the commercialization of SOECs is their durability under high temperature conditions. The degradation during high-temperature operation mainly comes from changes in the fuel electrode, the air electrode, the electrolyte layer, the contact areas between electrode and electrolyte, as well as the stack components [18, 19]. There are many studies on the degradation of fuel electrodes, and the main results show that nickel coarsening occurs in the fuel electrode structure [20-23]. The performance decline caused by oxygen electrode degradation may be related to strontium segregation, the formation of secondary phases such as strontium oxide and strontium zirconate, electrode delamination and the formation of Co rich phases [24, 25]. The degradation at the interface between electrodes and electrolyte includes the formation of grain boundaries, and the formation of nano-pores during long-term testing [26-29]. In a SOEC stack composed of

multiple units, the degradation mechanism becomes more complex, because of the addition of more components: Cr vapor poisoning from the interconnects and Si poisoning from the sealing materials can also seriously affect the activity of the oxygen exchange reaction in the air electrode [30-32]. Considering the stability and lifespan of the stack, it is generally necessary to add a coating on the surface of the interconnects to weaken or eliminate the toxic effect of chromium on the functional layer during large-scale or long-term energy storage operations [33, 34].

SOEC technology combined with intermittent renewable energy power plays an important role in energy intensive areas and is used for sustainable production of syngas for industrial sectors and transportation [35]. In practical industrial applications, large energy storage devices are hard to manage to ensure stable electricity, and exploring the operation under non-stationary conditions will be an even greater challenge. The reversible solid oxide cell (RSOC) system can realize power-to-gas and gas-to-power conversion by using CO-CO_2 as the energy storage medium, so as to store electricity when there is sufficient power and release power when the electricity is insufficient. However, there are still a lot of aspects to be considered to develop SOC energy storage device, which involve low carbon footprint, safety, continuity, and high energy efficiency, as well as high stability and energy storage capacity. There is hope to open up a promising new technical route for the improvement of grid quality and the realization

of carbon neutrality if satisfactory results can be achieved.

1.2 Aims and objectives

The purpose of this thesis was to clarify the durability and degradation mechanism of nickel-based flat-tube solid oxide electrolysis cell stacks under various operating conditions so as to achieve high CO_2 conversion and efficient power-gas-power conversion under long-term high-temperature operation. In the context of "carbon neutrality" and "energy storage", the research objectives of this thesis are as follows:

(1) Explore the optimal experimental conditions for CO_2 electrolysis in flat-tube solid oxide electrolysis cells, including initial performance, short-term durability and electrochemical impedance testing, as well as gas composition analysis. Thermodynamics of carbon deposition, energy conversion efficiency, and CO_2 conversion rate calculations were carried out. The results were intended to become the foundation for long-term durability experiments.

(2) Explore the influence of the fuel electrode and air electrode atmosphere on the long-term CO_2 electrolysis operation using solid oxide electrolysis cells, and analyze the degradation mechanism of each electrode under each atmosphere, propose improvement plans and provide reference data for various industrial application scenarios.

(3) Simulate the industrial application scenario of coupling SOECs with

intermittent renewable energy and simulate the application mode of power-gas and gas-power conversion through reversible charging and discharging cycles, to meet the high requirements of power grid connection. The energy storage capacity of solid oxide electrolysis cells was analyzed by exploring the long-term durability, energy conversion efficiency and the degradation mechanism of the cells under constant current, pulsed current and reversible cycle conditions. Further, the application prospect was proposed by comparing it with other electrochemical energy storage methods.

(4) Carry out research on the constant current CO_2 electrolysis in a three-unit solid oxide electrolytic stack based on the durability and degradation mechanism of single cells, and study the internal degradation mechanism of the stack under different operating currents, as well as the degradation mechanism at the electrolyte/electrode interface. Propose new methods for improving the performance, durability, structure, sealing, and assembly methods.

(5) Simulate the coupling with renewable energy using intermittent pulsed current, and analyze the degradation mechanism of the electrolytic stack during the long-term operation of CO_2 electrolysis. Determine if the interconnects in the stack can be further optimized with coatings to improve the lifespan of the stack in unsteady pulsed current.

1.3 The thesis structure

Chapter 1 covers the background, aims, and objectives of the research and the thesis structure. **Chapter 2** focuses on literature review, involving CO_2 utilization, the principles and materials of solid oxide electrolysis cells, the degradation of each component in solid oxide electrolysis cells and the current state of energy storage.

The experimental and characterization methods are presented in **Chapter 3**, including the preparation, assembly and test methods of cells and stack, electrochemical impedance test, scanning electron microscope analysis, gas composition analysis, energy conversion efficiency analysis and mechanical property test.

Chapter 4 illustrates the influencing factors of CO_2 electrolysis in solid oxide cells, encompassing temperature, protective gas type and volume fraction. The critical values of carbon deposition and the methanation reaction were calculated. Through short-term stability and gas chromatography analysis, the suitable condition for long-term operation was selected.

Chapter 5 elaborates the long-term performance of solid oxide electrolysis cells under the conditions with air and without air in the air electrode. The degradation of each electrode with or without air during long-term operation was compared. A long-term test without reducing gas in the fuel electrode was conducted for analyzing the oxidation resistance of

nickel-based fuel electrode.

To investigate the cell performance under unstable electrolytic current, the long-term performance and degradation mechanism of CO_2 electrolysis under intermittent renewable energy were explored in **Chapter 6**. For the aims of energy storage in the case of energy surplus, and electricity generation in the case of insufficient power, the reversible solid oxide cells were used in **Chapter 7**. Besides, carbon-contained fuels could be recycled in each cycle.

Chapter 8 and **9** feature the degradation of solid oxide electrolytic stacks during CO_2 electrolysis. **Chapter 8** mainly focuses on the degradation mechanism of the cells and interfaces inside the stack during constant current electrolysis. **Chapter 9** describes the stack structure and interconnects modified for CO_2 electrolysis with renewable energy. **Chapter 10** is the discussion and conclusion section.

Chapter 2. Literature review

2.1 Introduction to energy demand and security

Energy serves as the foundation of human societies, supporting human survival and development [36]. China is the world's largest energy consumer, characterized by abundant coal, scarce oil, and limited gas resources. The high dependence on overseas for crude oil and natural gas also highlights China's energy security issues [37]. To ensure China's energy security and prevent the continuous deterioration of the environment, it is necessary to continuously develop and utilize clean and environmentally friendly renewable energy to change the current energy pattern dominated by fossil fuels.

According to statistics from the International Energy Agency (IEA), although China has made significant progress in renewable energy since 2000, it still heavily relies on fossil fuels [38]: In 2020, about 85% of China's total primary energy demand was provided by fossil fuels, with coal alone accounting for nearly 60% and oil accounting for about 20%. From 2002 to 2013, the economic growth rate was the fastest. During this period, coal accounted for 77% of the total increase in China's primary energy demand. With the improvement of efficiency and policy restrictions on coal use expansion, coal consumption has been roughly stable since 2013, but in 2019-2020, coal demand once again increased. Although fossil fuels

continue to dominate, nuclear power, hydropower, bioenergy, and other renewable energy sources have experienced significant development in the past decade, with their share in the total demand for primary energy also increased by about 5%. The forecast results in World Energy Outlook 2023 indicated that coal demand in China would continue to increase until 2024, and then decrease from 2025 [39].

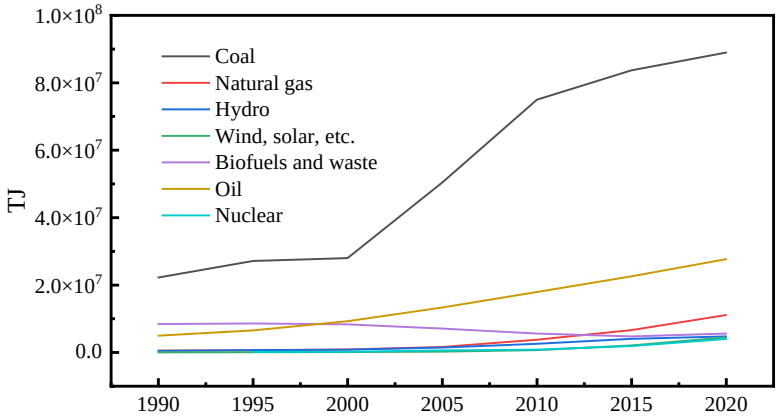

Figure 2.1. The total primary energy demand for different sources in China [38]

Table 2.1. The proportion (%) of primary energy demand for different sources in China from 1990 to 2020 [38]

	Coal	Natural gas	Hydro	Wind, solar, etc.	Biofuels and waste	Oil	Nuclear
1990	60.74	1.47	1.25	0.00	22.95	13.60	0.00
1995	62.02	1.44	1.57	0.12	19.60	14.94	0.32
2000	58.92	1.83	1.69	0.23	17.48	19.47	0.38
2005	67.55	2.18	1.92	0.30	9.45	17.84	0.78
2010	70.56	3.52	2.41	0.63	5.25	16.87	0.76
2015	66.65	5.29	3.19	1.64	3.79	17.96	1.48
2020	60.69	7.57	3.25	3.05	3.82	18.89	2.73

According to results of Our World in Data [40], the global primary energy consumption increased with year. In 2022, the total amount reached 178,899 TWh, coal accounted for 44,854 TWh, oil accounted for 52,970 TWh, solar energy reached 3,448 TWh and wind energy accounted for 5,488 TWh, as shown in **Table 2.2** and **Figure 2.2**.

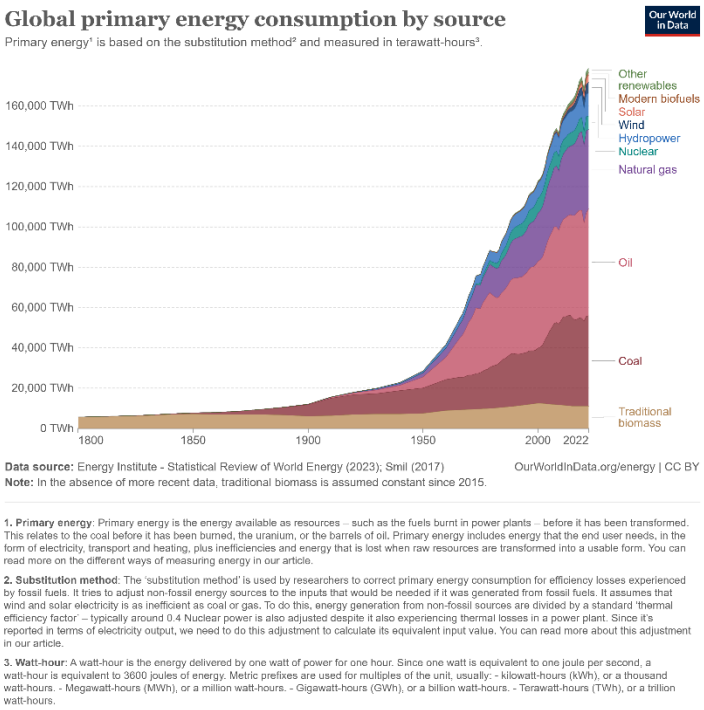

Figure 2.2. The total primary energy demand from different sources in the world [40]

Table 2.2. The amount of primary energy demand for different sources in the world in 2022 [40]

2022	Coal
Other renewables	2,414 TWh
Modern biofuels	1,199 TWh
Solar	3,448 TWh

Wind	5,488 TWh
Hydropower	11,300 TWh
Nuclear	6,702 TWh
Natural gas	39,413 TWh
Oil	52,970 TWh
Coal	44,854 TWh
Traditional biomass	11,111 TWh
Total	178,899 TWh

Carbon dioxide is an important medium in the global carbon cycle, but excessive emissions caused by the combustion of fossil fuels pose a threat to ecosystems. China is currently the world's largest emitter of carbon dioxide. By the end of 2022, the carbon emissions amount of China had reached 11.4 billion tons, mainly due to the industrial system dominated by fossil fuels and manufacturing [41]. Under increasing environmental pressure, "carbon neutrality" has become a consensus among various countries, but its implementation still faces many challenges such as politics, resources, technology, markets, and the structure of the energy economy. The proposed solutions for the "dual carbon" goal include: (i) Energy substitution and transformation, such as commercial applications of non-carbon energy such as renewable energy, green hydrogen and green methanol [42]; (ii) Energy conservation and emission reduction [43]; (iii) Carbon-based energy recycling [44]; (iv) Ecological carbon sequestration [45]. Among them, substitution and transformation of energy can be the main approach.

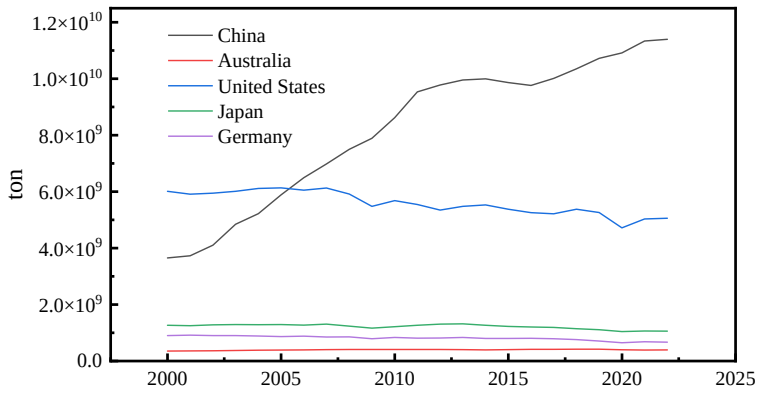

Figure 2.3. Carbon emissions of different countries from 2000 to 2022 [41]

Solar energy, wind energy, and tidal energy are several common types of renewable energy with abundant resources. Compared to traditional fossil energy, the development level of renewable energy is relatively low, along with broad development prospects [46, 47]. However, the above-mentioned renewable energy sources are “intermittent”, and their output power fluctuates with external energy, resulting in low competitiveness of renewable energy technology [48, 49]. The direct connection of intermittent energy to the grid may have an impact on the power grid and increase the burden of power grid, thus affecting the normal transmission of electricity [50]. Therefore, according to the status of China’s power grid, it is necessary to establish an energy consumption system that can solve the problem of integrating intermittent renewable energy into the grid [51].

Driven by factors such as energy security, economic development, and air quality, the promotion of renewable energy has always been an important part of China’s energy policy. To facilitate energy substitution and

transformation, the "14th Five Year Plan" has identified new energy and new automotive technology as strategic emerging industries [52]. The plan emphasizes the need to increase efforts to reform the energy market, promote low-carbon energy investment, and ensure energy security. In recent years, the rapid development of renewable energy in China has also provided a strong driving force for global energy transformation. According to data released by the International Renewable Energy Agency (IRENA), by the end of 2022, the global installed capacity of renewable energy generation had reached 3372 GW, with the stock of renewable energy increased by about 9.6%. Almost half of the newly installed capacity in 2022 was in Asia, with China contributing the most [53], which fully demonstrated China's efforts in energy provision reform.

Facing the intermittent challenges of renewable energy, developing scalable energy conversion technologies is the key to effectively utilizing renewable energy. Since the signing of the "Paris Agreement" in 2016, China, as the world's largest wind energy supplier, has taken action to promote renewable energy. According to statistics on renewable energy capacity, in 2022, the newly installed capacity of wind and photovoltaic power generation in China exceeded 120 million kilowatts, reaching a new historical high value. The newly installed capacity of all the kinds of renewable energy was 152 million kilowatts, accounting for 76.2% of the total newly installed power generation. By the end of 2022, the installed

capacity of renewable energy and pumped storage had exceeded 1.2 billion kilowatts, accounting for 47.3% of the total installed capacity of power generation in China, further indicating the gradual transformation of China's energy system towards a low-carbon energy system [54].

In the fields of industrial manufacturing and transportation, the development of hydrogen energy can effectively reduce the emissions of carbon containing gases [55]. Carbon conversion technology can be conducive to transition of the emitted waste carbon to "working carbon" [56]. According to the energy situation of China, CO_2 based power-to-gas and gas-to-power conversion technology is expected to become a key technology. However, carbon capture and storage (CCS) technology faces many challenges, such as CO_2 storage leakage as well as high energy consumption and cost of carbon capture, transportation, and storage processes [57]. Using renewable electricity to convert CO_2 into useful materials instead is an attractive solution that can promote the achievement of the "dual carbon" goal.

With the continuous increase in the proportion of renewable energy in various countries around the world, how to improve the energy storage capacity, peak shaving capacity, and flexibility of the power grid, and enhance the resilience of the energy system has become one of the main problems that needs to be dealt with during energy transformation. With the occurrence of various global emergencies, the energy industry and supply

chain are bound to be impacted. Ensuring national energy security and normal operation of both economy and society is of utmost importance. Therefore, it is essential to search for key technologies for the future energy blueprint. One promising emerging technology that may in future play a significant role is solid oxide electrolysis cells (SOECs).

2.2 Introduction to Solid Oxide Electrolysis Cells (SOECs)

2.2.1 CO_2 conversion in SOECs

The main technological routes for CO_2 utilization include thermochemical conversion, electrochemical conversion, biological conversion and photocatalytic conversion. The products may be methane, methanol, syngas, urea, organic carbonates and formic acid [58, 59]. Although these carbon utilization technologies have made significant progress in the past few years, most are still at the laboratory scale. Among these methods of carbon dioxide conversion, electrochemical methods are the most efficient and economical and are thus considered the most likely technologies to be commercialized and support the energy transformation from fossil fuels to renewable energy. Resulting from the unpredictability of intermittent energy generation from wind energy and solar energy, the generated power may be surplus. Electrochemical conversion methods can utilize or store excess energy that cannot be directly fed into the grid, eliminating the risk of energy being wasted. Alternatively, they offer an

opportunity of CO_2 to be selectively converted into low-carbon fuels or high economic value chemicals, and directly used to satisfy market demand [60].

Electrochemical CO_2 conversion methods can be further divided into high-temperature and low-temperature technologies. Low-temperature technology utilizing flow cell (<100 °C) and molten electrolysis cells (>400 °C) [61, 62] has not been widely used because of their low selectivity for target products, low energy efficiency, insufficient stability and short service life. High temperature reduction technology is known as an electrocatalytic electrolysis technology with solid oxide electrolysis cells as the core that is close to commercialization. The electrode reactions of SOECs are fast, simple and stable, and the start-stop process is easy to control. Additionally, SOECs have a higher Faraday efficiency because of the high working temperature. If industrial waste heat can be utilized, operating costs will be greatly reduced and the overall energy efficiency of the electrocatalytic electrolysis conversion system will be improved. More importantly, solid oxide cell systems can also reversibly use CO as the raw gas for discharge, i.e. function as reverse solid oxide cells (RSOCs), so as to promote the continuous operation of power-gas-power as a "carbon cycling" technology. They can thereby help reduce the environmental impact of power generation and lower energy supply costs. SOECs are now considered one of the most cost-effective options for long-term power storage [63].

Taking SOEC-O^{2-} as an example, during the electrolysis of CO_2, CO_2

enters from the fuel electrode of SOECs and undergoes a decomposition reaction with an external DC power to produce CO and oxygen ions. Oxygen ions are transported from the fuel electrode side to the air electrode side through a solid electrolyte, producing oxygen through oxygen evolution reaction. The specific reaction equation is:

Fuel electrode reaction: $CO_2 + 2e^- \rightarrow CO + O^{2-}$ (Eq. 2.1)

Air electrode reaction: $O^{2-} \rightarrow 1/2O_2 + 2e^-$ (Eq. 2.2)

Total reaction: $CO_2 \rightarrow CO + 1/2O_2$ (Eq. 2.3)

During the operation of the electrolysis cells, if H_2 is used as a reducing protective gas, the reverse water gas shift (RWGS) reaction will also happen in the fuel electrode under catalysis (such as Ni catalysts):

$$H_2(g) + CO_2(g) = CO(g) + H_2O(g) \quad \text{(Eq. 2.4)}$$

When the extent of RWGS reaction is large enough, the fuel electrode is more inclined towards CO_2/H_2O co-electrolysis reaction. Due to the easier occurrence of the steam electrolysis reaction, the electric potential of co-electrolysis reaction will be lower than that of the electrolysis of pure CO_2 [64]. From a thermodynamic perspective, the total energy required during the operation of CO_2 electrolysis in SOECs is composed of thermal and electrical energy, both provided by the external environment and Joule heat generated by the cells.

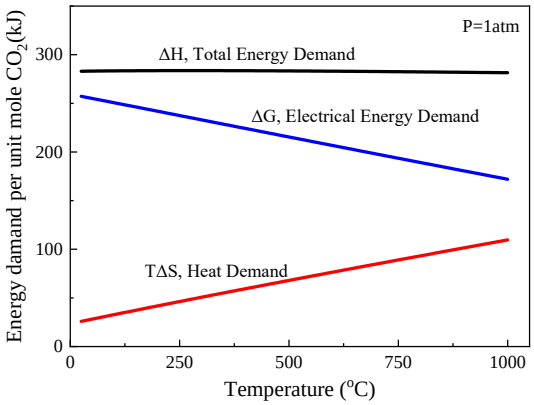

Figure 2.4. Thermodynamic analysis of carbon dioxide electrolysis reaction

According to the thermodynamic calculation results in **Figure 2.4**, as the reaction temperature increases, the total energy demand of the CO_2 electrolysis process remains basically unchanged, with an increase in thermal energy demand and a decrease in electricity demand. This is mainly because the CO_2 decomposition reaction belongs to an endothermic reaction. At room temperature (25 °C), the electrical energy required for CO_2 decomposition reaction accounts for more than 90% of the total energy demand, while at 750 °C, the proportion of electrical energy demand decreases to 68%, and the reduced electrical energy is replaced by thermal energy. As the temperature increases, the electrical energy consumption during the electrocatalytic conversion process decreases, which is more conducive to large-scale applications. If the industrial waste heat can be fully utilized to maintain the operating temperature of SOECs, the comprehensive economic benefits and cost competitiveness of SOECs can be significantly improved, and the cost for CO_2 electrolysis can be reduced [65].

If the energy demand is expressed as voltage, the following equation

can be obtained:

$$\Delta G_f = -nFE^0 \quad \text{(Eq. 2.5)}$$

where E^0 represents the reversible potential, the minimum cell potential required to maintain CO_2 splitting, n is the number of electrons involved in the reaction (for reducing CO_2 to CO, n=2) and F refers to the Faraday constant (96485 C/mol). According to the calculation results obtained from the HSC chemistry software, at 25 °C, ΔG_f is 256.94 kJ/mol, and corresponding E^0 is 1.33 V; while at 750 °C ΔG_f is only 193.36 kJ/mol, and E^0 is 1.002 V.

For reversible processes that are not in a standard state (1 atm), the reversible cell voltage depends on the reactant partial pressure, and the Nernst equation can be used to calculate the reversible cell voltage:

$$E^0 = \frac{\Delta G_f}{nF} - \frac{RT}{nF} ln \frac{p_{CO_2}}{p_{CO}\sqrt{p_{O_2}}} \quad \text{(Eq. 2.6)}$$

where R is the gas constant, T represents the absolute temperature, p_{CO_2} is the partial pressure of CO_2 on the cathode, p_{CO} denotes the partial pressure of CO on the cathode, and p_{O_2} means the partial pressure of oxygen on the anode. When the gas partial pressure changes, there will also be a slight change in E^0. When the current passes through the electrolysis cell to undergo CO_2 decomposition reaction, Joule effect heat is generated to compensate for the thermal energy demand during electrolysis. Joule heat can be utilized in high-temperature electrolysis cells to achieve higher efficiency. When the voltage of the electrolysis increases to a certain value, Joule heat generated by the current can exactly meet the thermal energy required for the electrolysis reaction without the need for additional heating,

and the voltage at this time is called the thermal neutral voltage [66]:

$$E_{th} = \frac{\Delta H}{nF} \quad \text{(Eq. 2.7)}$$

where ΔH is the total energy required for the high-temperature CO_2 electrolysis reaction (kJ/mol); E_{th} denotes the thermal neutral voltage (V); n is the number of electron transfers; F means the Faraday constant (C/mol).

The progress of the electrolysis reaction in SOECs is driven by external overvoltage. When CO_2 decomposition reaction occurs, the reactions occurring in the fuel electrode are related to multiple processes such as material adsorption, migration, dissociation, charge transfer, and desorption. The deviation of voltage from the thermodynamic equilibrium state is called polarization loss. Polarization of electrolysis cells can generally be divided into electrochemical polarization, ohmic polarization and concentration polarization. At low current density, electrochemical polarization plays a dominating role, while in high current density, concentration polarization tends to dominate [67]. Electrochemical polarization is mainly caused by insufficient catalytic performance of electrode materials, which means that reactions are hindered on the surface of electrodes. Electrochemical polarization can usually be reduced by modifying material properties and improving the microstructure of cells [68]. Ohmic polarization is the phenomenon that the electrode potential deviates from the equilibrium potential due to the resistance of the electrolysis cell component, which obeys Ohm's law. Ohmic polarization of SOECs is mainly generated by the

conduction of oxygen ions in the electrolyte. This is primarily because the electronic conductivity of electrode materials is much higher than that of electrolyte materials. Therefore, it is necessary to increase the conductivity of oxygen ions in electrolyte materials or shorten the transportation distance of oxygen ions to decrease ohmic polarization in the electrolysis cells [69]. Concentration polarization is a polarization phenomenon caused by the fast charge transfer rate in cells, which occurs when the concentration of reactants is insufficient to maintain the electrode reaction. Concentration polarization is determined by the mass transfer process, driven by concentration gradients, and is related to factors such as pressure, temperature, reaction flow rate, and electrode porosity. As a result, the usual solution is to strengthen the performance of the electrolysis cells by increasing the concentration of reactants or optimizing the cell structure [70].

According to the above definitions, the working voltage of SOEC can be expressed as:

$$V = E + \eta_{conc,c} + \eta_{conc,a} + \eta_{act,c} + \eta_{act,a} + \eta_{ohmic} \quad \text{(Eq. 2.8)}$$

where E is the equilibrium potential (V); $\eta_{conc,c}$ and $\eta_{conc,a}$ are the concentration overpotentials of fuel electrode and air electrode, respectively; $\eta_{act,c}$ and $\eta_{act,a}$ are the activation overpotentials of the fuel electrode and air electrode, respectively; η_{ohmic} refers to the ohmic overpotential.

2.2.2 The Principles of SOECs

An electrolysis cell is a device that converts electrical energy into

chemical energy, normally consisting of two electrodes and an electrolyte. Based on the technological maturity in hydrogen production through electrolysis of water, the US Department of Energy has classified four electrolysis technologies: alkaline (ALK) [71], proton exchange membrane (PEM) [72], anion exchange membrane (AEM) [73], and solid oxide (SOEC) [74], for reference by industry professionals.

Solid oxide electrolysis cells, such as cells used for high-temperature CO_2 electrolysis, can be regarded as an energy conversion device with an all-solid ceramic structure. The basic structure and design principle of a SOEC are displayed in **Figure 2.5**. The working temperature is usually above 600 °C. A typical SOEC consists of three layers, with a dense electrolyte layer in the middle, flanked by a porous fuel electrode (cathodes) and an air electrode (anodes). Solid electrolyte materials mainly play the role of ion transport in the electrolysis cells, achieving the transfer of oxygen ions (O^{2-}) from the fuel electrode to the air electrode. Another function is to separate the fuel electrode and the air electrode, preventing the mixing of the raw and product gases. This requires solid electrolyte materials to exhibit high ion conductivity, and to act as poor conductors of electrons to prevent short circuits [75].

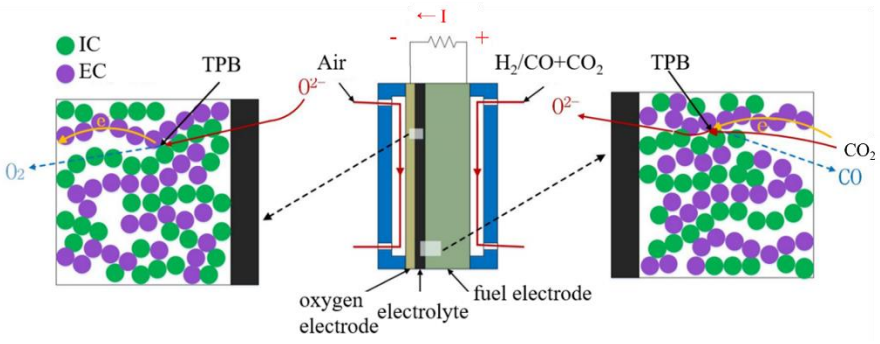

Figure 2.5. Schematic diagram of CO_2 electrolysis reaction in solid oxide

electrolysis cell, where IC= ionic conductor, EC=electronic conductor

The porous fuel electrode and air electrode are respectively connected to the negative and positive electrodes of the DC power supply, providing sufficient active sites for electrochemical reduction and oxygen exchange reactions, and also offering pathways for the transportation of electrons, ions, reactants, and products. Therefore, it is required that both fuel electrode and air electrode materials must be excellent electronic and ionic conductors with sufficient catalytic activity for CO_2 reduction and oxygen exchange reactions, respectively. Electrode materials also need to possess an appropriate porosity, which enables gas diffusion and transportation, and also creates sufficient triple phase boundaries (TPBs) for the electrode reaction of the electrolysis cells. The triple phase boundaries are interfaces between the oxygen ion conductor (electrolyte), electron conductor (electrode), and reaction gas (carbon dioxide) [76]. To obtain the required power capacity, cells are often connected in series to form an electrolytic stack. The cells in the stack are connected through interconnects, which are often made of stainless-steel materials with high-temperature electron conductivity. To prevent high-temperature oxidation and corrosion of interconnects, SUS441 grade steel is usually applied.

SOCs can achieve the required catalyst activity without expensive precious metals, which enables them to tolerate variable feed components such as steam and carbon containing fuels.

2.2.3 The Structure of SOECs

At the macro level, there are three common types of SOCs on the market, namely flat-tube, planar and tubular, as shown in **Figure 2.6**. The most advanced tubular SOC is being developed by Siemens Westinghouse Power Corporation (SWPC) [77]. The highly symmetrical structure endows the tubular SOCs with high mechanical strength and thermal stability, and the smaller sealing area makes it easier to assemble into SOC stacks. Although the performance test results in the laboratory stage are quite advantageous, the commercialization of the tubular structure still encounters great obstacles, such as long current transmission path, uneven current collection, insufficient utilization of fuel gas and high manufacturing cost. Consequently, it is better to turn to flat-tube structure [78-80].

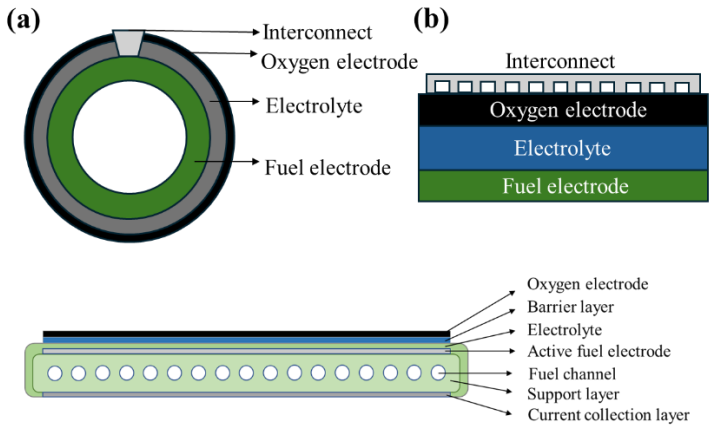

Figure 2.6. Three types of SOC structures: (a) tubular, (b) planar and (c) flat-tube

The planar structure is generally made of YSZ electrolyte (yttria-

stabilized zirconia), with shorter current transmission path and higher power density. With good flatness, cells with planar structure are easy to assemble into a stack. However, the traditional cells with planar structure planar structure also have some problems yet to be solved. Compared with the highly symmetrical tubular structure, the asymmetry of cells based on planar structure leads to poor oxidation-reduction performance. When the fuel electrode Ni is oxidized, the cell matrix tends to expand and break, causing serious irreversible degradation. Therefore, traditional planar SOECs propose strict sealing requirements [81-84].

SOCs with flat-tube structure combine the advantages of tubular and planar structures, constructing the fuel electrode channel in a thick matrix. The fuel gas first enters the channel and gradually diffuses to the porous fuel electrode, making the gas diffusion more sufficient inside the cell. This avoids insufficient reduction caused by a large active area of the cell, and greatly improves the utilization of fuel gas. In addition, flat-tube SOCs overcome the problem of poor mechanical strength of conventional thin cells and can satisfy the high strength requirements during high-temperature operation. Flat-tube SOCs are regarded as the most promising SOC type for large-scale industrial applications [85, 86].

SOCs are usually divided into two categories based on the supporting components: self-supporting and external supporting [87]. The self-supporting types can be divided into fuel electrode supported [88], air

electrode supported [89], and electrolyte supported [90]. In an externally supported SOC, the supporting element can be a metal interconnect, as shown in **Figure 2.7** [87]. Currently, fuel electrode supported and electrolyte supported structures are extensively studied and applied. Since fuel electrode materials exhibit high ion conductivity, using a fuel electrode supported structure can reduce the thickness of the electrolyte layer and effectively reduce ohmic impedance of cells [91]. The advantage of electrolyte supported cells lies in its better mechanical strength, which can contribute to improving the long-term redox stability and thermal cycling stability of cells. However, electrolyte supported cells require working temperatures above 800 °C to achieve high power requirements, which is not in line with the requirement of developing medium and low temperature cells in the interest of reducing energy use. By contrast, the fuel electrode supported type is more popular in the market [92]. Additionally, with the development of SOCs, some special structures have also appeared on the market, such as honeycomb-shaped [93] and cone-shaped [94]. Nevertheless, these structures are more complex to manufacture and have not been widely used.

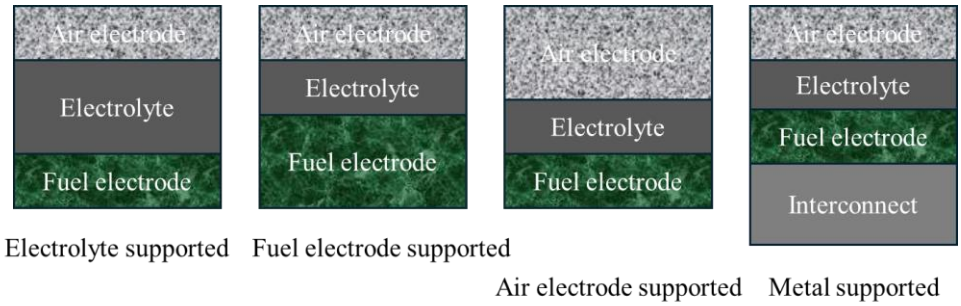

Figure 2.7. Different types of cell support architectures for SOC

According to the electrolyte conductivity mechanism, SOCs can also be separated into oxygen ion conduction types (SOC-O^{2-}) [95] and proton conduction types (SOC-H^{+}) [96]. Compared with SOC-O^{2-}, the electrode reaction of SOC-H^{+} is more complicated, and the options for electrode materials are also limited. SOC-H^{+} is suitable for working temperatures below 500°C, but the development still lags behind SOC-O^{2-}, mainly due to the lack of appropriate fuel electrode catalysts to enable cells to operate effectively at medium and low temperatures. According to the analysis results by Mojaver et al. [97], from the perspectives of energy, economy, and the environment, SOC-O^{2-} yields better performance than SOC-H^{+}.

2.2.4 Materials used for the SOECs' components

The active fuel electrode is the place where fuel (steam, CO_2, CH_4) conversion reactions occur. To facilitate the diffusion of fuel gas, electrode materials generally require a porous structure. A widely recognized fuel electrode material is Ni-YSZ cermet [98]. Ni can be used as the catalyst for multiple fuel electrode reactions. YSZ inhibits the coarsening of pure Ni to a certain extent, and high ionic conductivity of Ni-YSZ provides a conductive pathway for oxide ions. The YSZ polycrystalline ceramic phase reduces the thermal expansion coefficient of the fuel electrode material, making it better matched with the electrolyte material. Consequently, the

electrodes are hard to delaminate even under high temperature operation [99, 100]. Compared with other applied cermets, such as Ru/ZrO_2 and Mg-YSZ, Ni-YSZ is characterized with lower cost and more stable structure. However, traditional Ni-YSZ electrode still faces several problems. Firstly, in terms of redox instability, Ni is easily oxidized to NiO, especially in a no-H_2 (or CO) atmosphere. Oxidation makes the fuel electrode expand, such that the generated stress will break cells. Secondly traditional Ni-YSZ electrode presents poor resistance to carbon deposition. Ni is also employed as the catalyst for the carbon deposition reaction. When CO concentration at the gas outlet rises to a certain value, the disproportionation reaction of CO will take precedence over the CO_2 electrolysis reaction, and the generated carbon will block active sites of electrodes. Thirdly, nickel easily coarsens and agglomerates at high temperatures, which affects the service life of cells [101-107]. Nevertheless, as the most mature fuel electrode material, Ni-YSZ has been widely recognized for its fuel universality, making it difficult to find suitable alternative materials.

The air electrode of an SOEC, as the site for the oxygen exchange reaction, requires excellent ion and electron conductivity, a high oxygen ion surface exchange coefficient, and good high-temperature catalytic activity [108]. Besides, to ensure high-temperature stability of cells, air electrode materials not only need to maintain chemical and structural stability under high-temperature oxidation conditions, but also to retain chemical

compatibility with electrolyte materials. There are high oxygen vacancies in the perovskite structure. $La_{1-x}Sr_xCoO_{3-\delta}$ (LSC) based perovskite is one of the most extensively studied air electrode materials recently, because of excellent catalytic activity of Co. Therefore, the use of Co-based oxides can maintain better performance in cells [109]. However, the thermal expansion coefficient of Co-based oxides is much higher than that of the common electrolyte material YSZ, which can easily cause electrode detachment during high-temperature operation. The $(La,Sr)MnO_3$ (LSM) based air electrode performs well above 850 °C, but the catalytic activity is insufficient between 500-700 °C [110]. Therefore, $La_{0.6}Sr_{0.4}Co_{0.2}Fe_{0.8}O_{3-\delta}$ (LSCF) material with low polarization resistance, high oxygen diffusion performance, and a low thermal expansion coefficient has received widespread attention [111]. LSCF has high ionic and electrical conductivities (8.0×10^{-3} and 280 S cm^{-1} at 800 °C [112]) and high oxygen diffusion properties, with its oxygen self-diffusion coefficient (D*) and oxygen surface exchange coefficient (k) being 5×10^{-7} cm^2 S^{-1} [113] and 6×10^{-6} cm S^{-1} [114] at 800 °C, respectively. To improve chemical and thermal compatibilities, LSCF is usually enhanced with gadolinium-doped ceria (GDC), another popular electrolyte material of SOFCs. The thermal expansion coefficient (TEC) of LSCF is 14-15.2×10^{-6} K^{-1} [115], which is higher than that of YSZ (10.7×10^{-6} K^{-1}) [116]. Therefore, LSCF is usually mixed with GDC to decrease thermal expansion as well as reinforce the

electrochemical activity [117].

Electrolyte materials are usually made of dense solid oxides or ceramic materials, which can transport oxygen ions or protons. Materials without electron conductivity should be chosen as much as possible to minimize current leakage [118]. YSZ with its fluorite structure is the most common electrolyte material in fuel electrode supporting SOECs, as it can achieve diffusion of oxide ions within the lattice by generating oxygen vacancy defects and thus apply a driving force inside the lattice [119]. The ion conductivity of YSZ does not show significant changes when the oxygen partial pressure changes by more than ten orders of magnitude. When Y_2O_3 content is about 8 mol.%, both ion conductivity and chemical stability are the highest [120]. Limited by temperature, YSZ needs to function above 700 °C to exhibit good ionic conductivity and electrochemical performance. As for ScSZ (Sc_2O_3 stabilized zirconia), the strength of doped zirconia decreases with increasing Sc_2O_3 concentration due to crystal structure differences. As a result, ScSZ is usually utilized as an alternative electrolyte material at 650 °C [121]. The addition of Ce exerts a positive effect on the stability of ScSZ phase. For example, Nikonov et al. [122] reported that the microhardness of ScSZ doped with Ce increased by 4%. In metal-supported solid oxide cells, considering the medium to low temperature (500-600 °C) operating requirements of the metal skeleton, CGO can be used as the electrolyte with a thin layer of electronic blocking layer. For instance, Ceres

Power reported the cell test results using hydrogen fuel for continuous operation for more than 2500 h [123]. Moreover, YSZ electrolyte also exhibits good stability in metal-supported SOC. Button cells produced by DLR undergo 2000 h of stability testing, with the cell degradation rate less than 1.5%/kh [124].

2.2.5 The History of SOECs

The high-temperature electrolysis technology on SOECs originated from the Mars exploration mission in the 1960s, which adopted a SOEC reactor to electrolyze the Martian atmosphere and produce oxygen that supports human life activities. Early research was mainly carried out by NASA and Westinghouse. As early as 1970, NASA had already announced a 3-module CO_2/H_2O co-electrolysis oxygen production system. The system can operate continuously with an oxygen production rate of 481 sccm for over 250 h at 127 A and 880 °C, achieving Faraday efficiency nearly 100% [125]. In 1978, NASA reported that the electrolysis cell could perform CO_2 electrolysis or steam electrolysis operations under conditions not exceeding 538 mA/cm^2 [126]. In 1981, Siemens-Westinghouse Electric Company announced a 5000 h electrolysis duration for a solid oxide electrochemical cells, without observing any performance degradation of single cell components or stacks [127]. In 1997, the design and development of high-temperature steam electrolysis for hydrogen production were carried out at

the Japan Atomic Energy Research Institute (JAERI). 12 series of connected solid oxide cells were leveraged to form an electrolysis tube for laboratory-scale experiments, achieving a hydrogen production rate of 44 Nml/cm^{2}h at 950 °C. Afterwards, JAERI manufactured a metal-supported planar electrolysis cell, capable of continuously producing hydrogen at a rate of 33.6 Nml/cm^{2}h at 950 °C [128]. After the 1990s, due to a significant decrease in the prices of fossil fuels, the development of SOEC slowed down.

The Idaho National Laboratory (INL) has been dedicated to researching steam electrolysis for hydrogen production since 2005, and began conducting the laboratory scale test in 2008, with a duration period of 1080 h. The average H_2 production rate was about 1.2 Nm^3/hr, with a peak measured value of over 5.7 Nm^3/hr. During the initial 480 h, the degradation was dominated by the condensation of the generated hydrogen. After 480 h, modules 1 and 2 did not further degrade, while the performance of module 3 continued to deteriorate [129]. In 2008, INL cooperated with Ceramatec Inc. to expand steam electrolysis based on high-temperature solid oxides cells to CO_2/H_2O co-electrolysis to produce syngas, and carried out experiments on efficient and large-scale syngas production on electrolytic button cells (2.5 cm^2), 500 W stacks (640 cm^2) and 15 kW systems (three modules, 720 units) [129]. The results suggested that the co-electrolysis of H_2O/CO_2 to prepare hydrocarbon fuels was feasible, and the area specific resistance (ASR) of co-electrolysis was closer to steam electrolysis than CO_2

electrolysis, indicating that steam electrolysis served as the main electrolysis reaction under the co-electrolysis atmosphere.

Since 2008, due to the need for energy transformation, the number of institutions and labs studying SOECs has gradually increased, including the European Institute for Energy Research (EIFER) and the Risø National Laboratory at the Technical University of Denmark (DTU). Among them, EIFER utilized 45 cm^2 solid oxide electrolysis cells as their demonstration product. As early as 2004, EIFER achieved steam electrolysis operation for over 9000 hours, with a minimum degradation rate of only 1.7%/1000 h. In 2012, through technoeconomic technical analysis, they established a model for the hydrogen production cost by high temperature electrolysis as function of the electrolyser environment like external heat and electricity sources, which provided a reference for the development and deployment of subsequent synthetic gas production [130]. The demonstration product of Risø DTU consisted of 16 cm^2 planar electrolysis cells and stacks, with a typical operating temperature of 750-850 °C. In 2009, DTU reported a study on the durability of CO_2 electrolysis testing based on a nickel-based SOEC. The results showed that, the passivation rate of the cell was between 0.22 - 0.44 mV h^{-1} under 70 vol.% CO_2-30 vol.% CO and 98 vol.% CO_2-2 vol.% CO (industrial grade) at 850 °C and current densities were between -250 and -500 mA cm^{-2}. The degradation was found to be mainly caused by the adsorption of impurities in the fuel gas on active sites [131]. In 2020, DTU

developed nanocomposite structured perovskite materials for investigating the cell lifetime for syngas preparation by co-electrolysis. The test faculty operated at a current of -500 mA/cm^2 for 600 h with a voltage decay rate of approximately 10.5%/kh [132]. Other institutions such as the University of St. Andrews and Imperial College London tended to focus more on the modification of electrode materials for button cells, rather than the commercialization of large-sized cells or stacks.

The development of energy storage technology using SOECs in China started relatively late, just over 20 years ago. Active research institutions include Fuzhou University, Nanjing University of Technology, University of Science and Technology of China, Dalian Institute of Chemical Physics (Chinese Academy of Sciences), Ningbo Institute of Materials Technology and Engineering (Chinese Academy of Sciences), Shanghai Institute of Ceramics (Chinese Academy of Sciences), Chaozhou Three-Circle (Group) Co., Ltd., and H_2-Bank. Most research groups concentrate on improving anode, cathode, and electrolyte materials or developing SOFC stacks. There are currently few reports on the durability of CO_2 electrolysis for energy storage. For example, Dalian Institute of Chemical Physics, Chinese Academy of Sciences, focuses on the modification of LSM/YSZ anodes. In 2018, it was reported that doping RuO_2 nanoparticles can generate new oxygen vacancies, thereby boosting the oxygen evolution reaction (OER) performance of LSM/YSZ anodes [133]. Subsequently, a new triple phase

boundary was found to generate in the LSM-YSZ anode when loaded with Au nanoparticles, which improved the oxygen evolution reaction performance [134]. The research group led by Prof. Li from Huazhong University of Science and Technology developed a novel $La_{0.6}Sr_{0.4}Fe_{0.8}Ni_{0.2}O_{3-\delta}$ (LSFN) electrode for pure CO_2 electrolysis in a symmetrical SOEC, and found that the current density increased from 1.03 A/cm^2 at 800 °C to 1.52 A/cm^2 at 850 °C under an electrolytic voltage of 2.0 V [135]. Additionally, many other research institutes also have been dedicated to exploring the material modification and performance improvement of CO_2 electrolysis on SOECs. Relevant electrolysis cell structures and operating conditions are summarized in **Table 2.3** [133-141]142]. As for durability and stability, the symmetrical double anode SOEC (35 cm^2 × 2) developed by Ningbo Institute of Materials Technology and Engineering, Chinese Academy of Sciences, achieved stable operation of high temperature CO_2 electrolysis for nearly 2000 h, with a degradation rate of less than 5%/kh. The CO_2 conversion rate was more than 47%, with an electrolytic efficiency of 91.4%. This is currently the longest lifetime of CO_2 electrolysis, as far as the author knows [143]. Afterwards, Ningbo Institute of Materials Technology and Engineering (Chinese Academy of Sciences) focused on tackling the difficulties related to CO_2 electrolysis on 60 cm^2 large cells and stacks. There is to date no clear report on SOC stacks and systems for commercial energy storage in China. In a word, using SOEC

for high-temperature CO_2 electrolysis is still an immature technology, and there is still a long way to go to achieve industrial production.

Table 2.3. The structure, operating conditions, and performance of SOECs in China and abroad

	Cell structure	Fuel gas	Current/Voltage	Ref
Dalian Institute of Chemical Physics	Ni-YSZ|YSZ|LSM/YSZ + RuO_2	95% CO_2-5% N_2	-0.74A/cm^2@1.2 V	[133]
Dalian Institute of Chemical Physics	Ni-YSZ|YSZ|LSM/YSZ + Au	95% CO_2-5% N_2	-0.94A/cm^2@1.4 V	[134]
Huazhong University of Science & Technology	LSFN-GDC/GDC/YSZ/GDC/LSFN-GDC	pure CO_2	-1.52 A/cm^2@2V	[135]
KAIST	LSCM|LSGM half cell	35% CO_2-35% H_2O-10% H_2-20% N_2	-	[136]
University of St Andrews	LSCM-GDC|YSZ|LSM-ScSZ	90% CO_2-10% CO	1V	[137]
University of Alberta	LCN-GDC/YSZ/LCN-GDC	Pure CO_2	-2.32A/cm^2@2.0 V	[138]
Huazhong University of Science & Technology	LSFM-GDC|GDC||YSZ||GDC|LSFM-GDC	pure CO_2	-1.744 A/cm^2@2V	[139]
Nanjing Tech University	Ni-YSZ|YSZ|Gd-doped ceria|BSFTx	70% CO_2-30% CO	-0.81 A cm^{-2}@1.5V	[140]
Huazhong University of Science and Technology	Pt|LCaFN-GDC |GDC|YSZ|GDC|LCaFN-GDC|Pt	Pure CO_2	-1.41A/cm^2@2.0 V	[141]
Institute of Engineering Electronics, China Academy of Engineering Physics	GDC@(LSCrF)-YSZ-|YSZ|GDC@(LSCrF)-YSZ	CO-CO_2	-1.04 A/cm_2@1.5V	[142]

2.3.6 Other CO_2 conversion technologies

Besides using SOECs for the decomposition and electrocatalytic

reduction of CO_2, molten carbonate electrolysis cells (MCECs) can also be exploited. The operating temperature of MCECs is often slightly lower than that of SOECs, and the electrolyte of such cells is a carbonate melt, usually Li, Na and K single molten carbonate eutectics [144]. Carbonate possesses a better CO_2 absorption capacity and higher current efficiency, and using lithium carbonate as an electrolyte is conducive to the precipitation of carbon. The principle of carbon deposition on MCECs is displayed in **Figure 2.8**. CO_2 is first converted into CO_3^{2-} ions, which are further reduced to carbon on the cathode. The generated carbon products include amorphous carbon, carbon fibers and carbon spheres. Different morphologies of carbon result in different commercial values [145].

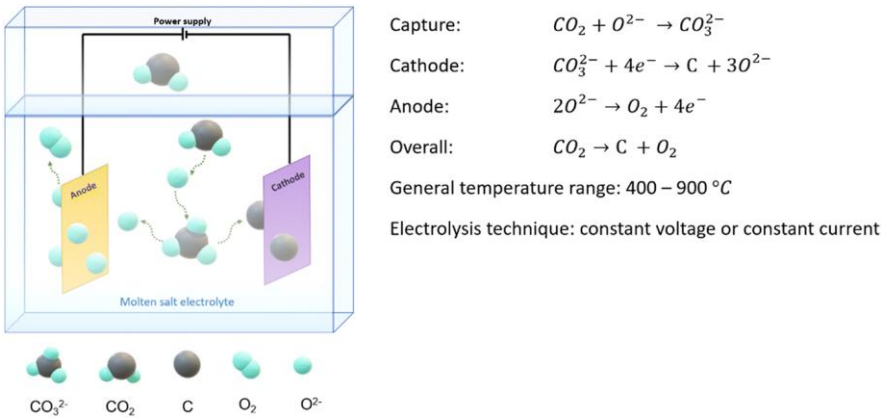

Figure 2.8. A schematic of molten salt electrochemical system for CO_2 reduction [145]

Compared with K_2CO_3, Li_2CO_3 is easier to handle, with a melting point of 723 °C. K_2CO_3 and Na_2CO_3 are not widely used because of their high melting points (900 °C and 860 °C), as high temperatures can lead to high

costs and material corrosion issues. Research on MCECs for CO_2 electrolysis in the industrial field is still unreported, and relevant studies to date are mainly conducted on a lab scale. Factors such as the electrolysis operation, corrosion of electrodes and equipment under high temperature and liquid carbonate, Ni electrode lifespan, and carbon deposition should also be considered. There are currently no reports on the durability of MCEC electrolysis systems. The theoretical analysis of electrolysis systems, such as process design, quality and energy balance, and economic analysis, are not yet comprehensively published and no references for industrial applications have been found.

Another option is to use flow batteries, whose products may usually contain CO, HCOOH, C_2H_5OH and C_2H_4. Comparatively, C_{2+} products should have a higher market value because of their higher energy density. But according to some current research, C_{2+} products have low current densities and poor product selectivity compared to C_1 products. Most catalysts adopted in flow batteries have a testing time of less than 100 h, which is far below industrial standards. The longest reported lifespan of the key components of a flow battery, the membrane electrode assembly (MEA), is about 4000 h, with a modified method of adding catalysts with imidazolium-functionalized polymers [146].

The CO_2 redox flow battery (CRB) is a rechargeable battery. P. Hosseini Benhangi et al. [147] proposed the concept of using CRB to directly convert

CO_2 for electrochemical energy storage in 2021. Electrochemical reactions are described in **Eq. 2.9**. They introduced and demonstrated a novel bifunctional catalytic system for CO_2 reduction and formats oxidation based on bimetallic PdSn or ternary PdSnPb and PdSnIn formulations. The results of CRB experiments revealed that a peak discharge power density of 19.2 mW/cm^2 was reached at 20.5 mA/cm^2, where the voltaic round-trip efficiency and energy efficiency at peak power were 50.5% and 36.7% respectively. This battery far surpassed other emerging non-metallic batteries that had been proposed. However, as of the completion of this thesis, research on this topic had been conducted for less than 2 years, and no results on continuity or durability have been reported.

$$CO_2(g) + H_2O(l) + 2Br^-(aq) \overset{charge\rightarrow}{\underset{discharge\leftarrow}{\Longleftrightarrow}} HCOO^-(aq) + HO^-(aq) + Br_2(l) \quad \text{(Eq. 2.9)}$$

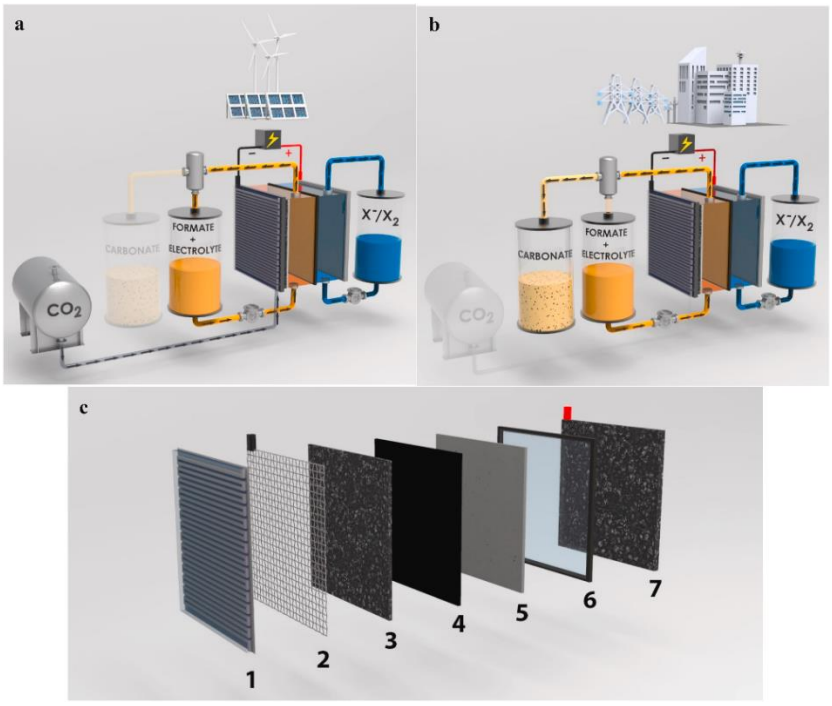

Figure 2.9. A schematic of the CO_2 redox flow battery (CRB) [147]

Among metal-CO_2 batteries, aqueous Zn-CO_2 batteries exhibit flexible CO_2 electrochemistry performance in terms of multi-carbon chemicals, which are in favor of the durability of aqueous battery systems. More intriguingly, compared with Li/Na-CO_2 batteries, Zn-CO_2 batteries have a wide range of products, since aqueous electrolytes enable multistep proton-coupled transfer processes [148]. Besides, the products stemming from Zn-CO_2 batteries are mainly gas or liquid, which protects the batteries from the issues of masking active sites. Generally, Zn-CO_2 batteries are composed of a catalyst cathode, a metal Zn anode, and an electrolyte [149]. Zn-CO_2 batteries belong to the rechargeable category of batteries. The chemical mechanism of reversible Zn-CO_2 batteries is as follows:

Cathode reaction: $CO_2(g) + 2H^+ + 2e^- \leftrightarrow HCOOH(aq)$ (Eq. 2.10)

Anode reaction: $Zn + 4OH^- \leftrightarrow Zn(OH)_4{}^{2-} + 2e^-$ (Eq. 2.11)

Total reactions:

$$CO_2 + 2H^+ + Zn + 4OH^- \leftrightarrow HCOOH(aq) + Zn(OH)_4{}^{2-} \quad \text{(Eq. 2.12)}$$

Zn-CO_2 batteries can generate electricity while converting CO_2 into value-added products, which is completely different from other energy consuming CO_2 conversion technologies. However, Zn-CO_2 batteries typically operate at low discharge current densities (mostly below 15 mA/cm^2), which leads to lower productivity [150, 151]. Compared with relatively mature Li/Na/K-CO_2 batteries, the emerging aqueous Zn-CO_2

batteries still require further in-depth research.

In bioelectrochemical systems (BES), microorganisms are used to catalyze oxidation or reduction reactions. Normally, microorganisms oxidize biodegradable substrates at the anode, known as the biological anode, and combine with the oxygen reduction reaction at the cathode to produce a current. This technology is called microbial fuel cell (MFC). Low potential cathode reactions, such as hydrogen evolution, are coupled with the oxidation of organic matter with the application of small external voltage. This system is called microbial electrolysis cell (MEC), and the specific principle is illustrated in **Figure 2.10**. The concept of microbial electrocatalytic reduction of CO_2 to produce multi carbon organic compounds was first proposed in 2010 [152], with the most widely reported being acetate/acetic acid, which undergoes the reaction shown in **Eq 2.13**. With the extended development of this technology, the products can be further reduced to more economically valuable products such as ethanol, butyrate, methane and ethylene. [153-155]. However, BESs still face challenges in stability, product selectivity, and yield. A robust and stable biological cathode is necessary to justify further research and development.

$$2CO_2 + 2H_2O \rightarrow CH_3COOH + 2O_2 \qquad \text{(Eq. 2.14)}$$

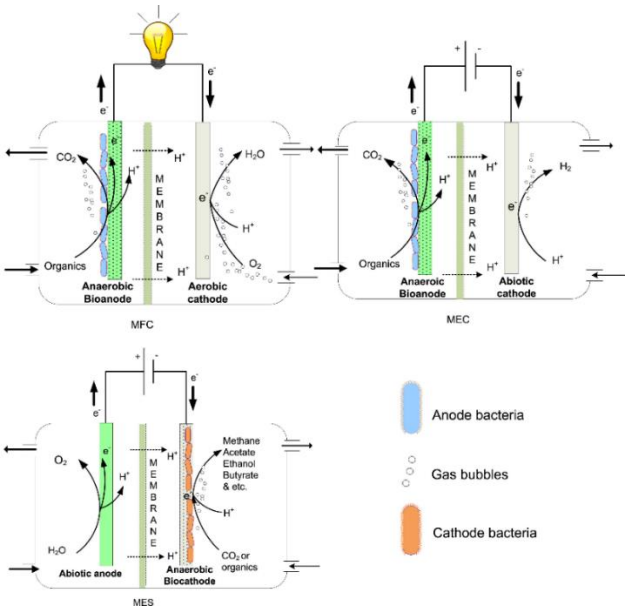

Figure 2.10. Principles of typical BESs [152]

The use of nanostructured Cu catalysts to carry out CO_2 reduction reactions is also a conventional approach. A new angle is that Cu nano foams contribute to producing HCOOH and CO. However, this foam system exposes the difficulty of identifying actual catalytic sites used for catalytic reaction [156]. In this regard, the ordered nano porous Cu structures have been developed. Despite the improved selectivity for CO_2 conversion, there are still limitations in the diffusion control process within the pore structure, making it difficult to achieve rapid exchange of reactants and products [157]. To avoid mass transfer limitation issues, an improvement strategy is to utilize Cu nanoparticles (Cu NPs). Coordination numbers and chemical interaction energy of Cu NPs are different on the surface, corner atoms, along the edges as well as in crystal planes. Therefore, the catalytic activity of CO_2RR can be changed by adjusting the size of NPs. For example, low-coordinated (< 8)

surface atoms are in favorable for the formation of CO, while atoms with CN > 8 can be used for hydrogenation of CO [158]. Currently, the maximum Faraday efficiencies of HCOOH, CO, CH_4, C_2H_4, and C_2H_6 obtained from Cu-based nanocatalysts are as high as 96%, 94%, 73%, 50%, and 24%, respectively [159-163]. C_{2+} products are far from meeting the practical application requirements. In addition, Cu-based nanocatalysts also have stability issues, as they may exhibit surface oxidation, particle aggregation, and structural deterioration under CO_2RR conditions. Consequently, their lifespan rarely exceeds 100 hours [164].

The concept of photocatalytic CO_2 conversion can be traced back to 1978, but after several decades of development, photocatalytic CO_2 conversion has not reached the level of conventional CO_2 hydrogenation in both reaction activity and selectivity. This is mainly because the complexity of photocatalysis limits the performance of the system [165]. Photocatalytic CO_2 conversion encompasses light absorption, charge generation, separation and transfer, and surface reactions. Although significant progress has been achieved in optimizing the first few processes, there has been little research on improving catalytic efficiency, as efficiency improvement requires the presence of promoters [166]. **Figure 2.11** illustrates the potential pathways for photocatalytic CO_2 conversion to various carbon-containing products, where carbon is uneconomical, CO may exist in the form of intermediates, and C_{2+} products such as ethylene, ethanol, acetaldehyde and propanol

demonstrate the highest economic value [167].

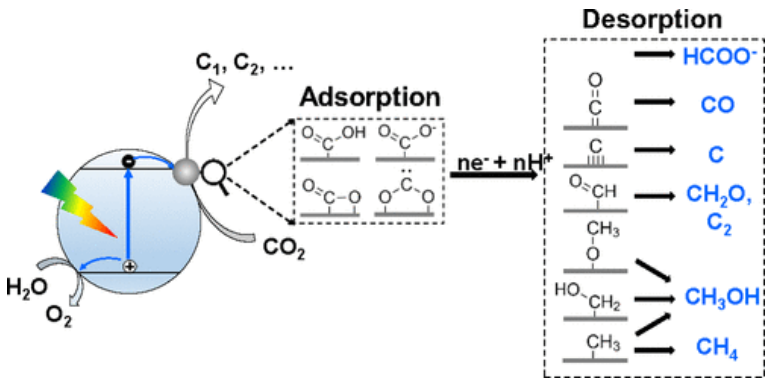

Figure 2.11. Possible reaction pathways and products of photocatalytic conversion of CO_2 [167]

Other types of technologies reported in the literature are dielectric barrier discharges, microwave and gliding arc discharges. Despite years of development, the energy efficiency of plasma reactions is still relatively low. Combining plasma with catalysis can activate catalysts at low temperatures, significantly heightening the CO_2 conversion rate, selectivity and yield of target products. For example, Mei et.al [168] developed a coaxial dielectric barrier discharge (DBD) for the plasma-photocatalytic CO_2 conversion, and investigated the synergistic effect resulting from the combination of plasma and photocatalysts, $BaTiO_3$ and TiO_2, for CO_2 conversion. The results proved that this synergistic effect significantly increased the CO_2 conversion rate and improved energy efficiency by 2.5 times. Ashford et al. [169] reported the optimum CO_2 conversion (24.5%) and energy efficiency (13.6%) using γ-Al_2O_3 supported 5Fe5Ce, almost twice the conversion attained using 10Fe (only 13.3%). However, based on current laboratory research results,

the CO_2 conversion rate of plasma-photocatalytic CO_2 conversion is still less than 30%, far lower than that of electrochemical methods. Moreover, expensive post-treatment separation steps have been reported [170]. Due to its emerging properties, plasma-photocatalytic CO_2 conversion undoubtedly still needs further research.

2.3 Degradation of SOECs in CO_2 electrolysis

The high energy efficiency of SOECs benefits from their higher operating temperature, but high temperatures also place high demands on SOEC materials. The long-term degradation of components caused by high temperatures is one of the key factors hindering the large-scale application of SOECs. Degradation is the main obstruct in the industrialization of SOECs, and research on the degradation mechanism is still in an early phase. With large active area and high operating temperature of cells, it is hard to in-situ monitor the degradation process. Degradation after cooling and disassembly has been reported in most of the literature. There is no clear evidence that these attenuation parts are caused by one or more factors in heating, reduction, testing or disassembly. The degradation of SOEC depends on materials, test process and operating conditions. Possible influencing factors during operation include operating temperature, type and ratio of fuel gas as well as current density. It has been reported that electrochemical degradation can exist at the oxygen electrode, electrolyte,

fuel electrode and even the interface of each active layer.

Ni-YSZ cermet is the most used fuel electrode (hydrogen electrode) material. The degradation rate can be simply classified as nickel coarsening, sulfur poisoning and carbon deposition [100, 171-173]. Ni coarsening exists in almost any fuel electrode atmosphere and can be considered as Ni agglomeration, Ni migration and Ni grain growth [174]. Ni agglomeration occurs at high temperature, which is a sintering process under thermal activation. The particle size after agglomeration is affected by sintering temperature and fuel electrode atmosphere. In humid environment, such as CO_2 electrolysis with H_2 as protective gas, the water generated by RWGS reaction reacts with Ni to produce volatile $Ni(OH)_2$, which accelerates the loss of Ni. The growth of Ni particles tends to be more obvious as RWGS reaction increases the humidity in fuel electrode [175]. Research on Ni migration basically focuses on two mechanisms. One is Ostwald ripening, which means Ni migrates and is captured by another Ni particle, and the other is to migrate on the carrier and merge with other Ni clusters [176]. The driving force for migration may come from the formation of $Ni(OH)_x$ or be related to the change of local oxygen partial pressure [177, 178]. For the case without driving force, it may be induced by Ni surface energy difference. There are few descriptions of Ni grain growth in the literature, but there has been consistent conclusion that the growth of nickel mainly occurs in the early stage, and the growth rate appears an obvious downward trend with the

extension of time [175].

Oxygen electrode (air electrode) is the place where oxygen evolution reaction occurs, usually requiring high electrocatalytic activity, certain porosity, high electronic and ionic conduction and suitable thermal expansion coefficient [179]. There are great disputes about the degradation mechanism of oxygen electrode, and there is still no definite conclusion so far. LSCF ($(La_{0.6}, Sr_{0.4})(Co_{0.2}, Fe_{0.8})O_3$) and LSM ($La_{1-x}Sr_xMnO_3$) are common materials for oxygen electrode. The most common failure mode of such kind of perovskite materials is the delamination of oxygen electrode / electrolyte interface caused by high oxygen partial pressure generated by anode overpotential [180-183]. Chen et al. [180] reported the irreversible delamination behavior of electrode / electrolyte at 500 mA/cm^2 electrolytic current density, and proposed that the infiltration of oxygen ions leads to the formation of manganese cation vacancy, inducing the local tensile strain of LSM particles. While Graves et al. [182] believed that the degradation between oxygen electrode / electrolyte can be eliminated by reversible operation between electrolysis and fuel cell mode, and the principle is similar to rechargeable battery. The ionic and electronic conductivities of LSCF are much higher than that of LSM. However, both LSM and LSCF are faced with instability under long-term operation. Specifically, with the electrostatic interaction between the cations at A-site of perovskite structure and oxygen vacancy, the enrichment of Sr secondary phase caused by Sr

segregation hinders the oxygen surface exchange process, resulting in the decline of the overall electrochemical performance of SOECs [184, 185].

A GDC barrier layer needs to be added at the boundary between the LSM or LSCF air electrode and the YSZ electrolyte to avoid the reaction between Zr and Sr at high temperatures. However, under the action of high temperature and high electrolytic current, there may generate pores along the grain boundaries of YSZ electrolyte close to the LSM/YSZ interface, which may be attributed to the nucleation and growth of oxygen clusters in the YSZ grain boundaries. Jacobsen et al. [186] calculated the distribution of the oxygen electromotive force inside ZrO, and they believed that oxygen formation may happen within the grain boundaries of YSZ under SOEC mode. The accumulation of oxygen at the grain boundaries blocks the transport process and increases the electrolyte resistance. As reported, voids develop along the grain boundaries to generate cracks in the electrolyte. The reaction formula for the formation of voids is as follows: [187]

$$4O_o + Zr_{Zr} \rightarrow 4O_i{}' + 2V_o + (V_{Zr} \cdot 2V_o)^x \downarrow + Zr \downarrow \quad \text{(Eq. 2.15)}$$

As for interconnects, it should be noted that significant interdiffusion of nickel and chromium component may occur at the interface of current collection layer of the fuel electrode and Fe-Cr alloy because of high diffusivity in nickel and alloy. The chromium components from interconnect may diffuse into the nickel fuel electrode, which may degrade the catalytic activity of nickel. The surface in contact with current collection layer of the

air electrode presents a normal oxide scale containing (Mn, Cr, Fe) spinels, which also leads to an increase in contact resistance and a deterioration in stack performance. Additionally, due to the strong activity of the air electrode and its continuous exposure to an oxidizing atmosphere during testing, a small amount of chromium evaporates from the interconnect, leading to chemical stability issues of air electrode materials [188, 189].

In the process of assembling cells and stacks, glass seals are usually leveraged, which have advantages such as good wettability, low cost, easy processing, adjustable composition, and wide temperature range for use. However, such materials also expose issues such as brittleness, susceptibility to damage during thermal cycling and easiness to react with other components. Also, the potential toxicity of volatile elements may damage electrode materials. Besides, in high temperature and high humidity environments, the silicate glass phase may form a thin film at the Ni-YSZ grain boundaries, thereby affecting the durability of cells [190]. Owing to technique issues during assembly, glass seals may fail under high temperature and mechanical pressure, which can also lead to oxidation and fracture of Ni-based electrode and supporting layer [191]. Considering different levels of mechanical interaction between the stack and cell components, the direct influence of creep deformation on the integrity of cells is obvious with glass-ceramic sealants [192]. Due to the low level of commercialization, many current studies focus on chemical degradation, and

there is no reliable analysis of mechanical performance degradation in both stacks and systems.

So far, the degradation mechanism under high-temperature CO_2 electrolysis operation is not clear, and the main difficulties faced by large-scale commercial use include insufficient fuel conversion capacity, high cost of electricity consumption, contact loss between cells and interconnects, as well as oxidation and corrosion of interconnects. It is crucial to conduct research on the high-temperature degradation mechanism relying on low strain flat-tube RSOC technology to solve the above issues as well as meet the demand for renewable energy consumption and storage.

2.4 Industrialization degree and application scenarios

With the continuous growth of energy demand and the increasing emphasis on environmental protection in various countries around the world, recently, numerous countries have increasingly attached importance to the development of hydrogen energy. Some of them have released the latest plans in the field of hydrogen energy, and using SOECs for hydrogen production has become a popular development direction. In 2012, INL reported a study on the kilowatt-scale SOEC stack for thousands of hours of steam electrolysis hydrogen production, with a minimum performance degradation rate of 3.2%/kh [193]. Two years later, the demonstration results of a 4-kW steam electrolysis hydrogen production system were reported,

which achieved stable operation for 830 h with a total degradation rate of 3.1%/kh [194]. The latest research results of EIFER on high-temperature electrolysis for hydrogen production suggest that single piece electrolyte-supported SOEC (Ni-GDC/GDC/6Sc1CeSZ/GDC-LSCF, 45 cm^2) manufactured by Kerafol (Germany) has been stably operated for 23000 h, with a cell voltage degradation of 7.4 mV/kh (0.57%/kh), proving that the service life of SOEC can meet commercial standards [195].

There are only few reports on the adoption of SOEC stack for CO_2 electrolysis or co-electrolysis. For example, in 2011, Topsoe Fuel Cell A/S (TOFC) and Technical University of Denmark designed and assembled 10-unit stack for CO_2/H_2O co-electrolysis tests. The electrolysis time exceeded 1150 h, and the highest electrolysis current reached -0.75 A/cm^2 [196]. In 2014, starvation was tested on a 10-cell stack when running in CO_2 electrolysis at -345 mA/cm^2 [197]. In 2015, Reytier et.al [198] reported co-electrolysis performances of 10-unit stack with a ratio $H_2O/CO_2 \geq 1$. For the atmosphere of 65 vol.% H_2O + 25 vol.% CO_2 + 10 vol.% H_2, the maximum current density applied was -800 mA/cm^2 with a conversion rate of 52%. The syngas production rate of the stack was 0.34 Nm^3/h at -80 A and 800°C. In 2017, Haldor Topsoe A/S summarized research on CO_2 electrolysis in 5-unit stacks (named A-E) and also measured the robustness of each stack, providing certain reference value for system development and commercialization. Stack C (air side modification) and stack D (fuel side

improvement) operated for over 2000 h with CO_2 electrolysis, indicating that appropriate thermal cycling might be beneficial for activating stack performance [199]. In 2023, Li et.al [200] investigated the effect of interconnect rib width on the co-electrolysis of water and carbon dioxide in cells, and demonstrated that the cell with a rib width of 0.6 mm yielded the optimal performance.

Compared to cells with other structures, SOECs are less sensitive to fuel impurities. Moreover, since there are no moving parts in the fuel cell except for the Balance of Plant (BoP) components, the system is expected to improve reliability and reduce maintenance costs. The size of SOECs is very flexible, supporting any power range from several watts to megawatt level, and SOECs can be installed as a fixed CO_2 treatment device in urban or suburban areas [201]. Up to now, CO_2 electrolysis by SOECs has not yet been widely used in daily life, and the specific reasons can be divided into the following aspects: (i) Higher operating temperatures accelerate the corrosion of metal components, limiting the durability of various components in the stack; (ii) Excessive heating and cooling time limits their use in situations that require rapid temperature oscillations; (iii) Complex assembly structure and high manufacturing cost require to optimize the assembly process and search for alternative materials that are cheaper and economically valuable.

2.5 Summary

SOECs are experiencing tremendous growth recently since they are deemed as a pioneering and evolving technology and can provide solutions to alleviate carbon emissions. In terms of usage scenarios, SOECs present fuel flexibility and are not sensitive to impurities, which makes them more economically advantageous than some low-temperature cells and batteries. As for energy conversion efficiency, due to high-temperature operation, reactions in SOECs are simple, with almost no by-product generated. From the perspective of service time, most of the stability and durability test results of cells and stacks are still in the demonstration and verification stage. Under high-temperature electrolysis operations, cell microstructures, stack components, and sealing materials may fail. Consequently, exploring the high-temperature degradation mechanism of SOECs is necessary and important.

There have been plenty of research and developments on CO_2 electrolysis based on SOECs in the past decade, but most of them have focused on the button cells and lab stage, and the technological maturity of large-sized cells and stacks still needs to be verified. Developing high-performance SOEC electrolytic stacks for CO_2 electrolysis can take full advantage of existing resources such as carbon dioxide, wind energy, and solar energy, which is more in line with practical use.

Chapter 3. Experimental Methods

This chapter describes the preparation, assembly and test methods of cells and stacks, electrochemical impedance test, scanning electron microscope analysis, gas composition analysis, energy conversion efficiency analysis and mechanical property test.

3.1 Preparation and assembly of the cell

A flat-tube asymmetrical solid oxide electrolysis cell was adopted, with Ni-3YSZ used as the supporting layer. The size of the cell was 155 mm × 63 mm × 4.6 mm (thick cell), and further developed to 155 mm × 63 mm × 2.7 mm (thin cell), with an active area of 60 cm^2 (air electrode). LSC-15%Ag was used as a current collection layer on the surface of the air electrode because of high conductivity. The cell structure was be marked as NiO-3YSZ|NiO-8YSZ|8YSZ|GDC|LSCF-GDC|LSC-Ag. The specific preparation process is as follows:

Firstly, NiO, 3YSZ, PMMA (pore forming agent), PVA (binder) and other ingredients were extruded into a supporting layer containing fuel flow channel, and calcined at 1100 °C. The fuel electrode and electrolyte were successively printed on the surface of the supporting layer by screen printing, and then calcined at 1300 °C for 4 hours to obtain the half-cell. Then the barrier layer (1~2 μm) was printed on the electrolyte and calcined at 1250 °C, and finally the air electrode slurry was screen-printed and calcined at

1050 °C to obtain the full cell. Notably, the surface of the air electrode also needed to be hand-brushed or screen-printed with a layer of LSC slurry, which was then dried at 110 °C to serve as the current collection layer. The appearance, cross-sections and microstructure of the flat-tube SOEC are introduced in **Figure 3.1**. The material composition and thickness of each functional layer are illustrated in **Table 3.1**. Generally, the thickness of current collection layer is related to that of the sealing material.

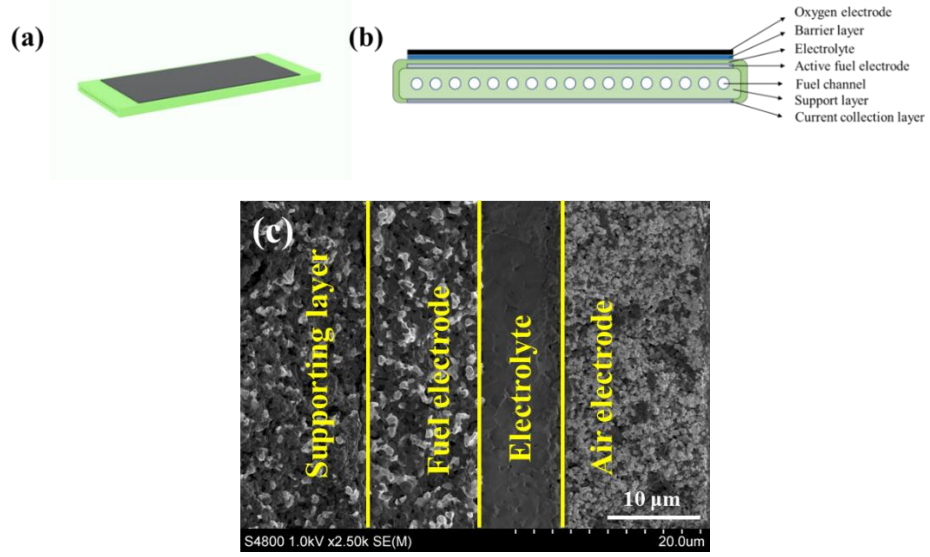

Figure 3.1. Schematic diagrams of (a) the flat-tube SOEC; (b) Cross-section illustration of the flat-tube SOEC; (c) SEM image of the flat-tube SOEC

Table 3.1. Parameters of SOEC

Composition	**Material**	**Thickness**
Supporting layer	NiO-3YSZ (3 mol. % yttria stabilized zirconia)	2.8~4.6 mm
Fuel electrode (cathode)	NiO-8YSZ (8 mol. % yttria stabilized zirconia)	15~20 μm

Electrolyte	8YSZ (8 mol. % yttria stabilized zirconia)	10~15 μm
Barrier layer	GDC ($Gd_{0.1}Ce_{0.9}O_{2-\delta}$)	1~3 μm
Air electrode (anode)	LSCF-GDC ($La_{0.6}Sr_{0.4}Co_{0.2}Fe_{0.8}O_{3-\delta}$)	15~20 μm
Current collection layer	LSC-Ag ($La_{0.6}Sr_{0.4}CoO_{3-\delta}$)	> 60 μm

The assemble process of the thick cell and the high-temperature furnace are shown in **Figure. 3.2a** and **Figure. 3.2b**. Firstly, the fuel electrode of the cell was installed on the clamp with holes, and the inlet and outlet needed to be fixed with stainless steel long bolts. To ensure the sealing of the fuel electrode, the gap between the cell and the clamp was filled with glass powder. Before assembling the anode and cathode cover plates, both nickel mesh (with nickel paste) and silver mesh (with silver paste) were added between the cover plates and electrodes for enhancing the current collection effectiveness. Finally, the inlet and the outlet pipes were installed and conductive columns were added to construct a complete SOEC test system. The assembled cell was put vertically into the resistance furnace and heated to the specified temperature of 750 °C.

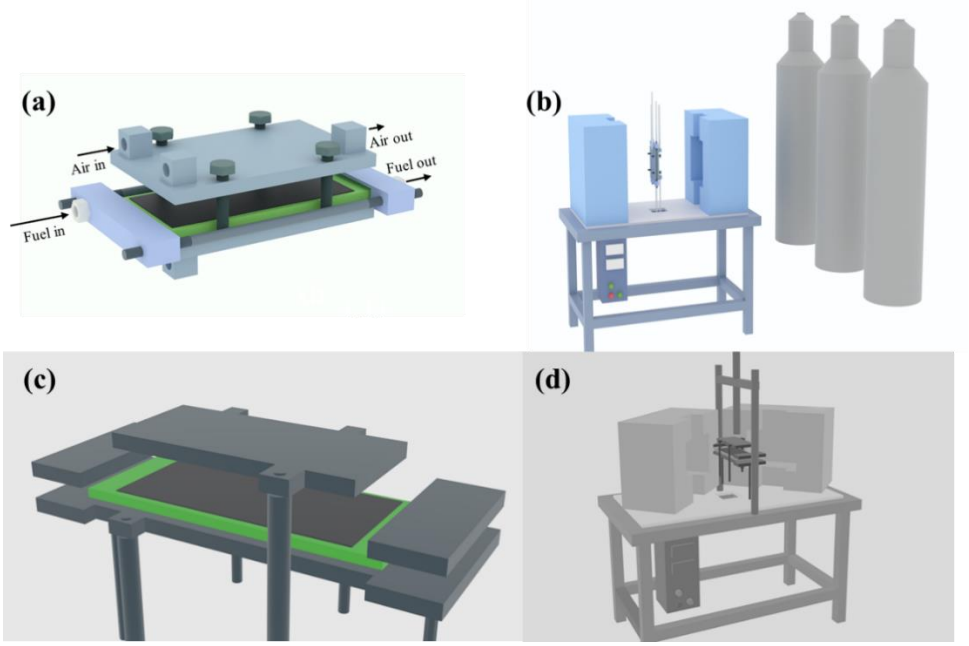

Figure 3.2. Assembly diagram of SOEC: (a) Assemble method of thick cell; (b) High-temperature furnace of thick cell; (c) Assemble method of thin cell; (d) High-temperature furnace and pressurization device of thin cell

The assembly process and the high temperature furnace of the thin cell are shown in **Figure. 3.2c** and **Figure. 3.2d**, slightly different from the assembly method of the thick cell. First, the thin cell was fixed from top to bottom with stainless steel short bolts to prevent cracking during assembly. To enhance the performance of the cell, the air electrode of the thin cell needed to be coated with LSC-Ag (15%Ag) slurry as the current collection layer. Subsequently, the assembled cell was placed and fixed horizontally in the high-temperature furnace, as shown in **Figure. 3.2d**, and pressurized to 100 kg (experience value) to enhance sealing and current collection

effectiveness. The furnace temperature was raised at the rate of 3~4 °C/min to 750 °C.

3.2 Preparation and assembly of the stack

The 3-unit SOEC stack required for the experiment was composed of three cells, four interconnects and two conductive plates. The interconnect in contact with the cathode of the SOEC stack had no gas flow path, and the interconnects in contact with the anode (air electrode) of the three cells had air flow paths. The four interconnects are made of ferritic stainless steel with manganese-cobalt spinel coating ($(Mn,Co)_3O_4$). The structure of the SOEC stack is illustrated in **Figure 3.3**. During the preparation of the stack, silver mesh and nickel mesh were firstly added to the air electrode contact surface and fuel electrode contact surface of each cell to enhance the current collection effectiveness. The air electrode surface of the cell was also brushed with LSC-15%Ag as the current collection layer. Afterwards, nickel-chromium wires with high mechanical strength were inserted on the contact surface between the cell and interconnects to monitor real-time impedance and voltage of each unit in the stack. Usually, nickel-chromium wires under high temperature can exhibit antioxidant properties and remain relatively stable below 800 °C. The meanings of each unit in the stack are summarized in **Table 3.2**. The stack was sealed with commercial glass sealing materials provided by H_2-Bank Technology Co., Ltd (Ningbo, China),

which are named No. 4 and No. 7. Notably, different melting points of the two sealing materials contribute to different processes of temperature rise and pressure increase. The glass sealant 4 sealing material has good high-temperature fluidity and can enhance sealing performance through pressure. The glass sealant 7 sealing material has a high melting point and requires external pressure to be applied when the temperature exceeds 800 °C, since it contents large content of MgO and CaO. Before assembly, the most suitable assembly process should be determined. Firstly, a specific amount of binder, dispersant, and terpineol was added to glass sealant 4 and 7 grade powders to form sealing slurries with different solid contents (usually 70%-85%) which then needs to be homogenized. Sealing performance tests must also be conducted after each assembly stage. More importantly, to ensure electron conduction in the stack at high temperatures, the thickness of the sealing material and the thickness of the current collection layer (including nickel mesh, silver mesh, and current collection layer slurry) after drying were measured. The thickness difference should not exceed 0.1 mm. After sealing, the stack structure was pressurized and fixed with short bolts and pressure plates.

Finally, both gas pipes and conductive columns were fitted to the assembly. The stack was further transferred to a high-temperature furnace for hot-pressing treatment, to further improve sealing and current collection.

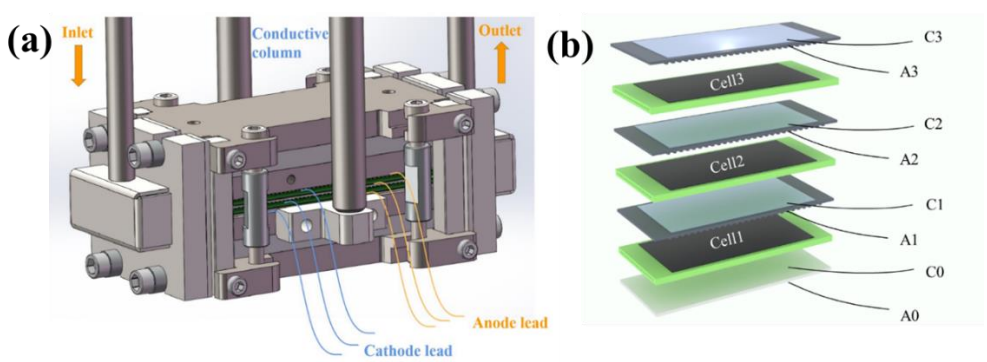

Figure 3.3. Assembly diagram of SOEC stack: (a) External structure, (b) Internal structure

Table 3.2. Meanings of the component labels in the single voltage of SOEC stack

Number	Unit	Meaning
CV1	C0A1	Cell1
CV2	C1A2	Cell2
CV3	C2A3	Cell3
CV5	A0C1	Cell1, cathode contact and anode contact
CV6	A1A2	Cell2 and cathode contact
CV7	C1C2	Cell2 and anode contact
CV8	A2A3	Cell3 and cathode contact

Table 3.3. Process parameters for stack sealing

	Ni-YSZ side	LSCF-GDC side	Sealing	Dry temperature	Dry time
1	0.4 mm NiO (mesh+paste)	Wet LSCF+Ag (mesh+paste)	Glass sealant 4	90 °C	30 min
2	0.4 mm NiO (mesh+paste)	Wet LSC+Ag (mesh+paste)	Glass sealant 4	90 °C	30 min
3	0.4 mm NiO (mesh+paste)	Wet LSCF+Ag (mesh+paste)	Glass sealant 7	90 °C	30 min

4	0.4 mm NiO (mesh+paste)	Wet LSC+Ag (mesh+paste)	Glass sealant 7	90 °C	30 min
5	0.4 mm NiO (mesh+paste)	Dry LSCF+Ag (mesh+paste)	Glass sealant 4	90 °C	30 min
6	0.4 mm NiO (mesh+paste)	Dry LSC+Ag (mesh+paste)	Glass sealant 4	90 °C	30 min
7	0.4 mm NiO (mesh+paste)	Dry LSCF+Ag (mesh+paste)	Glass sealant 7	90 °C	30 min
8	0.4 mm NiO (mesh+paste)	Dry LSC+Ag (mesh+paste)	Glass sealant 7	90 °C	30 min
9	0.4 mm NiO (mesh+paste)	Dry LSCF+Ag (mesh+paste)	Glass sealant 4	90 °C	10 min
10	0.4 mm NiO (mesh+paste)	Dry LSC+Ag (mesh+paste)	Glass sealant 4	90 °C	10 min
11	0.4 mm NiO (mesh+paste)	Dry LSCF+Ag (mesh+paste)	Glass sealant 7	90 °C	10 min
12	0.4 mm NiO (mesh+paste)	Dry LSC+Ag (mesh+paste)	Glass sealant 7	90 °C	10 min
13	0.3 mm NiO (mesh+paste)	Dry LSCF+Ag (mesh+paste)	Glass sealant 4	90 °C	10 min
14	0.3 mm NiO (mesh+paste)	Dry LSC+Ag (mesh+paste)	Glass sealant 4	90 °C	10 min
15	0.3 mm NiO (mesh+paste)	Dry LSCF+Ag (mesh+paste)	Glass sealant 7	90 °C	10 min
16	0.3 mm NiO (mesh+paste)	Dry LSC+Ag (mesh+paste)	Glass sealant 7	90 °C	10 min
17	0.3 mm NiO (mesh+paste)	Dry LSCF+Ag (mesh+paste)	Glass sealant 4	90 °C	0 min
18	0.3 mm NiO (mesh+paste)	Dry LSC+Ag (mesh+paste)	Glass sealant 4	90 °C	0 min
19	0.3 mm NiO (mesh+paste)	Dry LSCF+Ag (mesh+paste)	Glass sealant 7	90 °C	0 min
20	0.3 mm NiO (mesh+paste)	Dry LSC+Ag (mesh+paste)	Glass sealant 7	90 °C	0 min

Table 3.3 summarizes several common assembly sealing parameters of the stack. After dozens of assemblies and gas leakage rate tests, it was found that No. 7 sealing slurry drying time of 10 minutes, 0.3 mm foam nickel and

nickel oxide slurry applied on the Ni-YSZ electrode, as well as the LSC-Ag current collection layer coated on the LSCF-GDC electrode side and covered with silver mesh constituted the most appropriate process parameters. To ensure electron conduction, the thickness of silver mesh was determined by the height difference between the sealing material after drying and the rib height on the interconnect. Usually, the thickness of silver mesh ranges from 0.1 to 0.4 mm.

The gas chambers of the fuel electrode and the air electrode were installed and securely fixed in place. Further, the gas chambers were sealed again with the above-mentioned commercial glass sealing materials. The insulating plates were added in the gap between the gas chambers and stacks cores to prevent short circuiting. The complete stack appearance, fuel side and air side photos after assembly, are shown in **Figure 3.4**.

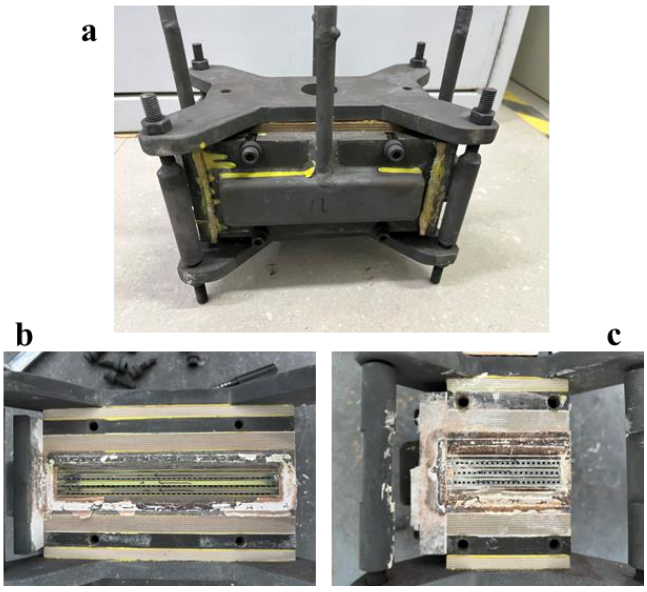

Figure 3.4. (a) Photo of SOEC stack; (b) Photo of air side; (c) Photo of fuel side

3.3 Testing of cells and stacks

Reduction treatment should be conducted on the cell or stack when heated to the operating temperature (usually 750 °C) because nickel in the fuel electrode was in the oxidized state during the preparation of the cell and stack, incapable of catalyzing or conducting electricity. Before reduction, first the gas tightness was first tested by introducing 0.3 SLM N_2 into the inlet of the cell and stack. Usually, good gas tightness requires the flow rate measured at the outlet to be greater than 0.29 SLM (3% leakage rate). Then the fuel electrode channel was purged with N_2 for at least 5 minutes to remove air in the system. After that, 0.3 SLM of H_2 (99.9%) and 1 SLM of air were injected into the fuel electrode and the air electrode, respectively. When nickel oxide in the fuel electrode was completely reduced to nickel, that is, when the open-circuit voltage (OCV) remained stable, the performance test was conducted. Instantaneous discharge and charge performance tests were initially performed using the charge-discharge test system from Bate Measurement and Control Technology Co., Ltd, (Ningbo, China). During the instantaneous SOFC and SOEC modes, the gas on the fuel electrode was 0.6 SLM H_2 and 25 vol.% H_2-75 vol.% CO_2, respectively. During the performance test of the three-unit stack, the total gas volume should not be less than three times of the single cell.

3.3.1 Instantaneous performance test

The instantaneous performance test mainly produced polarization curves (I-V curves), namely the current-voltage relationship curves, including the discharge polarization curve (I>0) and the charge polarization curve (I<0), as shown in **Figure 3.5**. **Figure 3.5a** depicts the I-V curve under the discharge mode. The discharge procedure was set by the test system, making the current increase in a stepwise manner. The voltage decreased with the increase of current density, while the power increased with the increase of current density, and decreased after reaching the maximum value. The discharge performance could be compared by observing the discharge voltage under the same current density, and the higher the discharge voltage is, the better the performance is.

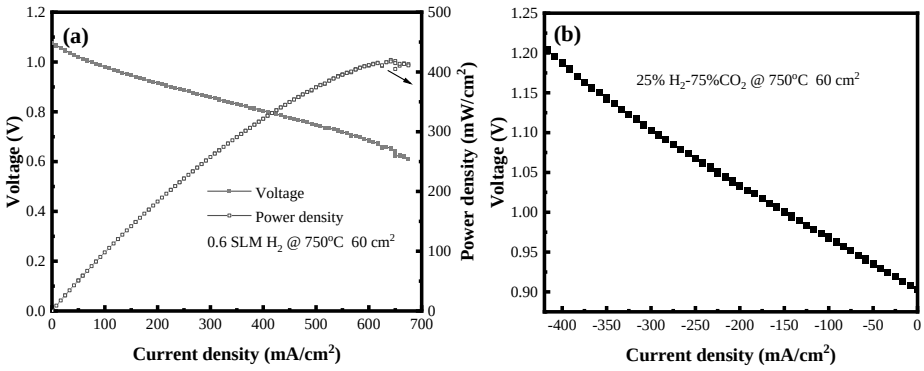

Figure 3.5. Polarization curves (a) Sischarge mode (b) Charge mode

Figure 3.5b shows the I-V curve under the charging mode. The test procedure and the current clamps were switched to the charging mode. As observed, when the current increased in a stepwise manner through the

setting procedure, the charge voltage increased with the increase of current density. Under the same current density, the lower the charge voltage, the better the performance, and the less electricity energy consumed to convert certain amount of fuel. When the load current rose to a certain value, the slope of the polarization curve suddenly changed, as further explained in **Chapter 4**, indicating that concentration polarization began to dominate the electrode reaction process.

3.3.2 Durability testing

Durability testing is important to characterize the lifespan of cells. V-t or I-t curves are usually used to observe the variation of real-time voltage or current. The current and voltage conditions required for long-term durability test are usually obtained from charge I-V curve.

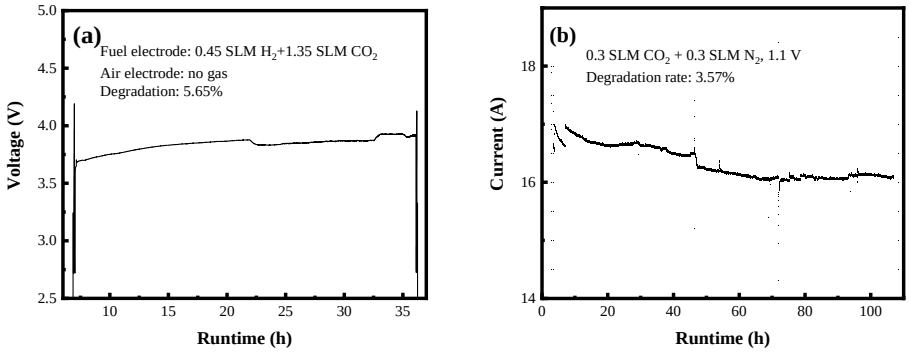

Figure 3.6. (a) V-t curve of 3-unit SOEC stack under constant current charge mode, (b) I-t curve of SOEC under constant voltage charge mode

Figure 3.6a shows the variation of the stack voltage with runtime under the constant current electrolysis mode. **Figure 3.6b** shows the trend of the

real-time electrolysis current with runtime under the constant voltage electrolysis mode. The degradation rate represents the slope of the V-t or I-t curve.

3.4 Electrochemical impedance

Electrochemical impedance spectroscopy (EIS) is a powerful in-situ tool used for characterizing SOFC and SOEC systems, to collect information about electrodes and interfaces [202, 203]. During the test, a disturbance signal, usually current or voltage, is applied to the test system to obtain a feedback signal. The ratio of the voltage signal to the current signal indicates the impedance. Impedance means the blocking effect of the current in the circuit, which is a complex value, usually expressed as Z. The real part Z' is called resistance, and the imaginary part Z'' is called reactance. Reactance exists in AC circuit, which is used to indicate the blocking effect of inductance and capacitance on current. Impedance is usually represented by the Nyquist diagram, as shown in **Figure 3.7a**. **Table 3.4** shows the meanings of each part in EIS curve. The intercept between the high frequency region and the real axis refers to the ohmic impedance (Rs), the intersection between the low frequency region and the real axis is total impedance (Rt), and the difference between Rt and Rs denotes the polarization impedance (Rp).

Table 3.4. The meanings of each part in EIS curve

Ohmic impedance (Rs)	The intercept between the high frequency region and the real axis
Total impedance (Rt)	the intersection between the low frequency region and the real axis
Polarization impedance (Rp)	the difference between Rt and Rs

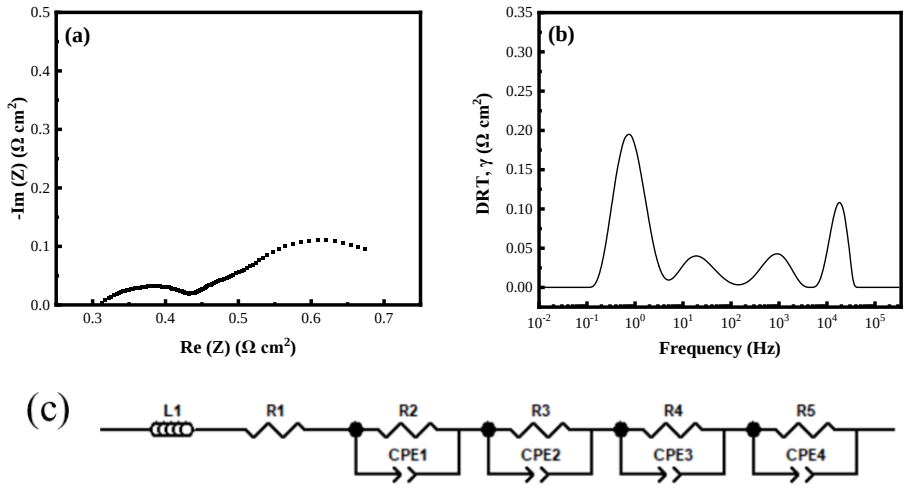

Figure 3.7. Electrochemical impedance and analysis method: (a) Nyquist diagram; (b) DRT diagram; (c) Effective equivalent circuit

The distribution of realization time (DRT) is usually employed for deconvolution analysis of a single impedance spectrum. This method is based on the principle that different (electro) chemical processes correspond to different relaxation times, which can be applicable for distinguishing (electro) chemical processes in the SOEC system [204]. This method can effectively separate the overlapping processes in EIS with high resolution. The effective equivalent circuit (EEC) can be obtained by analyzing DRT

spectral. Therefore, DRT analysis of impedance diagram can be regarded as a pre-identification tool to select suitable EEC for system. The combination of DRT and EEC can more objectively analyze EIS and reflect the polarization process. The typical DRT spectrum and equivalent circuit model are shown in **Figure 3.7b** and **Figure 3.7c**.

3.4.1 Testing under open circuit voltage

The impedance test is usually conducted in an open circuit state, and the EIS spectrum is recorded by the electrochemical workstation (VMP3B-20, Bio-Logic, France). Since the electrolysis equipment can not directly measure impedance, an additional electrochemical workstation is required. In this research, the electrolysis mode should be first disconnected in order to connect to the electrochemical workstation. The current range of the electrochemical workstation was 20 A. Impedance measurement was performed under OCV conditions considering its stability. The fuel electrode was filled with 25 vol.% H_2-75 vol.% CO_2 fuel gas, and the air electrode was filled with a certain amount of air. The frequency scanning range was set from 30 kHz to 20 mHz, and the AC amplitude was usually set to 10 mV.

The analysis of the DRT spectrum is usually based on the DRT tools box in Matlab. The normal regularization factor is 10^{-2}~10^{-3}, with a Gaussian second-order function for impedance fitting. The calculation of DRT is as follows:

$$R_t = R_s + R_p = R_s + \int_{-\infty}^{\infty} \frac{\gamma(ln\tau)}{1+i2\pi f\tau} dln\tau \quad \text{(Eq.3.1)}$$

$$f = 1/\tau \quad \text{(Eq.3.2)}$$

where R_t, R_s, and R_p represent the total impedance, ohmic impedance, and polarization impedance, respectively. τ and f are the relaxation time and frequency, respectively.

3.4.2 Test with loading

In addition to measuring impedance under open circuit conditions, EIS can also be tested under loading conditions in a process similar to that described in **Section 3.4.1**. After setting the frequency scanning range and amplitude, the loading voltage should also be set. The appropriate loading voltage is usually obtained from the I-V polarization curves, due to range limitations of the electrochemical workstation, usually selecting the corresponding voltages under 6~18 A.

3.5 Microscopic characterization

3.5.1 Scanning electron microscope

Scanning electron microscopy (SEM) images samples at nanometer resolution by an electron beam. The electron beam is scanned in a raster scan pattern, and then the corresponding image can be produced by combining the position of the beam with the intensity of the detected signal. In this thesis,

micro-morphology characterization of the cross-section of the cell sample was carried out. Since a nickel-based electrode with good conductivity was selected as the fuel electrode material in the experiment, it was unnecessary to carry out pretreatment of the sample. But to fix and strengthen the conductivity, the sample on the sample table should be fixed with special conductive adhesive. The SEM devices used for micro-morphology characterization were cold field emission SEM (S4800, Hitachi, Japan) and hot field SEM (FEI QUANTA 250 FEG, US; Gemini300, Zeiss, Germany).

3.5.2 Energy Dispersive Spectrometry

Energy dispersive spectrometry (EDS) is a powerful technology for analyzing the elemental composition of samples. The basic principle is to analyze the chemical composition through the characteristic X-ray energy spectrum generated by the interaction between the electron beam and the sample. EDS can be applied to estimate the relative abundance of elements in the sample. However, some elements such as Y and Zr may appear overlapping X-ray emission peaks, thus affecting the accuracy of measured components. To avoid errors, this paper adopted EDS only to analyze the distribution of nickel in the fuel electrode after the CO_2 electrolysis experiment, Sr segregation of the air electrode and the toxicity of chromium. The energy dispersive spectrometer used in this thesis was the Bruker EDS QUANTAX (Germany) available with SEMs employed.

3.5.3 Raman spectroscopy

Raman spectroscopy is a light scattering technology. When a laser light source with high intensity irradiates the surface of a sample, most of the scattered light has the same wavelength as the incident light (Rayleigh scattering), and only a small part of the scattered light scatters at different wavelengths, according to the chemical structure of the sample (Raman scattering). Raman spectroscopy determines the vibration mode of molecules. The monochromatic light source from a laser in the visible, near-infrared or near-ultraviolet range can be used, and even X-rays. Raman spectrum analysis is a nondestructive testing technology, without requiring additional sample preparation operation. In this thesis, Raman spectroscopy (Renishaw inVia Reflex, UK) was used for analyzing carbon deposition in the fuel electrode and the chromium poisoning effect in the air electrode after CO_2 electrolysis testing.

3.6 Gas composition analysis

Gas chromatography (GC) is a technology to separate the components in the mixture using different distribution behaviors between the mobile phase and the stationary phase. The mobile phase represents a carrier gas, usually nitrogen or helium, while the stationary phase means a high boiling point liquid which can be adsorbed on a solid. Because of differences in

physical and chemical properties of each component, such as boiling point and polarity, the retention time in the chromatography column may be different. In this paper, qualitative analysis of the separated components was carried out according to the sequence and retention time of each component flowing out of the column, as shown in **Figure 3.8**.

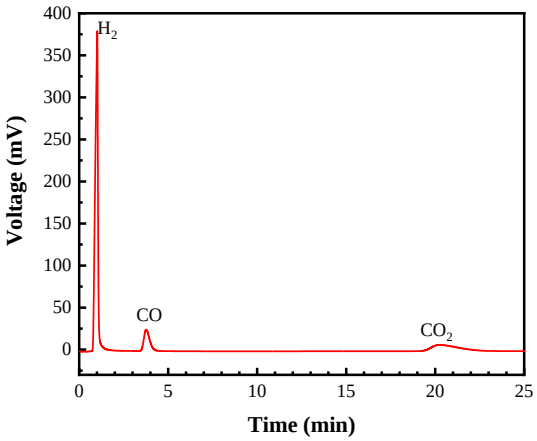

Figure 3.8. Gas chromatogram of fuel electrode exhausted gas

After the assignment of chromatographic peaks, the normalization method should be used for quantitative analysis of sample components. For this project, GC-7820 (Shimadzu, China) gas chromatograph and GC-7890B (Agilent, USA) gas chromatograph were utilized to characterize the composition of the exhaust gas.

3.7 Energy conversion efficiency

CO_2 electrolysis at high temperatures using SOECs is a way to convert electricity or heat energy into chemical energy, which is a power-to-gas conversion process. The efficiency is usually more than 75% because of the

heat loss of stack components, but the value is still far more than that of other electrolysis cells. Efficiency reflects the degree of energy utilization and is one of the important indicators that determine future development prospects of the device. In view of the current international situation of energy storage, it is necessary to deeply explore the efficiency of energy conversion and corresponding influencing factors.

3.7.1 Open circuit voltage

In the actual situation of SOEC operation, the gas tightness of electrolysis cells is extremely important. Therefore, considering the open circuit voltage (OCV) of cells under various atmospheres is necessary. The theoretical OCV of SOECs is caused by the difference of oxygen partial pressure between the gas chambers on both sides of the fuel electrode and the air electrode, which can be calculated by **Eq.3.3** [205].

$$OCV_{theroretical} = \frac{RT}{4F} ln \frac{[O_2]_{Air}}{[O_2]_{Fuel}} \quad \text{(Eq.3.3)}$$

where $R = 8.314\, J \cdot mol^{-1} \cdot K^{-1}$, $F = 96485\, C \cdot mol^{-1}$, $[O_2]_{Air}$ and $[O_2]_{Fuel}$ are the oxygen partial pressure of air electrode and fuel electrode. In this research, when introducing pure CO_2 into the fuel electrode, the oxygen partial pressure of the fuel electrode could be calculated by the following reaction:

$$CO_2(g) + Ni = NiO + CO(g); \quad K_1 \text{ (Eq.3.4)}$$

$$CO_2(g) = 1/2O_2(g) + CO(g); \quad K_2 \text{ (Eq.3.5)}$$

$$[O_2]_{Fuel} = \frac{(K_2)^2}{(K_1)^2} \quad \text{(Eq.3.6)}$$

$$[O_2]_{Air} = 0.21 \quad \text{(Eq.3.7)}$$

The reaction equilibrium constants K_1 and K_2 were calculated by HSC 6.0 thermodynamic software, to obtain the theoretical OCV of SOEC with pure CO_2 at different temperatures. In CO-CO_2 fuel electrode atmosphere, where **Eq. 3.5** was the dominant reaction, the oxygen partial pressure of the fuel electrode was calculated by **Eq. 3.8**. In this way the theoretical OCV under different CO/CO_2 ratio could be calculated.

$$[O_2]_{Fuel} = \left(\frac{K_2[CO_2]}{[CO]}\right)^2 \quad \text{(Eq.3.8)}$$

In H_2-CO_2 fuel electrode atmosphere, with the existence of reverse water gas shift (RWGS) reaction, the equilibrium constant K_3 of **Eq. 3.9** was calculated by HSC thermodynamic software as well. Subsequently, the content of each component was calculated according to **Eq. 3.10**.

$$CO_2(g) + H_2(g) = H_2O(g) + CO(g); \quad \text{K}_3\text{(Eq. 3.9)}$$

$$K_3 = \frac{[CO]_{equi} \times [H_2O]_{equi}}{[CO_2]_{equi} \times [H_2]_{equi}} \quad \text{(Eq. 3.10)}$$

3.7.2 Conversion rate

The conversion rate of reactants is also an important index to evaluate the performance of SOECs. The calculation of CO_2 conversion rate is as follows:

$$\alpha_{CO_2} = \frac{F_{out,CO} - F_{in,CO}}{F_{in,CO_2} - F_{out,CO_2}} \times 100\% \quad \text{(Eq. 3.11)}$$

where, α_{CO_2} represents the CO_2 conversion rate (%); $F_{out,CO}$ indicates the measured output value of CO (SLM); $F_{in,CO}$ denotes the inlet value of CO (SLM); F_{in,CO_2} represents the amount of CO_2 introduced to the fuel electrode (SLM); F_{out,CO_2} represents the amount of CO_2 in the fuel electrode outlet (SLM). Notably, the CO_2 conversion rate is equal to the CO generation rate in the case of no by-product produced in the CO2 electrolysis reaction.

3.7.3 Energy efficiency

SOECs can be deemed as an energy conversion device. The ability of SOEC to convert electric energy and heat energy into chemical energy can be evaluated by the concept of energy conversion efficiency (ECE). ECE is an important parameter in the process of CO_2 electrolysis, which is the ratio of the output available energy to the input energy, and can represent the degree of energy utilization of the device [206].

In this paper, the energy conversion efficiency was found to be related to the exhaust gas composition measured in the fuel electrode during electrolysis. When CO was used as the protective gas, the energy conversion efficiency of CO_2 electrolysis could be calculated by **Eq. 3.12** - **Eq. 3.17**:

$$ECE(CO, exclude\ Q) = \frac{E_{CO,out}}{E_e} \times 100\% \quad \text{(Eq. 3.12)}$$

$$ECE(CO, exclude\ Qair) = \frac{E_{CO,out} \times 100\%}{E_e + E_{th} + Q_{extra,CO} + Q_{extra,CO_2}} \quad \text{(Eq. 3.13)}$$

$$ECE(CO) = \frac{E_{CO,out} \times 100\%}{E_e + E_{th} + Q_{extra,CO} + Q_{extra,CO_2} + Q_{extra,air}} \quad \text{(Eq. 3.14)}$$

$$Q_{extra,CO} = \frac{Q_{CO} \times V_{CO,consume}}{V_m} \quad \text{(Eq. 3.15)}$$

$$Q_{extra,CO_2} = \frac{Q_{CO_2} \times V_{CO_2,consume}}{V_m} \quad \text{(Eq. 3.16)}$$

$$Q_{extra,air} = \frac{Q_{O_2} \times V_{air,consume} \times 0.21}{V_m} + \frac{Q_{N_2} \times V_{air,consume} \times 0.78}{V_m} \quad \text{(Eq. 3.17)}$$

When H_2 was used as protective gas, ECE could be calculated by formula **Eq. 3.17** - **Eq. 3.21**:

$$ECE(H_2, exclude\ Q) = \frac{E_{CO,out}}{E_e + E_{H_2,consume}} \times 100\% \quad \text{(Eq. 3.18)}$$

$$ECE(H_2, exclude\ Qair) = \frac{E_{CO,out} \times 100\%}{E_e + E_{th} + E_{H_2,consume} + \Delta H(RWGS) + Q_{extra,H_2} + Q_{extra,co_2}} \quad \text{(Eq. 3.19)}$$

$$ECE(H_2) = \frac{E_{CO,out} \times 100\%}{E_e + E_{th} + E_{H_2,consume} + \Delta H(RWGS) + Q_{extra,H_2} + Q_{extra,co_2} + Q_{extra,air}} \quad \text{(Eq. 3.20)}$$

$$Q_{extra,H_2} = \frac{Q_{H_2} \times V_{H_2,consume}}{V_m} \quad \text{(Eq. 3.21)}$$

where ECE is the energy conversion efficiency; Q is the heat energy; $E_{CO,out}$ is the energy of CO generated by the SOEC system; E_e refers to the electric energy that consumed by CO_2 electrolytic reaction; E_{th} is the compensation energy required by the system to maintain the reaction temperature if the electrolytic voltage is lower than thermal neutral voltage of the reaction (1.464 V); $E_{H_2,consume}$ means the energy of H_2 consumed in the RWGS reaction; V_m is the molar volume of gas at room temperature and ambient pressure, with the calculated value of 24.5 SLM; $V_{H_2,consume}$, $V_{CO,consume}$, $V_{CO_2,consume}$, and $V_{air,consume}$ are the volume flow of H_2, CO, CO_2 and air consumed respectively (SLM); Q_{extra,H_2} , $Q_{extra,CO}$, Q_{extra,co_2} and, $Q_{extra,air}$ are the heat consumed by H_2, CO, CO_2 and air respectively (J/min);

Q_{H_2}, Q_{CO}, Q_{CO_2}, Q_{O_2}, Q_{N_2} are the heat capacities of the five kinds of gas, with the calculated values of 21456.41, 22511.23, 34672.43, 23178.4, and 22458.23 J/mol respectively. $\Delta H(RWGS)$ denotes the heat energy to be absorbed in RWGS reaction, with the calculated value of 34.64 kJ/mol. When calculating the energy conversion efficiency, the flow rate at the inlet / outlet of the cell should be calibrated to reduce the flow rate error.

3.7.4 Generation rate of target product

During the actual operation of the SOEC, the generation rate of the target product CO was calculated from the GC results of the fuel electrode tail gas and the actual outlet flow rate of the fuel electrode, as shown in **Eq. 3.22**:

$$F_{out,CO} = [CO] \times F_{total} \quad \text{(Eq. 3.22)}$$

where $F_{out,CO}$ is the flow rate of the target product CO (L/min), $[CO]$ represents the volume concentration of CO in the exhausted gas of the fuel electrode (%), and F_{total} is the total flow rate measured at the outlet of the fuel electrode.

3.8 Mechanical property testing

After high-temperature experiment, the structure of the cell might be damaged, resulting in the decrease in mechanical strength. To quantify the damage of the cell structure, the mechanical properties of the cell sample were measured through the universal material testing machine. This testing

machine can carry out tensile, compression, peel and bending tests. The mechanical properties of the cell samples in this research were determined by a three-point bending test, that is, the rectangular cell sample was supported at both ends, and then loaded in the middle with the increased force until failure. The schematic diagram is described in **Figure 3.9a**. The mechanical properties of the sample were deduced from the stress-strain curve constructed using the deflection of the specimen. The support span used in the test was 30 mm, and the test sample was cut into multiple rectangle structures with a length of 40 mm, a width of 4 mm, and a height of 3 mm, as shown in **Figure 3.9b**. The relationship curves of strength and deformation are illustrated in **Figure 3.9c**.

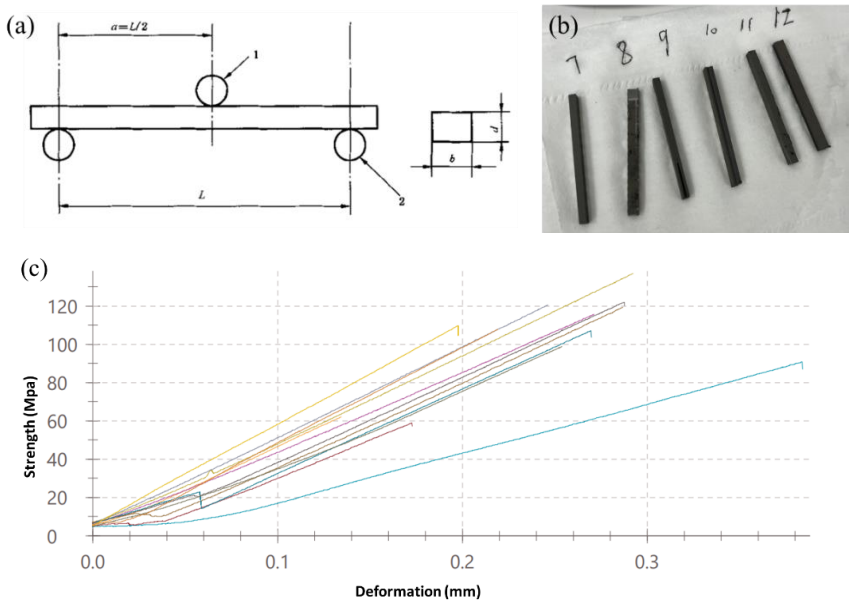

Figure 3.9. (a) Schematic diagram of mechanical property test; (b) The cell sample to be tested; (c) The relationship curves of strength and deformation

Chapter 4. Factors affecting CO_2 electrolysis in SOECs

4.1 Introduction

High temperature CO_2 electrolysis in SOECs is often faced with different environmental conditions, such as operation without a H_2 protective atmosphere. For example, in recent years, the use of SOEC stacks to generate oxygen on Mars (i.e. Moxie) has been discussed enthusiastically. The advantage of employing CO as the fuel electrode reduction atmosphere lies in that it can directly return to the fuel electrode to form a carbon cycle. However, it is inevitable that with nickel catalysis, CO produces carbon deposition by the disproportionation reaction, which affects long-term performance of cells [207]. One of the objectives of the present research was to investigate the performance of the Ni-YSZ electrode during high temperature CO_2 electrolysis in the SOEC with the flat-tube structure under different fuel electrode atmospheres, different reaction temperatures and different loading currents. In addition, the thermodynamic analysis of the whole electrolysis system was carried out to provide useful reference value for its application in different practical scenarios.

4.2 Effect of sealing material

To explore the optimal sintering temperature and applied pressure of

the stack, the NO.7 sealing material with 70% solid content was applied to three SUS441 interconnects and placed in the sintering furnaces. The temperature was raised to 850 °C, 900 °C, and 930 °C respectively according to a fixed program, and should remain constant for at least 3 hours before cooling down. Afterwards, the interconnects coated with sealing materials were cut into 1 cm × 0.5 cm for SEM analysis, and the results are organized in **Figure 4.1**. It was found that the higher the temperature, the greater the deformation of the interconnects. When the temperature was above 900 °C, delamination of the interconnects and sealing materials appeared. The sealing materials sintered at three different temperatures all exhibited good density, in which the glass sealing material sintered at 930 °C was the densest, while the one sintered at 850 °C had slightly lower density.

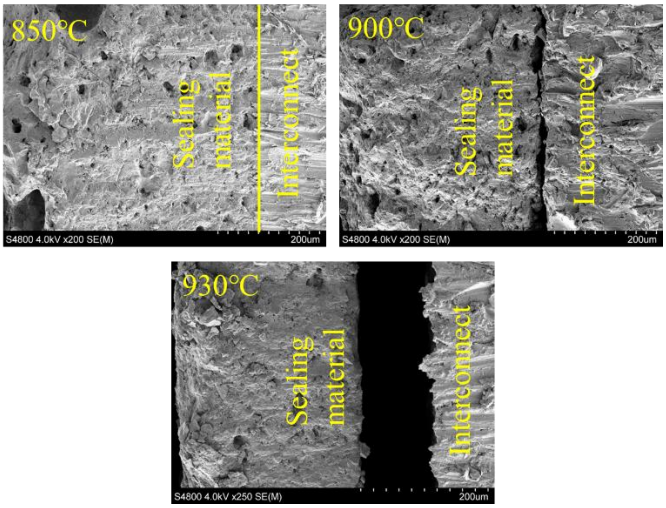

Figure 4.1. Morphology of sealing materials after calcination at 850 °C, 900 °C and 930 °C

After sintering at 850 °C, the temperature was lowered to 750 °C and

hydrogen was introduced for reduction. Then, after cooling down to room temperature, the stack was disassembled for analysis. Sealing materials at different positions on the conductive plate were taken for microstructure analysis. The results are shown in **Figure 4.2**. Because of structural limitations, there were differences in the adhesive dispensing ability of sealing materials at different positions during the heating process, resulting in different microstructures. To alleviate the above-mentioned sealing problems, increasing the sintering time could be feasible to prevent slow organic emissions from sealing materials in some positions. Additionally, sealing materials with a solid content of over 80% should be used on the flow channel side.

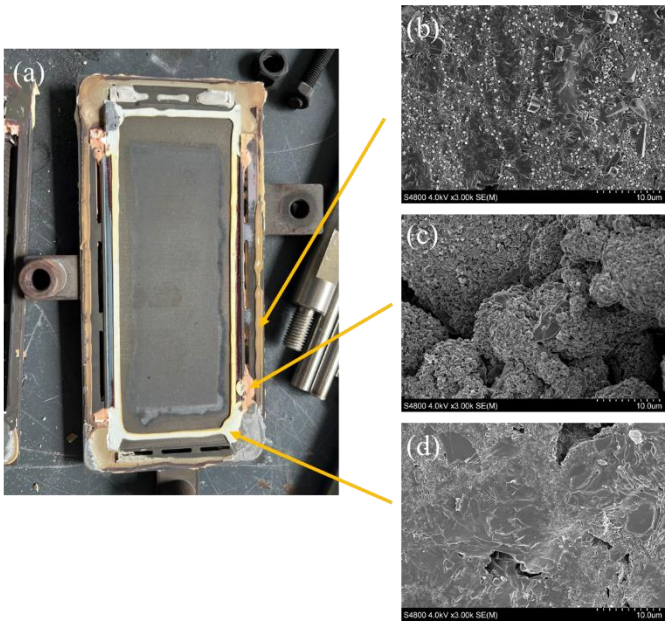

Figure 4.2. Morphology of sealing materials after calcination at 850 °C for 3 h, and reduction at 750 °C

To investigate the effects of temperature and pressure on the density of

sealing materials during the sintering process, microstructure analysis was performed on the sample cross-sections sintered under four conditions: 750 °C-0 kg, 750 °C-150 kg, 800 °C-200 kg, and 800 °C-250 kg, as shown in **Figure 4.3**. According to the SEM results, pressurization slightly improved the density of sealing materials, and the sealing material under the conditions of 800 °C-200 kg basically met the sealing requirements. This was because increasing the pressure could enhance the interfacial adhesion and reinforce the sealing performance. Considering the strength of the cell and the melting point of sealing materials, 800 °C was chosen as the highest temperature for hot- pressing treatment, and 200 kg was selected as the highest pressure of the stack.

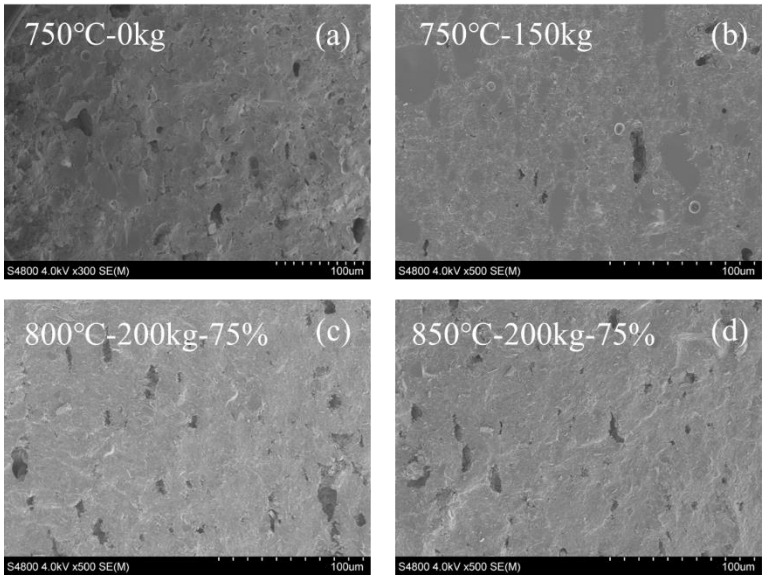

Figure 4.3. Morphology of sealing materials after calcination at different temperatures and pressures

4.3 Effect of temperature and gas volume

To determine the minimum temperature for electrolysis, the cell performance was tested at 750 °C, 650 °C, 600 °C, 550 °C and 500 °C respectively. The results are displayed in **Figure.4.4**. It was found that the higher the temperature, the better the performance and lower OCV of the cell. This was mainly because the higher the temperature, the higher the conductivity of YSZ. For a stack composed of three cells and four interconnects, the fuel gas used was at least three times that of a single cell. Further, the charging and discharging performance at 650 °C-800 °C was investigated. The results are shown in **Figure 4.5**, which were similar to the conclusion from a single cell. Within the temperature range of 650 °C-800 °C, the higher the temperature, the better the charging and discharging performance of the stack, the lower the open circuit voltage. This was mainly due to the fact that high temperature promoted ion transportation in the electrolyte and accelerated electrode reaction kinetics [208].

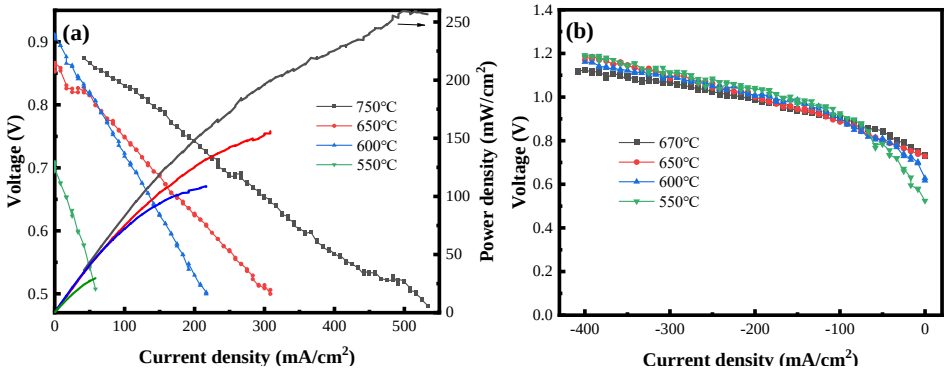

Figure 4.4. Performance test of the cell at different temperatures: (a) SOFC mode; (b) SOEC mode

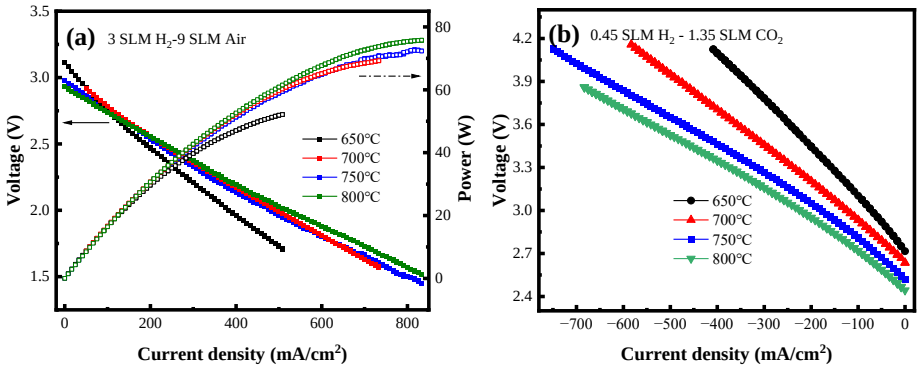

Figure 4.5. Performance test of the SOEC stack at different temperatures: (a) SOFC mode; (b) SOEC mode

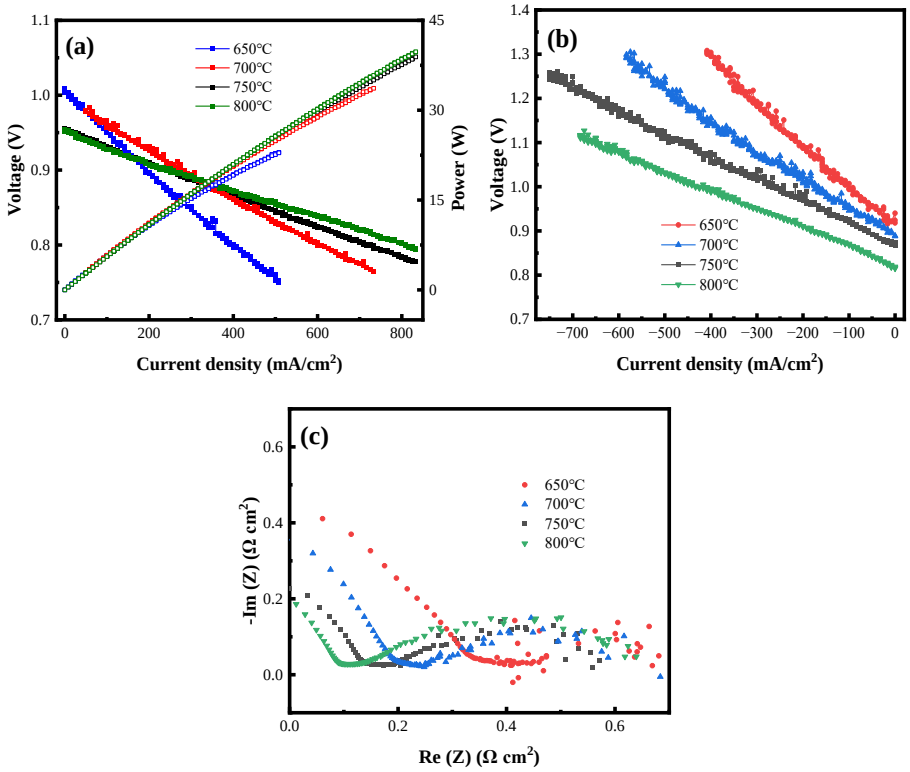

Figure 4.6. Performance test of the cell unit in the stack at different temperatures: (a) SOFC mode; (b) SOEC mode; (c) Impedance

To study the variation of cell impedance with temperature, voltage probes were used for internal monitoring single unit of the stack, with each

unit containing a cell and an interconnect. The results are shown in **Figure 4.6**, indicating that the higher the temperature, the higher the charging and discharging performance; The area specific resistance (slope of I-V curves) and OCV of the cell decreased with increasing temperature. **Figure 4.6c** shows the impedance changes at different temperatures. As observed, total impedance and polarization impedance decreased with increasing temperature.

Based on the charging and discharging performance and EIS results, higher operating temperatures might be more advantageous. However, such a high temperature also caused several challenges related to sealing, electrode morphological stability, chemical stability of cell components, and thermal shock resistance of accessories. Considering cell performance, OCV, sealing performance, and the lifespan of stack components, 750 °C was selected for long-term performance and degradation mechanism research.

To study the appropriate gas volume required for the fuel electrode reaction, 25 vol.% H_2-75 vol.% CO_2 was selected as the fuel ratio, and the total gas volume of the fuel electrode was changed to examine the electrolytic performance of the cell. Due to a malfunction in the gas control valve of the air, no air was introduced during the experiment. The results are presented in **Figure 4.7**. Due to the lack of air in the air electrode, the gas pressure was lower and the OCV became lower than the theoretical value. When the total gas volume increased from 0.6 SLM to 0.8 SLM, the OCV

remained above 0.74 V. When the fuel gas increased to 1.06 SLM, the flow rate difference between the fuel and air electrodes exceeded 1 SLM, which might affect the sealing, making the OCV below 0.6 V. When the total gas volume increased from 0.6 SLM to 0.8 SLM, the electrolytic voltage of the electrolysis cell showed a slight downward trend. When the total gas volume of the fuel electrode increased to 1.06 SLM, the performance of the electrolysis cell recovered and almost overlapped with the curve of 0.6 SLM in the current range of -50 to -250 mA/cm^2. Considering fuel utilization and cost, 0.6 SLM was chosen as the total fuel gas volume for the single cell for subsequent experiments.

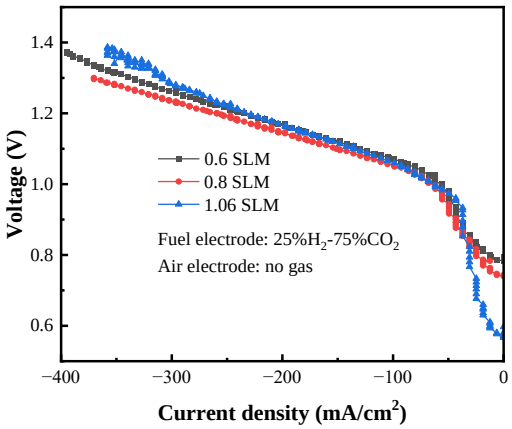

Figure 4.7. The electrolytic performance of SOEC under different total fuel volumes

4.4 Effect of protective gas type and content

4.4.1 Electrochemical impedance and DRT analysis

Figure 4.8a delineates the relationship between the oxygen partial pressure of the fuel electrode and the gas composition at 750 °C. It is worth

noting that the two curves for H_2 and CO were almost identical. When CO_2 content in the feed gas of the fuel electrode moved to both ends of the curves, a greater change in the oxygen partial pressure of the fuel electrode was observed. According to **Eq.3.3**, the larger the change of oxygen partial pressure of the fuel electrode, the more obvious the OCV changes. When CO_2 content in the inlet gas was between 0.25 and 0.8, the change in the oxygen partial pressure of the fuel electrode was much slower. The oxygen partial pressure and OCV under two kinds of fuel electrode atmospheres are shown in **Table 4.1**, where the values remained consistent with those reported in the literature [209, 210].

Figure 4.8b illustrates the instantaneous performance of CO_2 electrolysis in the two fuel electrode atmospheres. The experiment was carried out maintaining good air tightness in the system. The electrolytic voltage increased linearly with the increase of current density. When the current density reached the critical value, defined as the limited current density [143], the voltage rose sharply and concentration polarization acted dominantly. 25 vol.% H_2-75 vol.% CO_2 and 23.8 vol.% CO-71.7 vol.% CO_2 displayed the same oxygen partial pressure, and 50 vol.% H_2-50 vol.% CO_2 and 46.7 vol.% CO-53.3 vol.% CO_2 exhibited the same oxygen partial pressure, and so on. The electrochemical performance results under the same oxygen partial pressure and different fuel electrode atmosphere manifested that when the volume fractions of hydrogen were 25%, 50%, and 75%, the

limiting current densities of CO_2 electrolysis were -550 mA/cm^2, -480 mA/cm^2, and -250 mA/cm^2, respectively. While using CO as the protective gas with 23.8%, 46.7% and 71.7% volume fractions, the limiting current densities decreased to -480 mA/cm^2, -415 mA/cm^2 and -220 mA/cm^2, which were lower than the critical current density in H_2-CO_2 atmosphere. In general, the limiting current density in a CO atmosphere tended to be lower than that in a H_2 atmosphere with the same oxygen partial pressure. Also, the higher the ratio of reducing gas, the lower the limiting current density [143, 211-212].

According to the EIS impedance spectrum (**Figure 4.8c**) in the OCV state, ohmic impedance remained almost the same in the two fuel electrode atmospheres, but polarization impedance was quite different. In the CO-CO_2 reducing atmosphere, polarization impedance was significantly higher than that under the protection of H_2. This might be related to the adsorption and diffusion processes under two protective atmospheres. Another important factor was that in the H_2-CO_2 atmosphere, the electrolysis reaction moved towards the equilibrium of RWGS reaction with fast catalytic kinetics, so as to reduce the overpotential of CO_2 electrolysis [213].

To determine the basic electrode reaction process under two kinds of reducing gas compositions, the influence on the cell performance was analyzed, and the distribution of relaxation time (DRT) curves (**Figure 4.8d and e**) were plotted. The two figures in **Figure 4.8d** show DRT analysis of

different reducing gas, in which the upper and lower figures correspond to the same coordinate axis. The high frequency region P5 near 10^4 Hz was related to charge transfer reaction on the surface and O^{2-} transport through the YSZ electrolyte, with the area in this region not responding to the change in gas concentration. Comparing the upper and lower figures, it was found that when CO was used as protective gas, the area of P5 characteristic peak increased and shifted to high frequency. The medium frequency region P4 near 10^3 Hz exhibited obvious response to the type of reducing gas (**Figure 4.8e**), which was attributed to the reaction at TPB, since the RWGS reaction would not occur when using CO as the protective gas. P3 near 10^2 Hz represents the process of oxygen exchange. With the decrease of CO_2 in fuel gas, the areas of the peaks became smaller. The low frequency region P2 near 10^1 Hz represents the gas diffusion process in porous material. Therefore, the peak area tended to be similar under the same oxygen partial pressure. The characteristic peak of P1 at 10^0 Hz obviously corresponded to the type and concentration of protective gas, illustrating that P1 was related to the gas diffusion rate in the fuel electrode, because the diffusion rate varied with the gas concentration and molecular weight [214, 215]. In H_2-CO_2 atmosphere, the area of P5 was slightly lower, which was consistent with the analysis result that RWGS reaction reduced polarization impedance produced by O^{2-} transport. There was no significant difference in P4 when H_2 concentration changed, but in CO-CO_2 atmosphere，the characteristic peak area P4 was

larger, which meant that the kinetics of the reaction might affect the adsorption and dissociation of CO_2. It is important to note that the P1 process was significantly different in the two atmospheres. In CO-CO_2, the area of P1 process corresponding to gas diffusion was much larger than that in the H_2-CO_2 atmosphere. This was also consistent with the view that the molecular weight determines the diffusion rate in the electrode channel.

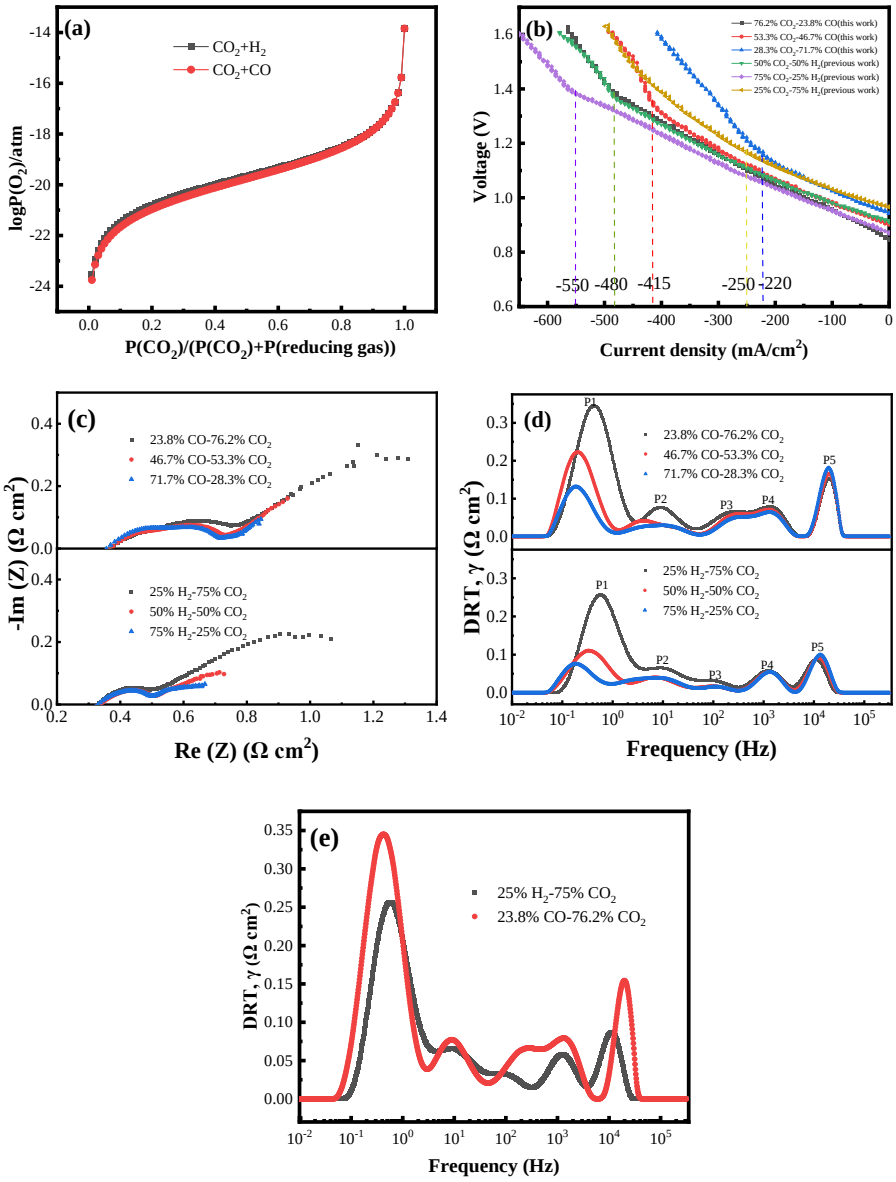

Figure 4.8. The partial pressure of oxygen and instantaneous electrolysis performance of H_2-CO_2 and CO-CO_2 fuel electrode atmosphere at 750 °C:

(a) Oxygen partial pressure varying with CO_2 content; (b) I-V curves of CO_2 electrolysis (including previous research [143]); (c) The Nyquist diagram of impedance spectra and (d) DRT diagram in H_2-CO_2 and CO-CO_2 atmospheres at OCV and 750 °C; (e) DRT diagram in two reducing atmospheres

To summarize the three reaction processes, the polarization resistance in the CO-CO_2 atmosphere was larger, leading to the decrease of instantaneous performance of CO_2 electrolysis. The areas of P1 and P5 being much larger than those of P2, P3 and P4, suggested that the P1 and P5 electrode processes controlled the whole electrolysis reaction. In other words, under the CO-CO_2 atmosphere, the P1 process attributed to gas diffusion dominated the whole electrode reaction.

Table 4.1. Theoretical and practical OCV under two reducing atmospheres at 750 °C

Ratio of content		**Velocity ratio (SLM)**	**Theoretical $[O_2]_{fuel}$**	**Theoretical OCV**	**Actual OCV**
Pure H_2	**100**	0.6	/	/	1.111
H_2/CO_2	25/75	0.15/0.45	1.76×10^{-19}	0.917	0.894
	50/50	0.3/0.3	2.20×10^{-20}	0.963	0.935
	75/25	0.45/0.15	2.75×10^{-21}	1.009	0.975
CO/CO_2	23.8/76.2	0.143/0.457	1.76×10^{-19}	0.917	0.90
	46.7/53.3	0.28/0.32	2.24×10^{-20}	0.963	0.945
	71.7/28.3	0.43/0.17	2.69×10^{-21}	1.009	0.990

Based on the results of **Figure 4.8**, the limiting current density was lower in the CO-CO_2 fuel electrode atmosphere. When reaching the limiting current density, the concentration polarization began to dominate the electrode reaction. The diffusion of both reactants and products brought about concentration polarization. The diffusion and adsorption rates of CO_2 in the porous electrode were slower than that of CO generation in electrochemical reactions, resulting in the lower concentration of CO_2 at the triple phase boundary. Also, a large number of molecules produced by the reaction could not be released fast enough, which occupied the active sites of TPB reaction, thus limiting the electrolysis reaction. According to the theoretical analysis of the concentration polarization reported in the literature, the limiting current density is also related to diffusion coefficient, boundary layer and gas diffusion channel of porous electrodes [216-218].

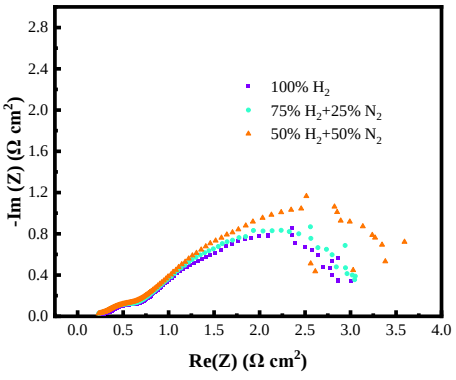

Figure 4.9. The electrochemical impedance in OCV state under different fuel electrode atmospheres

When the cell was in a high temperature state, the oxidizing gas should be isolated from the nickel electrode to prevent the oxidation of the nickel electrode. Using a reducing gas or inert gas should be a good choice. The impedance of the cell might be affected by the type of fuel gas introduced. To investigate the variation of impedance, N_2 and H_2 were selected to explore impedance under OCV conditions. **Figure 4.9** shows the EIS curves under 100 vol.% H_2, 75 vol.% H_2-25 vol.% N_2 and 50 vol.% H_2-50 vol.% N_2 fuel electrode atmospheres. The results indicated that as the hydrogen content decreased, the total impedance gradually increased.

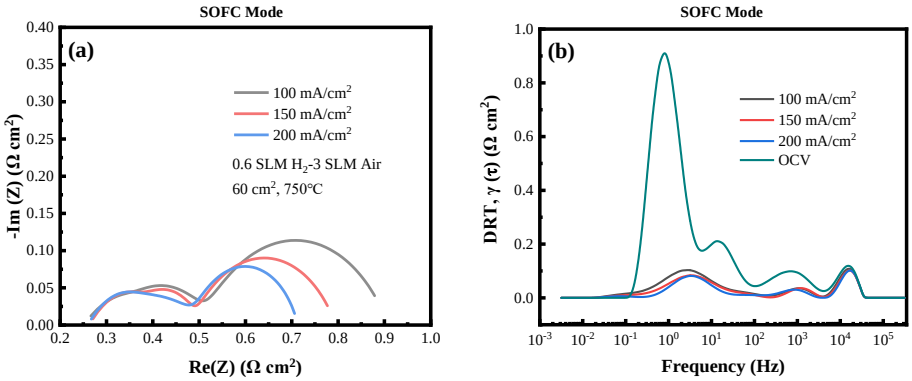

Figure 4.10. The electrochemical impedance and DRT in SOFC mode with different currents: (a) EIS curves; (b) DRT curves

Electrochemical impedance spectroscopy (EIS) is a non-destructive technique that can quickly provide a large amount of electrochemical information while maintaining the integrity of the cell. In this paper, EIS was measured under OCV conditions, as well as under loading conditions.

Conducting impedance testing with a constant load, current or voltage could more accurately reflect the electrochemical processes inside the cell. In **Figure 4.10**, EIS curves under SOFC mode were measured to compare the effect of different applied discharge currents.

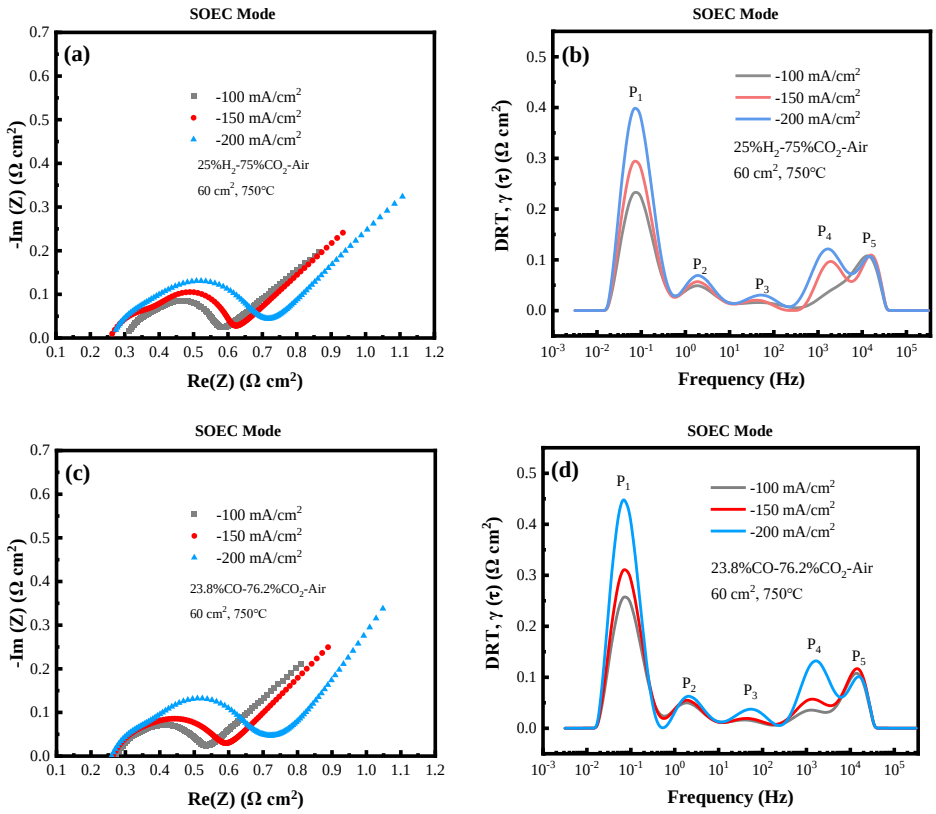

Figure 4.11. The electrochemical impedance and DRT in SOEC mode with different currents and fuel electrode atmospheres: (a) EIS curves in H_2-CO_2 atmosphere; (b) DRT curves in H_2-CO_2 atmosphere; (c) EIS curves in CO-CO_2 atmosphere; (d) DRT curves in CO-CO_2 atmosphere

DRT results in **Figure 4.10b** revealed that compared to EIS under OCV conditions, the impedance of each part decreased after applying discharge

current. The current transformation within 100-200 mA/cm^2 imposed little effect on the impedance results, which was because the applied current was small and had little change in the conversion rate of the fuel. Due to the diffusion impedance of water vapor being much smaller than H_2, the peak at around 10 Hz was significantly reduced compared to the OCV state. The larger the loading current, the more H_2O generated in the fuel electrode, which caused a slight decrease of the gas diffusion impedance in both fuel electrode and porous structures. When applying current, the number of diffusion characteristic peaks in the low-frequency region decreased, which might be due to insufficient decomposition of characteristic frequencies in multi-impedance analysis.

Similarly, the EIS curves and DRT were analyzed in SOEC mode to explore the effects of different electrolytic currents and fuel electrode atmospheres. **Figure. 4.11a**, **Figure. 4.11c** and **Table 4.2** show the impedance changes under different fuel electrode atmospheres and different applied electrolysis current densities. The two fuel electrode atmospheres (CO-CO_2 and H_2-CO_2) appeared the same oxygen partial pressure, as shown in **Table 4.1**, and the applied electrolytic current density changed from -100 to -200 mA/cm^2 during the test. The results manifested that as the electrolytic current density increased, the ohmic impedance of the cell remained almost unchanged, while polarization impedance in the mid-frequency range increased significantly, and total impedance also increased remarkably,

which is different from SOFC mode, where total impedance decreased with increasing current density. **Figure 4.11b** and **Figure 4.11d** display the DRT analysis under different fuel electrode atmospheres and different current densities. The results demonstrated that the diffusion impedance (P1) [219-221] increased most significantly with the increase of applied current, indicating that the fuel gas diffusion process was a control step that restricted the performance of the cell. In addition, the charge transfer impedance (P4) [222-224] of the fuel electrode triple phase boundaries and the oxygen exchange reaction impedance (P3) of the air electrode [225-227] also increased with the increase of electrolytic current, indicating an increase in polarization loss. Under the fuel electrode atmosphere of 23.8 vol.% CO-76.2 vol.% CO_2, when the load current changed from -100 mA/cm^2 to -200 mA/cm^2, the total polarization impedance rose from 0.86 Ω cm^2 to 1.36 Ω cm^2. While under the fuel electrode atmosphere of 25 vol.% H_2-75 vol.% CO_2, when the load current changed from -100 mA/cm^2 to -200 mA/cm^2, the total polarization impedance rose from 0.84 Ω cm^2 to 1.35 Ω cm^2.

Comparing ohmic impedance and polarization impedance in **Figure 4.11a** and **Figure 4.11c**, when the electrolysis current density exceeded -150 mA/cm^2, ohmic impedance remained unchanged, indicating that the electrochemical reaction process began to dominate the SOEC performance.

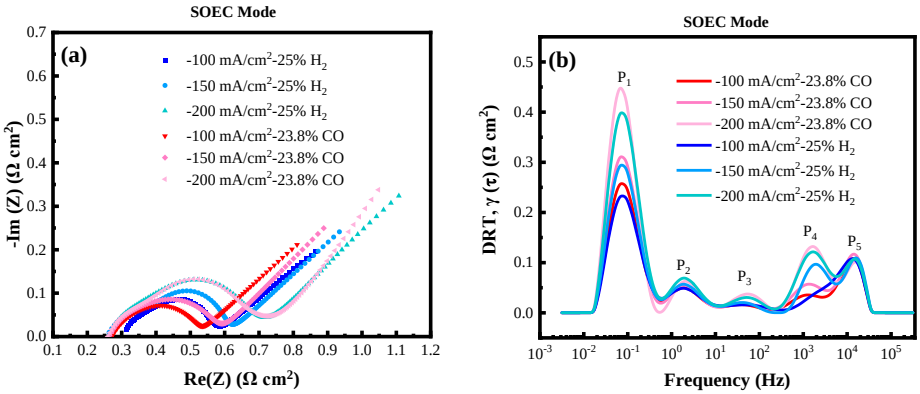

Figure 4.12. The electrochemical impedance and DRT in SOEC mode with different currents and fuel electrode atmospheres: (a) EIS; (b) DRT

Table 4.2. The impedance variation of each part of the cell with loading 100-300 mA/cm^2 current density under 25 vol.% H_2-75 vol.% CO_2 and 23.8 vol.% CO-76.2 vol.% CO_2

Reducing gas	Current density	R_{P1}/Ω cm^2	R_{P2}/Ω cm^2	R_{P3}/Ω cm^2	R_{P4}/Ω cm^2	R_{P5}/Ω cm^2	Rp_T/Ω cm^2
25%H_2	-100 mA/cm^2	0.44	0.12	0.04	0.13	0.11	0.84
	-150 mA/cm^2	0.56	0.12	0.04	0.18	0.13	1.03
	-200 mA/cm^2	0.75	0.14	0.06	0.27	0.13	1.3
23.8%CO	-100 mA/cm^2	0.49	0.11	0.03	0.10	0.14	0.86
	-150 mA/cm^2	0.58	0.11	0.04	0.14	0.15	1.02
	-200 mA/cm^2	0.80	0.10	0.07	0.26	0.12	1.36

Figure 4.12a and **Figure 4.12b** provide a more intuitive comparison of EIS and DRT analysis results under six different fuel electrode protective

atmospheres. The results revealed that under the same oxygen partial pressure and same applied current, the gas diffusion polarization impedance P1 in CO-CO_2 atmosphere was slightly greater than that in H_2-CO_2 atmosphere. The difference in gas diffusion polarization impedance between these two protective gases became apparent as the load current increased. In **Figure 4.12b**, the P4 characteristic peaks related to the triple phase boundary reaction of the fuel electrode showed significant differences when the current was less than -150 mA/cm^2. This was mainly because under low current operation, the RWGS reaction in 25 vol.% H_2-75 vol.% CO_2 atmosphere tended to dominate the fuel electrode reaction, while in 23.8 vol.% CO-76.2 vol.% CO_2 atmosphere, the fuel electrode reaction was dominated by electrochemistry reaction. The above results confirmed that the impedance changes in SOFC and SOEC mode were opposite. In SOFC mode, the impedance decreased with increasing current, while in SOEC mode, the impedance increased with increasing current. In the SOEC mode, when CO was used as a protective gas, the gas diffusion process was hindered due to the diffusion barrier of CO being greater than that of H_2. In the SOEC mode with H_2 as the protective gas, P4 tended to be larger. This might be due to the presence of the RWGS reaction affecting the impedance at low load current.

Table 4.2 shows the values of impedance of each part of the cell, which could be calculated in Origin. The DRT curves in **Figure 4.12** were

integrated to obtain the values of each peak. As observed, under same current density, the impedance values were very similar in CO and H_2 protection.

4.4.2 Carbon deposition

Nickel plays a catalytic role in the CO disproportionation reaction (the carbon deposition reaction) in the CO-CO_2 fuel electrode atmosphere (**Eq.4.1**). When the thermodynamic conditions for coke formation are reached, the carbon deposition reaction tend to occur [228]. The coke generated by disproportionation was deposited on the catalytically active sites, thus reducing the catalytic activity of the Ni-YSZ electrode and the cell performance of CO_2 electrolysis. Consequently, the conversion rate of CO_2 should be considered in the electrolysis process, indicating that the CO proportion in both reactants and products should be lower than the critical equilibrium value of carbon deposition.

$$2CO \rightarrow C + CO_2 \qquad \text{(Eq.4.1)}$$

Considering thermodynamics, the critical equilibrium values of CO content during carbon deposition formation were calculated according to the reaction equilibrium constants at different temperatures. **Table 4.3.** shows the reaction equilibrium constants at 650-800 °C at an interval of 50 °C.

Table 4.3. Equilibrium constant of Boudouard reaction and critical

equilibrium value of CO content at different temperatures

Temperature °C	650	700	750	800
K ($\boldsymbol{2CO \rightarrow C + CO_2}$)	3.138	0.998	0.356	0.140
Critical equilibrium value of CO (%)	42.73	61.84	78.21	88.91

The equilibrium composition of the reaction was calculated by HSC 6.0 to obtain Boudouard equilibrium curve (**Figure 4.13**). The area above the Boudouard balance curve represents the carbon deposition area. It could be seen from **Figure 4.13a** that the higher the reaction temperature, the higher the critical equilibrium value of CO content. The CO equilibrium fractions corresponding to 650 °C, 700 °C, 750 °C and 800 °C were 42.73%, 61.84%, 78.21% and 88.91%, respectively. To put it another way, when supplying CO as the protective gas, the content of CO flowing into the fuel electrode should decrease with the decrease in temperature. When the electrolysis of CO_2 took place, with the increase of electrolytic current density, the conversion rate of CO_2 and the content of CO in the product increased. This led to a new problem: if CO in the product could not be transported to the outlet of the electrolysis cell in time, CO would be disproportionate on the Ni surface to form coke, and occupy active reaction sites, which might reduce the electrochemical reaction performance. According to **Figure 4.13**, the critical equilibrium value of CO content was 78.21% at 750 °C. This theoretical result gave evidence that if CO content at the reaction site of the fuel electrode was lower than this value, carbon deposition reaction was unlikely

to occur. However, the influence of potential was not considered in the above calculation process, and under the action of overpotential, the carbon deposition reaction might be promoted. When additional CO was added into the inlet component of the fuel electrode as the protective gas, the maximum critical value of electrolytic current density would be reduced. The reason lied in that with the increase of electrolytic current density, theoretically, the content of CO produced increased. If the intake component contained CO, the content of CO in the whole fuel electrode tended to be easier to reach the critical equilibrium value of carbon deposition.

As shown in **Figure 4.13b**, at 750 °C, there was a linear relationship between the CO content in the fuel electrode and the current density, and with the increase of CO content in the inlet component of the fuel electrode, the relationship curve between CO content and the current density shifted to the left. In other words, to reduce the risk of carbon deposition, the higher the CO content in the inlet component, the smaller the theoretical electrolysis current density. According to **Figure 4.13**, at 750 °C, the critical equilibrium value of CO content was 78.21%, where carbon deposition started to occur. When the volume content of CO added into the inlet composition raised from 0% to 23.8%, 46.7% and 71.7%, the maximum allowable current density changed to -1027 mA/cm^2, -713 mA/cm^2, -414 mA/cm^2 and -87 mA/cm^2, respectively.

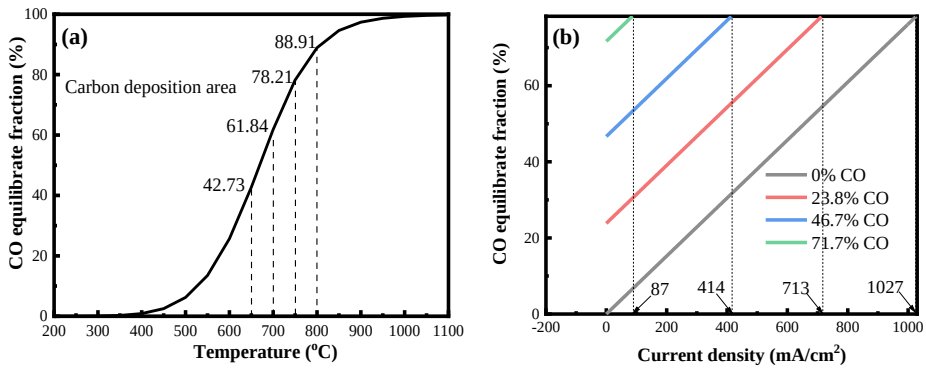

Figure 4.13. (a) Boudouard equilibrium diagram; (b) Equilibrium diagram of current density and carbon deposition at 750 °C with different CO contents

4.4.3 Methanation reaction

When H_2 was supplied as the protective gas, under suitable thermodynamic conditions, methane could be directly formed by the methanation reaction of H_2 and CO_2 over Ni-based catalysts. As shown in **Eq.4.2**, methanation is an exothermic reaction, and it is easy to form methane at low temperatures with a catalyst. The results in **Figure 4.14a** indicated that when the ratio of CO_2/H_2 was 3:1, almost complete methanation occurred below 300 °C, while above 300 °C, the reaction was limited on account of the domination of the RWGS reaction, and the total reaction moves towards the direction of CO formation **(Eq.4.3)**. When the ratio of CO_2/H_2 is 3:1, there was no methane formation at 600 °C and above, and the CO selectivity reached almost 100%. Therefore, to achieve a high CO selectivity in CO_2 electrolysis, 3:1 ratio of CO_2/H_2 became possible. And the operating temperature should be at least 500 °C.

$$CO_2(g) + H_2(g) \rightarrow CH_4(g) + 2H_2O(g) \quad \Delta H = -165kJ/mol$$

$$\Delta G = -113kJ/mol \quad @298.15K \qquad \text{(Eq.4.2)}$$

$$CO_2(g) + H_2(g) \rightarrow CO(g) + H_2O(g) \qquad \Delta H = 41.1\,kJ/mol$$

$$\Delta G = 29\,kJ/mol \quad @298.15K \qquad \text{(Eq.4.3)}$$

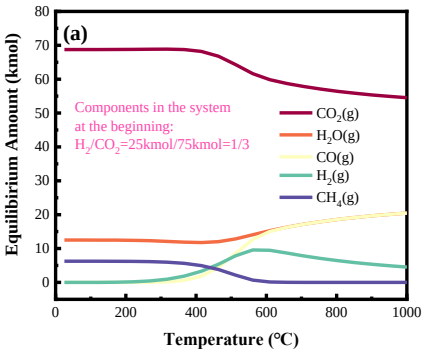

Figure 4.14. Mass balance diagram: (a) Mass balance diagram for CO_2/H_2 = 3/1

4.4.4 Short-term stability

The short-term constant current electrolysis experiments with -100 mA/cm^2, -200 mA/cm^2, and -300 mA/cm^2 were carried out at different $[O_2]_{fuel}$ concentrations with H_2 as the reducing protective gas at 750 °C. $[O_2]_{fuel}$ was controlled by the inlet composition of the fuel electrode. The stability curves are shown in **Figure 4.15a**. To evaluate the influence of different types of protective gas on electrolysis, the CO/CO_2 atmosphere with a high CO content of 71.7% was used for comparison with the test under 75 vol.% H_2-25 vol.% CO_2 atmosphere. The result is shown in **Figure 4.15b**.

For H_2-CO_2 feed, the stability curves of CO_2 electrolysis under different

compositions are shown in **Figure 4.15a**. With the increase of applied electrolytic current, the voltage of electrolysis cell increased as expected.

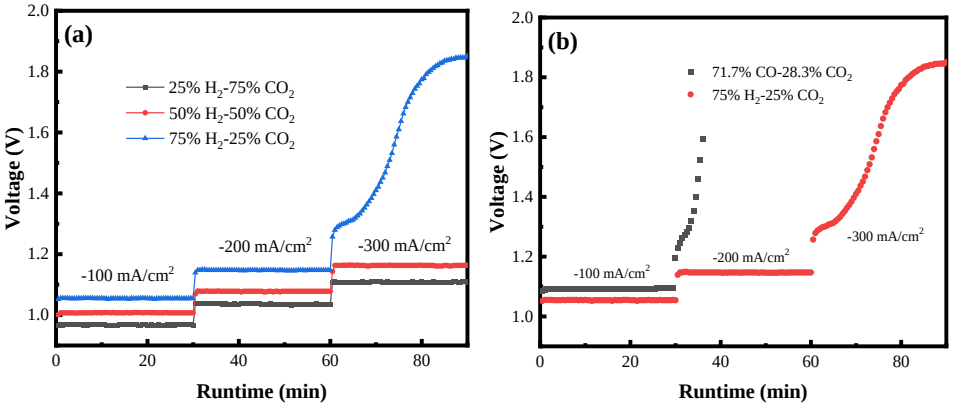

Figure 4.15. Short-term stability curves under various contents and types of protective gas: (a) V-t curves under different H_2 content; (b) Comparison of V-t curves under different protective gas

Table 4.4. Relationship between electrolytic voltage and current density at 750 °C in different fuel electrode atmospheres

H_2/CO_2		**25/75**	**50/50**	**75/25**
Electrolytic voltage (V)	-100 mA/cm^2	0.969	1.008	1.055
	-200 mA/cm^2	1.037	1.078	1.147
	-300 mA/cm^2	1.108	1.163	Not stable
Polarization voltage (V)	-100 mA/cm^2	0.075	0.073	0.08
	-200 mA/cm^2	0.143	0.143	0.172
	-300 mA/cm^2	0.214	0.228	--
CO/CO_2		**23.8/76.2**	**46.7/53.3**	**46.7/53.3**
Electrolytic voltage (V)	-100 mA/cm^2	-	-	1.093
	-200 mA/cm^2	-	-	Not stable
Polarization voltage (V)	-100 mA/cm^2	-	-	0.103
	-200 mA/cm^2	-	-	-

The relationship between the stable value of electrolytic voltage and current density under three fuel atmospheres of 25 vol.% H_2-75 vol.% CO_2, 50 vol.% H_2-50 vol.% CO_2 and 75 vol.% H_2-25 vol.% CO_2 is described in **Table 4.4**. When -100 mA/cm^2 electrolytic current density was applied to the cell, the electrolytic voltage was 0.969 V, 1.008 V and 1.055 V, respectively, and the polarization voltage was 0.075 V, 0.073 V and 0.08 V, respectively. When the electrolytic current density reached - 200 mA/cm^2, the polarization voltages of the three kinds of fuel atmosphere were 0.143 V, 0.143 V and 0.172 V respectively.

In low electrolytic current density (less than or equal to -200 mA/cm^2), the electrolytic voltage remained stable in the three atmospheres. However, when the electrolytic current density increased to -300 mA/cm^2, the electrolytic performance in 25 vol.% H_2-75 vol.% CO_2 and 50 vol.% H_2-50 vol.% CO_2 atmosphere remained generally stable, and the electrolytic voltage corresponded to 1.108 V and 1.163 V respectively. In contrast, the CO_2 electrolysis at -300 mA/cm^2 in 75 vol.% H_2-25 vol.% CO_2 atmosphere became unable to maintain stability **(Figure 4.15a)**.

Based on the above findings, it could be concluded that when an electrolytic current was applied externally, the polarization voltage of the cell increased with the increase of the electrolytic current density in a constant fuel atmosphere. However, certain difference in the polarization loss under different fuel atmospheres existed, suggesting that the value of

the loss increased with increase of the protective gas in the feeding gas in the fuel electrode. This might be because of the concentration polarization caused by the insufficient reactants (CO_2) in the inlet fuel electrode component, which was also one of the reasons why CO_2 electrolysis could not remain stable in a high reduction atmosphere and with high electrolytic current density.

Figure 4.15b compares the effects of different reducing gases on the electrolytic stability under the same oxygen partial pressure. The results suggested that the electrolysis voltage in the CO-CO_2 atmosphere was slightly higher than that in the H_2-CO_2 atmosphere at the same electrolytic current density, and that the electrolytic voltage was more difficult to hold steady in the CO-CO_2 atmosphere.

In summary, it could be concluded that more reducing atmosphere contributed to reducing the polarization resistance and limiting the current density of the CO_2 electrolysis reaction, and boosting the instantaneous performance of electrolysis reaction. However, on account of the shortage of reactants, the electrolysis process failed to run stably. Therefore, how to improve, the instantaneous performance, the operation stability and electrolysis efficiency of CO_2 electrolysis, needs to be investigated further.

4.4.5 Product analysis

Figure 4.16 depicts the GC gas analysis of the product gas composition plotted against runtime under constant current electrolysis at -200 mA/cm^2 with 23.8 vol.% CO-76.2 vol.% CO_2 and 25 vol.% H_2-75 vol.% CO_2. The analysis result showed that when H_2 was used as the protective gas, the CO yields obtained from CO_2 decomposition reaction and RWGS reaction were 17.681% and 23.315%. When CO was used as protective gas, the CO content in product gas was 22.343%. Thus, for CO-CO_2 feed, the conversion of CO_2 was slightly higher.

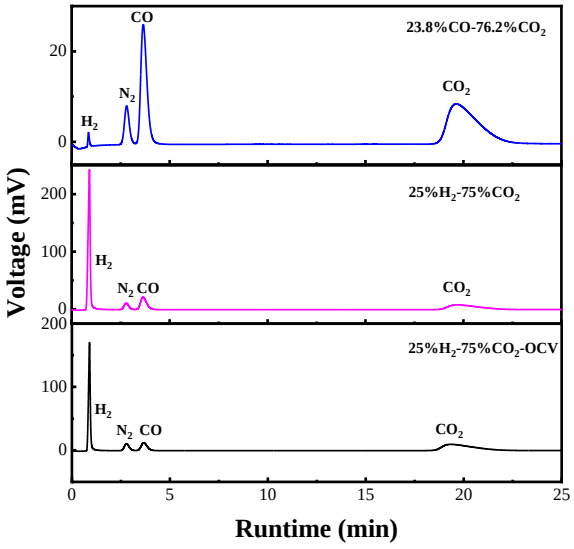

Figure 4.16. Gas chromatography (GC) analysis of -200 mA/cm^2 constant current electrolysis in different fuel electrode atmospheres at 750 °C

Table 4.5 delineates the composition of product gas measured under different fuel electrode atmospheres. Based on these results and **Eq. 3.12** - **Eq. 3.17**, the energy conversion efficiency under the protection of different

protective gas was calculated. When calculating the energy conversion efficiency, the flow rate at the inlet / outlet of the fuel electrode of the cell should be calibrated to reduce the flow rate error, and the results are shown in **Table 4.6**.

Table 4.5. Exhausted gas composition of -200 mA/cm^2 constant current CO_2 electrolysis in different fuel electrode atmospheres

Fuel electrode composition	**H_2**	**CO**	**CO_2**
23.8 vol.% CO%-76.2 vol.% CO_2	0.14	44.30	51.71
25 vol.% H_2-75 vol.% CO_2	10.09	34.29	49.35
25 vol.% H_2-75 vol.% CO_2 (OCV)	6.64	20.38	67.03

Table 4.6. Calculation of energy conversion efficiency in -200 mA/cm^2 electrolysis under different gas components in fuel electrode

Gas composition	**ECE**	**ECE (exclude Q)**	**ECE (exclude Q_{air})**
23.8 vol.% CO-76.2 vol.% CO_2	23.8%	171.0%	81.1%
25 vol.% H_2-75 vol.% CO_2	33.3%	130.0%	81.6%

4.5 Summary

In this chapter, the flat-tube SOECs were used for carrying out CO_2 electrolysis test, and the performance of the Ni-YSZ electrode for CO_2

electrolysis under the protection of H_2 and CO was studied. The results showed that under the same oxygen partial pressure, the limited current densities of CO_2 electrolysis were -550 mA/cm^2, -480 mA/cm^2, and -250 mA/cm^2 when the volume fractions of H_2 in the fuel electrode were 25%, 50% and 75%, respectively. As for CO as the reducing gas, the limited current densities decreased to -480 mA/cm^2, -415 mA/cm^2 and -220 mA/cm^2 with 23.8%, 46.7% and 71.7% CO volume fractions, which were lower than the critical current density under H_2 protection. EIS analysis indicated that in CO-CO_2 gas atmosphere, polarization impedance was significantly greater than that in the H_2-CO_2 fuel electrode atmosphere. To gain insight into the voltage degradation, electrolysis tests under different current densities with 75 vol.% H_2-25 vol.% CO_2 and 71.7 vol.% CO-28.3 vol.% CO_2 were carried out. Irreversible degradation occurred when the current density reached -300 mA/cm^2 in 75 vol.% H_2-25 vol.% CO_2, while in 71.7 vol.% CO-28.3 vol.% CO_2. The same irreversible decay phenomenon happened at -200 mA/cm^2 accompanied with cell cracking and electrolyte detachment. The thermodynamic analysis of the reaction system manifested that when the CO_2/H_2 ratio was 3:1, no methane generated in the reaction process, with the CO selectivity reached 100%. In the process of -200 mA/cm^2 constant current electrolysis, the highest energy conversion efficiency reached 171% (disregarding energy consumption for heating the gas) and 81.6% (disregarding energy consumption for heating air).

Chapter 5. Long-term performance and degradation mechanism under constant current CO_2 electrolysis

5.1 Introduction

The key to achieving commercial use of SOEC is the stability during high temperature operation. Usually, air is introduced at the air electrode to balance heat, rather than participating in electrode reactions. However, introducing air increases energy consumption and reduces energy conversion efficiency by 20% -30%. When air flows out from the outlet of the air electrode, a large amount of heat will be carried away, causing uneven temperature distribution inside cells. To accurately understand the degradation mechanism of the air electrode with and without air purging, researchers have designed and performed various experiments. In 2017, Mahmoud et al. [229] demonstrated using Mossbauer spectroscopy that iron could reduced from the pentahedral Fe (IV) to the octahedral Fe (III) form in a 9000-h test. In the same year, Laurencin et al. [230] analyzed the diffusion and accumulation of cobalt in the barrier layer region after 2000 h of electrolytic testing, further proving the loss of Sr in the LSCF lattice after anodic polarization. In 2015, Chen et al. [231] found that SrO-based compounds might appear in the air electrode during sintering and reduction.

The above studies are all based on cells with air purging of the air electrode. However, when CO is used as the protective gas for the fuel

electrode, there may be extreme working conditions on the air electrode such as no air sweep. For example, Moxie (a Mars exploration device studied by NASA) was reported to achieve the goal of electrolyzing CO_2 to oxygen in the no air environment of Mars [232]. Furthermore, if the air electrode can maintain stable operation without an oxidation atmosphere, the heat energy required can be greatly reduced, thus significantly strengthening the total efficiency of the electrolysis process. Therefore, if CO can be adopted as the protective gas on the fuel electrode and stable CO_2 electrolysis can be carried out without any oxidizing atmosphere on the air electrode, it is of great significance not only for improving the service life of cells in extreme environments like that of Mars, but also for increasing the total efficiency of the electrolysis process on the ground.

During long-term operation, the selection of fuel electrode atmosphere is also crucial. As traditional Ni-based catalysts are prone to oxidation, a reducing atmosphere, such as CO and H_2, is usually required to protect the stability of the Ni electrode. However, the introduction of a reducing atmosphere inevitably causes some problems. For example, the addition of H_2 protective gas increases the difficulty of separating fuel electrode products. The introduction of CO protective gas promotes the accumulation of carbon in the fuel, thereby accelerating cell degradation. To address the above issues, this chapter explored the long-term CO_2 electrolysis under physical pressure mode when nitrogen was used as the equilibrium

component of the fuel electrode. The future development trend of SOEC maybe to achieve long-term operation without protective gas in the fuel electrode, which is expected to provide a new research direction for the transition from “waste carbon” to “working carbon”.

5.2 Long-term performance with air in the air electrode

5.2.1 Stability test

The cells used in this chapter were named Cell5.1, Cell5.2, Cell5.3 and Cell5.4, respectively. First, the charge and discharge performances of Cell5.1 under SOFC / SOEC modes were measured. The discharge performance was tested with 0.6 SLM H_2 in the fuel electrode and 1 SLM air in the air electrode. The electrolytic performance was examined with 0.15 SLM H_2 and 0.45 SLM CO_2 in the fuel electrode and 1 SLM air in the air electrode, and the results are shown in **Figure 5.1**. **Figure 5.1a** presents the comparison of J-V-P curves under SOFC mode before and after long-term CO_2 electrolysis, and **Figure 5.1b** displays the comparison of J-V curves under SOEC mode before and after long-term electrolysis. The experimental results revealed that after 471 h long-term CO_2 electrolysis operation in Cell5.1, the maximum discharge power decreased from 403.3 mW/cm^2 to 311.1 mW/cm^2, with a degradation rate of about 22.86%. The electrolytic voltage at -200 mA/cm^2 increased from 1.189 V to 1.28 V, an increase of

16.2%/kh.

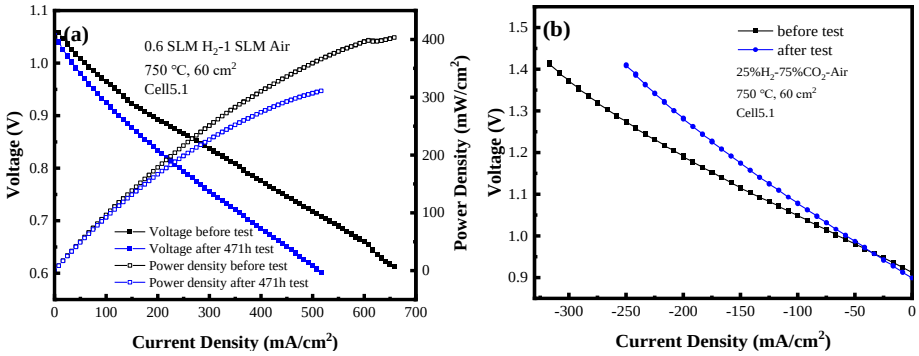

Figure 5.1. Comparison of performances of Cell5.1 with air in the long-term operation: (a) Discharge performance before and after the test; (b) Electrolytic performance before and after the test

To explore the effect of air addition on the stability and efficiency of CO_2 electrolysis, Cell5.1 was used for long-term electrolysis with a mixture of 23.8 vol.% CO-76.2 vol.% CO_2 supplied to the fuel electrode and 5 SLM air supplied to the air electrode. **Figure 5.2** shows the real-time electrolytic voltage for CO_2 electrolysis with air purging. The cell was operated for 471 h, with a long-term degradation rate of about 24.2%/kh. The total degradation of Cell5.1 was much higher than the degradation of instantaneous performance shown in **Figure 5.1b**. This was probably because the instantaneous performance was tested in H_2-CO_2 fuel atmosphere, and presence of air in the air electrode might prevent excessive accumulation of oxygen partial pressure and alleviate degradation.

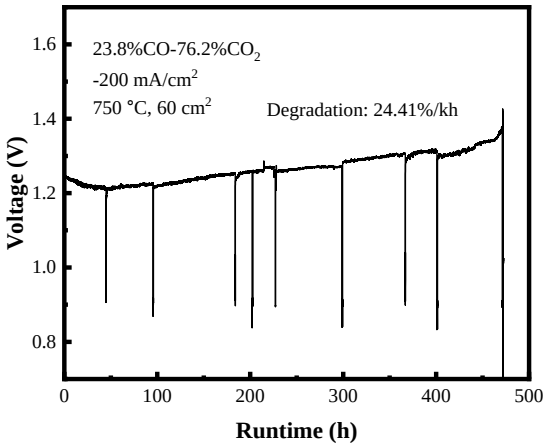

Figure 5.2. V-t diagram of CO_2 electrolysis of Cell5.1 with air in the LSCF-GDC air electrode

5.2.2 Electrochemical impedance and DRT analysis

In the durability test, the real-time voltage was recorded, and the EIS was measured at intervals with the electrochemical workstation with a frequency sweep range of 30 kHz-20 mHz. The EIS curve was analyzed and fitted with EC-lab software, with an equivalent circuit of L1R1(Q2R2)(Q3R3)(Q4R4)(Q5R5), as shown in **Figure 5.3a**. The fitted curves exhibited an increasing trend of ohmic and polarization impedance, and polarization impedance change was mainly in mid-frequency.

For analyzing the trend of polarization impedance in each region, the EIS data was run in a DRT program in Matlab, and the results are shown in **Figure 5.3b**. The polarization impedances P3 and P4 related to the fuel electrode reaction at TPB and ion transport in the electrode increased significantly at 471 h, which explained the surge of electrolytic voltage at that time. For quantifying the polarization impedance generated by various

electrochemical processes, the peaks in the DRT diagram were fitted and integrated in OriginLab to obtain the approximate values of R_{P1}-R_{P4}. The area specific resistance (ASR) was calculated by the following formula:

$$ASR = (V_e - OCV)/I \qquad \text{(Eq.5.1)}$$

where V_e is the electrolytic voltage before impedance measurement (V); OCV is the corresponding open circuit voltage during impedance measurement (V); I represents the electrolytic current (A).

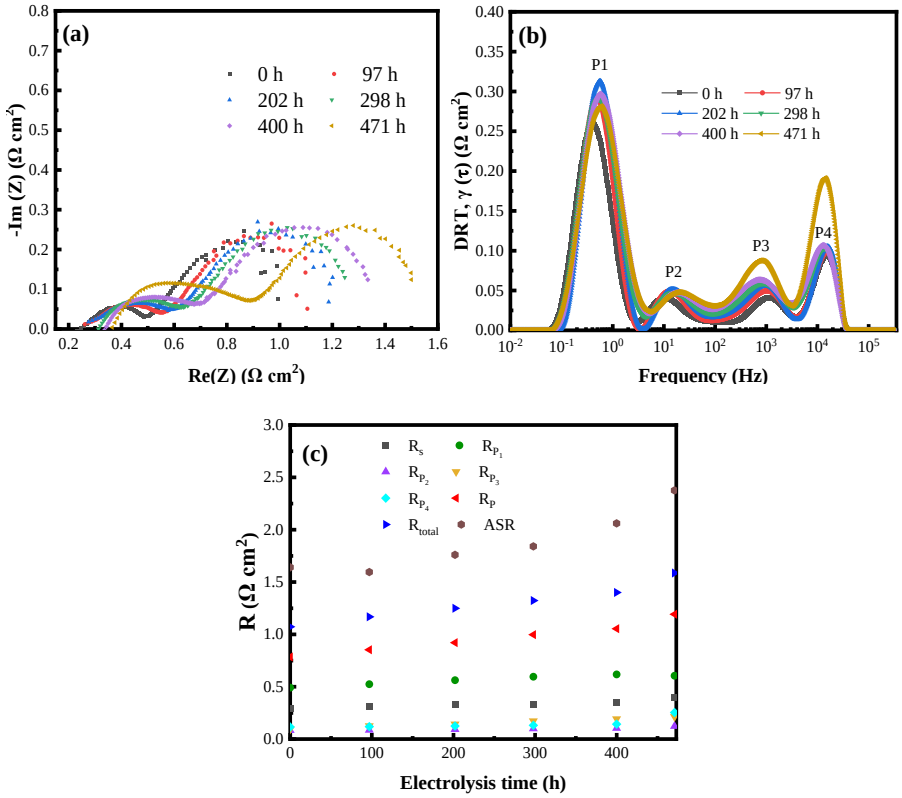

Figure 5.3. Impedance and DRT of Cell5.1 when introducing 5 SLM air at the LSCF-GDC air electrode: (a) The impedance curve versus time; (b) DRT diagram; (c) Impedance values of each region with electrolytic time

The variation results of impedance with electrolytic time are

summarized in **Figure 5.3c** and **Table 5.1**. Since this research aimed to probe into the trend of impedance variation, rather than the precise value of impedance, it was permissible to integrate the DRT curve to obtain the impedance value in the case of small DRT error. The calculated results manifested that the increase of ASR might dominate cell degradation. Comparing the calculated data in **Figure 5.3c** and **Table 5.1**, after 471 h CO_2 electrolysis with 5 SLM air in the air electrode, the increments of ASR, R_t, R_p, R_s, R_{P1}, R_{P2}, R_{P3}, and R_{P4} were 0.735 Ω cm^2, 0.51 Ω cm^2, 0.41 Ω cm^2, 0.10 Ω cm^2, 0.11 Ω cm^2, 0.04 Ω cm^2, 0.12 Ω cm^2 and 0.14 Ω cm^2, respectively.

Table 5.1. Impedance values of each part of Cell5.1 with 5 SLM air during 471 h test

Impedance	**0 h**	**97 h**	**202 h**	**298 h**	**400 h**	**471 h**
R_s / Ω cm^2	0.29	0.31	0.33	0.33	0.35	0.39
R_{P1}/Ω cm^2	0.49	0.52	0.56	0.59	0.62	0.60
R_{P2}/Ω cm^2	0.08	0.08	0.09	0.10	0.10	0.12
R_{P3}/Ω cm^2	0.10	0.13	0.14	0.17	0.19	0.21
R_{P4}/Ω cm^2	0.11	0.12	0.12	0.13	0.14	0.25
R_P/Ω cm^2	0.78	0.85	0.92	0.10	1.05	1.19
R_t/Ω cm^2	1.07	1.17	1.25	1.32	1.40	1.59
ASR/Ω cm^2	1.64	1.60	1.76	1.84	2.06	2.38

5.2.3 Conversion rate and energy conversion efficiency

For the situation that using excessive air during CO_2 electrolysis, a lot of heat energy might be consumed for heating the air. Therefore, the energy conversion efficiency (ECE) could be calculated according to **Eq. 3.13** and **Eq. 3.14** in **Section 3.7.3** [233]:

Table 5.2. Results of tail gas composition and energy conversion efficiency of Cell5.1 during CO_2 electrolysis with 5 SLM air in the air electrode

CO% in the outlet	CO generated in the system	Electrolytic Voltage	Runtime	ECE
44.07%	20.27%	1.269 V	259 h	25.33%/89.32%

Due to the electrolytic voltage being lower than the thermoneutral voltage, the compensation energy required to maintain the reaction temperature could not be ignored. Similarly, due to the introduction of excess air, the energy consumption required to heat the air seemed to be enormous, but this portion of heat energy would be negligible if it could be combined with industrial waste heat. Considering two application scenarios, the calculated ECE were 25.33% (consider heating air) and 89.32% (ignore the heat consumed by air), respectively, as shown in **Table 5.2**.

5.3 Long-term performance without air in the air electrode

5.3.1 Stability test

To verify the impact of air electrode gas on the cell stability, long-term CO_2 electrolysis experiments were carried out without any gas supply, utilizing two cells from the same batch, named Cell5.2 and Cell5.3, respectively. Cell5.2 used an electrolytic current of -200 mA/cm^2 and a fuel atmosphere of 23.8 vol.% CO-76.2 vol.% CO_2, and was compared with Cell5.1 to investigate the cell degradation of CO_2 electrolysis under airless conditions. Cell5.3 used an electrolytic current of -218.8 mA/cm^2 and a 20 vol.% CO-80 vol.% CO_2 fuel electrode atmosphere, under which the amount of CO generated in the fuel electrode was equals that of CO protected. The purpose was to demonstrate that product recycling could be achieved in SOEC systems.

Figures 5.4 (a) and **(c)** show the J-V-P discharge curves of Cell5.2 and Cell5.3 before and after long-term CO_2 electrolysis. It was found that constant current electrolysis under no air conditions imposed a significant impact on the instantaneous discharge performance. In Cell5.2, after 1070 h of CO_2 electrolysis without air supply to the air electrode, the OCV of the cell decreased from 0.99 V to 0.98 V, the area specific resistance (ASR) increased from 0.64 Ω cm^2 to 1.04 Ω cm^2 (slope of polarization curves), and the maximum discharge power density declined from 350.2 mW/cm^2 to

203.2 mW/cm^2. In Cell5.3, after 858 h of CO_2 electrolysis testing under no air condition, the OCV of the cell decreased from 1.1 V to 0.97 V, and the maximum discharge power density decreased from 532.3 mW/cm^2 to 165.2 mW/cm^2. The degradation of OCV and discharge power might be caused by carbon deposition in the cell during long-term testing.

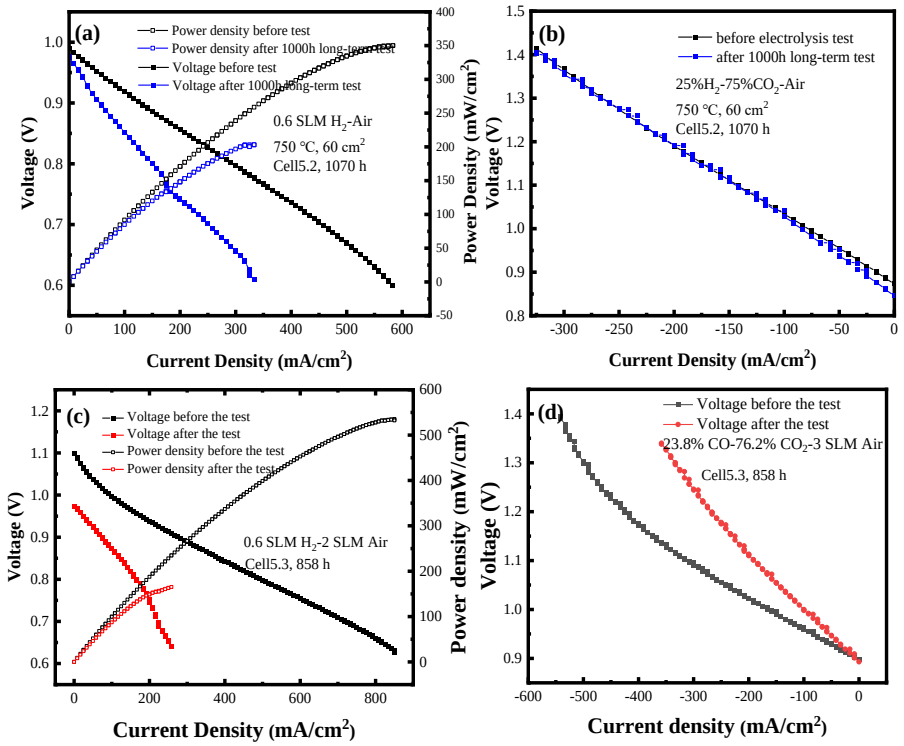

Figure 5.4. Comparison of cell performances of Cell5.2 and Cell5.3 without air supply in the long-term operation: (a) Discharge performance of Cell5.2; (b) Electrolytic performance of Cell5.2; (c) Discharge performance of Cell5.3; (d) Electrolytic performance of Cell5.3

Figures 5.4 (b) and **(d)** show the electrolytic polarization curves of Cell5.2 and Cell5.3 before and after long-term electrolysis. To achieve a

stable state of OCV in the instantaneous curves, a certain amount of air was introduced during the instantaneous performance test. For Cell5.2, the degradation was mainly reflected in OCV, which decreased from 0.873 V to 0.846 V, and the change in ASR during electrolysis was not significant; For Cell5.3, there was a significant degradation in the instantaneous electrolytic performance and ASR, with the instantaneous electrolytic voltage corresponding to -200 mA/cm^2 increasing from 1.022 V to 1.11 V (approximately 10%/kh).

The durability of cells is an important parameter for measuring the quality of cell preparation and testing processes. Cell5.2 and Cell5.3 were tested for 1070 hours and 858 hours respectively, with degradation rates of 8.37%/kh and 10%/kh, respectively, as shown in **Figures 5.5**. Afterwards, the experiment was manually stopped and cooled down for analyzing the degradation mechanism of cells. Experiments with LSCF-GDC electrodes without air are not common. Hence, the mechanism of cell degradation still needs further exploration. For Cell5.2, there were some fluctuations in the V-t curve during the early stages of electrolysis (the first 450 hours), which might be due to cell activation and electrode reaction equilibrium; CO depletion occurred in approximately 460 hours during long-term electrolysis, and continued for about 0.5 hours until CO was resupplied. After 470 hours, the change in cell degradation rate tended to stabilize, the voltage steadily increased, and the degradation rate increased. For Cell5.3, the degradation

rate was stable, no cell activation phenomenon was observed in V-t curve, and there were no accidents during the long-term operation.

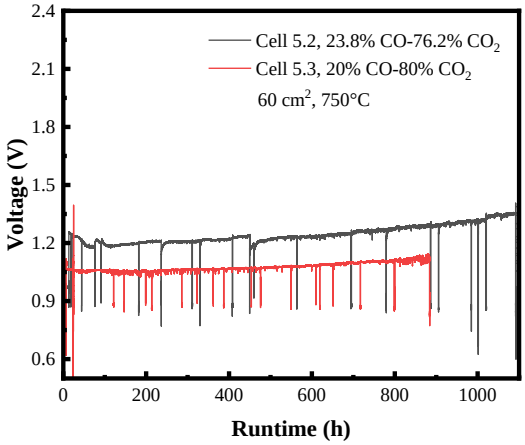

Figure 5.5. V-t diagram of Cell5.2 and Cell5.3 without air in the LSCF-GDC air electrode

5.3.2 Electrochemical impedance and DRT analysis

During the long-term durability test, the impedance changes of Cell5.2 and Cell5.3 were measured at time intervals, and the impedance was analyzed and fitted using EC-lab software (**Figure 5.6a**). The equivalent circuit diagram used for fitting was also L1+R1+Q2/R2+Q3/R3+Q4/R4+Q5/R5. The change in impedance during long-term electrolysis mainly derived from the intermediate frequency, followed by the gas diffusion impedance in the high-frequency region. To analyze the detailed variation trend of polarization impedance, the DRT program was employed with the original impedance data, with a regularization factor of 10^{-3}. The results are shown in **Figure 4b**.

For Cell5.2, where the air electrode was not supplied with air during electrolysis, the variation of gas diffusion polarization impedance at 0.4 Hz was very small according to the impedance results. The characteristic peak P2 (10-10^2 Hz) related to the oxygen exchange reaction of LSCF-GDC increased and shifted towards the high-frequency region [234]. The characteristic peak P3 representing the triple phase boundary reaction at 10^2-10^3 Hz [235-237] and the polarization impedance P4 (10^4 Hz) related to O_2 transport [234, 238-239] also exhibited a similar trend to P2, but not as pronounced as for P2. The above results suggested that the gas diffusion polarization impedance RP1 of the fuel electrode remained almost unchanged during the long-term electrolysis process during durability test of Cell5.2. The increase in polarization impedance RP2 caused by the oxygen exchange reaction on the surface of LSCF-GDC electrode indicated that the air electrode reaction was suppressed, and the microstructure of air electrode was damaged. In addition, the O^{2-} transport process (RP4) was hindered, possibly due to the loss of nickel leading to the loss of electron transport pathways.

To quantify the polarization impedance generated by these electrochemical processes, peak splitting was conducted in the DRT curves to obtain approximate values of RP1-RP4. ASR was calculated using formula 5.1, and the results are shown in **Figure 5.6c** and **Table 5.3**. With the extension of long-term testing, the total impedance of Cell5.2 increased

from 1.7 Ω cm^2 to 2.49 Ω cm^2, mainly due to the contribution of RP2 related to oxygen exchange polarization impedance in the air electrode. There were no significant changes in ohmic impedance Rs during the long-term electrolysis process of 1070 h, indicating that the electrolyte structure was intact, and the contact between the electrodes and the cover plates remained sufficient. Despite this, many uncontrollable factors still existed in the long-term operation of large cells, such as uneven pore distribution, uneven gas distribution, uneven current distribution, uneven pressure distribution, and gradual sealing failure. Also, using different cells inevitably resulted in some differences in impedance variation. For Cell5.3, the impedance variation trend during the first 773 h was similar to that of Cell5.2, but the DRT results at 858 h displayed an increase in gas diffusion impedance RP1, which was mainly because carbon deposition at the fuel electrode hindered gas transport.

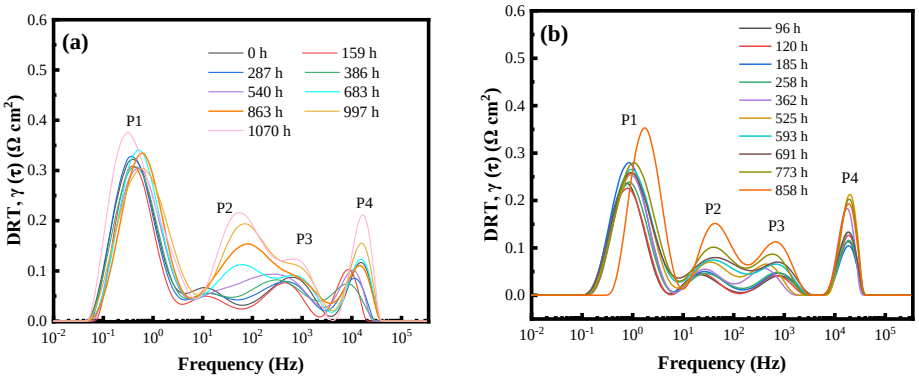

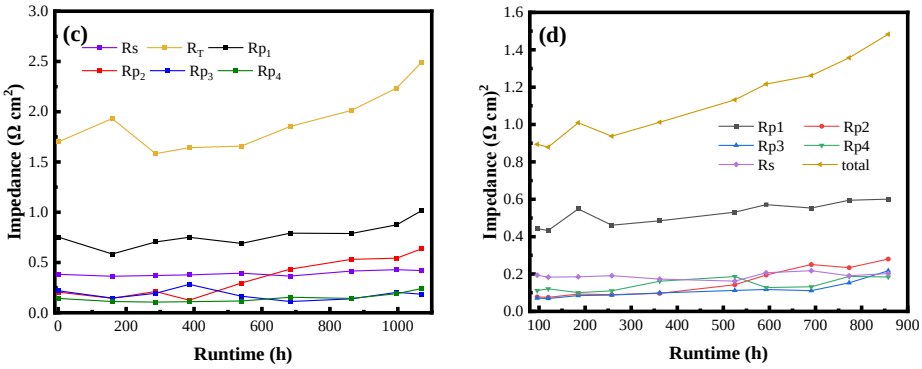

Figure 5.6. DRT and impedance values of Cell5.2 and Cell5.3 with operation time: (a) DRT of Cell5.2; (b) DRT of Cell5.3; (c) Impedance values of Cell5.2; (d) Impedance values of Cell5.3

According to the impedance calculation results in **Figure 5.6d** and **Table 5.4**, during the 858-h long-term CO_2 electrolysis, the total impedance of Cell5.3 increased from 0.89 Ω cm^2 to 1.48 Ω cm^2, i.e. by about 0.59 Ω cm^2. The polarization impedance increased from 0.70 Ω cm^2 to 1.28 Ω cm^2, i.e. by about 0.58 Ω cm^2. Overall, when air was not introduced for long-term CO_2 electrolysis, ohmic impedance of the cell remained basically unchanged, but the air electrode impedance increased.

Table 5.3. Variations of impedance values of Cell5.2

Impedance	0 h	159 h	287 h	386 h	540 h	683 h	863 h	997 h	1070 h
R_s / Ω cm^2	0.38	0.36	0.37	0.38	0.39	0.36	0.41	0.43	0.42
R_{P1}/ Ω cm^2	0.75	0.58	0.70	0.75	0.69	0.79	0.79	0.87	1.01
R_{P2}/ Ω cm^2	0.20	0.14	0.21	0.12	0.30	0.43	0.53	0.54	0.64
R_{P3}/ Ω cm^2	0.22	0.14	0.19	0.28	0.16	0.11	0.14	0.20	0.18
R_{P4}/ Ω cm^2	0.14	0.11	0.11	0.11	0.12	0.15	0.14	0.19	0.24

R_p / Ω cm^2	1.32	1.57	1.21	1.27	1.26	1.49	1.60	1.81	2.07
R_T / Ω cm^2	1.70	1.93	1.58	1.64	1.66	1.85	2.01	2.24	2.49
ASR/ Ω cm^2	1.86	1.60	1.68	1.74	1.83	1.92	2.12	2.32	2.50

Table 5.4. Variations of impedance values of Cell5.3

Impedance	**96 h**	**120 h**	**185 h**	**258 h**	**362 h**	**525 h**	**593 h**	**691 h**	**773 h**	**858 h**
R_s / Ω cm^2	0.19	0.18	0.18	0.19	0.17	0.16	0.21	0.22	0.19	0.20
R_{P1}/ Ω cm^2	0.44	0.43	0.55	0.46	0.48	0.53	0.57	0.55	0.59	0.60
R_{P2}/ Ω cm^2	0.08	0.07	0.093	0.09	0.10	0.14	0.19	0.25	0.23	0.28
R_{P3}/ Ω cm^2	0.07	0.07	0.08	0.09	0.10	0.11	0.12	0.11	0.15	0.21
R_{P4}/ Ω cm^2	0.11	0.12	0.10	0.11	0.16	0.19	0.13	0.13	0.19	0.18
R_p / Ω cm^2	0.70	0.70	0.83	0.75	0.84	0.97	1.01	1.04	1.17	1.28
R_T / Ω cm^2	0.89	0.88	1.01	0.94	1.01	1.13	1.22	1.26	1.36	1.48
ASR/ Ω cm^2	0.80	0.83	0.89	0.93	0.99	1.05	1.09	1.18	1.29	1.47

5.3.3 Conversion rate and energy conversion efficiency

During the long-term electrolysis test, the exhaust gas composition of Cell5.2 was analyzed at set intervals, and the energy conversion efficiency was calculated according to **Eq.5.2**. The results and relevant parameters are organized in **Table 5.5**. With the extension of testing time, the electrolytic

voltage gradually increases, and the CO content in the exhaust gas of the fuel electrode declined, which directly led to a decrease in the conversion efficiency of CO_2 electrolysis system. The OCV of the Cell5.2 during the long-term electrolysis process remained stable, which meant the decrease of ECE was not caused by seal failure. A preliminary suspicion was that microstructural obstructed in the fuel or air electrodes hinder the occurrence of electrode reactions.

Table 5.5. Results of energy conversion efficiency of Cell5.2 during long-term CO_2 electrolysis test

Electrolytic time (h)	Gas flow rate at the outlet (sccm)	Electrolytic Voltage (V)	CO% at the outlet	ECE (%)
100	651	1.185	44.55	82.08
190	646	1.216	43.65	78.16
353	628	1.221	43.43	77.65
523	653.5	1.239	40.02	64.16
625	660	1.25	39.56	62.34
863	667	1.29	38.42	57.83
960	685	1.311	38.68	58.86

5.4 Long-term performance without protective gas in the fuel electrode

During the operation of SOECs, there exist application scenarios where the fuel electrode cannot be protected by reducing gases. To cope with this, the overall sealing of cells and the redox stability of the fuel electrode are very important. For enhancing the sealing and oxidation resistance of the

electrolysis cell, this research made improvements to the cell structure, glass sealing materials, and assembly process. Specifically, the cell thickness was reduced from 4.6 mm to below 3 mm, and short bolts and pressure columns were used to physically pressurize the cell to improve the sealing and contact between electrodes and cover plate. During operation, the external pressure of the pressurized column was 100 kg (about 1 bar), and a 50 vol.% CO_2-50 vol.% N_2 mixture was introduced into the fuel electrode, where N_2 served as the equilibrium gas to help the fuel gas diffuse to the triple phase boundaries.

The cell manufactured according to the improved process was named Cell5.4, and the initial charging and discharging performance results are shown in **Figure 5.7**. The OCV and maximum power of Cell5.4 were 1.057 V and 18.6 W under 0.6 SLM H_2 fuel electrode atmosphere and 2 SLM air electrode atmosphere. Under the electrolytic atmosphere of 25 vol.% H_2-75 vol.% CO_2, the maximum current density was reached at approximately -500 mA/cm^2, corresponding to an electrolytic voltage of approximately 1.18 V. Based on the initial electrolytic performance, an electrolytic voltage of 1.1 V was selected for the long-term potentiostatic CO_2 electrolysis test. After 100 hours of operation, the experiment was manually stopped, and instantaneous charging and discharging performance tests were conducted again to compare with the initial performances. According to I-t curve in **Figure 5.8**, the starting current, ending current, and electrolytic voltage were calculated to obtain a current degradation rate of approximately

35.7%/kh. Compared with the instantaneous performances before and after long-term potentiostatic CO_2 electrolysis, it was found that the maximum discharge power decreased from 18.6 W to 13.4 W. The corresponding electrolytic voltage at an electrolytic current of -500 mA/cm^2 increased from 1.176 V to 1.204 V, with a degradation rate of 23.8%/kh.

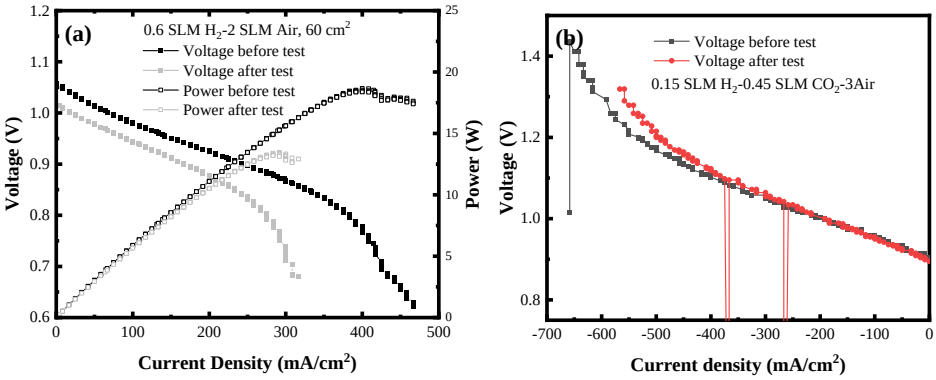

Figure 5.7. Instantaneous performance of Cell5.4 before and after long-term test (a) Discharge performance; (b) Charge performance

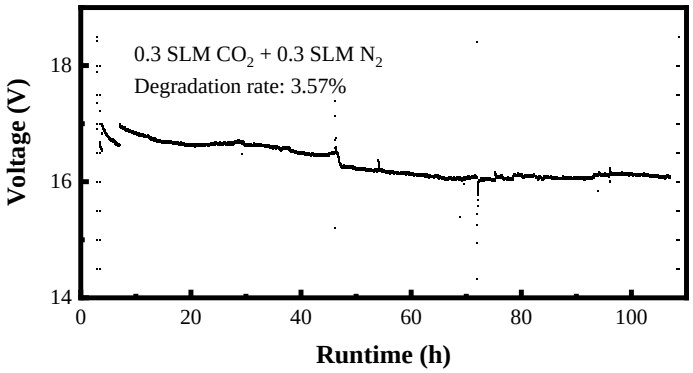

Figure 5.8. Long-term performance of Cell5.4 in 50 vol.% N_2-50 vol.% CO_2 fuel electrode atmosphere

5.5 Analysis of degradation mechanisms

After the long-term CO_2 electrolysis test, the temperature was cooled from 750 °C to room temperature at a rate of 1-2 °C/min for further disassembly analysis.

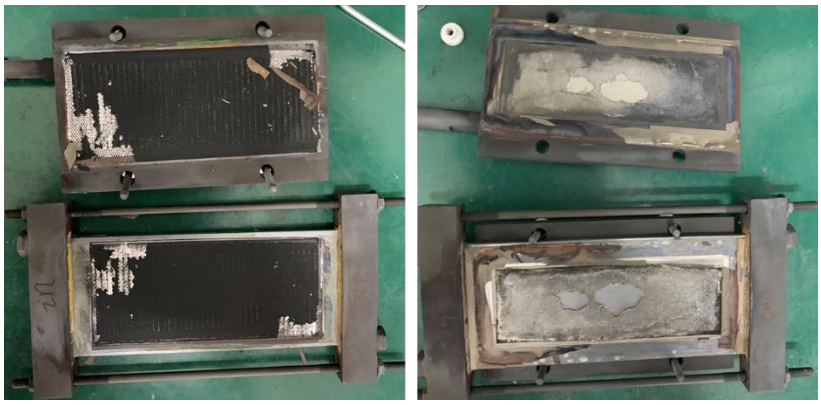

Figure 5.9. Macro morphology of Cell5.1 after durability test

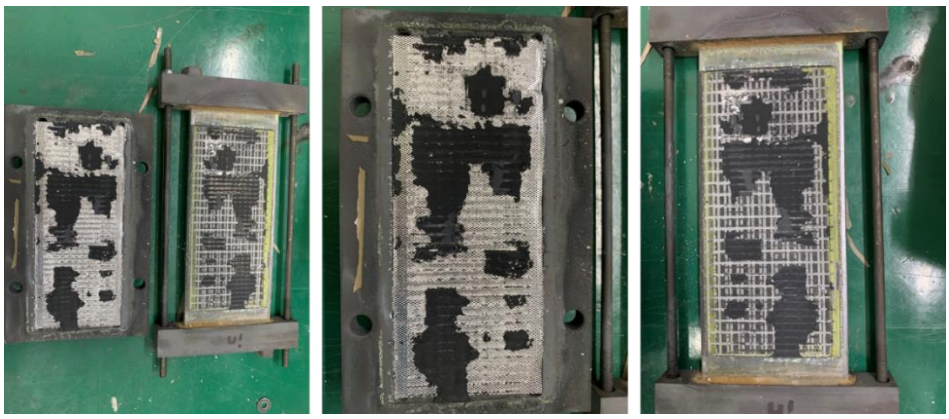

Figure 5.10. Macro morphology of Cell5.2 after durability test

Figure 5.11. Macro morphology of Cell5.3 after durability test

Figure 5.12. Macro morphology of Cell5.4 after durability test

Figures 5.9 to **5.12** show the macroscopic morphology of four cells after high-temperature testing. Among them, Cell5.1, Cell5.2, and Cell5.3 still kept good contact of the air electrode with cover plate, and no damage caused by high-temperature testing was discovered on the overall macro structure of the cells. The fragmentation on the side of Cell5.3 was mainly caused by violent disassembly. For Cell5.4 tested without reducing gas in the fuel electrode, the inlet to the center of the cell body was in an oxidized state (green color), while the center part leading to the outlet was not

oxidized due to the production of CO by the CO_2 electrolysis reaction.

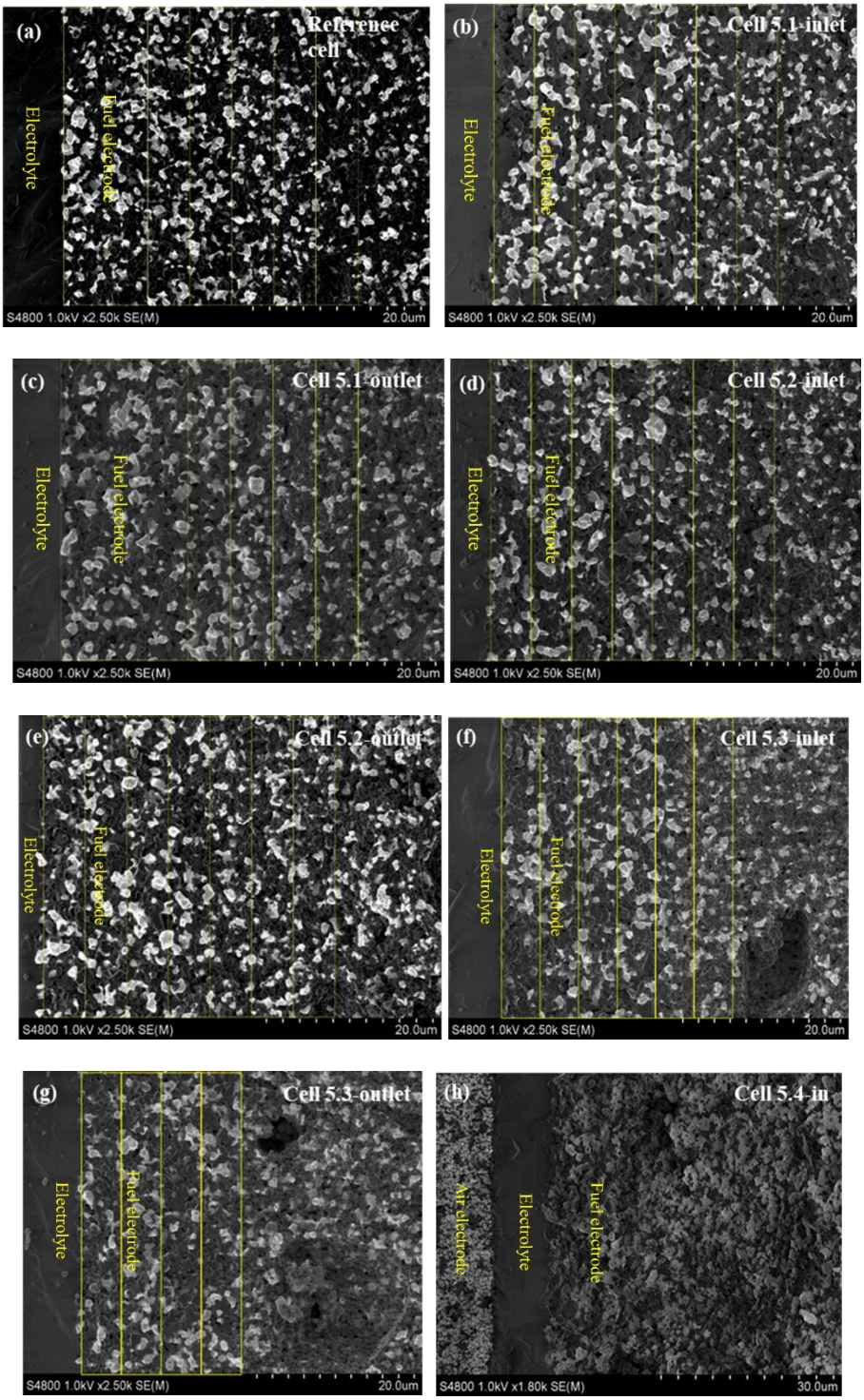

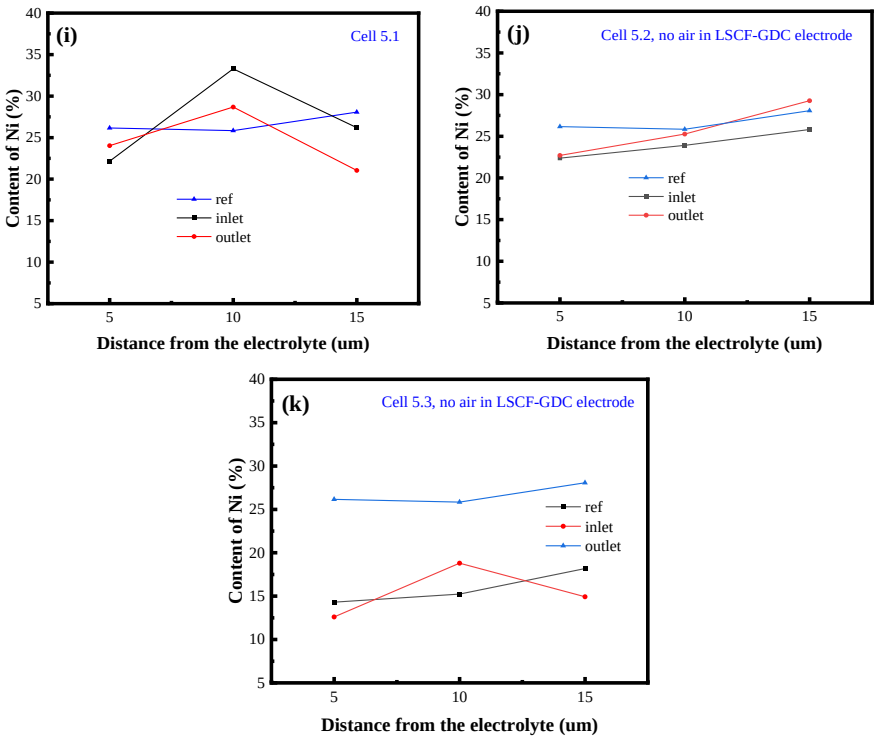

Figure 5.11. SEM photos of the tested cells and reference cell: (a) Reference cell (reduction only); (b) Inlet of Cell5.1; (c) Outlet of Cell5.1; (d) Inlet of Cell5.2; (e) Outlet of Cell5.2; (f) Inlet of Cell5.3; (g) Outlet of Cell5.3; (h) Inlet of Cell5.4; (i) Ni Content at different regions of Cell5.1; (j) Ni Content at different regions of Cell5.2; (k) Ni Content at different regions of Cell5.3

To quantify the change in the amount of percolating Ni, Ni content in the fuel electrode was calculated. Starting from the edge of the electrolyte and the fuel electrode, slices of 5 μm each were designed and analyzed, and the proportion of percolating Ni (bright area) in each slice was calculated with ImageJ software [240]. Considering 2D images provided by SEM, and 3D structure of the fuel electrode, the particle size in SEM images did not

match the actual situation, only being used as a reference. To reduce randomness, multiple sets of microscopic images were selected for calculating the average value. **Figure 5.11i** shows the results for Cell5.1 after 471 h electrolysis testing with 5 SLM air. The results indicated that the loss of percolating Ni occurred in the area that 5 μm away from the electrolyte, with Ni content being 22.15% at the inlet region and 24.02% at the outlet region. However, in the second area, 10 μm away from the electrolyte, Ni% was higher than that in the reference cell. The results in **Figure 5.11j** revealed the Ni content in the fuel electrode of Cell5.2 was lower than that of the untested reference cell, especially in the area close to the electrolyte. As reference cell was untested, Ni content of reference cell could be regard as theoretical value. Ni content in the area 5 μm away from the electrolyte in the inlet, the outlet of Cell5.2 and the reference cell were about 22.37%, 22.7% and 26.15% respectively, which further confirmed the loss of nickel. **Figure 5.11k** reveals Ni content at different region of Cell5.3, as seen from the SEM image. The nickel content at the inlet and outlet was significantly lower than that of the reference cell. The loss of percolating nickel particles at the inlet and outlet of Cell5.3 might be related to the decrease in gas tightness and OCV, such that the leakage of fuel electrode gas directly affected the structure of Cell5.3. Comparing the trend of nickel migration of Cell5.1 and Cell5.2, it was found that the nickel migration trend of Cell5.1 tended to be more obvious.

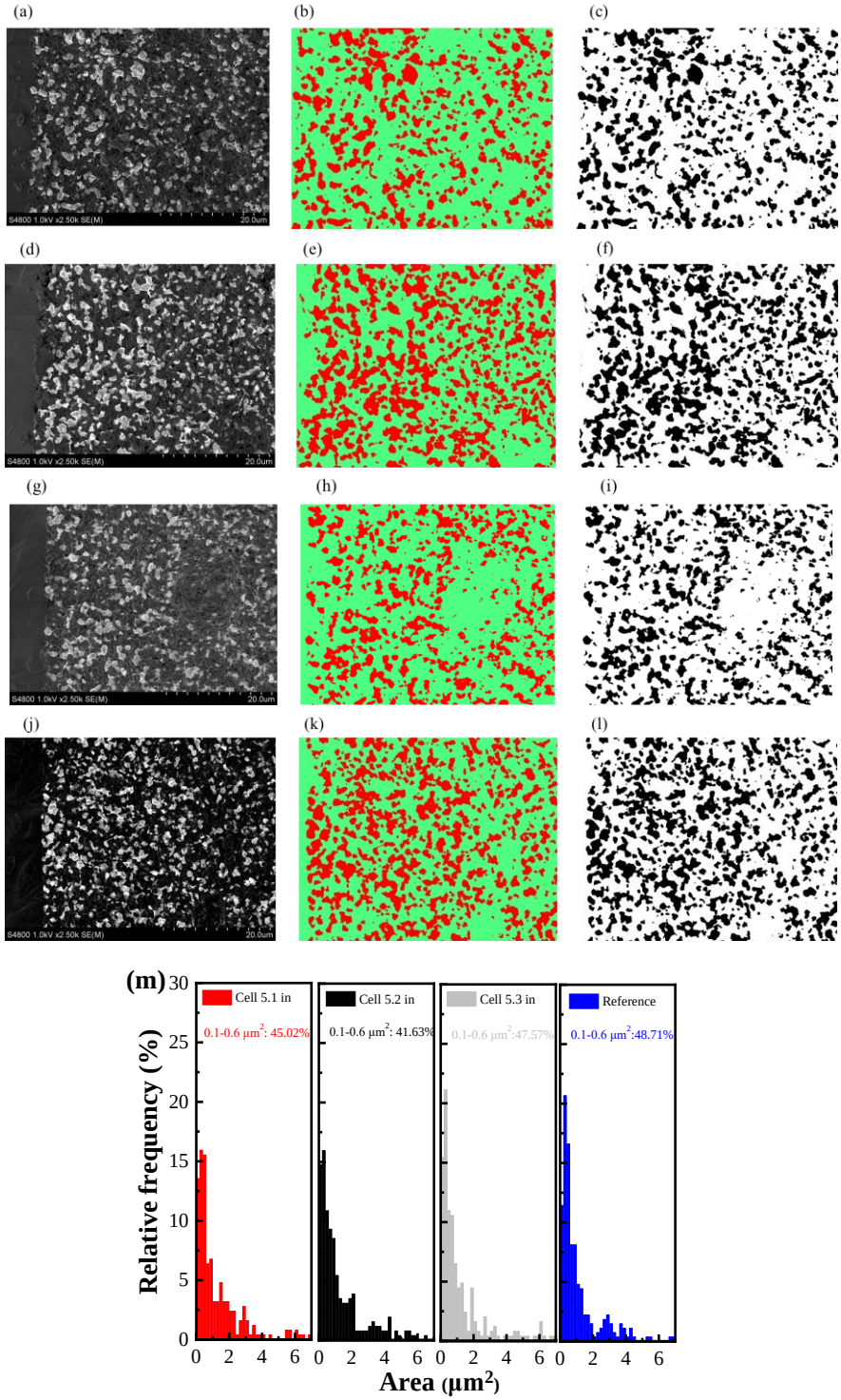

Figure 5.12. Nickel particles identified in SEM: (a)-(c): Cell5.1; (d)-(f): Cell5.2; (g)-(i): Cell5.3; (j)-(l): Reference cell; (m) Relative frequency of content of Ni with different areas

The nickel particle sizes in Cell5.1, Cell5.2, Cell5.3 and the reference cell were also calculated using the segmentation function in the ImageJ analysis software, and further processed by descriptive counts in OriginPro. The statistical results are shown in **Figure 5.12**. Since the cells were operated under high temperature for a long time, nickel agglomeration (coarsening) occurred at the inlet of Cell5.1, Cell5.2 and Cell5.3, being more obvious in Cell5.2. This might be because the test time of Cell5.2 was much longer than that of Cell5.1. In Cell5.2, the percentage of percolating Ni particles between 0.1 μm^2-0.6 μm^2 decreased by about 7%, while in Cell5.1 it only decreased by 3.7%. As for Cell5.3, the percentage of nickel particles between 0.1 μm^2-0.6 μm^2 only decreased by about 1.14%. The phenomenon of nickel agglomeration was not obvious, but from the morphology of **Figure 5.12g**, nickel migration and loss became obvious, which might be associated with fuel electrode oxidation in the later stage. Moreover, due to the slightly higher operating current of Cell5.3 compared to Cell5.2, the larger current and more severe electrode polarization further promoted nickel migration. These results manifested that with the occurrence of the fuel electrode reaction, nickel coarsening and nickel migration were involved in cell degradation, and the degree of it might depend on the operating time and electrolytic current [241, 242].

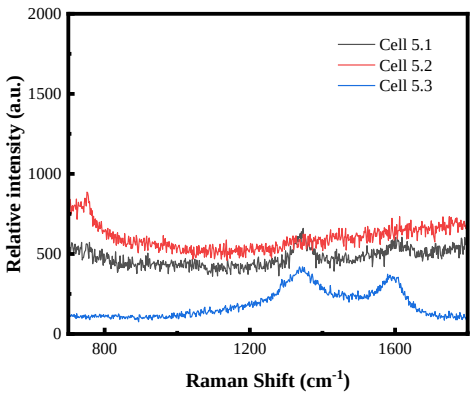

Figure 5.13. Raman spectrum of the outlet of Cells 5.1, 5.2 and 5.3

To further confirm the local carbon deposition during long-term CO_2 electrolysis test, samples of Cell5.1, Cell5.2 and Cell5.3 were prepared along the flow direction of the fuel gas for Raman spectrum measurements. Due to the higher CO content at the outlet of the cell, carbon deposition was more likely to occur there. Therefore, the focus on conducting Raman analysis on the outlet of the tested cells became necessary and important. Based on the results in **Figure 5.13**, signal peaks appeared at 1350 cm^{-1} and 1600 cm^{-1} at both the outlet of Cell5.1 and Cell5.3, indicating carbon deposition on the fuel electrodes, while for Cell5.2 tested without air for 1070 h, no carbon deposition was found at the outlet. Local carbon deposition at the outlet of the fuel electrode might be one of the reasons for the increased degradation rate of Cell5.1 and Cell5.3. It should be noted that carbon deposition of Cell5.1 and Cell5.3 was not caused by the addition of air to the air electrode. It therefore was speculated that local CO concentration at the fuel electrode might exceed the thermodynamic critical value for carbon deposition.

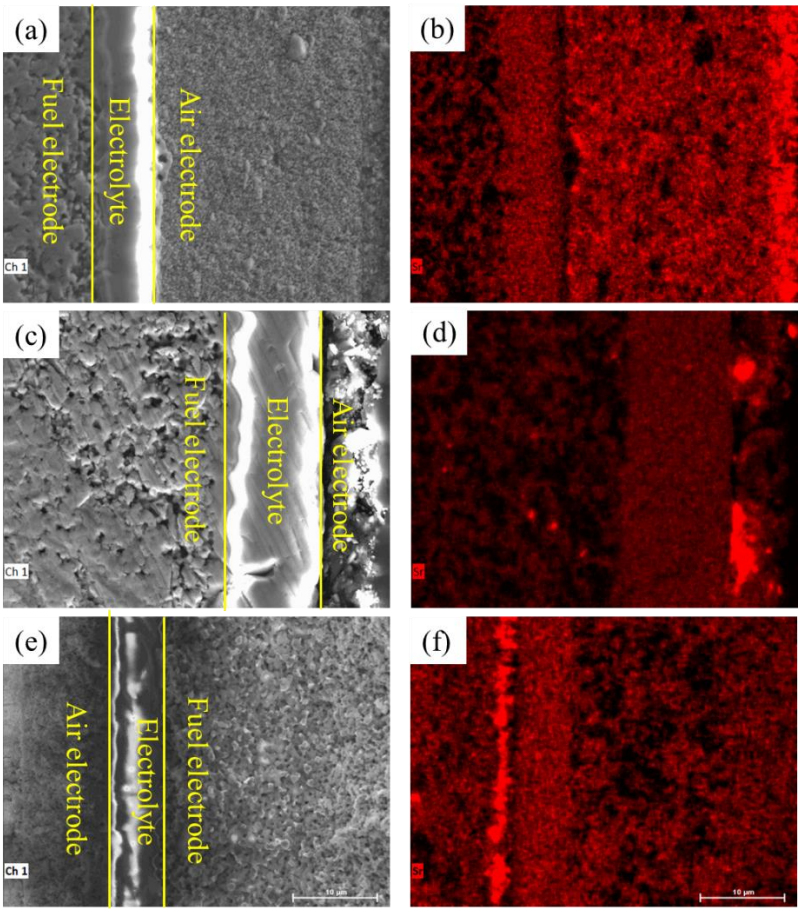

Figure 5.14. Micro morphology and energy spectrum of the outlet of tested cells: (a) and (b) Cell5.1; (c) and (d) Cell5.2; (e) and (f) Cell5.3

Subsequently, the interface characteristics of the cell samples after the CO_2 electrolytic test were analyzed. To increase the reliability of the analysis results, the tested Cell5.1, Cell5.2 and Cell5.3 were filled with epoxy resin in vacuum, cut and polished, and then cleaned ultrasonically. The results of the micro morphology and energy spectrum analysis are shown in **Figure 5.14**. Several Sr enriched phases were found in Cell5.2 and Cell5.3 (**Figure 5.14d** and **Figure 5.14e**). It was speculated that strontium zirconate or strontium oxide secondary phases might be formed due to the higher oxygen

partial pressure at the outlet of Cell5.2 and Cell5.3, and that the lower concentration of oxygen vacancies initiated SrO precipitation. It should be noted that the LSCF-GDC air electrode in this research was directly exposed to the lab environment, and any small amount of residual CO_2 might undergo an oxygen exchange reaction on the LSCF surface, which would not be inhibited with the increase of oxygen partial pressure [242].

There was no obvious elemental segregation in Cell5.1 (**Figure 5.14b**), but several cracks in the LSCF-GDC air electrode were observed. It was reasonable to infer that at room temperature excess air entered the high-temperature furnace through the air inlet pipe and gradually heated to the set temperature. Because of the limited heating capacity of the high-temperature furnace, there was a temperature difference between the gas at the inlet and the outlet of the SOEC, resulting in uneven distribution of thermal stresses. The uneven distribution of thermal stresses caused damage to the air electrode structure.

5.6 Summary

In this chapter, flat-tube solid oxide electrolysis cells were employed to investigate the effects of different fuel electrode atmospheres, air electrode atmospheres, electrolytic current or voltage on the durability of the cells. The degradation mechanism of flat-tube structure SOECs during long-term electrolysis was analyzed by virtue of electrochemical impedance, DRT, gas

chromatography, SEM, EDS, and Raman spectroscopy. The operating conditions and degradation rate during the operation of CO_2 electrolysis in the test cells are organized in **Table 5.6**. The degradation reasons of tested cells are summarized in **Table 5.7**.

Table 5.6. Comparison of operating parameters of four tested cells

	Runtime	**Fuel electrode**	**Air electrode**	**Current / Voltage**	**Degradation rate**
Cell5.1	471 h	23.8 vol.% CO-76.2 vol.% CO_2	air	-200 mA/cm^2	24.41%/kh
Cell5.2	1070 h	23.8 vol.% CO-76.2 vol.% CO_2	-	-200 mA/cm^2	8.37%/kh
Cell5.3	859 h	20 vol.% CO-80 vol.% CO_2	-	-218 mA/cm^2	10%/kh
Cell5.4	100 h	50 vol.% N_2-50 vol.% CO_2	air	1.1 V	35.7%/kh

Table 5.7. Degradation reasons of tested cells

	Runtime	**Degradation reason**
Cell5.1	471 h	Migration and agglomeration of nickel particles in the fuel electrode, carbon deposition in fuel electrode channels
Cell5.2	1070 h	Loss and agglomeration of nickel particles in the fuel electrode, Sr segregation in air electrode
Cell5.3	859 h	Loss of nickel particles in the fuel electrode, Sr segregation in air electrode, carbon deposition in fuel electrode channels
Cell5.4	100 h	Oxidation of fuel electrode

Through post-mortem analysis, the following results were obtained:

(1) During the long-term operation of CO_2 electrolysis in a flat-tube SOEC, a large amount of air entering the air electrode was not conducive to the

long-term operation of the cell. This was mainly because the introduction of a large amount of cold air (limitations on experimental conditions) increased the local temperature difference of the cell, causing structural damage. The total electrolytic time of Cell5.1 was 471 h, and DRT results reflected the degradation of fuel electrode with increasing time. The ECE calculated through GC results was about 25% when 5 SLM of air was introduced into the air electrode. Through SEM characterization, it was found that the main reason for fuel electrode degradation was the migration and loss of nickel catalysts.

(2) Under the CO-CO_2 fuel electrode atmosphere, the constant current CO_2 electrolysis experiment was conducted without air in the air electrode. Cell5.2 ran stably for 1070 h at -200 mA/cm^2, and Cell5.3 ran stably for 858 h at -218 mA/cm^2, with degradation rates below 10%/kh. The impedance and DRT results demonstrated that the degradation of the air electrode was one of the important reasons for the cell degradation. By calculating the ECE through GC results, it was found that the energy conversion efficiency increased to over 80% without air supply to the air electrode. Microstructure characterization proved that the main cause of air electrode degradation was the formation of strontium rich phases between LSCF-GDC air electrode and YSZ electrolyte.

(3) Under the condition of the fuel electrode being unable to obtain a reducing atmosphere, by physically pressurizing Cell5.4 to improve

sealing performance, stable CO_2 electrolysis test was achieved for about 100 h, but there was still a risk of oxidation of the fuel electrode.

Chapter 6. Long-term performance and degradation mechanism of CO_2 electrolysis in an intermittent renewable energy associated scenario

6.1 Introduction

The transformation of energy supply and decarbonization are important measures to mitigate climate change [5, 243-244]. Wind power and photovoltaic solar cells and other new energy sources are some of the most important clean energy sources. However, because of the mismatch between new energy power sources and the existing of the power grid, insufficient power exchange between regions, and the lack of large-scale energy storage equipment, the abandonment rate remains high, which limits the market share of new energy power generation [245, 246]. Wind energy and photovoltaic energy possess strong randomness, as wind and light can rapidly change according to season, location, and time, leading to significant fluctuations in the output power of the generator set [247]. The existing power grid system is more suitable for traditional power plants with fixed power generation, such as thermal power plants and nuclear power plants. For nonlinear wind and solar power generation, the energy generated is intermittent. Therefore, combining or developing new energy storage systems is the key to improving the efficiency of intermittent new energy generation.

The electrochemical response of SOECs can be completed almost instantaneously. Therefore it has been proposed by researchers for effective management of intermittent renewable energy [248, 249]. Compared to other types of electrolysis cells, SOECs can withstand a wider range of currents, capable of converting unstable and nonlinear electricity generated by wind power into fuel and additional products. (Power-to-X, where X refers to various chemical products) [250, 251]. In recent years, many researchers have reported on the progress of CO_2 electrolysis to prepare CO fuel by SOECs [1, 252-254]. Compared to using other types of electrolysis cells for CO_2 reduction, the reaction occurring in SOECs is much simpler ($CO_2 \rightarrow CO+1/2O_2$), with a conversion rate of over 50% and almost 100% CO selectivity.

Due to the high operating temperature, the performance degradation of SOECs is common. However, most studies on the degradation mechanism of cell performance are mainly carried out under constant conditions, such as constant current or constant potential [233, 255], and only few reports exist on the direct combination with renewable energy power with its periodic fluctuations. Periodic currents are one of the main modes of periodic fluctuations in renewable energy power, which is also known as pulsed current. Although SOECs are less effective under pulsed current conditions, some researchers have proposed that pulsed current can improve stability and Faraday efficiency [256]. Therefore, this chapter attempted to

simulate an intermittent renewable energy power involved in industrial application scenarios utilizing a flat-tube SOEC to study the cyclic pulsed current based on CO_2 electrolysis and fuel preparation, and investigate the performance changes and degradation mechanisms under this working condition. The purpose was to provide support for the adaptability research of CO_2 electrolysis for renewable energy power conversion and storage under fluctuating operating conditions.

6.2 Long-term performance with intermittent renewable energy

6.2.1 Stability test

The cell preparation process and assembly methods are described in detail in **Chapter 3.1**. The initial performance test results of Cell6.1 are shown in **Figure 6.1**. In the discharge mode, 0.6 SLM H_2 and 2.5 SLM air were introduced to the fuel electrode the air electrode respectively. The voltage and power values at 0.5 A intervals were recorded and collected, with the data plotted as a J-V-P curve. After completing the instantaneous discharge test in SOFC mode, the intake components of the fuel electrode were switched to a mixture of 23.8 vol.% CO-76.2 vol.% CO_2, and 3 SLM air was introduced into the air electrode. After the cell reached chemical equilibrium, i.e. the open circuit voltage tended to stabilize, and the electrolysis mode was started. The J-V relationship curve was obtained.

Figure 6.1a shows the instantaneous performance curves of the SOFC mode before and after the pulsed current cyclic electrolysis. As observed, after 808 hours of (101 cycles) testing, the maximum power density decreased from 271.8 mW/cm^2 to 182.8 mW/cm^2, and the OCV decreased from 1.03 V to 0.99 V, indicating a damage to the gas tightness or structure of Cell6.1. **Figure 6.1b** shows the instantaneous performance curves of Cell6.1 in SOEC mode before and after pulsed current cyclic electrolysis.

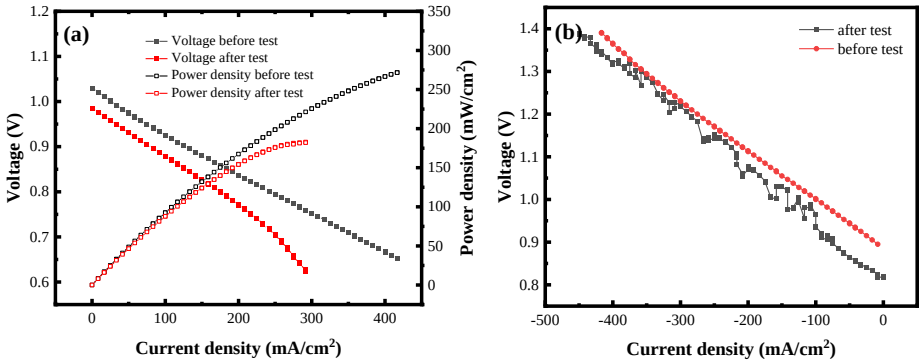

Figure 6.1. Comparison of instantaneous performance before and after cyclic testing: (a) Discharge; (b) Electrolysis

After 808 hour of (101 cycles) testing, there was a significant fluctuation in the instantaneous performance curve of Cell6.1. The slope (area specific resistance) of the J-V curve increased, and the OCV decreased from 0.90 V to 0.817 V. According to the previous research, when using 25 vol.% H_2-75 vol.% CO_2 as the fuel electrode atmosphere for pulsed current CO_2 electrolysis under the same oxygen partial pressure and current density as this work, the discharge power and OCV of the cell did not show a downward trend after 100 cycles of electrolysis. And the corresponding

electrolytic voltage of -300 mA/cm^2 in the electrolysis I-V curve only increased by 4% [254]. That is to say, when CO was used as protective gas in the fuel electrode, even if the electrolytic current was below the critical value of carbon deposition, the degradation of the electrolysis cell was higher than that of the electrolysis cell operating under H_2 protection. During long-term operation, using 8 h as a cycle, each cycle consisted of 2 h at -100 mA/cm^2, -200 mA/cm^2, -300 mA/cm^2 and OCV, respectively. The operation time and corresponding conditions are organized in **Table 6.1**.

Table 6.1. Current variations with time in each cycle.

Runtime (h)	0-2 h	2-4 h	4-6 h	6-8 h
Current	-100 mA/cm^2	-200 mA/cm^2	-300 mA/cm^2	OCV

Figure 6.2 shows the real-time voltage recorded in the 808 h pulsed current testing, corresponding to 101 cycles. From the V-t diagram, it could be seen that for the first 63 cycles the cell was in a stable electrolytic state. After the 63rd cycle, due to equipment failure, the air volume decreased over time, resulting in the lack of air in the subsequent cycles, resulting in a significant decrease in the OCV. At the beginning of the 68th cycle, the air supply stopped. As a result, the OCV in the 68-71st cycles dropped to 0 V, and electrolytic voltage fluctuated. After restoring the air supply at 71st cycle, CO was depleted in the 71st cycle and then the CO gas cylinder was replaced. During the 71-76th cycles, the electrolytic voltage remained fluctuating,

indicating that the electrolysis cell was affected by the replacement of the CO cylinder and carbon deposition was generated inside the cell. In the 76-80th cycles, Cell6.1 ran smoothly, and in the 81st cycle, the degradation of cell voltage began to accelerate. In summary, the degradation of Cell6.1 was mainly concentrated in the 71-100th cycles. It was thus speculated that as the electrolytic time increased, due to diffusion limitations, the concentration of CO at the triple phase boundaries increased, resulting in carbon deposition, which further contributed to the increased degradation rate and the reduced open circuit voltage. In the instantaneous electrolytic performance test before cooling down, the curve fluctuated a lot, which might also be caused by carbon deposition.

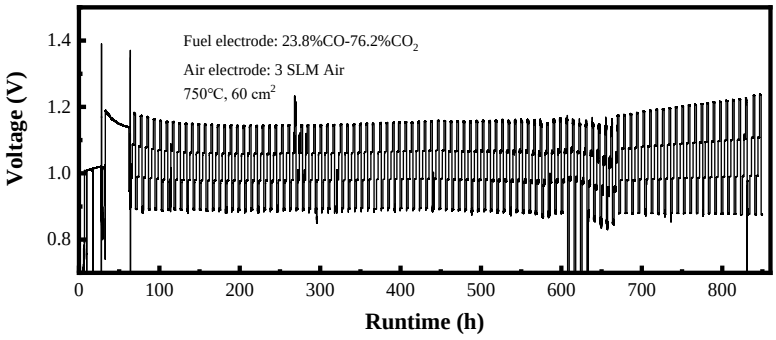

Figure 6.2. V-t diagram of CO_2 electrolysis under long-term pulsed current

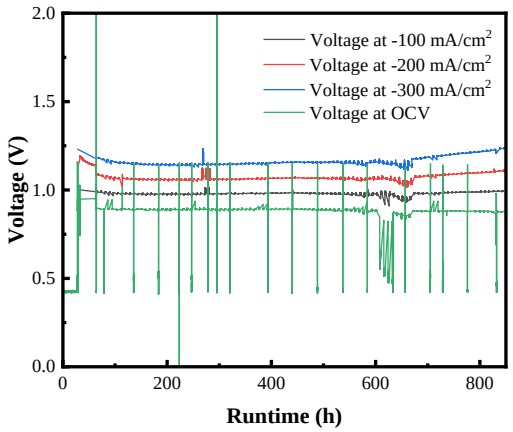

Figure 6.3. Electrolytic voltages at different current under long-term pulsed current operation

Figure 6.3 reveals the relationship between electrolytic voltage and time under different currents. As observed, the electrolytic voltage at -100, -200 and -300 mA/cm^2 showed a decreasing trend in the first 8 cycles, mainly due to cell activation. Starting from the 9th cycle, the cell ran smoothly until the air solenoid valve failure occurred. During the long-term pulsed electrolysis period, the OCV of the SOEC decreased from 0.890 V to 0.809 V. The decrease of OCV of the electrolysis cell was mainly concentrated in the 71st to 100th cycles, which was related to the carbon deposition on the fuel electrode channel and the microstructure damage of the cell.

6.2.2 Electrochemical impedance and DRT analysis

During the long-term pulsed current CO_2 electrolysis in the electrolysis cell, the electrochemical impedance spectra under open circuit voltage were regularly tested, and a regularization factor of 10^{-2} was selected for DRT analysis. The results are shown in **Figure 6.4**. The impedance of Cell6.1 gradually increased with testing time, and polarization impedance and ohmic impedance in the high-frequency region were affected by the wire inductance, making it difficult to obtain accurate values. Therefore, the values of ohmic impedance and mid-frequency polarization impedance were

obtained through fitting. In addition, some fluctuations appeared in the electrochemical impedance of the intermediate frequency arc in **Figure 6.4a**, which might be associated with the cell structure and the gas in the fuel electrode. In order to analyze specific impedance changes in each part, the peaks in DRT curves in **Figure 6.4b** were fitted and integrated to obtain the impedance values in **Table 6.2**. The results showed that from the 2nd cycle to the 93rd cycle, there was no significant decrease in ohmic impedance of the cell, indicating a good electrolyte structure and excellent cell contact. The gas diffusion polarization impedance R_{P1} increased from 0.153 Ω cm^2 to 0.177 Ω cm^2, with a small increase, indicating that the supporting layer and gas flow channels were not blocked. The polarization impedance R_{P2} related to the air electrode reaction remained almost unchanged, suggesting that the air electrode structure and electrode reaction activity were not significantly decreased. The polarization impedance R_{P3} related to the fuel electrode reaction increased from 0.031 Ω cm^2 to 0.066 Ω cm^2, approximately doubled, indicating the presence of some microstructural changes in the fuel electrode during long-term pulsed CO_2 electrolysis testing.

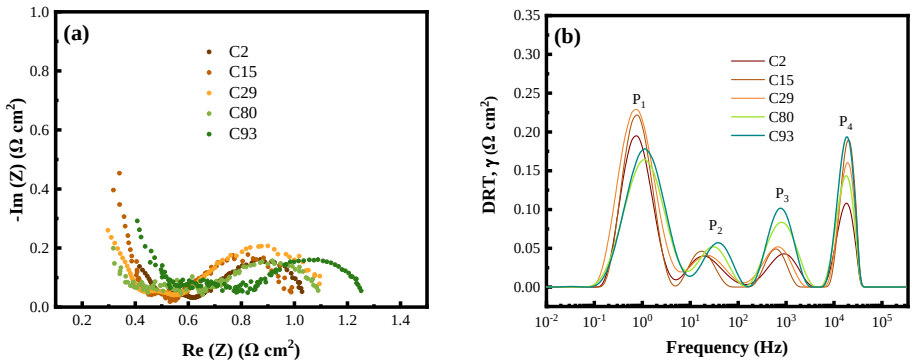

Figure 6.4. Variation of EIS curves (a) and DRT curves (b) of Cell6.1 during cyclic pulsed current CO_2 electrolysis

Table 6.2. Impedance at different cycles (Ω cm^2)

Cycle number	Ohmic impedance	RP1	RP2	RP3
2	0.445	0.153	0.033	0.031
15	0.334	0.168	0.028	0.026
29	0.332	0.036	0.036	0.064
80	0.352	0.168	0.036	0.063
93	0.442	0.177	0.039	0.066

6.2.3 Conversion rate and energy conversion efficiency

The tail gas components were analyzed by gas chromatography with a thermal conductivity cell detector (TCD). Given the long gas outlet pipeline, the tail gas obtained from the SOEC reaction needed to be cooled to room temperature before entering to the gas chromatograph. According to the results of gas chromatography, the tail gas was composed of CO and CO_2, without detecting methane or other by-products. Considering that the molar ratio of CO/CO_2 in CO_2 electrolysis reaction was 1, the number of CO moles

generated was equal to that of CO_2 moles consumed, without regard to any side reactions. Therefore, the total conversion rate of CO_2 could be defined as the ratio of generated CO and input CO_2, as shown in **Eq. 3.11**.

However, it should be noted that when using H_2 as the fuel electrode protection gas, due to the occurrence of RWGS reaction, more CO was generated through the fuel electrode reaction and the conversion rate of CO_2 also became higher. However, owing to the heat absorption of the RWGS reaction, even if the system generated more CO, the energy conversion efficiency might not be higher. Therefore, during the 96^{th} cycle, the exhausted gas was analyzed and the energy conversion efficiency was calculated. When the gas supplied to the air electrode was not considered, only the heat energy required to maintain the furnace temperature and heating fuel electrode gas was taken into account. The ECE at each electrolytic current could be calculated by **Eq. 3.13**, and the calculated results are displayed in **Table 6.3**:

Table 6.3. CO_2 conversion rate and energy conversion efficiency of Cell6.1 at different currents

	-200 mA/cm^2	**-300 mA/cm^2**
CO_2 conversion rate	17.9%	25.8%
ECE (no air)	91.99%	88.1%

Based on the results, in the 96^{th} cycle, when Cell6.1 was electrolyzed at

-200 mA/cm^2, the electrolytic voltage was near 1.109 V and the calculated ECE was 91.99%. While electrolyzed at -300 mA/cm^2, the electrolytic voltage was approximately 1.237 V and the ECE was about 88.1%. It was also found that when using cells with the same structure, electrode atmosphere, and electrolytic voltage (-200 mA/cm^2), ECE remained similar, presenting a high level. For example, the ECE of Cell5.1 was 89.32%, while that of Cell6.1 was 91.99%. This further indicated that the flat-tube type SOEC yielded high energy conversion efficiency.

6.3 Analysis of degradation mechanisms

After the durability testing, the cell was cooled to room temperature at 1 °C/min and disassembled for further analysis. During disassembly, the inlet and outlet were marked and used for microstructure characterization. **Figure 6.5a** displays the air electrode of Cell6.1 after disassembly. The silver mesh was firmly adhered to the cover plate, and the air electrode buffer layer was adhered to the silver mesh, indicating good contact between the air electrode and the cover plate. **Figure 6.5b** introduces the fuel electrode of Cell6.1 after disassembly, with the outlet slightly green, indicating slight oxidation at the outlet, which was also one of the reasons for the decrease of OCV.

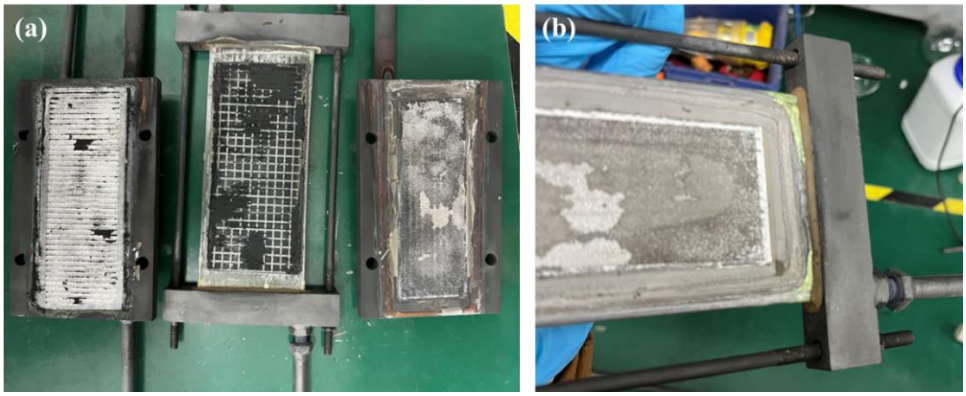

Figure 6.5. Macro structure of Cell6.1 after disassembly: (a) Air electrode, (b) Outlet of fuel electrode

Figure 6.6a shows the SEM image of Cell6.1 after testing. After pulsed current CO_2 electrolysis testing, the cell structure was not damaged, and there were no signs of electrolyte cracking. Additionally, there was slight loss of nickel particles at the interface between the fuel electrode and electrolyte, which further led to an extension of YSZ and an increase in fuel electrode polarization impedance. In addition, in **Figure 6.6b** with a higher magnification, black impurities were found on the nickel particles, which suggested carbon deposition. Due to the limitations of the SEM analysis method, the black substance was not further analyzed.

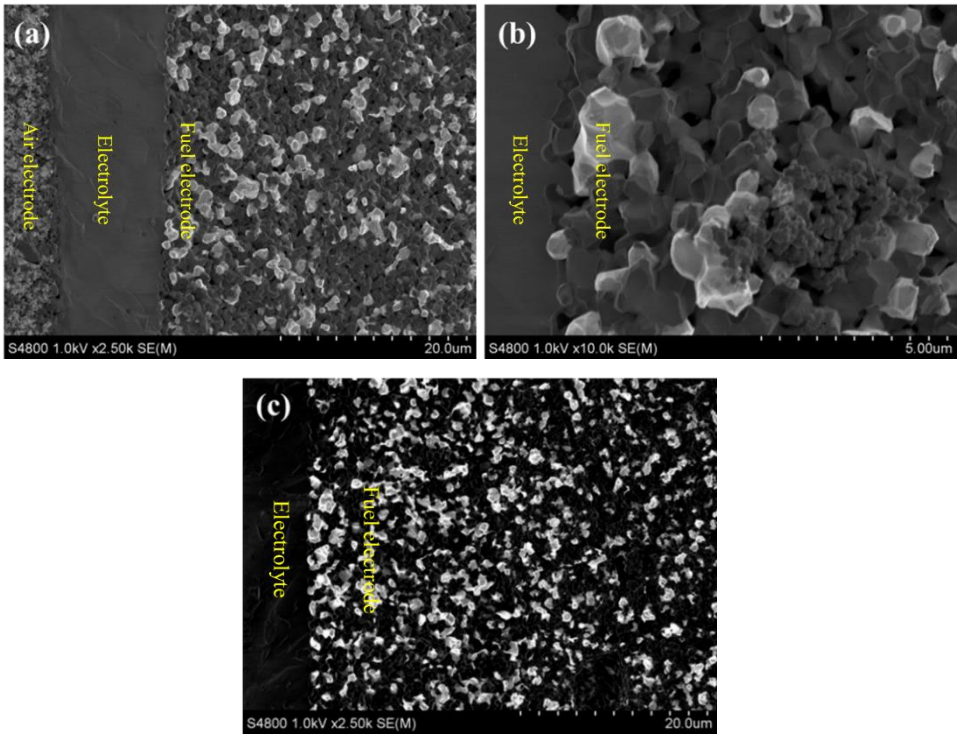

Figure 6.6. SEM images: (a) and (b) Cell6.1 after cyclic pulsed current CO_2 electrolysis; (c) reference cell

In addition, percolation nickel particles were clearly observed in SEM images taken under SE2 and low voltage. In order to calculate the migration and agglomeration of nickel particles in the fuel electrode, **Figure 6.6a** and **Figure 6.6b** were processed with ImageJ software to analyze the areas of Ni particles, and then Origin was used for frequency statistics. The results are shown in **Figure 6.7**. The SEM results reflected that the proportion of the percolation Ni particles between 0.1-0.6 μm^2 in the fuel electrode of Cell6.1 after testing was about 36.19%, while in the fuel electrode of the reference cell, the proportion of nickel particles was around 49.7%, indicating that after long-term pulsed cyclic CO_2 electrolysis testing with CO protection,

serious nickel agglomeration appeared in the fuel electrode, resulting in approximately 13.51% of small nickel particles (0.1-0.6 μm^2) being transformed into large particles (>0.6 μm^2).

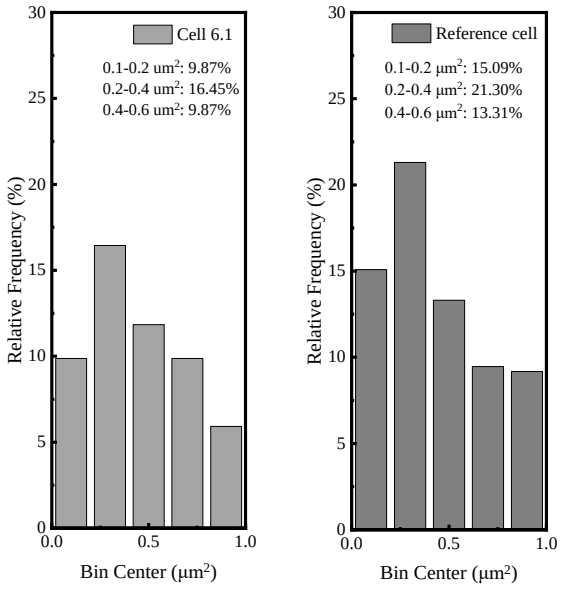

Figure 6.7. Proportion of nickel particles of different sizes: (a) Inlet of Cell6.1; (b) Inlet of reference cell

When disassembling the cell, it was found that there existed some black powder in the outlet pipeline of the fuel electrode. The powder was collected and characterized by Raman spectroscopy with a wavelength of 532 nm. The morphology of the powder under a 50x objective is shown in **Figure 6.8**. In general, carbon deposition is more easily to be observed near the bright area. Accordingly, the bright area was focused for Raman testing. Moreover, Raman characterization was conducted on the gas flow channels of the cell samples at the inlet and outlet, and the Raman spectra were obtained, as shown in **Figure 6.8c**. Two characteristic peaks appeared in the Raman

spectra, with Raman shifts of 1350 cm^{-1} (D peak) and 1580 cm^{-1} (G peak), respectively. The intensity and position of D and G peaks reflected the structure and properties of carbon materials [257]. According to the spectral results in **Figure 6.8c**, no carbon deposition occurred in the gas flow channels of the inlet and outlet of the Cell6.1, but obvious carbon powder was found in the outlet pipe.

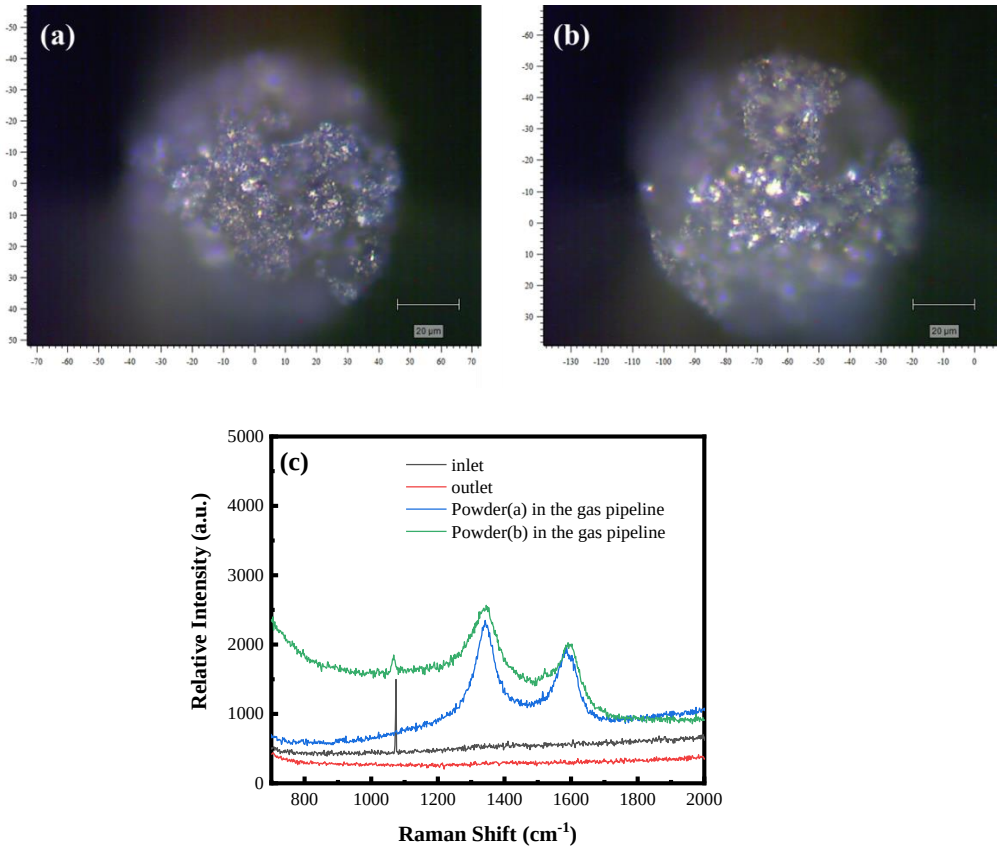

Figure 6.8. (a) and (b) Raman photos of powder in the pipelines; (c) Raman spectra of cell samples and powders in the gas pipeline

According to the calculation results in **Section 4.4.2**, the critical equilibrium value of CO content was about 61.84% at 700 °C, but declined to 42.73% at 650 °C. If the temperature was below 650 °C, the allowable

concentration of CO tended to be lower than 42.73%. Because the length of the gas pipe outside the high-temperature furnace was approximately one meter, the fuel gas in the outlet pipeline was natural cooled, and the temperature of the gas flowing out from the pipeline would be below 300 °C, making it possible for the occurrence of carbon deposition in the pipeline.

6.4 Summary

Taking 23.8 vol.% CO as the fuel electrode protection gas, this chapter simulated intermittent renewable energy power supply to carry out CO_2 electrolysis test based on SOECs. Using-100 to -300 mA/cm^2 as the pulsed current for long-term operation, the cell was conducted for 101 cycles (808 hours). It was found that the electrolysis cell operated stably in the first 70 cycles, with electrolytic voltage degradation mainly concentrated in the 71-100th cycles. For gaining insight into the degradation mechanism, EIS, SEM, and Raman were used for in-situ detection and microstructure characterization. It is believed that the agglomeration of nickel particles at the fuel electrode is one of the important reasons for electrolytic voltage degradation. The agglomeration of nickel particles results in fewer contact points at the triple phase boundaries of the fuel electrode, thus reducing electrode reaction activity. Carbon deposition may be another main cause of cell degradation. Although evidence suggests that carbon deposition occurs at the gas outlet pipeline of the fuel electrode, carbon deposition in the

pipeline can cause limited gas diffusion, which may increase the degradation rate and reduce the open circuit voltage. In the instantaneous electrolytic I-V curve after long-term testing, the voltage fluctuated a lot, indicating that the fuel supply in the fuel electrode was unstable, which might also be caused by carbon accumulation and blockage in the gas pipe. Besides, the GC results manifested that the energy conversion efficiency of Cell6.1 reached over 88% without considering air heat. This further demonstrated the feasibility of operating a flat-tube SOEC with non-stationary renewable energy power supply.

Compared to using 25 vol.% H_2-75 vol.% CO_2 fuel electrode atmosphere for pulsed current CO_2 electrolysis, it was found that under 23.8 vol.% CO-76.2 vol.% CO_2 fuel electrode atmosphere, even if the electrolytic current was below the theoretical threshold of carbon deposition reaction, the degradation of the SOEC was higher than that operated under 25 vol.% H_2-75 vol.% CO_2 fuel atmosphere. This might be attributed to the occurrence of RWGS reaction when H_2 was mixed with CO_2.

Chapter 7. CO_2 electrolysis in reversible solid oxide cells for energy storage

7.1 Introduction

Reversible operation is particularly important in sustainable energy with a high proportion of intermittent renewable energy supply, as it can not only provide fuel production, but also power load balance [258]. The high energy efficiency of reversible solid oxide cells (RSOCs) is attributed to higher operating temperatures. Additionally, RSOC systems can promote the continuous operation of power-to-gas and gas-to-power reversibly using "carbon cycling" technology, thereby reducing environmental pressure and energy supply costs [259, 260]. RSOC system is considered as one of the most cost-effective options for long-term power storage [261, 262]. However, to prevent degradation of components under high temperature and oxidation atmosphere, high requirements are also placed on RSOC materials. Currently, the degradation mechanism under reversible operation is not clear, and the main difficulties faced by large-scale commercial operations include insufficient fuel conversion capacity, high cost, contact loss between cells and interconnects, oxidation and corrosion of interconnects [182,263-266]. To respond to the above issues and satisfy the requirements for renewable energy storage, this chapter adopted flat-tube RSOC technology to conduct research on the reaction of electrochemical

reversible conversion. CO_2 and CO were used as energy storage media for power-to-gas and gas-to-power conversion, providing reference for the development of new energy storage modules.

7.2 Design of reversible solid oxide cells system

Figure 7.1 is a schematic diagram of an electric energy storage system based on RSOC technology. The system included the energy conversion device based on the RSOC and the CO_2/CO gas storage tanks, with CO_2 used as the medium for energy storage. In the power storage process (SOEC mode), CO_2 entered the RSOC system after pre-heating, and CO_2 was decomposed into CO and O_2 by renewable electricity. With part of CO produced used for industrial purposes, the remaining CO entered the compression tank as fuel for power generation. In the power generation process (SOFC mode), CO in the storage tank was fed into the RSOC system, and then oxidized to generate electrical power and CO_2. Generally, the electricity generated can either be connected to the grid for distributed power generation or used for industrial or transportation purposes. The newly generated CO_2, after being separated, entered the compression tank. The amount of CO_2 consumed in the SOEC mode and the amount of CO_2 generated in the SOFC mode could be balanced by adjusting the CO_2/CO ratio and the operating current, so as to achieve “zero carbon emissions”.

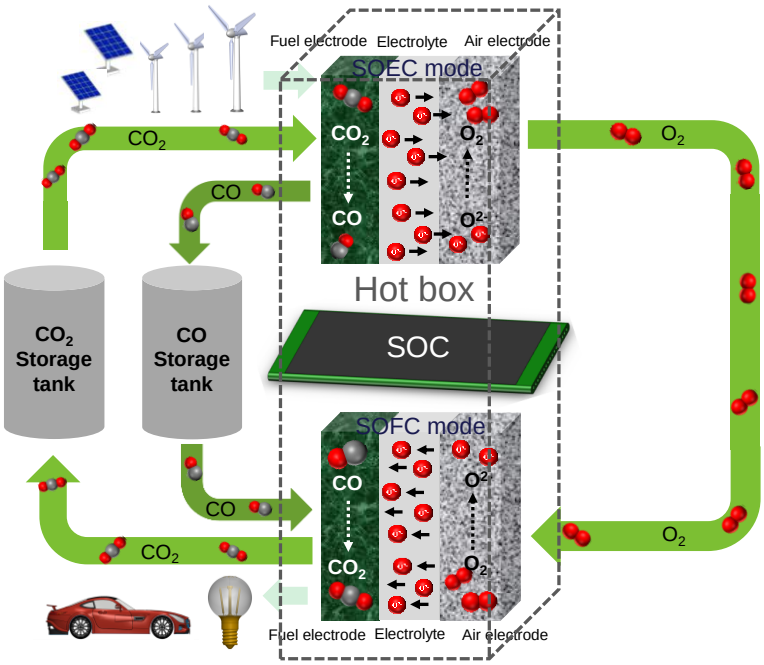

Figure 7.1. Schematic diagram of RSOC in energy storage system

Figure 7.2 shows the assembly method for a single cell. The experiment in this chapter used thin flat-tube cells (<3 mm), and the assembly method were mentioned in **Chapter 3.1**. The cells and fixture were fixed with external pressure devices, with a pressure of 100 kg, to improve air tightness and enhance contact between the cells and the cover plates. Additionally, due to the reduced gap between the fuel electrode of the cell and the fixture, the assembly time should be decreased, and the assembly process should be simplified.

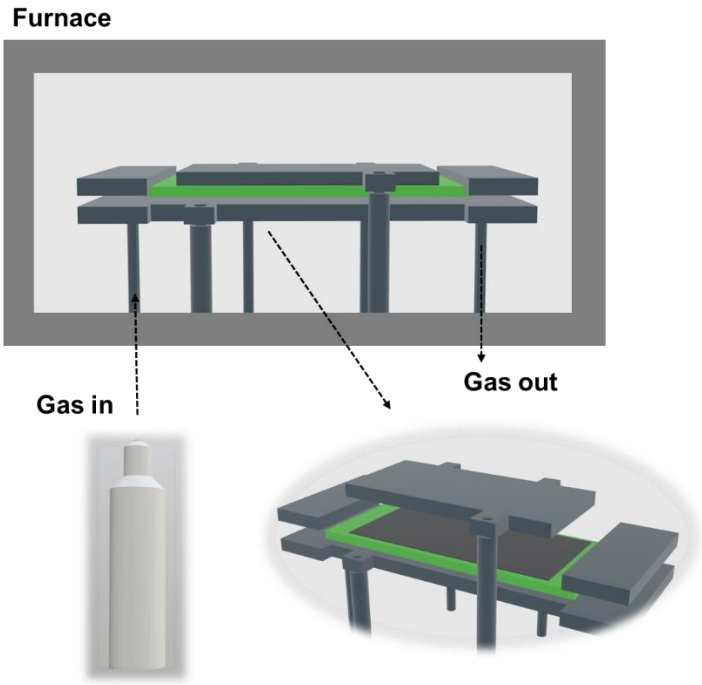

Figure 7.2. Schematic diagram of the test system

The instantaneous discharge and charge performance and long-term durability of the cells were tested. To analyze the conversion efficiency of the operated cells, the exhausted gas composition of the fuel electrode was measured. After the durability test, the instantaneous charge and discharge performance was tested again, and compared with the initial results to analyze the degradation of the RSOC. The post-mortem analysis of the cell was performed through SEM, EDS, and Raman spectroscopy. Because CO was used as the reversible operating medium, the degradation of fuel electrode was emphasized during experiments.

7.3 Long-term performance in reversible solid oxide cells

7.3.1 Stability test

The cells used in this chapter were named Cell7.1 and Cell7.2. The difference in the initial performance of the two cells could be attributed to the degree of interface contact. The initial performance test results of Cell7.1 and Cell7.2 are shown in **Figure 7.3**. Firstly, the initial performance of the cell was tested in SOFC mode. During the test, 0.6 SLM H_2 was supplied to the fuel electrode and 2 SLM air was introduced to the air electrode. Subsequently, the intake component of the fuel electrode was switched to a CO-CO_2 mixed atmosphere, and the air volume of the air electrode was changed to 3 SLM. After the open circuit voltage stabilized, an initial performance test was conducted in SOEC mode. During the instantaneous performance test, the electrolytic current increased by 0.5 A/5 seconds. After the long-term reversible test, the instantaneous charging and discharging performance was measured again under the same conditions as the initial performance, and the degradation rate was calculated after comparison. **Figure 7.3a** shows the discharge I-V curves of Cell7.1. After 10 reversible cycles, the maximum discharge power decreased from 380.7 mW/cm^2 to 257.7 mW/cm^2, with a degradation rate of 3.23%/cycle. **Figure 7.3b** shows the electrolytic I-V curves of Cell7.1. After 10 reversible cycles, there was no significant change in OCV, but the corresponding instantaneous voltage

at -300 mA/cm^2 increased from 1.255 V to 1.403 V, with a voltage increasing rate of 1.18%/cycle. **Figure 7.3c** shows the discharge I-V curves of Cell7.2 before and after long-term test. After 101 reversible cycles, the maximum discharge power decayed from 637.1 mW/cm^2 to 571.4 mW/cm^2, with a degradation rate of 0.1%/cycle. **Figure 7.3d** reveals the electrolytic I-V curves of Cell7.2 before and after long-term operation. After 101 reversible cycles, there was no significant change in OCV, but the corresponding instantaneous voltage at -300 mA/cm^2 increased from 1.068 V to 1.118 V, with a voltage degradation rate of 0.05%/cycle.

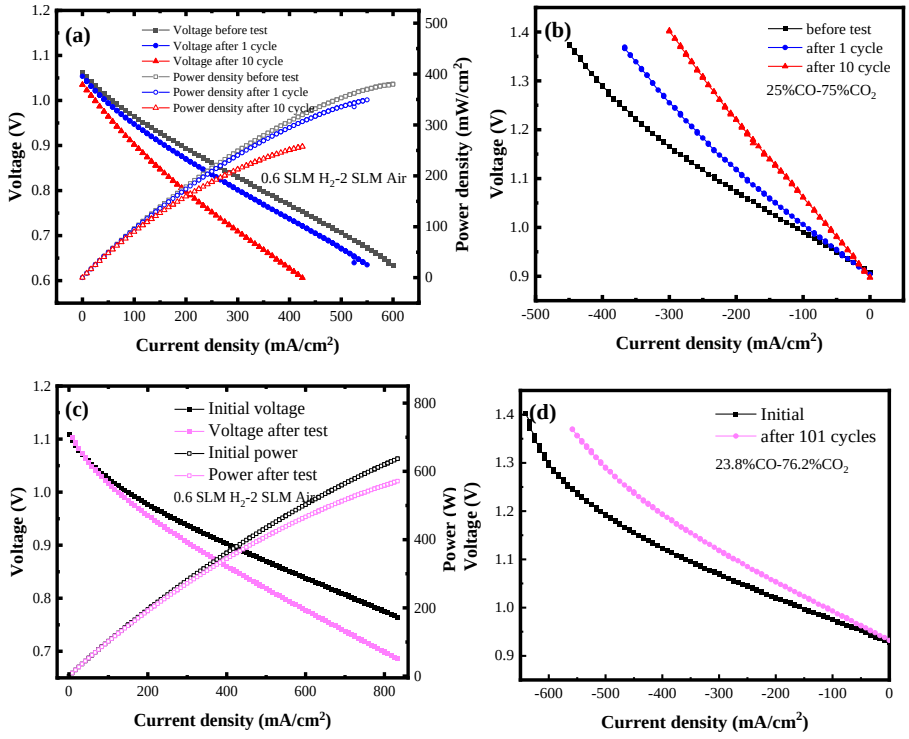

Figure 7.3. Charge and discharge I-V curves before and after long-term reversible operation: (a) Discharge I-V curves of Cell7.1; (b) Charge I-V curves of Cell7.1; (c) Discharge I-V curves of Cell7.2; (d) Charge I-V curves of Cell7.2

Due to defects in the structure of Cell7.1, the experiment was manually terminated after only 10 cycles of long-term operation. To maintain the same electrode atmosphere in both SOFC and SOEC mode, 0.3 SLM CO-0.3 SLM CO_2 (50 vol.% CO-50 vol.% CO_2) was chosen as the fuel electrode working condition for long-term operation, with the air electrode continuously supplying 3 SLM of air. The total duration of the first cycle was 12 h, including 8 h discharge in 150 mA/cm^2 (0.854 V), 3 h electrolysis in -300 mA/cm^2 (1.177 V) and 1 h OCV in the same fuel electrode atmosphere. After the first cycle, due to the significant degradation of the area specific resistance in the I-V curve, the experimental plan was also adjusted accordingly. Starting from the second cycle, the time in each cycle was changed to 24 hours, using 150 mA/cm^2 for 9 h for SOFC and -150 mA/cm^2 for SOEC mode and OCV for 2 h. The V-t curve demonstrated that during long-term operation, there was significant degradation in both charging and discharging processes, and carbon deposition (black powder) gradually appeared in the fuel electrode outlet pipe. The abnormal degradation of Cell7.1 might be caused by overburning during the manufacturing process, where the pores in the supporting layer were too small, resulting in slow CO diffusion and excessive local concentration, further leading to severe carbon deposition. In addition to thermodynamics, Cell7.1 exhibited a high voltage during operation, and electrode overpotential also promoted carbon

deposition [267].

Afterwards, Cell7.2 was used for long-term “carbon cycling” experiments, with a total of 101 reversible cycles. In each cycle, the cell was operated in SOEC mode for 40 minutes, with a current density of -200 mA/cm^2, and in SOFC mode for 77-84 minutes, with a current density of 100 mA/cm^2. The specific discharge time was adjusted appropriately based on the GC results of the exhausted gas. Through adjusting the discharge time, the CO_2 consumed by electrolysis was equal to the CO_2 generated by discharge, thus achieving “carbon cycling utilization”. For the long-term reversible cycling experiment, 0.3 SLM CO-0.3 SLM CO_2 (50 vol.% CO-50 vol.% CO_2) was also selected as the fuel electrode working condition, with 3 SLM of air continuously supplied in the air electrode. During the experiment, the single round-trip efficiency of each cycle was about 86%. When running to the 99th cycle, the fuel electrode pipe was blocked by carbon, leading to an increase in fuel gas pressure. After 101 cycles, the test was manually stopped. According to **Figure 7.4b**, the voltage degradation rate was 0.03%/cycle in SOEC mode and 0.043%/cycle in SOFC mode.

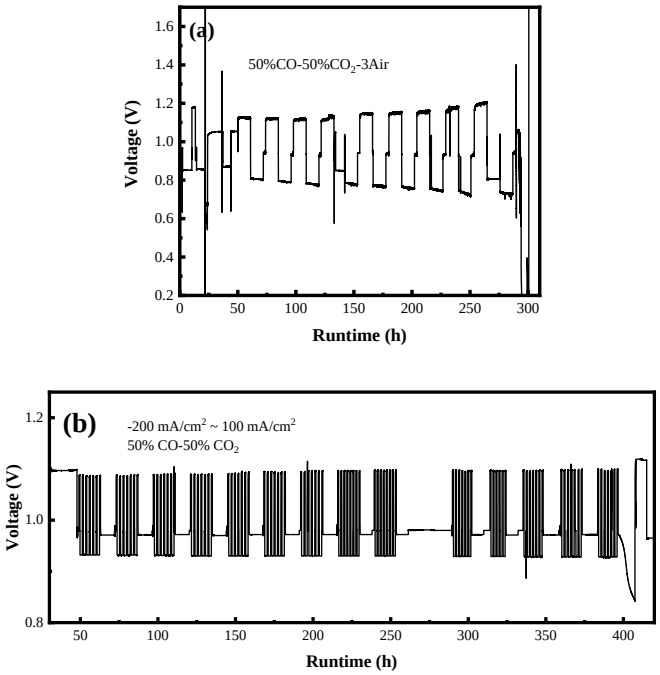

Figure 7.4. V-t curves of cells during long-term reversible operation: (a) Cell7.1; (b) Cell7.2

7.3.2 Electrochemical impedance and DRT analysis

During the long-term operation of Cell7.1 and Cell7.2, the electrochemical impedance under OCV state was measured every certain number of cycles, as shown in **Figure 7.5**. **Figure 7.5a** shows the EIS curve of Cell7.1 at the end of each cycle during reversible operation. It could be clearly seen that ohmic impedance of the first four cycles presented an increasing trend, and the polarization impedance in the mid frequency range increased at 4-10th cycles, indirectly reflecting the degradation of the electrode reaction process. **Figures 7.5b** and **c** show the Nyquist diagrams and DRT changes of Cell7.2 during the reversible cycle operation. During Cycle 0 to Cycle 85, ohmic impedance of Cell7.2 increased significantly,

while polarization impedance remained almost unchanged. The increase in ohmic impedance mainly derived from the destruction of the electrolyte and the contact resistance between the electrode and the current collection layer. This indicated an increase in contact resistance, making it more difficult for ions/electrons to transfer in the electrolyte and electrodes. During Cycle 85th to Cycle 101st, the change in total impedance mainly originated from polarization impedance. According to **Figure 7.5c,** both P4 and P5 peaks exhibited a trend of high-frequency shift (positive shift), which might be due to temperature changes during the electrolysis process [268].

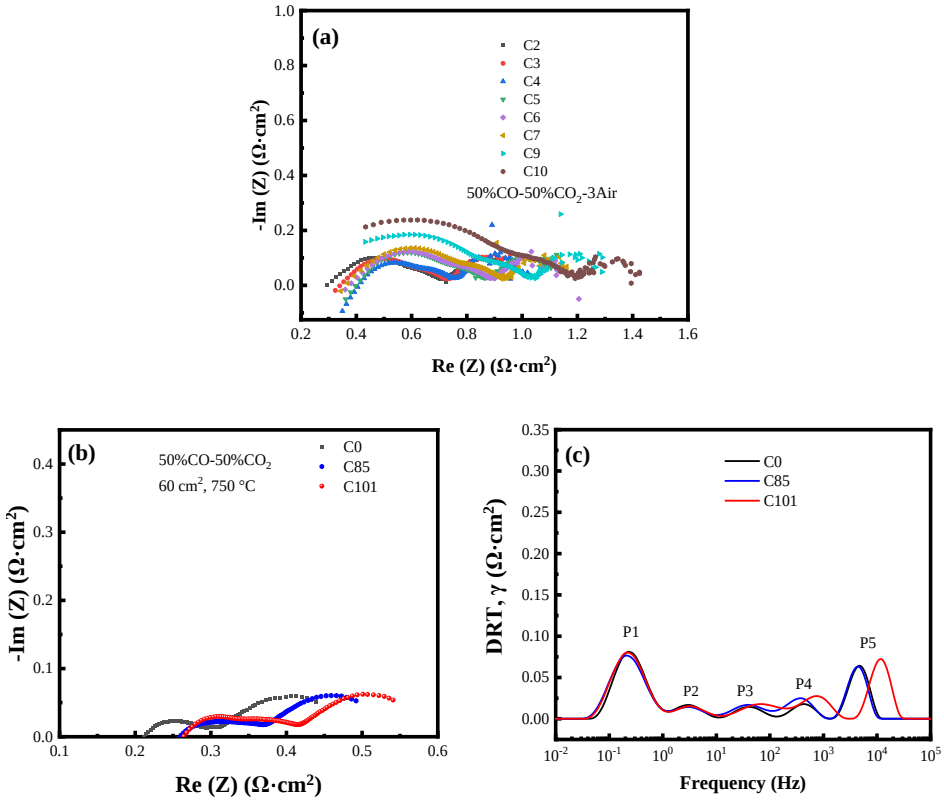

Figure 7.5. EIS and DRT curves of cells during reversible cycles: (a) EIS of Cell7.1; (b) EIS of Cell7.2; (c) DRT of Cell7.2

7.3.3 Conversion rate and energy conversion efficiency

To evaluate the efficiency of energy conversion during operation, the composition of the exhaust gas in the fuel electrode was analyzed by gas chromatography. The energy conversion efficiency of the power-to-gas process was calculated, as shown in **Table 7.1**. Considering the recycling of the heat energy generated by the reaction gas, the heat energy consumed by the fuel gas was ignored [269].

$$\eta_{EC} = N_{out,CO} \times q_{CO} / V_m \times (I \times V + Q_{th}) \quad \text{(Eq.7.1)}$$

$$\eta_{FC} = I \times V \times V_m / (N_{consumed,\ CO} \times q_{CO}) \quad \text{(Eq.7.2)}$$

where, η_{EC}, and η_{FC} represent the energy conversion efficiency of SOEC and SOFC mode (%); $N_{out,CO}$ refers to the volume flow rate of CO in the fuel electrode tail gas (SLM); q_{CO} is the energy density of CO (J/mol), equals to 282963.93 J/mol; V_m denotes molar volume of gas at room temperature, equal to 24.5 L/mol; I indicates electrolytic current (A); V means electrolytic voltage (V); Q_{th} is the compensating energy absorbed from the environment in the case of the input electric energy being less than the total energy required for electrolysis system (J/s).

The energy conversion efficiency was calculated from **Eq. 7.1** and **7.2**. When the electrolytic voltage was lower than the thermal neutral voltage of CO_2 electrolysis reaction (1.46 V), the compensation energy could not be ignored, owing to heat absorbed from the environment by the CO_2 electrolysis reaction. According to the calculated results, under the

electrolytic current of -200 mA/cm^2, the electrolytic energy conversion efficiency of Cell7.2 reached up to 103%. The energy conversion efficiency mainly depended on the generation or consumption of CO. Even under discharge current of 100 mA/cm^2, the energy efficiency still reached 62%.

Table 7.1. Calculation of efficiency of Cell7.2

	Electrolytic voltage	cycles	CO generated or consumed in the cell	ECE
Cell7.2	1.095 V	100	93.7 sccm, 47.15 sccm	103% @ -200 mA/cm^2 62% @ 100 mA/cm^2

Round-trip energy conversion efficiency is the key factor in evaluating the capacity of the RSOC system. When ignoring the loss of thermal transmission, the round-trip efficiency of the cell, η, can be expressed by **Eq.7.3** [182]:

$$\eta = V_{FC} \times Q_{FC} / V_{EC} \times Q_{EC} \quad \text{(Eq.7.3)}$$

where V represents the cell voltage; and Q represents charge, the electrolytic current multiplied by the electrolytic time. Energy can be expressed as the product of the cell voltage V and charge Q. Assuming the Faraday efficiency is 100%, when Q_{FC} equals Q_{EC}, the efficiency can be expressed simply as the ratio of the discharge voltage (0.932 V) to the electrolytic voltage (1.089 V), as shown in **Eq.7.3**. When selecting the test conditions, to maximize η, V_{FC} and V_{EC} should be as close as possible [270]. In the reversible operation

of Cell7.2, the single round-trip efficiency reached 86% according to **Eq.7.4**.

$$\eta = V_{FC}/V_{EC} \quad \text{(Eq.7.4)}$$

7.4 Analysis of degradation mechanisms

To investigate the degradation of the fuel electrodes of the tested cell, micro-morphology analysis was conducted after cooling and compared with a reference cell (without any testing). The results are shown in **Figure 7.6**. **Figure 7.6a** shows the inlet of Cell7.2 after 100 reversible cycles, which was compared to the reference cell in **Figure 7.6b.** The loss of percolating nickel particles near the surface of fuel electrode and electrolyte could be clearly observed.

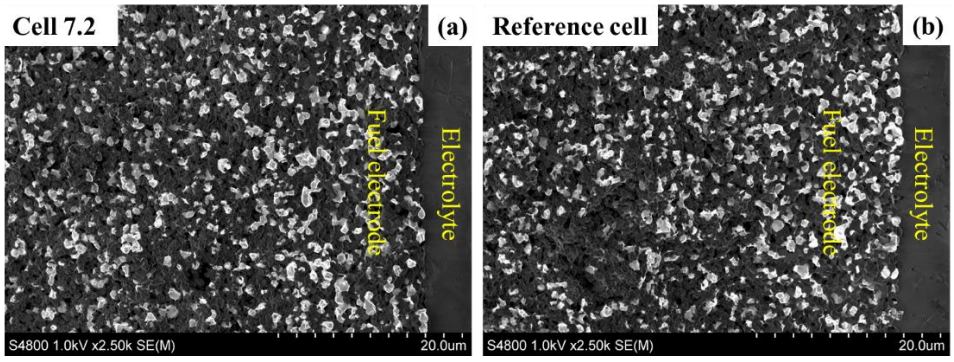

Figure 7.6. SEM photos of inlet of the tested Cell7.2 and the reference cell

After long-term testing, the same method as in **Chapter 5** and **Chapter 6** was adopted to analyze the agglomeration of percolating Ni particles of Cell7.2 and compare it with the reference cell. The calculation results are shown in **Figure 7.7**. The percolating Ni particles between 0.1-0.4 μm^2 in

Cell 7.2 was 42.69%, which decreased by about 2.58% compared with the reference cell. Ni particles between 0.4-0.6 μm^2 in Cell7.2 was 13.44%, which decreased by about 0.88% compared with the reference cell, indicating no significant change in nickel particle size. The occurrence of inevitable nickel agglomeration at high temperatures suggested that the degree of agglomeration depended on the operating time. Cell7.2 had the shortest operating time, less than 400 h, which implied the degree of agglomeration was relatively small.

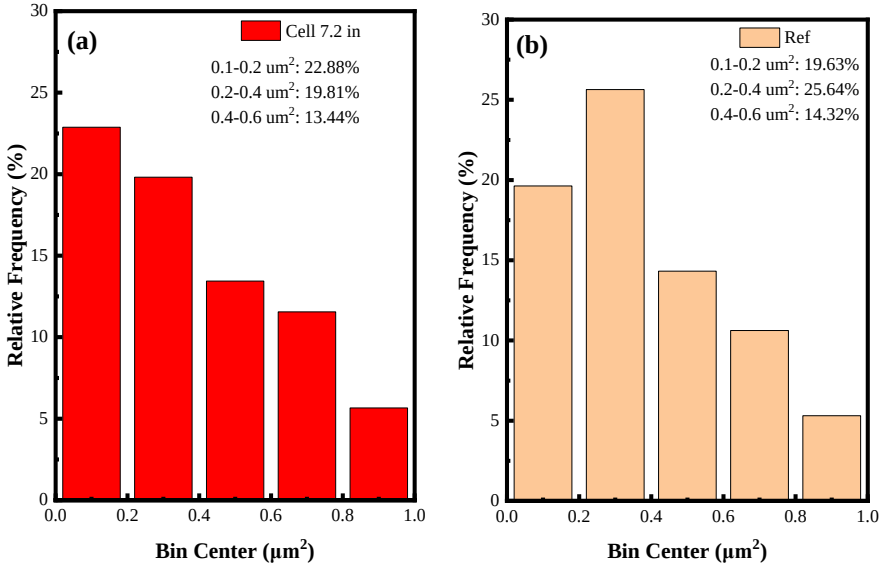

Figure 7.7. Nickel agglomeration level: (a) Inlet of Cell7.2; (b) Inlet of the reference cell

Figure 7.8 shows the nickel migration analysis results of Cell7.2 after 101 reversible cycles in 50 vol.% CO-50 vol.% CO_2 atmosphere. As the thickness of the active fuel electrode was about 15 μm, and the degree of nickel migration varied between the near electrolyte region and the far

electrolyte region. Therefore, the fuel electrode was divided into three regions for calculating nickel content. The region closest to the electrolyte was region 1, and so on. For the reference cell, the same method was used for calculation. The difference in nickel content of each area between the tested cell and the reference cell was calculated as the basis for nickel migration. The advantage of this analysis method lied in that the errors in reference cell and tested cell remained similar, making it possible to determine whether nickel migrated by comparing relative values. The results implied that the loss of Ni also occurred in the fuel electrode, with Ni content decreased by 6.76% in the first region, while in the second and third areas, Ni% decreased by 5.44% and 3.02%, respectively.

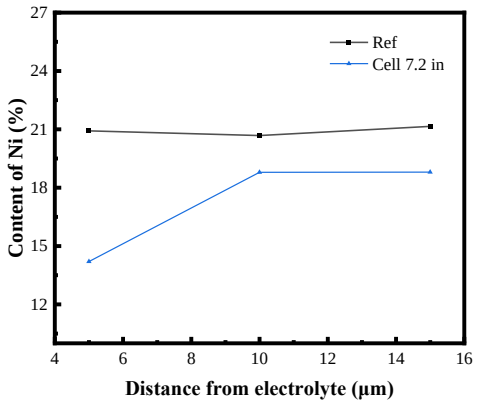

Figure 7.8. Ni content of Cell7.2 and reference cell at different distance from electrolyte

Figure 7.9 shows the Raman spectrum of the inlet gas channel of Cell7.2 after 101 reversible cycles. Both D and G peaks of carbon were clearly identified, which was consistent with the analysis results of Cell7.1.

According to the actual testing conditions, the concentration of CO at the outlet was about 65 vol.%, including 50 vol.% introduced CO and CO generated by CO_2 electrolysis reaction, which was lower than the thermodynamic conditions for carbon deposition (CO%>78.2 vol.%). Nevertheless, due to diffusion limitations and the loss of nickel catalyst during the testing process, the thermodynamic equilibrium at the triple phase boundaries was disturbed, promoting the occurrence of local carbon deposition. In addition, as the exhaust gas cooled down in the outlet pipeline, the temperature in the pipeline gradually dropped below 750 °C, resulting in a decrease in the critical CO concentration of carbon deposition. And carbon deposition occurred under the catalysis of metal in the pipeline. Therefore, the critical value of CO concentration calculated through thermodynamics only served as a reference for the selection of long-term operating conditions. To completely extend the service life of RSOCs, the occurrence of the carbon deposition reaction should be suppressed by changing the electrode structure and materials.

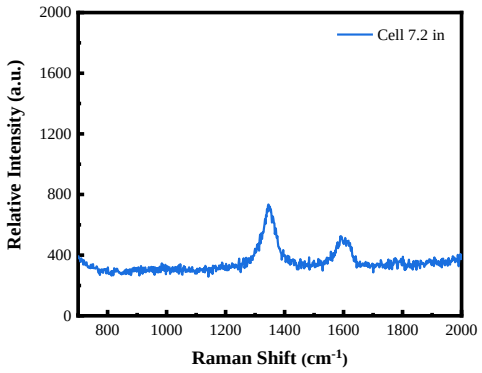

Figure 7.9. Raman spectrum of the inlet of Cell7.2 after reversible cycles

7.5 Comparison under constant, pulsed and reversible current

In **Chapters 5**, **6**, and **7**, long-term durability tests were conducted on flat-tube SOECs under different operating conditions. Due to different operating conditions and durations, the degree of nickel agglomeration was slightly different. **Figure 7.10** presents the statistical results of nickel particle size at the fuel electrode of the three tested cells and the reference cell, in which the three tested cells were operated under steady-state energy storage mode for 858 h (Cell5.3), intermittent non-stationary energy storage mode for 808 h (Cell6.1), and reversible cycle mode for more than 400 h (Cell7.2). By comparison, it was found that the nickel particles between 0.1-0.4 μm^2 in Cell5.3 decreased by approximately 11.53%; the nickel particles between 0.1-0.4 μm^2 in Cell6.1 decreased by about 18.95%; the proportion of nickel particles in Cell7.2 decreased by about 2.58%. Current evidence suggests that reversible round-trip cycles may tend to suppress fuel electrode degradation, but nickel agglomeration at fuel electrode is a complex process, which is closely related to high-temperature testing time, electrolytic atmosphere, electrolytic current, and operating conditions. Therefore, further mechanism research is still needed.

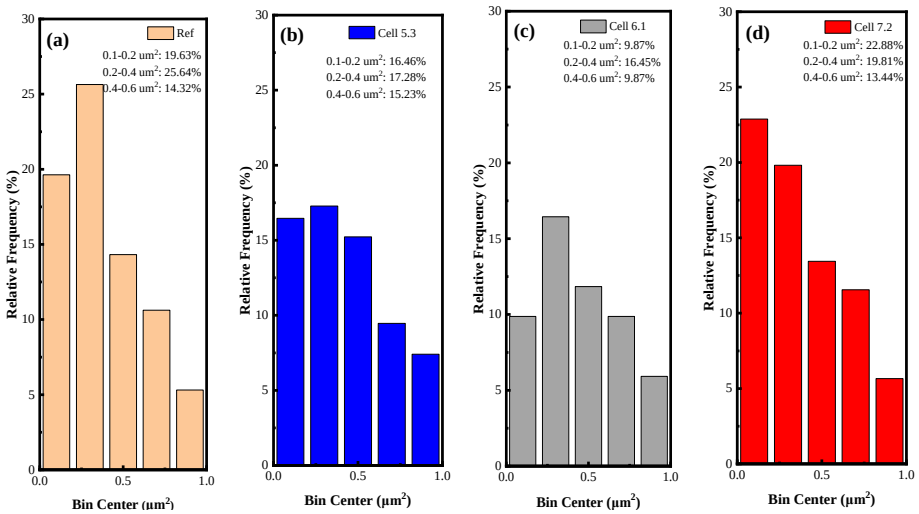

Figure 7.10. Comparison of Ni content in the inlet of: (a) Reference cell; (b) Cell5.3; (c) Cell6.1; (d) Cell7.2

According to existing literature reports, the migration of Ni is driven by the electrical potential gradient and oxygen partial pressure gradient. Cheng et al. [271] proposed a possible mechanism for nickel migration related to nickel oxidation at the Ni-YSZ interface under polarization. In the absence of current flow or SOEC/SOFC operation, NiO was not generated. In the fuel cell mode, NiO existed as a thin film at the Ni-YSZ interface. But in the electrolysis cell mode, NiO also grew at the interface. In RSOC mode, the NiO phase was porous, granular, and polycrystalline, and accumulated extensively near TPB. When the cell was cooled from high temperature to room temperature in a reducing atmosphere containing hydrogen, NiO was reduced to Ni, and the reduced Ni repositioned and exhibited migration behavior. As it should be, the proposed mechanism may not be responsible for all reported Ni migrations, or it may not be the only mechanism. In this

research, the fuel electrode atmospheres used in the three cells were all dry gases, and no steam was generated during the reaction process. Therefore, steam content was not the main factor affecting nickel migration, and oxygen atoms in NiO were likely to come from CO_2. According to the calculation results in **Figure 7.11**, at a distance that 15 μm away from the electrolyte, all three cells appeared a clear trend of nickel migration, with Cell5.3 showing the highest degree of nickel migration and Cell7.2 showing the lowest degree of nickel migration. Comparison of the test conditions of the three tested cells suggested that the loss or oxidation of nickel was likely dependent on the duration of high-temperature electrolysis and the extent of applied current.

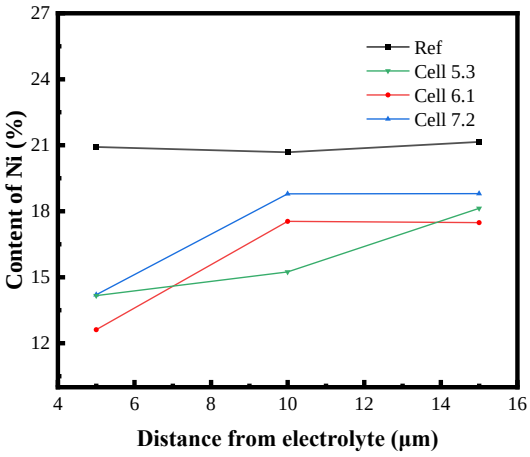

Figure 7.11. Comparison of nickel migration in different regions of the fuel electrodes of three tested cells

The Raman spectra of three tested cells operated under three different operating conditions were compared in **Figure 7.12**. Two intense bands

related to the deposited carbon appeared, including the D (defect) band associated with disorder structure of carbon and the G (graphite) band featuring the graphitic layers and the tangential vibration of carbon atoms. The degree of graphitization of a carbon material was related to the ratio of the intensity of D-peak (1360 cm^{-1}) and G-peak (1580 cm^{-1}), and the lower the ratio of intensity between the D and G peaks, the higher the degree of graphitization of carbon and the more difficult the removal of carbon matter [272, 273]. According to calculations, the I_D/I_G ratio of the three cells was 1.399, 1.187, and 1.277, respectively. The carbon deposited in the three tested cells demonstrated a high degree of graphitization, making it difficult to completely remove the carbon deposit in the fuel electrode by simply adding steam [274]. Therefore, how to prevent carbon deposition through material and structural modification is an important research direction in the future.

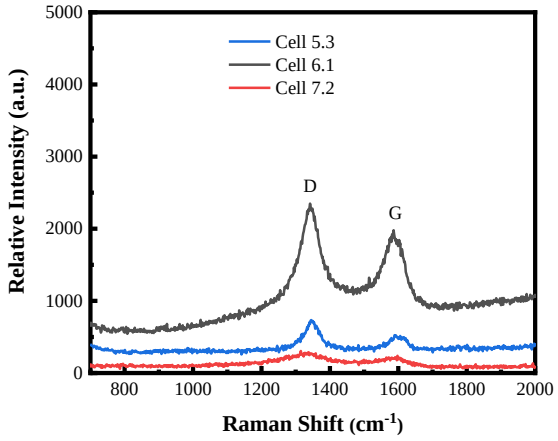

Figure 7.12. Comparison of Raman spectra after long-term testing under different operating conditions

In order to further evaluate the application of RSOCs in the field of large-scale long-term energy storage, the efficiency, lifespan, as well as advantages and disadvantages of common electrochemical energy storage technologies were summarized, including lithium-ion batteries, lead-acid batteries, flow batteries, and solid oxide cells, as shown in **Table 7.2** [270, 275-283]. The research scope of RSOC energy storage systems can cover various gases such as CO_2, H_2O, CH_4, as well as various application scenarios combined with wind, solar, or other renewable energy sources [284-286]. Currently, the theoretical durability of the RSOC system can exceed 10 years, and the efficiency of the reversible cycle system is about 60-90%. The efficiency mainly depends on parameters such as gas pressure, operating temperature, and current density [287-289].

Table 7.2. Comparison of advantages and disadvantages of energy storage technologies [270, 275-283]

Technique	Round trip efficiency	Lifespan	Advantage	Disvatange
lithium-ion batteries	85%-97%	5-15 years	High power and energy density	Flammable, low safety
Lead-acid battery	63-90%	5-15 years	Easy installation with low self-discharge	High maintenance costs
Liquid flow battery	65%-85%	15 years	Easy installation, low self-discharge, fast response, and	Low efficiency, low energy density

			replaceable electrolyte	
Solid oxide cell	60%-90%	10 years	High safety, high efficiency, and continuous operation	Technology maturity is still being validated

The round-trip efficiency of each cycle under the operating conditions of Cell7.2 was about 86%, which was close to the efficiency of traditional electrochemical energy storage technologies, such as lithium-ion batteries, Na-S batteries, liquid flow batteries, and lead-acid batteries, etc. Compared to these batteries, the attraction of RSOCs mainly lies in the power-to-gas-to-power storage mode and long-term energy storage characteristics. Moreover, a RSOC energy storage system can operate under a variety of scenarios utilizing CO_2, H_2O, CH_4 and other fuel gases, combined with wind, solar or other renewable energies. Therefore, with the explosive growth of intermittent renewable energy power and global concerns about carbon neutralization, RSOCs with carbon dioxide as an energy medium is a promising technology for long-term power storage. Although the maturity of solid oxide cells in the commercialization process still needs to be verified, and several factors that lead to performance degradation, such as nickel agglomeration, carbon deposition and electrode layering, have not been solved, it is believed that they will have a place in the energy storage market once the problem of durability can be overcome.

7.6 Summary

This chapter considered the utility of SOC in energy storage and carbon neutrality. Using CO as the energy storage medium, power-to-gas and gas-to-power processes were simulated under CO-CO_2 fuel electrode atmosphere and reversible current. A comparison was made with the constant current energy storage and intermittent renewable energy storage in the previous two chapters. The results indicated that the flat-tube SOEC achieved stable operation for hundreds of hours under all three operating conditions. The fuel electrode degradation was mainly due to nickel agglomeration and migration, and the degradation degree mainly depended on the distance from the electrolyte and the duration of high-temperature testing. Carbon deposition in the flow channel was also proved to be an important reason for the accelerated degradation rate of the electrolysis cell, but it caused no significant impact in the short-term operation. Strontium segregation in the air electrode was mainly dominated by oxygen partial pressure, which demonstrated that it might only occur under test conditions where the air electrode was not supplied with air, regardless of the operating conditions of the fuel electrode. Assuming that the thermal energy of the SOEC system can be recovered, the energy conversion efficiency during operation can reach over 100%. If the future energy storage system can be applied to other fields, such as peak shaving and distributed applications, the value of energy storage may also increase.

Although RSOC technology is a very promising and potential technology, it still requires longer lifespan and lower prices to reach a comprehensive commercial stage. In recent years, some representative enterprises or projects have reported large-scale research on reversible operating systems. For example, Sunfire GmbH presented the largest RSOC prototype currently available, with peak power reaching 25 kW in SOFC mode and 200 kW in SOEC mode [290]. Sylfen proposed the concept of using RSOC for building storage [291], but it has not yet reached commercial level. Therefore, further experiments are needed to deeply explore and balance its availability through lifetime prediction, operational cost analysis, and other methods.

Chapter 8. Stability and degradation of interface contact in SOEC stacks under constant current CO_2 electrolysis

8.1 Introduction

In **Chapter 5**, the durability and degradation mechanism of constant current CO_2 electrolysis on flat-tube electrolysis cells for producing fuel were studied. However, for cells assembled into stacks in series, component materials also include stainless steel interconnects, current collection materials, and sealing materials. In addition to the electrolytic performance and stability of CO_2 electrolysis on single cells verified in **Chapter 5**, the destruction of key components such as interconnects and sealing materials, the design of stack structure and heat consumption also constitute critical factors that determine the durability and efficiency of SOEC stacks.

Based on the exploration of single cells in **Chapters 4-7**, this chapter performed constant current CO_2 electrolysis testing through connecting single cells in series to form a stack. By gaining insight into the interaction effects of various components, the reasons for the performance degradation of the stack during long-term CO_2 electrolysis process were analyzed. During the assembly process of the electrolytic stack, the real-time voltage and electrochemical impedance of each unit were monitored by taking nickel chromium wires as voltage probes. At the same time, the

reliability of CO_2 electrolysis in the SOEC stack was further analyzed through fuel electrode product analysis and energy conversion efficiency calculation.

8.2 Long-term performance of flat-tube SOEC stacks

8.2.1 Stability test under different current

To achieve industrial applications of solid oxide cells, relying on single cells is not enough. It is also necessary to research on large-scale stacks to achieve larger scale energy storage and fuel production. Considering the complexity of the assembly process and numerous influencing factors inside the stack, research on CO_2 electrolysis in this chapter was mainly focused on three-unit stacks. The main degradation detected in the operation of SOEC stacks was reflected in the layer of functional layers, Cr poisoning of the air electrode, microstructure degradation, and gas leakage. The current collection effectiveness of the cell influenced the initial performance of the stacks, while airtightness, Cr poisoning, and microstructure degradation affected the durability of SOEC stacks. After research and development, a total of 8 stacks were successfully selected for long-term CO_2 electrolysis testing, named Stacks8.1-8.8. Stacks8.1-8.5 were complete sealed, without the addition of voltage probes. Only the overall voltage, power, degradation rate, and electrolytic efficiency of the stacks could be monitored and calculated, which were used for exploratory experiments. **Figure 8.1a** shows

the real-time voltage of Stacks8.1-8.5 during the constant current CO_2 electrolysis test, and the performance parameters are summarized in **Table 8.1**. The gas leakage rate of the fuel gas at room temperature was lower than 3.3%, indicating good air tightness at room temperature. However, after heating to 750 °C, larger gas leakage occurred due to the expansion and contraction of the glass sealing materials. In Stacks8.1-8.5, the initial maximum discharge power reached 73.9 W with 3 SLM H_2 and 9 SLM air, while the minimum power was 31 W. The maximum and minimum electrolytic voltage degradation rates were 188%/kh and 12%/kh respectively. The discharge power and electrolytic voltage degradation rate of SOEC stacks were mainly influenced by the cell manufacturing process and interface contact. For the stacks with the long electrolytic operation time, the energy efficiency was also calculated, as shown in **Table 8.2**. The above results proved the feasibility of using SOEC stacks as an energy conversion device despite a certain gap with the ideal value of SOECs.

When exploring the sealing and assembly methods of the stacks, the process gradually became mature, and Stack8.6, Stack8.7, and Stack8.8 were successfully assembled. The internal structure of Stack8.6 is shown in **Figure 8.2**, which was divided into three units. Unit 1 contained a cell and a flat fuel electrode interconnect, while Unit 2 and Unit 3 consisted of a cell and an air electrode interconnect (with ribs used for the air electrode). A total of 8 wires were connected inside Stack8.7, to in-situ monitor the changes in

the cells, cathode contact, and anode contact. The meanings of each individual voltage are shown in **Table 3.2**. Stack8.8 was assembled using thinner cells with the same overall structure as Stack8.1-Stack8.5. Since the air electrode was not open or connected to voltage probes, the single voltage of each unit of Stack8.8 could not be detected. The degradation in SOEC stacks was analyzed through microscopic characterization after testing.

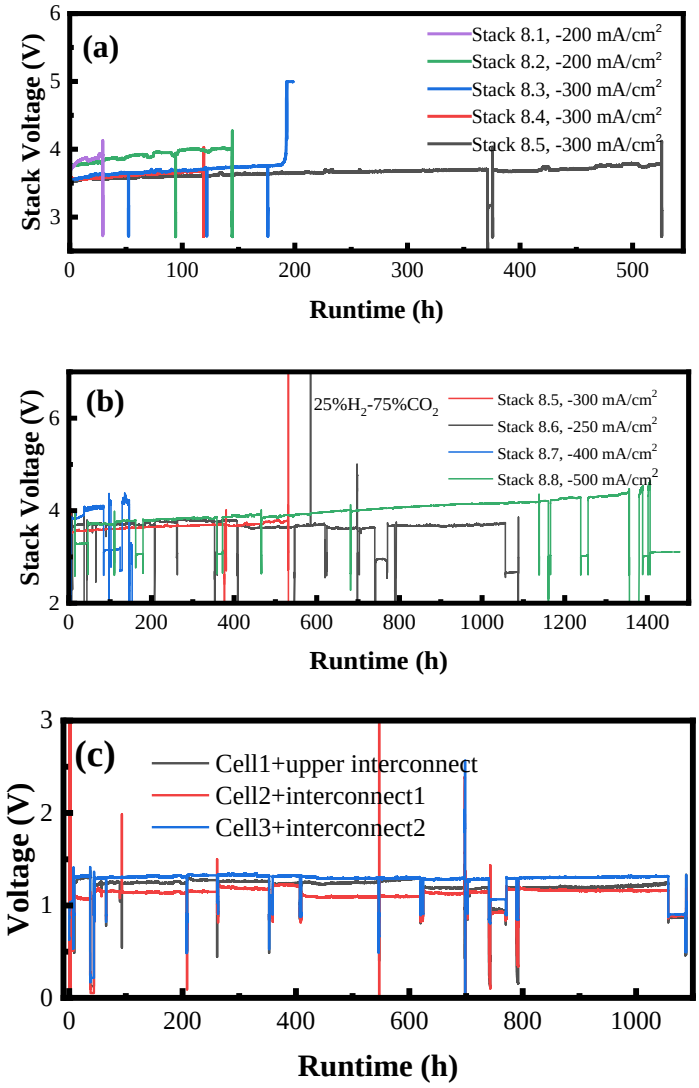

Figure 8.1. V-t diagrams of (a) Stack8.1-Stack8.5; (b) Stack8.5-Stack8.8; (c) Single electrolytic voltage of Stack8.6

Figure 8.1b displays the real-time voltage curves of Stack8.5-Stack8.8 during long-term operation. The long-term electrolytic currents of the four stacks were -300 mA/cm^2, -250 mA/cm^2, -400 mA/cm^2, and -500 mA/cm^2, respectively. The V-t curves of Stack8.5, Stack8.6, and Stack8.8 suggested that if the supplied fuel electrode atmosphere remained the same, the larger the current, the faster the voltage degradation rate. **Figure 8.1c** reveals the real-time voltage of three units during the long-term testing of Stack8.6. The degradation rates of electrolytic voltage of each unit were 0.16%/kh, 6.35%/kh, and 0.68%/kh, respectively. This indicated that the second unit composed of the second cell and the air electrode interconnect of Cell1 exhibited the fastest decay. The stack was manually stopped and cooled after long-term CO_2 electrolysis testing, and then disassembled for micro-morphology characterization.

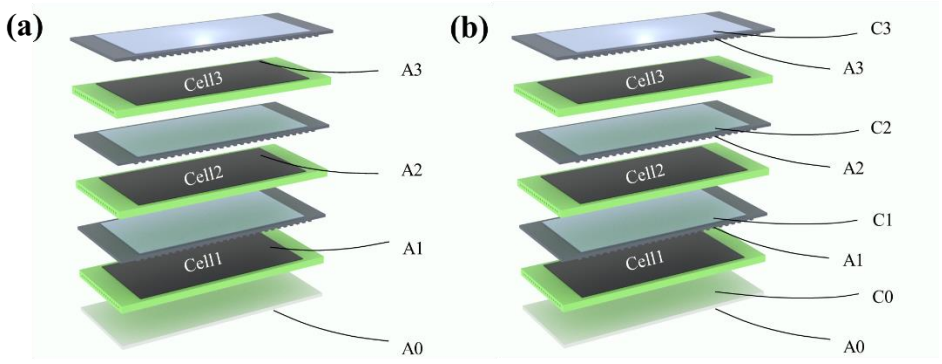

Figure 8.2. Schematic diagram of inserting voltage probes in Stack8.6 (a) and Stack8.7 (b)

Table 8.1. Experimental parameters and test results of each stack

	Electrolytic time (h)	**Degradation rate / kh**	**Electrolytic current**	**Max power (W)**	**Gas leakage**
Stack8.1	30	188%	-200 mA/cm^2	38.8	3.3%
Stack8.2	143	12%	-200 mA/cm^2	31	1.3%
Stack8.3	190	73%	-300 mA/cm^2	73.9	1.36%
Stack8.4	118	20%	-300 mA/cm^2	68.1	0.41%
Stack8.5	525	14.2%	-300 mA/cm^2	72.9	0.93%
Stack8.6	1008	2.3%	-250 mA/cm^2	85	-
Stack8.7	110	165%	-400 mA/cm^2	74.9	
Stack8.8	1265	18%	-500 mA/cm^2	75.2	

Figure 8.3 shows the instantaneous charging and discharging performance curves of the stack before and after long-term operation. It was found that the OCV of Stacks8.1, 8.4, 8.7, and 8.8 did not show significant changes after long-term operation, indicating good sealing performance during the long-term high-temperature CO_2 electrolysis testing. Additionally, comparing the voltage degradation under SOFC mode and SOEC mode, it was found that the degradation of charging performance was larger than that of the discharge performance. The instantaneous voltage decay rates of Stack8.5, Stack8.7, and Stack8.8 under long-term operating current were calculated, reaching to 15.1%/kh @-300 mA/cm^2, 194.3%/kh @-400 mA/cm^2, and 14.1%/kh @-500 mA/cm^2, respectively, while the long-term degradation rates were 14.2%%/kh @-300 mA/cm^2, 165%/kh @-400 mA/cm^2, and 18%/kh @-500 mA/cm^2, respectively. Comparing the voltage

degradation rate of instantaneous performance and stability performance, the two degradation rates were close, indicating that the stack performance decayed at a steady rate.

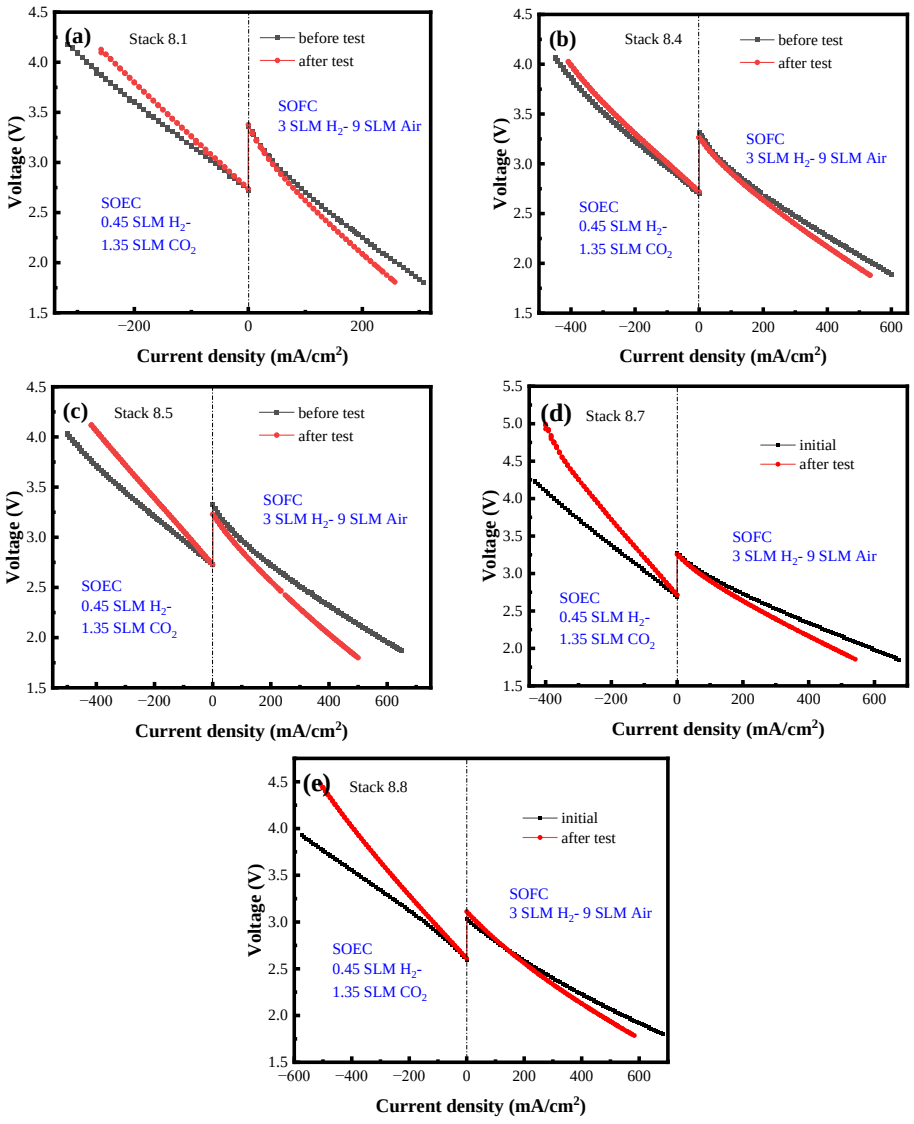

Figure 8.3. Instantaneous performances of stacks in SOFC and SOEC mode before and after test

8.2.2 Electrochemical impedance and DRT analysis

During the testing process of Stack8.6 and Stack8.7, the impedance changes of each unit in the stack were tested using nickel chromium wire

leads, and the results are shown in **Figure 8.4**. **Figure 8.4a-c** show the AC impedance change of Stack8.6 during the long-term CO_2 electrolysis, and **Figure 8.4e-f** represents the corresponding DRT. The results implied that the overall ohmic impedance of Unit 1 corresponding to Cell1 and interconnect1 increased at the first 208 h, then decreased until 727 h, and further increased again until manually stopped at 1008 h.

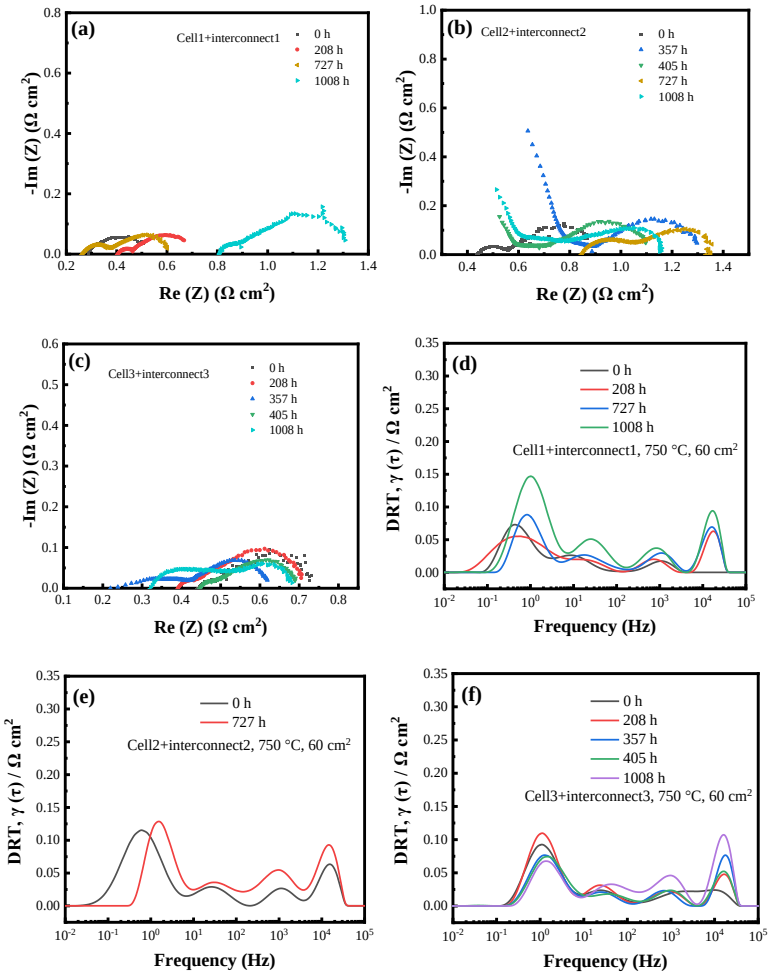

Figure 8.4. EIS curves and DRT curves of Stack8.6 during 1008 h CO_2 electrolysis test

As observed, polarization impedance increased with the electrolytic

time, and the decay rate accelerated after 727 h, especially the gas diffusion polarization impedance. Ohmic impedance of Unit 2 corresponding to Cell2 and interconnect2 reached its maximum value at 727 h, and then recovered slightly. The overall polarization impedance showed a slow decay trend during the test. Ohmic impedance of Unit 3 corresponding to Cell3 and interconnect3 decreased after 405 h, and the increase in polarization impedance was mainly dominated by the ionic transport in the electrolyte (>10^4 Hz) [292].

However, it should be noted that due to the complex structure of the stacks, the degradation of each unit in the stacks depended on temperature, pressure, gas distribution, and the structure of the cells. Additionally, the impedance measured through the leads might be affected by factors such as position of lead wires, making it difficult to accurately determine the universal law of the stack performance degradation. In the future, more research is necessitated on 2 units, 3 units and 5 units short stacks to explore the main factors contributing to the attenuation of each part of the stacks.

8.2.3 Conversion rate and energy conversion efficiency

During the long-term operation of the stacks, the exhaust gas composition at the outlet of the fuel electrode was analyzed at time intervals. The energy conversion efficiency and CO production rate in the stacks were calculated based on **Eq. 3.19** and **Eq. 3.22**, as shown in **Table 8.2**. The

results revealed that the 3 units stack could stably generate 500-700 sccm of CO, with an energy efficiency of 58.6%-73.9% (not consider heating the air), which was lower than that in a single cell. This was attributed to three reasons. Firstly, some components in the stacks presented high internal resistance, easily consuming electrons. Secondly, the unstable contact between the cells and the interconnect interface inside the stacks hindered the electron conduction. Thirdly, a large amount of gas in the stacks prevented RWGS reaction, resulting in lower CO generation rate than the theoretical value.

Table 8.2. Analysis of fuel electrode exhaust gas composition, energy conversion efficiency, and CO production rate of each stack during CO_2 electrolysis testing

	Electrolytic current	**Electrolytic time**	**Stack voltage**	**Flow rate (ml/min)**	**CO%**	**ECE1 (%)**	**ECE2 (%)**	**CO production rate (ml/min)**
Stack 8.3	-300 mA/cm^2	150 h	3.733 V	1650	37.03%	89.1	69.0	611
Stack 8.4	-300 mA/cm^2	93 h	3.666 V	1624	39.66%	95.8	73.9	644
Stack 8.5	-300 mA/cm^2	35 h	3.581 V	1494	38.76%	81.7	63.7	579
		68 h	3.584 V	1484	39.22%	84.9	65.8	582
		130 h	3.619 V	1489	39.03%	81.3	63.6	581
		334 h	3.694 V	1484	38.18%	82.2	63.7	567
		447 h	3.711 V	1506	40.14%	89.6	69.2	605
Stack 8.6	-250 mA/cm^2	147 h	3.79 V	1486	35.31%	82.4	62.8	525
		373 h	3.794 V	1593	38.43%	102.2	76.7	612
		517 h	3.635 V	1660	32.8%	84.9	64.8	544
		817 h	3.7 V	1527	32.61%	76.6	58.6	498

Stack 8.8	-500 mA/cm^2	319 h	3.9 V	1488	48.77%	78.2	64.4	726

8.3 Analysis of degradation mechanisms of SOEC stacks

8.3.1 Seal analysis

Figure 8.5 shows the oxidation status on the air electrodes of 8 stacks after long-term testing. Stack8.6 and Stack8.7 did not require sealing at the air electrode outlet because of inserting voltage monitoring probes. Stack8.1-8.5 and Stack8.8 required adding a layer of white sealing slurry on the air electrode outlet.

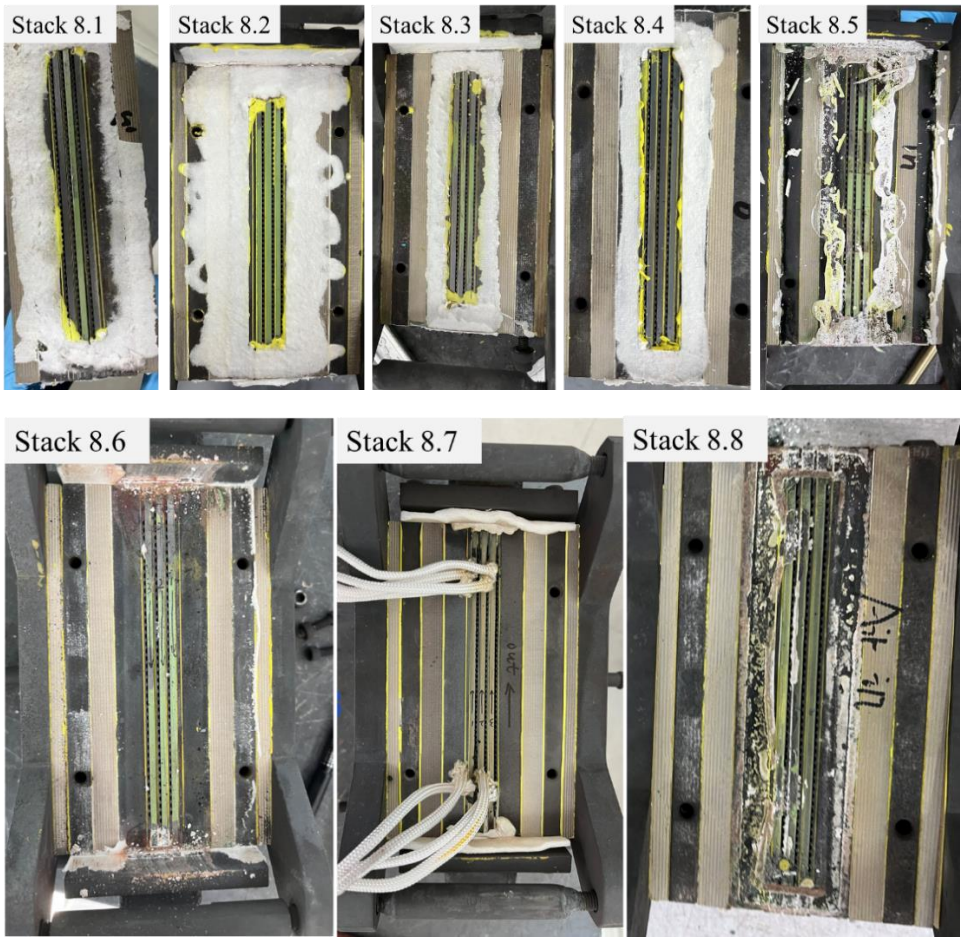

Figure 8.5. Oxidation of the air side of Stack8.1-Stack8.8 after cooling to

room temperature

According to the results on **Figure 8.5,** the side edges of Stack8.1, Stack8.4, Stack8.7, and Stack8.8 were gray, indicating that the air tightness of the four stacks remained good after long-term testing, without the occurrence of cell oxidation, which was consistent with the OCV in **Figure 8.3**. Although there existed partial oxidation on the air side in Stack8.6, the parts near the fuel electrode were still gray, indicating that the oxidation on the air side was caused by direct contact with air, instead of gas leakage. Therefore, the sealing of the fuel electrode of Stack8.6 was still acceptable.

8.3.2 Morphology analysis of cells

To analyze the degradation of the fuel electrodes of the cells in the stacks during long-term CO_2 electrolysis operation, the microstructure analysis of the fuel electrodes was conducted on three stacks with electrolytic time exceeding 500 h. The results are shown in **Figure 8.6**, **Figure 8.7**, and **Figure 8.8**. **Figure 8.6** shows SEM photos of Stack8.5 after electrolysis of CO_2 at a current density of -300 mA/cm^2 for 525 h. **Figure 8.6a** shows the cross-section of Cell1, illustrating that the microstructure of the cell was not affected by long-term high-temperature operation. The fuel electrode was magnified to 7k and 12k for observation, and nickel particles in the fuel electrode seemed to display a migration trend, which was mainly

presented as the gradual decrease of small nickel particles at the interface of electrolyte and fuel electrode. The small nickel particles moved towards the areas far from the electrolyte and adhered to larger nickel particles. The migration of nickel was mainly attributed to the formation and decomposition of nickel hydroxide. Since the evaporating temperature of nickel hydroxide was lower than the working temperature of the stacks, it might evaporate and move to the surface of the active fuel electrode, and be condensed into nickel again by H_2. Additionally, as the operation time increased, the migration of nickel from the interface became significant, and this effect has been confirmed by many studies [293-298].

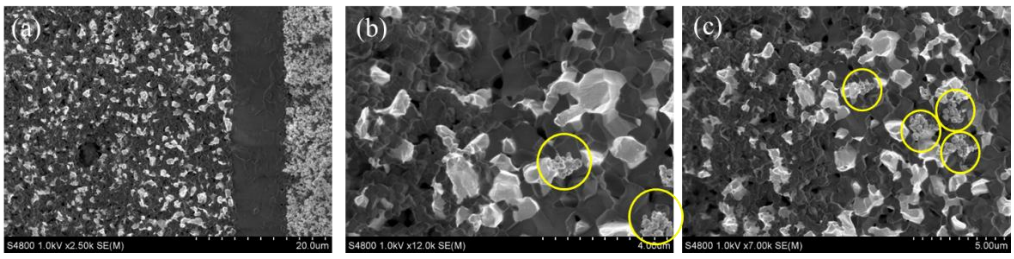

Figure 8.6. Cell morphology analysis of Stack8.5 after long-term CO_2 electrolysis testing (a) Overall morphology; (b) and (c) Fuel electrode

Figure 8.7 shows the microstructure of each cell in Stack8.6 after thousands of hours of CO_2 electrolysis. Horizontal cracks inside the electrolyte were observed near the barrier layer of several cells in Stack8.6 (see **Figure 8.7b** and **c**), which seemed to preferentially follow the grain boundary. Besides, the electrolyte in Cell3 exhibited fracture along grain boundaries and honeycomb-like small particles (**Figure 8.7c-f**). This might

be caused by the mutual diffusion of substances with different diffusion rates, called Kirkendall voids. The generation of Kirkendall voids affected ohmic impedance. The formation of Kirkendall voids was attributed to the diffusion of YSZ and GDC, usually reported in long-term operation of SOECs, but not common in SOFCs. When operating in SOFCs, the difference of oxygen potential between the anode and cathode was not particularly significant, and the driving force was lower, which was not conducive to the appearance of voids. In SOEC mode, higher temperatures and greater driving force jointly promoted the formation of voids. It should be noted that the decrease in ohmic impedance of the third unit in **Figure 8.4c** was not observed in the SEM image. Hence, it was speculated that the decrease of ohmic impedance was because of the increased contact between Cell3 and the air electrode interconnect [299-301].

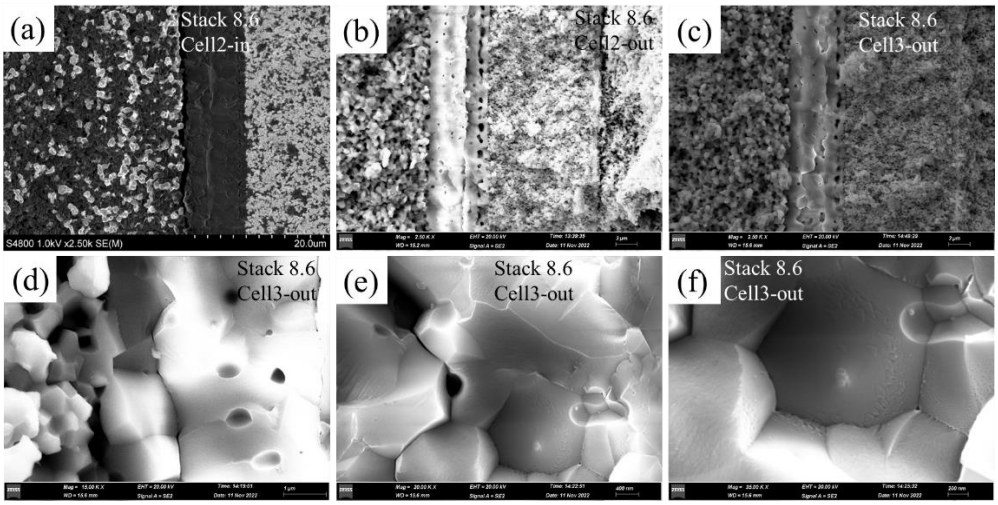

Figure 8.7. Analysis of cell morphology in Stack8.6 after long-term CO_2 electrolysis testing

Similarly, the microstructure characterization of Stack8.8 was performed after 1265 h CO_2 electrolysis at a current density of -500 mA/cm^2, as shown in **Figure 8.8**. Like the results of Stack8.6, electrolyte fracture was observed in the SEM photos of the cross-sections of the tested cells. According to research by Knibbe et al. [302], such fracture is mainly due to the increase in potential in the YSZ electrolyte under high current density in the SOEC mode, which causes oxygen to accumulate at the YSZ grain boundaries near the air electrode. Laguna-Bercero et al. [183] also reported the analysis results of oxygen atom content in various parts of the YSZ electrolyte, and underlined that the oxygen content along the YSZ electrolyte showed almost linear changes, reaching its maximum value near the air electrode. This also confirms the theory of oxygen accumulation at the boundary of electrolyte and air electrode. **Figure 8.8** also shows the microstructure of the cell cross-section and the thickness of each functional layer in Stack8.8. The thickness of the electrolyte ranged from 2-4 μm, and the thickness of the fuel electrode and air electrode was between 6-7 μm. The thickness of the entire functional layer was not more than 18 μm. Compared to the flat-tube cells used in Stack8.6, the cells in Stack8.8 were reduced by about two-thirds. From the perspective of long-term operational stability, thinner cells demonstrate certain research and application value since they not inferior to thick cells in terms of both electrolytic capacity and stability[302, 303].

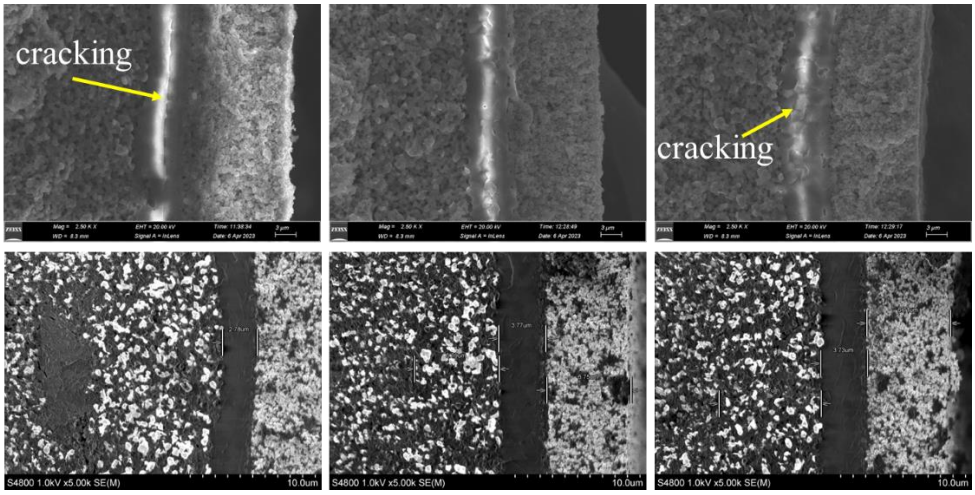

Figure 8.8. Analysis of cell morphology on Stack8.8 after long-term CO_2 electrolysis testing

8.3.3 Analysis of carbon accumulation in fuel electrode

Raman spectroscopy analysis was conducted on the gas flow channels of the cells in Stack8.6 and Stack8.8, which had been running for over a thousand hours. The results showed that after thousand hours testing, there was slight carbon deposition in Cell3 in Stack8.6 (**Figure 8.9**), corresponding to an increase in fuel electrode polarization impedance in **Figure 8.4c**. Analysis along the gas flow direction of Cell3 revealed carbon deposition near both inlet and outlet (**Figure 8.9b**). The D and G bands of carbon in the inlet and outlet areas of the electrolysis cell displayed different degrees of offset, and the R value (I_D/I_G) at the outlet was higher, indicating a higher density of carbon defects at the outlet. However, no carbon deposition was found in Stack8.8 (**Figure 8.10**). There was no sufficient evidence to suggest that CO_2 electrolysis by the stacks in an H_2-CO_2

atmosphere could easily trigger CO disproportionation reaction. Carbon deposition in Stack8.6 was speculated to be caused during cooling temperature process and shutdown.

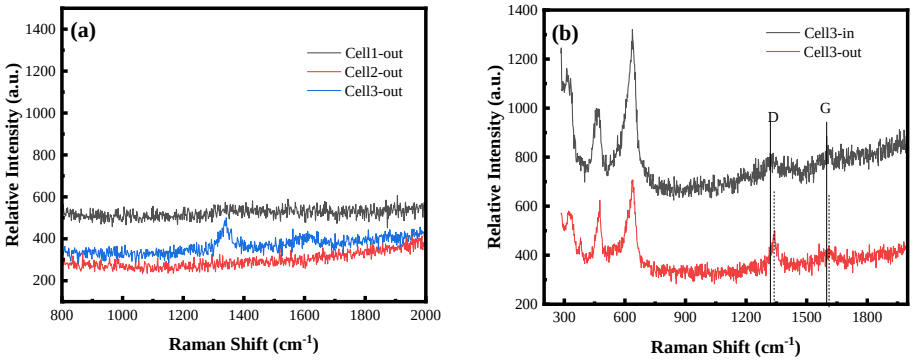

Figure 8.9. Analysis of carbon deposition in fuel electrode channels in Stack8.6 after long-term CO_2 electrolysis testing

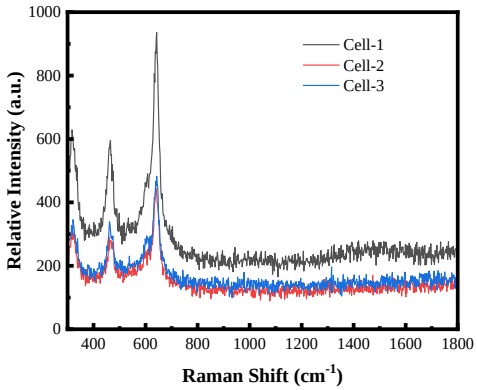

Figure 8.10. Analysis of carbon deposition in fuel electrode channels in Stack8.8 after long-term CO_2 electrolysis testing

8.3.4 Morphology and EDS analysis of air electrode

According to the results of **Chapter 5**, when air was not used in the air electrode during long-term CO_2 electrolysis testing, due to the lack of gas

blowing, the generated oxygen was prone to accumulate and form high oxygen pressure between the electrolyte and the air electrode, thereby driving strontium segregation. When a certain amount of strontium was enriched at the interface between YSZ and LSCF-GDC air electrode, insulating phases such as SrO might be generated, hindering the oxygen exchange reaction in the LSCF-GDC electrode. However, strontium segregation is influenced by various factors, such as polarization current, oxygen partial pressure, fuel type. Therefore, energy spectrum analysis was conducted on three stacks with operating time exceeding 500 h, and the results are shown in **Figure 8.11**. No significant element segregation was observed at the interface between LSCF-GDC air electrode and YSZ electrolyte in Stack8.5, Stack8.6, and Stack8.8. This revealed that in the external pressurized structure of the stack, even if the air electrode was not supplied with air, strontium enrichment phase did not occur at the electrolyte/air electrode interface, which was different from the previous conclusions of single cells. Based on comprehensive analysis, the following reasons were summed up: (i) The dense GDC barrier layer alleviated the formation of $SrZrO_4$ in the boundary of air electrode and electrolyte; (ii) LSCF exhibited high oxygen ion conductivity. Under anodic polarization, the concentration of positively charged oxygen vacancies on the electrode surface decreased, which overcame elastic interactions and led to a decrease in the driving force of Sr segregation, thereby suppressing Sr segregation. (iii)

The interconnect in the stack structure was not coated with a protective coating. When LSC and LSCF electrodes were exposed to the CrO_3 environment, Cr preferentially deposited on the outermost electrode surface, resulting in the formation of a dense $SrCrO_4$ layer [304, 305].

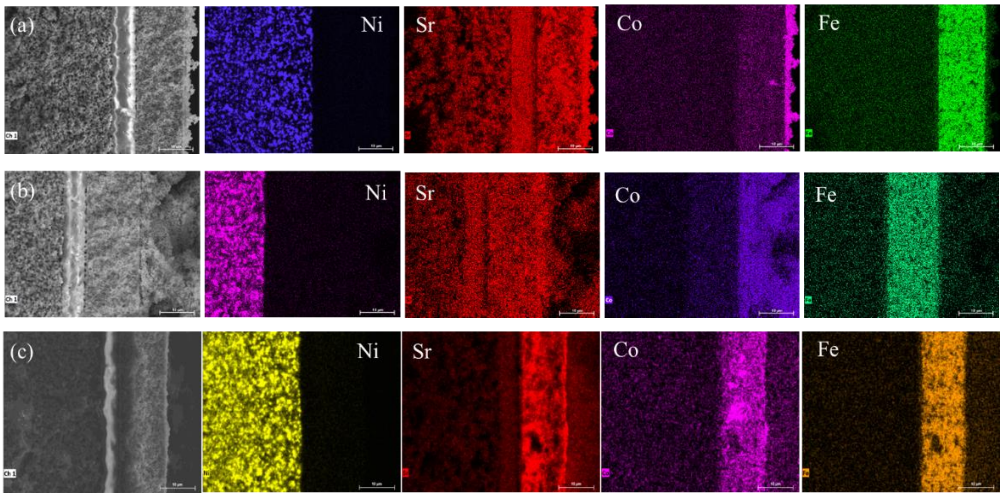

Figure 8.11. EDS analysis of cell cross-sections after long-term CO_2 electrolysis operation: (a) Stack8.5; (b) Stack8.6; (c) Stack8.8

8.3.5 Analysis of the air electrode current collection layer

Compared to single cells, interconnects and other components were also required in the stacks. The interconnects material used in this research was SUS441, which is a Cr-contained stainless steel with excellent high-temperature corrosion resistance. When Cr containing stainless steel was in direct contact with the LSC current collection layer, the Cr containing steam evaporated from the interconnects and reacted quickly with the Sr species segregated to the electrode surface to generate $SrCrO_4$ species. $SrCrO_4$

demonstrated a lower conductivity and higher coefficient of thermal expansion, thus limiting oxygen surface exchange reactions and promoting air electrode layering. To verify morphology evolution on the surface of the LSCF-GDC air electrode and LSC current collection layer during long-term CO_2 electrolysis testing on the stacks, the surface compounds of the air electrode and current collection layer were identified through Raman spectroscopy, as shown in **Figure 8.12-14**.

Figure 8.12a shows the Raman spectrum of the air electrode of Stack8.5 after 525 h of CO_2 electrolysis testing. Since the LSC current collection layer was brushed on the air electrode, even though most of the current collection layer had peeled off during the disassembly process of the stack, there were still some residues on the samples. Weak characteristic peaks of Cr_2O_3 and $SrCrO_4$ were detected in the air electrode samples of three cells, proving that the LSC current collection layer was poisoned by Cr. Usually, the formation of $SrCrO_4$ is generated by the reaction of SrO on the electrode surface with Cr vapor, as shown in **Eq.8.1**. The segregation of SrO is related to water content, current density, working temperature, and surface compressive stress, and is the result of a comprehensive effect of various factors [306, 307].

$$SrO(s) + CrO_3(g) \rightarrow SrCrO_4(s) \qquad \text{(Eq.8.1)}$$

Figure 8.12b introduces the Raman spectrum of the air electrode of Stack8.6 after running for 1008 h. The current collection layer of Cell1 in

Stack8.6 displayed a high peak between 691-702 cm^{-1}, which was assigned to Co_3O_4 or $LaCoO_3$ (**Figure 8.12b**). When the laser power was increased, a signal of Cr_2O_3 appeared, which further indicated that the LSC current collection layer had been poisoned by Cr during long-term operation. The air electrode of Cell1 exhibited obvious characteristic peaks of Cr_2O_3 and $SrCrO_4$ (**Figure 8.12c**), with strong signal strength and symbolic $SrCrO_4$ doublet peak, indicating the impact of Cr precipitation on cell performance and air electrode structure. This was also confirmed by the increase in air electrode polarization impedance in the DRT diagram in **Figure 8.4d**.

The analysis results of Stack8.7 manifested that when the stainless-steel interconnect was not coated due to technical reasons, even only running for a hundred hours, there was still a toxic effect of Cr element on the LSC current collection layer. After long-term testing, the Raman signals of Co_3O_4 and $LaCoO_3$ appeared, indicating that Co existed in various valence states in the perovskite structure after long-term testing, which might also be involved in the structural changes of LSC. This analysis seemed to confirm the inevitability of Cr poisoning at high temperatures, high oxygen partial pressures, and anodic polarization. Since strontium oxide and other substances were easily dissociated from LSCF under non-polarized conditions, which led to Cr deposition on the surface of the electrode material, the use of coatings seemed to be a good solution to isolate the structural damage of Cr to the LSCF or LSC air electrode [306, 308-311].

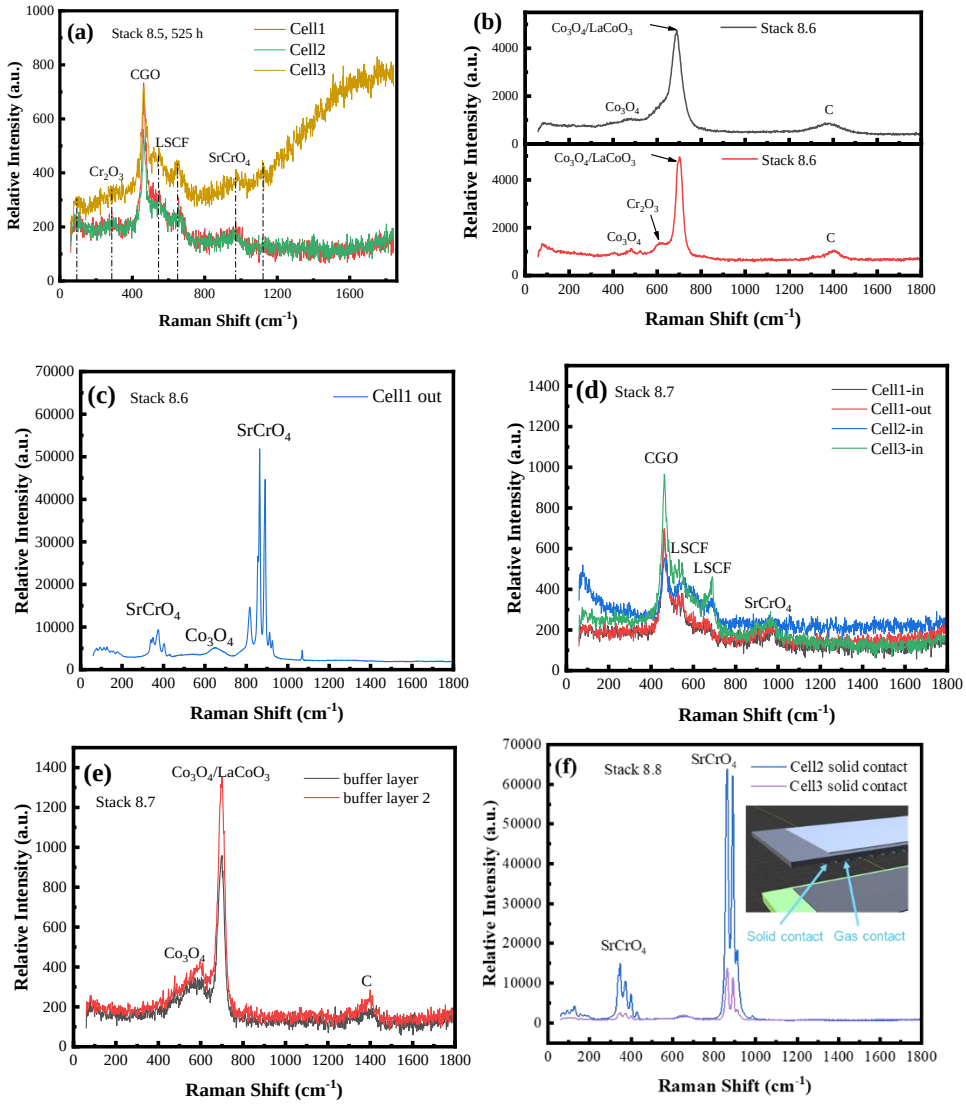

Figure 8.12. Raman spectrum of the air electrode of the cells after long-term operation of CO_2 electrolysis: (a) Stack8.5; (b)(c) Stack8.6; (d)(e) Stack8.7; (f) Stack8.8

Through literature review, it is found that the poisoning effect of Cr element is mainly carried out through gas deposition and surface diffusion. To verify the poisoning mechanism of Cr, Stack8.8 with the longest testing time, was analyzed. The solid phase contact point and the gas phase contact point in **Figure 8.12f** were characterized. The results showed that there was

$SrCrO_4$ signal at the solid phase contact points on the contact surface between the current collection layer and the interconnect. This further validated that the oxygen partial pressure dominated by reaction current preferentially occurred on the electrode surface [312-314].

When disassembling the tested stack, the LSC air electrode current collection layer might fall off, and the microstructure analysis of the current collection layer, as the part directly contacting with the interconnect, became crucial. During the disassembly of Stack8.8, the sheet-like current collection layer samples were collected and Raman spectroscopy analysis was performed on the surface in direct contact with the interconnect. Under the Raman objective, five randomly selected points were recorded, and the corresponding Raman spectra were measured, named 1-5. It was found that the structure of 1-5 points of was different from that of the reference air electrode, as shown in **Figure 8.13**. According to the Raman spectrum, obvious $SrCrO_4$ phases were measured at positions 1, 2, 3, and 5, while weak Ag_2CrO_4 signals (about 810 cm^{-1}) were also observed at position 4. These findings indicated that Cr containing species infiltrated the surface of the current collection layer, and then reacted chemically with the Ag-LSC current collection layer and the Sr containing species on the surface [315, 316].

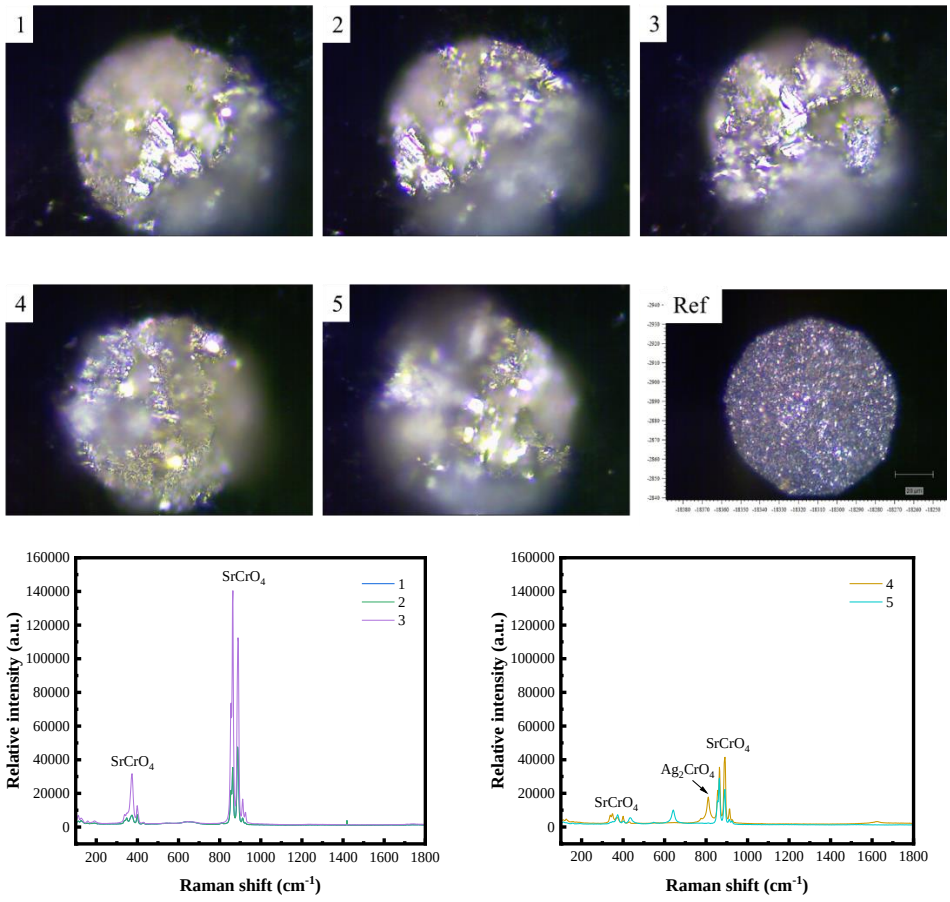

Figure 8.13. Raman photos and spectra of LSC current collection layer sample of Stack8.8

To verify the region where Cr poisoning occurred, Raman analysis was performed on the cross-sections of Stack8.8 after 1265 h CO_2 electrolysis testing at -500 mA/cm^2. Firstly, the edge of current collection layer of the sample was located under the objective lens, and moved towards the middle of the sample. Subsequently, the Raman spectrum was tested at an interval of 5 μm. The results implied that the thickness of the $SrCrO_4$ layer generated on the surface of LSC current collection layer was about 10 μm, and the area that 20-150 μm away from the surface contained Ag_2CrO_4 components. This

indicated that after long-term electrolysis with high current, most areas in the current collection layer were poisoned by Cr which was then preferentially deposited on the surface of the electrode, contributing to the formation of a dense $SrCrO_4$ layer. Therefore, the chromium containing species on the surface were $SrCrO_4$ and the internal ones were Ag_2CrO_4 [305].

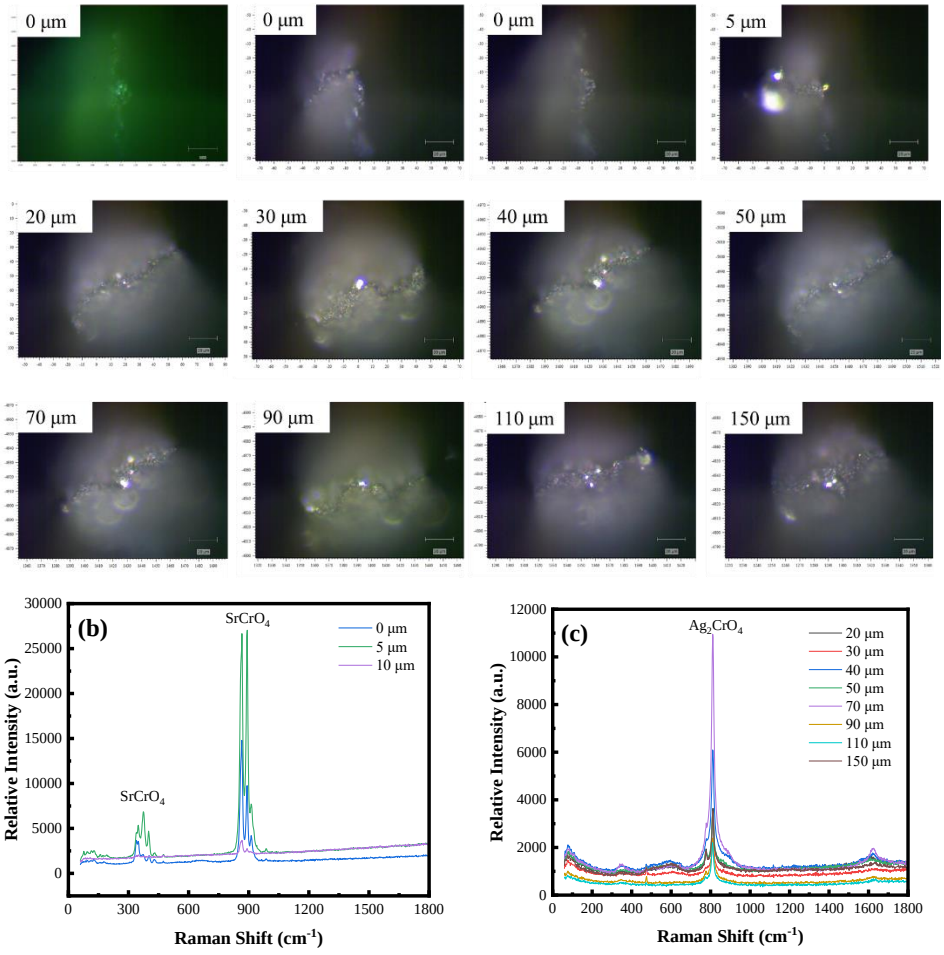

Figure 8.14. Raman spectroscopy characterization of the cross-sections of the cells (including the current collection layer) in Stack8.8, from the surface to the interior of current collection layer

8.3.6 Analysis of the contact surface of the air electrode interconnect

Figure 8.15 and **Table 8.3** show the SEM and EDS analysis of the fuel electrode interconnect (without ribs) and three air electrode interconnects (with ribs) in Stack8.7 after 110 h of constant current CO_2 electrolysis testing at -400 mA/cm^2. Cr was not detected on the contact surface between the fuel electrode interconnect and Cell1, while Cr was found on the ribs where air electrode interconnects contacted with the air electrodes of the cells, with the proportion of Cr accounting for 9.58%, 9.17%, and 5.33%, respectively.

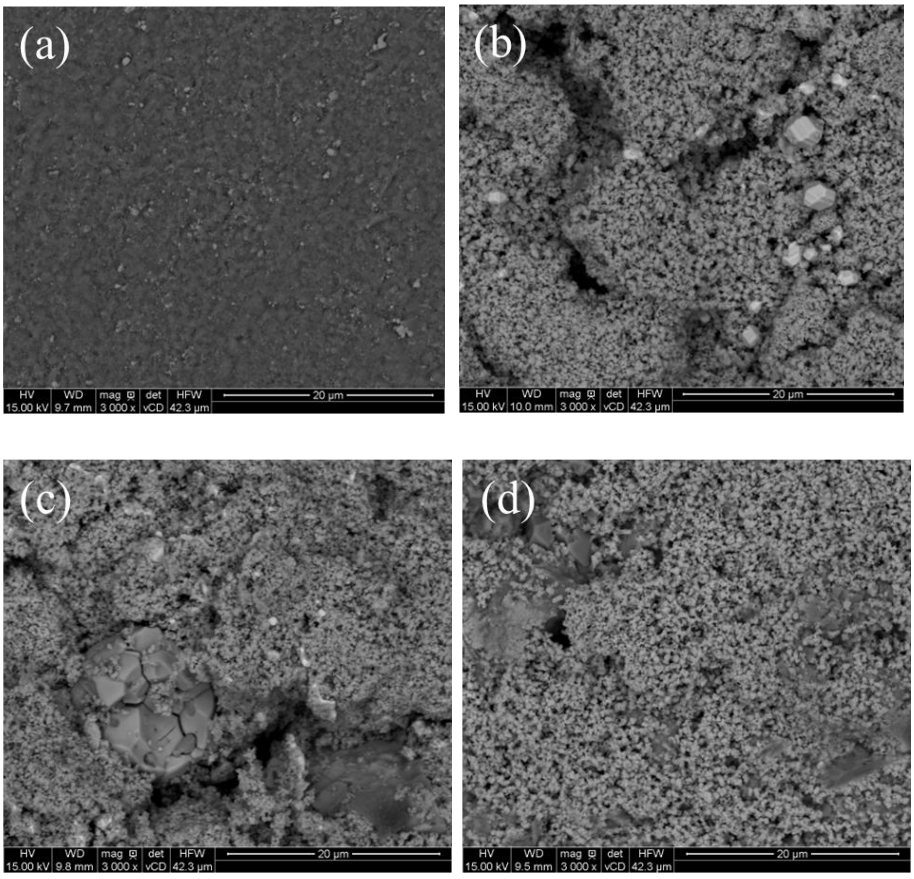

Figure 8.15. SEM images of interconnect of Stack8.7: (a) Fuel electrode side of interconnect1; (b) Air electrode side of interconnect2; (c) Air electrode side of interconnect3; (d) air electrode side of interconnect4

Clear crystalline substances were found in SEM images, indicating that under high current conditions, polarization accelerated the precipitation of Cr in the interconnect, resulting in the formation of $SrCrO_4$ and Cr_3O_4 on the surface of the interconnects or the current collection layer of the cells. However, due to the short electrolytic time (only 110 h), no Cr poisoning phenomenon was observed on the air electrode or current collection layer of Cell2 in Stack8.7 (blue spectrum in **Figure 8.12d**) [313].

Table 8.3. Analysis of element content on the fuel electrode interconnect and air electrode interconnects after test of Stack8.7

Element	Fuel electrode interconnect1	Air electrode interconnect2	Air electrode interconnect3	Air electrode interconnect4
O	60.22	30.53	28.97	25.20
Al	0.24	0.28	0.66	0.25
P	0.00	0.00	0.00	0.00
Ti	3.09	0.00	0.00	0.00
Cr	-	9.58	9.17	5.33
Mn	31.89	1.10	0.00	20.09
Fe	-	0.00	0.00	2.09
Co	0.00	58.53	61.20	47.04
Ni	4.56	0.00	0.00	0.00
Total	100	100	100	100

8.3.7 Mechanical strength analysis after cell testing

Table 8.4 and **Figure 8.16** show the mechanical strength of each cell in Stack8.5 and Stack8.7 after 525 h and 110 h of constant current CO_2

electrolysis testing. It was found that the strength of the cells after electrolytic operation significantly decreased compared to the untested reference cell, with a decrease of about 30 N, indicating that the electrolytic operation caused a damage to the mechanical structure of the cell. The table below also summarizes the mechanical strength of the cell before reduction. Compared to the reference cell, the reduction operation and one thermal cycle operation caused a decrease of about 37 N in cell strength, and the damage intensity was higher than that of the electrolytic operation.

Table 8.4. Mechanical properties analysis of Stack8.5 and Stack8.7 after long-term CO_2 electrolysis testing, sample size approximately 45 mm × 4 mm × 3 mm

Number		Electrolytic time	deformation	Load	Strength
			%	N	MPa
Stack8.7	Cell1	110 h	0.287109	60.97034	136.9991
Stack8.7	Cell2	110 h	0.258397	50.13958	115.707
Stack8.7	Cell3	110 h	0.276324	51.89607	119.35
Stack8.5	Cell1	525 h	0.246509	56.76104	120.6379
Stack8.5	Cell2	525 h	0.271004	49.88603	107.13
Stack8.5	Cell3	525 h	0.287957	57.98215	122.0009
After reduction		0	0.283773	86.93829	137.5417
Before reduction		0	0.22375	124.353	225.2807

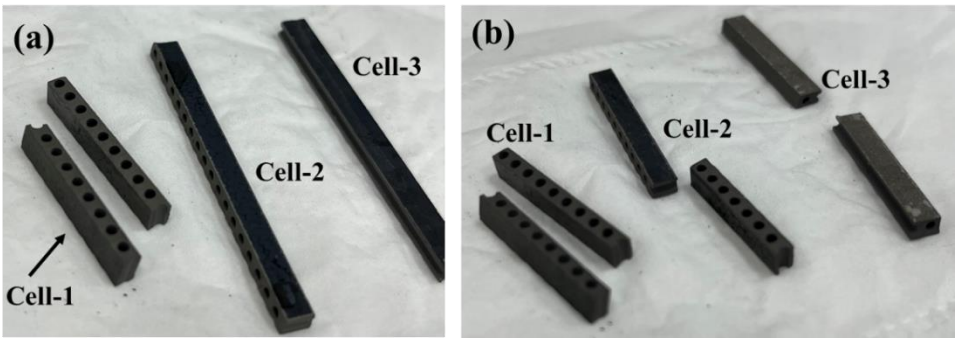

Figure 8.16. Photos of cell samples used for mechanical strength analysis: (a) Before fracture; (b) After fracture

8.4 Summary

This chapter mainly investigated the long-term stability of SOEC stacks in a 25 vol.% H_2-75 vol.% CO_2 fuel environment, and analyzed the durability, degradation mechanism, and electrolytic energy conversion efficiency of CO_2 electrolysis in stacks when the air electrode was not suppled with any gas. The purpose was to provide technical support for the optimization of stack component materials, structures, and sealing processes in the future. The main conclusions are as follows:

(1) A breakthrough was achieved in the long-term stability of stacks in a 25 vol.% H_2-75 vol.% CO_2 fuel environment. Stack8.5 operated stably for 525 h with a voltage degradation rate of 14%/kh at -300 mA/cm^2, Stack8.6 operated stably for 1008 h with a voltage degradation rate of 2.3%/kh at -250 mA/cm^2, and Stack8.8 operated stably for 1265 h with a decay rate of 18%/kh at -500 mA/cm^2. If external factors were not considered, the durability of flat-tube SOEC stacks might exceed 5000 h.

(2) A three-unit stack generated 500-700 sccm of CO from electrolysis, with an energy conversion efficiency of 58.6% -73.9%. Three possible reasons were analyzed for low energy efficiency. Firstly, some components in the stack demonstrated high internal resistance after high-temperature oxidation, easily consuming electrons. Secondly, the interface between the cells and the interconnects in the stack maintained poor contact and higher interface resistance, affecting electron conduction. Thirdly, a large amount of gas in the stack led to the suppression of RWGS reaction, resulting in the CO generation rate being lower than the theoretical equilibrium value.

(3) According to the analysis of the degradation mechanism of each stack after long-term CO_2 electrolysis testing, it was found that the fuel electrode of the cells in the stack showed a trend of nickel migration. Nickel at the electrolyte/fuel electrode interface gradually decreased, then moved towards the area far away from the electrolyte, and attached to large nickel particles. With the increase of Ni depletion, the electrochemical reaction expanded away from the interface of electrode and electrolyte. Currently, the mechanism of Ni migration is controversial, and more research and investigation on Ni migration inhibition are necessitated in the future to improve the overall durability of SOECs. Some parts of the electrolytes generated Kirkendall voids, which in turn increased the polarization impedance of the oxygen ion transport process.

(4) The chemical reaction between Cr element and the LSC current

collection layer of the air electrode generated $SrCrO_4$ phase, resulting in poor contact between the interconnects and the cells. $SrCrO_4$ was mainly formed by the reaction of Cr containing vapor with Sr species segregated to the surface, with a thickness of approximately 10 μm. However, the poisoning area of Cr element on the LSC current collection layer was far more than 10 μm. Raman results revealed that the area containing Ag_2CrO_4 components was about 150 μm, from surface to the interior of the current collection layer. The poor interface contact hindered electronic transmission and resulted in the performance degradation of the stack.

(5) According to the mechanical strength analysis of Stack8.5 and Stack8.7 after CO_2 electrolysis testing, it was found that the strength of the cell after long-term CO_2 electrolysis operation decreased by about 30 N compared to the reference cell, indicating that CO_2 electrolysis operation impacted the mechanical structure of the cell. The reduction operation and thermal cycle operation gave rise to a decrease in the cell strength of about 37 N, and the damage intensity to the cell was higher than that of high-temperature CO_2 electrolysis operation.

Chapter 9. Stability and degradation of interface contact in SOEC stacks under intermittent renewable energy

9.1 Introduction

Energy storage is crucial to the penetration and integration of intermittent renewable energy. Pumped energy storage and compressed air energy storage are currently the most large-scale physical energy storage methods, but they are largely limited by geographical location [317]. With the "double carbon" goal and the "energy storage" policy proposed, electrochemical energy storage has attracted extensive attention. However, H_2 with high energy density is usually used as the energy storage medium, and mainly produced by water electrolysis [318-320]. Recently, CO_2 has also been proved to be an energy carrier [321]. For example, in 2017, Qiao et al. [322] proposed a rechargeable Li-CO_2 battery based on ruthenium-based cathode for carbon fixation, which successfully fixed CO_2 into Li_2CO_3/Li_2O and carbon, providing strong theoretical support for the design of renewable energy storage equipment; In 2021, Duranti et al. [323] developed a new type of perovskite composed of $La_{1.2}Sr_{0.8}Fe_{0.6}Mn_{0.4}O_4$ (LSFMn) and Ni-$Ce_{0.85}Sm_{0.15}O_{2-\delta}$ (NiSDC). The composite material (LSFMn+NiSDC) composed of fluorite was used as the multifunctional fuel electrode of RSOC, achieving the maximum power of 527 mW/cm^2 in 90 vol.% CO-10 vol.%

CO_2 fuel electrode atmosphere. Chemical energy carriers and storage mechanisms play a decisive role in the development of future energy systems. Common energy storage technologies include compressed gas energy storage [324], liquefied gas energy storage [325] and electrolytic energy storage [326], which are widely reported methods for CO_2 storage. Among different storage concepts and technologies, high-temperature solid oxide electrolysis cells are extremely attractive and considered as the most cost-effective long-term power storage option [327].

Due to high temperature operation, both components and materials in the electrolytic stack may be damaged and corroded, resulting in the decrease of electrolytic efficiency. Consequently, the life extension and performance optimization of cells and stack components are important [328]. Because of the complexity of the structure of SOEC stacks, Ni migration of the fuel electrode and delamination of the air electrode may become the main microstructure degradation action caused by large-current electrolysis. Furthermore, Cr poisoning from the interconnects and Si poisoning from the sealing materials also seriously affect the activity of the oxygen exchange reaction in the air electrode [329-331]. Fortunately, after long-term operation, most Cr species is trapped in the non-active surface near the end of air electrode region, and only a few can enter the functional layer, which has been confirmed in the study of Schuler et al. [332]. The Cr-containing substances evaporated from the chrome oxide scale are closely related to the

oxygen partial pressure and water vapor partial pressure in the air flow. Due to the occurrence of gas leakage, Cr poisoning has been widely reported in the fuel cell mode and water electrolysis conditions [333-335]. In large-scale or long-term energy storage operation, considering the stability and service life of the stacks, it is necessary to add a coating on the surface of the interconnects or a barrier layer (collecting layer) at the interface between the cells and the interconnects to eliminate the toxic effect of chromium on the functional layer [336, 337].

In **Chapter 6**, the intermittent renewable energy was used to explore durability on flat-tube SOECs, and verify the stability of SOECs under non-steady power. However, research on the combination of flat-tube structured stack and renewable energy is deficient. To fill this gap, this research carried out the test of CO_2 electrolysis on flat-tube SOEC stacks with intermittent renewable energy. The cycle period and electrolytic current were determined according to the actual working conditions of solar energy in winter. To prolong the life of SOEC stacks, the manganese-cobalt coating was performed on the interconnects, and a current collection layer was added at the interface between the functional layer and the interconnect to prevent the side reaction. Considering the uncertainty caused by intermittent energy supply, in-situ monitoring under dynamic load was necessitated. Each contact component of SOEC stacks was connected to a probe to monitor degradation in real time.

9.2 Long-term performance of flat-tube SOEC stacks

9.2.1 Experimental setup

To reproduce the power supply under solar energy in winter, the Gaussian model was adopted to design an unsteady cyclic pulse current for CO_2 electrolysis. The total duration time of each cycle was set at 9 hours, and each current at 1 hour. The current density increased from -50 mA/cm^2 to -250 mA/cm^2 and then gradually increased from -250 mA/cm^2 to -50 mA/cm^2 according to the I-t curve in **Figure 9.1**.

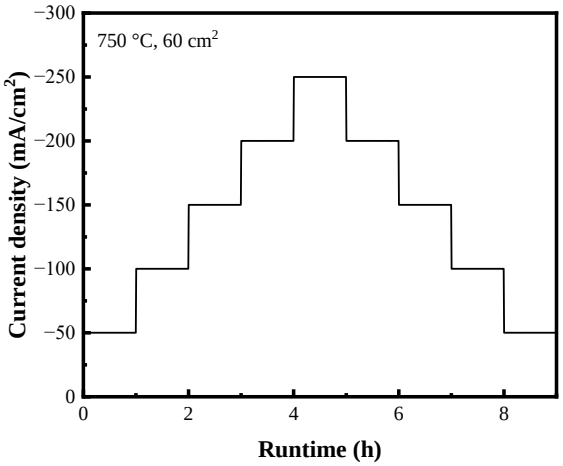

Figure 9.1. Current variation per cycle

The SOEC stack required for the pulsed current CO_2 electrolysis experiment consisted of two cells, three interconnects and two conductive plates. The cell structure and parameters are organized in **Table 9.1**. The interconnect1 in contact with the fuel electrode of the electrolytic stack had no gas flow channel, and interconnects1 and 2 in contact with the air

electrode of the two cells had an air flow channel. The three interconnects are made of SUS441 with manganese cobalt-based spinel coatings. The stack assembly structure and SOEC test system are shown in **Figure 9.2**.

During the assembly of SOEC stacks, silver mesh and nickel mesh were added to the contact surfaces of the air electrode and the fuel electrode of each cell to enhance the current collection effectiveness. The air electrode contact surface of the cell was brushed with LSC-Ag to improve the electrode performance. A voltage probe was inserted on the contact surface between the cell and the interconnect to monitor real-time impedance and voltage degradation of each cell in the stack. The inner main part of the stack was sealed with NO.7 glass sealing materials, and then placed in a high-temperature furnace for heat-pressing treatment to reinforce the sealing and current collection effect. The installed processes remained similar to that in **Chapter 3**.

Table 9.1. Parameters of SOEC

Composition	**Material**	**Thickness**
Supporting layer	NiO-3YSZ	2.8 mm
Cathode (Fuel electrode)	NiO-8YSZ	15 μm
Electrolyte	8YSZ	10 μm
Barrier layer	GDC	2 μm
Anode (Air electrode)	LSCF-GDC	15 μm
Current collection layer	LSC-Ag	>60 μm

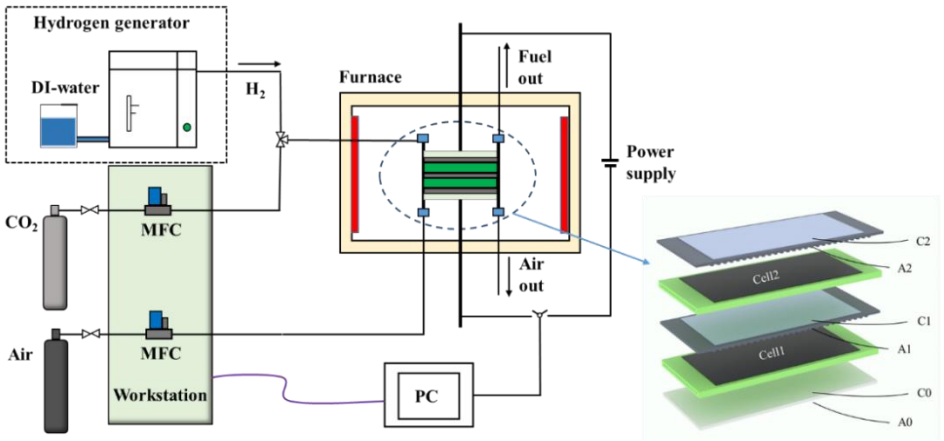

Figure 9.2. (a) Schematic diagram of SOEC stack test system

After raising up to the reaction temperature (750 °C), the voltage clamps, current clamps and five monomer voltage clamps were connected on the conductive columns and Ni-Cr wire probes. Afterwards, 1 SLM N_2 was introduced to test the air tightness and the fuel electrode was purged to exhaust the air in the system. The meanings of monomer voltage are summarized in **Table 9.2**. During the reduction operation, 0.4 SLM H_2 and 1.2 SLM air were introduced into the fuel electrode and the air electrode, respectively. During the test, H_2 was supplied by the hydrogen generator and then fed into the stack after passing through the drying tubes. The stack needed to be reduced for 3-4 h. After OCV became stable, the initial performance tests of the stack were conducted.

The initial performance test of the stack mainly included the instantaneous performance under the discharge modes, and the AC impedance under the OCV state. After the completion of the initial

performance test, the durability test of electrolytic stack shall be conducted according to the current shown in **Figure 9.4**.

During the test, the four-electrode method was used for the electrochemical impedance test, and further analysis was performed by DRT. The frequency sweep range and regularization factor were same as that in **Chapter 3**. During the durability test, the charge and discharge performances and AC impedance curves of the repeated units in the SOEC stack were measured at time intervals to analyze the performance changes of the SOEC stack. After the long-term test, the instantaneous charging and discharging performances and impedance were tested to compared with the initial results to analyze the degradation of the stack.

Table 9.2. Meaning of single voltage of SOEC stack

Unit number	Access unit	Meaning
CV1	C0A1	Cell1+LSC-Ag
CV2	C1A2	Cell2+ LSC-Ag
CV3	A0A1	Cell1+ LSC-Ag +interconnect1
CV4	C0C1	Cell1+ LSC-Ag + interconnect2
CV5	A1A2	Cell2+ LSC-Ag + interconnect2

After the durability test, the SOEC stack was cooled down to room temperature with a cooling rate of about 1 °C/min. For microscopic characterization, the electrolytic stack was disassembled layer by layer. For the two cells in the SOEC stack, the current collection layers were first

scraped with a clean knife for Raman spectrum analysis, with a wavelength of 532 nm. Subsequently, fresh, flat and pollution-free cross-section cell samples were prepared for SEM analysis (1 kV), EDS analysis (15 kV) and Raman spectrum analysis (532 nm).

9.2.2 Stability test

Figure 9.3 shows the I-V polarization curves of the stack on SOEC and SOFC modes under the initial state. In the discharge state, the OCV of the stack reached to 2.213 V, with an average of 1.1065 V of each cell, indicating good sealing performance of the stack. The initial peak power of the stack was about 58.4 W, corresponding to the power density of 490 mW/cm^2. **Figure 9.3b** shows that in the electrolytic state, the OCV of the stack was about 1.81 V, which was close to the theoretical value of 1.834 V. The voltage of the stack was 2.299 V under the electrolytic current of -250 mA/cm^2. At the thermal neutral voltage of CO_2 electrolysis (2.928 V of 2-unit stack), it could be predicted that the current density of this stack reached more than -600 mA/cm^2. However, as the stack might suffer from excessive polarization under large voltage, the current densities not exceeding -250 mA/cm^2 were selected for pulse electrolysis research in this paper.

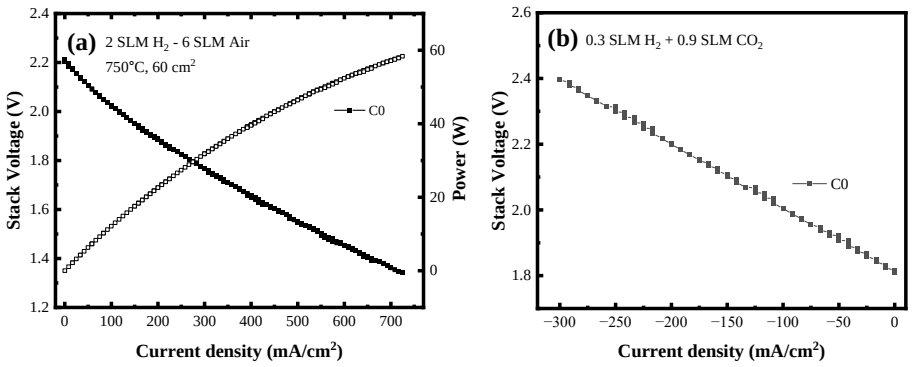

Figure 9.3. Initial performance of SOEC stack: (a) Discharge; (b) Charge

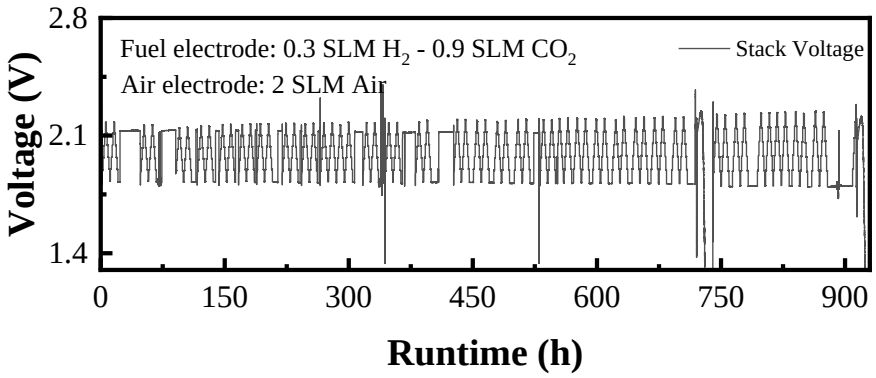

Figure 9.4. long-term V-t curve of SOEC stack

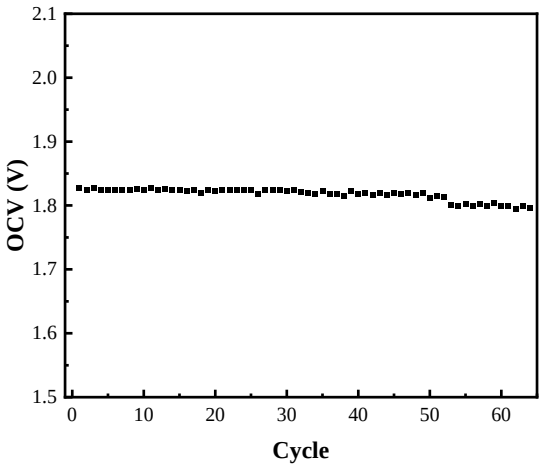

Figure 9.5. Variation of OCV during long-term operation

Figure 9.4 shows the long-term V-t curve of the SOEC stack under the

condition of pulse current cyclic electrolysis. During the CO_2 electrolysis test, 0.3 SLM H_2 and 0.9 SLM CO_2 were introduced into the fuel electrode, and 2 SLM air was introduced into the air electrode. The results manifested that the SOEC stack operated stably for 64 cycles, with an operation time of more than 900 h. Under the pulse current densities of -50 mA/cm^2, -100 mA/cm^2, -150 mA/cm^2, -200 mA/cm^2 and -250 mA/cm^2, the voltage degradation rates were -0.004%/cycle, 0.007%/cycle, 0.019%/cycle, 0.029%/cycle and 0.039%/cycle, respectively. The average degradation rate was about 0.018%/cycle, and if maintaining this degradation trend, the lifespan of the SOEC stack was expected to more than 1100 cycles. **Figure 9.5** reflects the OCV changes during 64 cycles. At cycles 1st, 52nd, 53rd, and 64th, the OCV values were 1.824 V, 1.813 V, 1.801 V, and 1.796 V, respectively, with degradation mainly concentrated on cycles 53-64th. The accelerated degradation of the stack during cycles 53rd to 64th might be related to thermal cycling after cycle 52nd. To minimize the impact on the analysis of degradation mechanism, the long-term experiment was manually terminated at cycle 65th. Thermal cycling further accelerated the degradation of the contact layer, which was because of the TECs mismatch between cell components and internal shear stress produced during thermal cycling.

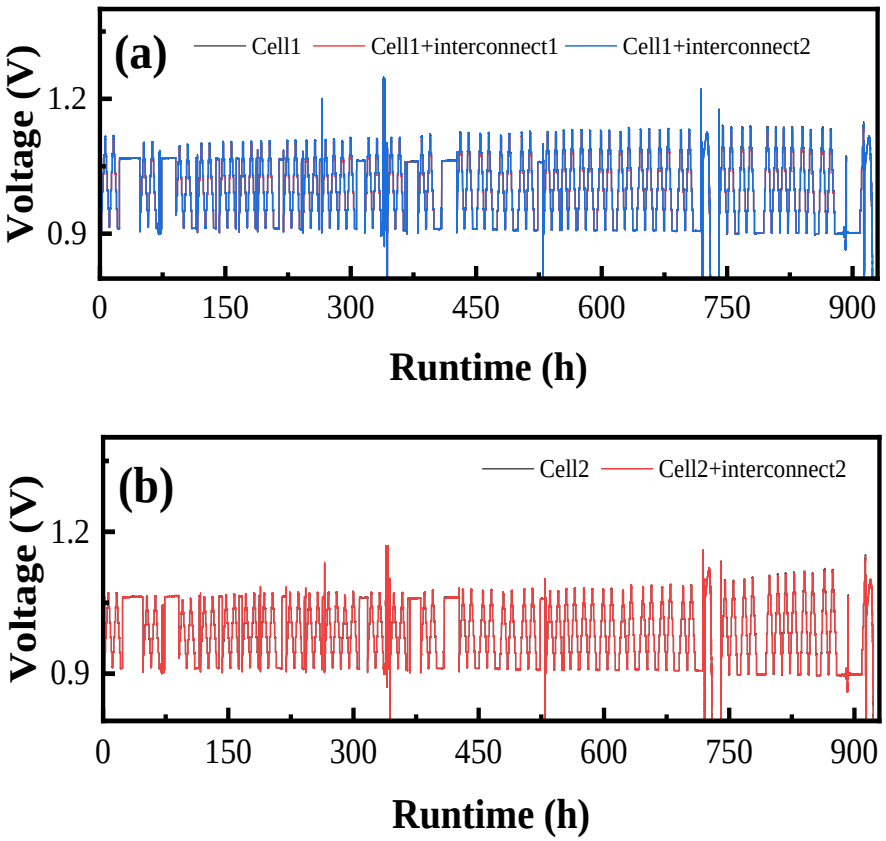

Figure 9.6. Long-term stability curves of CO_2 electrolysis of each repeating unit in the SOEC stack under pulsed current: (a) Unit related to Cell1; (b) Unit related to Cell2

Figure 9.6a and **Figure 9.6b** exhibit the voltage variation of Cell1 and Cell2 in the SOEC stack during the pulsed current electrolysis. The results demonstrated the largest degradation of Cell2 was about 0%~0.0715%/cycle, and the repeating unit of Cell1+interconnect2 indicated the smallest degradation was about -0.0098%~0.0084%/cycle.

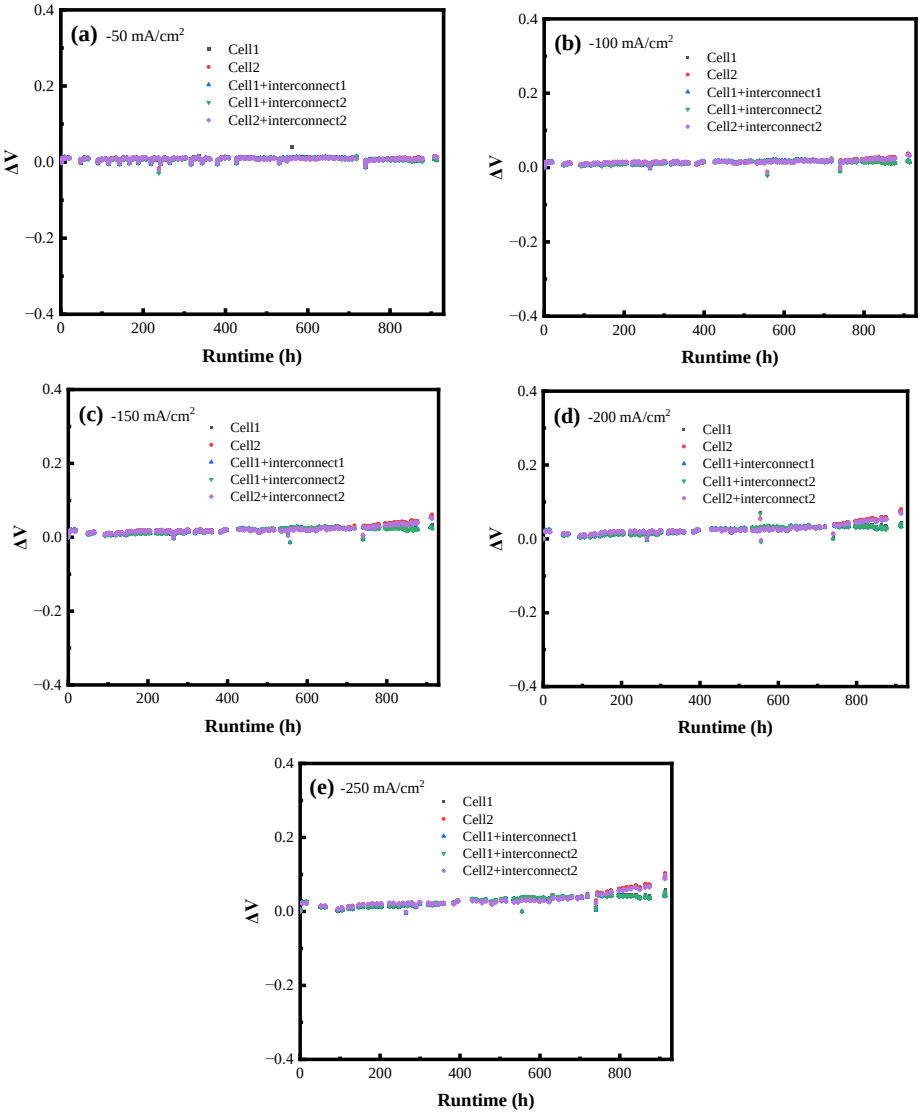

Figure 9.7. The difference between the real-time voltage and the initial value under different current densities during long-term testing: (a) -50 mA/cm^2; (b) -100 mA/cm^2; (c) -150 mA/cm^2; (d) -200 mA/cm^2; (e) -250 mA/cm^2

Moreover, the difference between the real-time voltage and the initial value under different current densities during long-term testing were calculated, as shown in **Figure 9.7**. The voltage difference (ΔV) gradually increased after 52nd cycles. Comparing the ΔV-t curves at five currents, it

was found that ΔV increased with the current, indicating that the larger the electrolytic current, the faster the degradation.

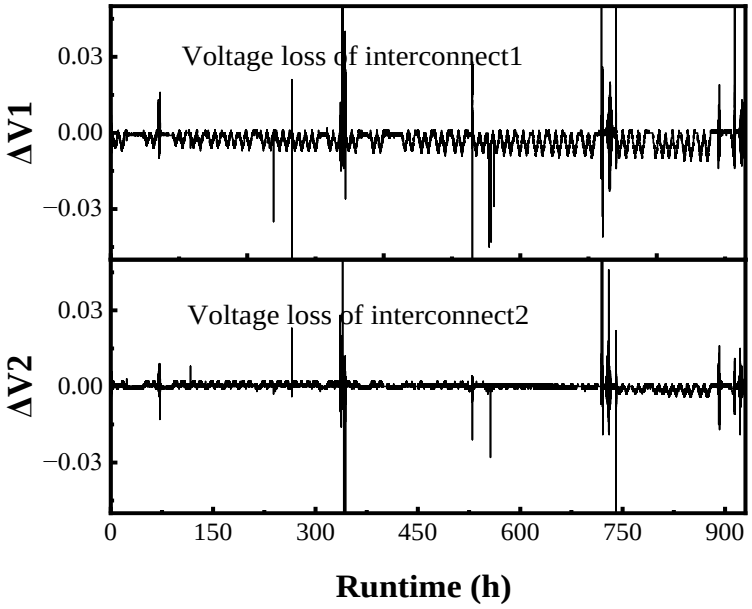

Figure 9.8. Polarization voltages of the interconnects

Table 9.3. Degradation rate (%/cycle) of stack components and the combined units under -50~250 mA/cm^2 (-3A~15A)

Current	Cell1	Cell2	Cell1+ interconnect1	Cell1+ interconnect2	Cell2+ interconnect2
-3 A	-0.0066	0	-0.0082	-0.0098	0
-6 A	0.0016	0.0208	0	-0.0015	0.016
-9 A	0.0106	0.0403	0.006	0.0045	0.0356
-12 A	0.0174	0.0571	0.0102	0.0116	0.0511
-15 A	0.0238	0.0715	0.0268	0.0084	0.0657

To explore the oxidation, corrosion and contact of the interconnect, the voltage consumed by each interconnect was calculated, as shown in **Figure**

9.8. The results revealed that the voltage loss of each interconnect was close to 0 V, indicating that the interconnects had no effect on the stack degradation. Therefore, the degradation was mainly concentrated on the cell or the contact interface.

9.2.3 I-V polarization curves

Figure 9.9 shows the discharge I-V-P curves of the stack and the repeating units in H_2 environment. **Figure 9.9a** presents the overall I-V-P curve of the stack during the durability test. As observed, the overall discharge performance of the stack reached the peak value in the electrolytic activation stage at the 24^{th} pulsed cycle, and then displayed a decreasing trend. During the total operation (64 cycles) of the stack, the instantaneous power at 1.6 V decreased by about 0.52%/cycle.

Figure 9.9b-f shows the discharge I-V-P curves of each cell and the repeating unit (cell + interconnect) in the stack. The calculation results suggested that Cell2 yielded the optimal discharge performance, up to 32 W. In the process of 64 cycles, the corresponding degradation rates of the instantaneous powers of Cell1 and Cell2 at 0.8 V were 0.32%/cycle and 0.74%/cycle, respectively.

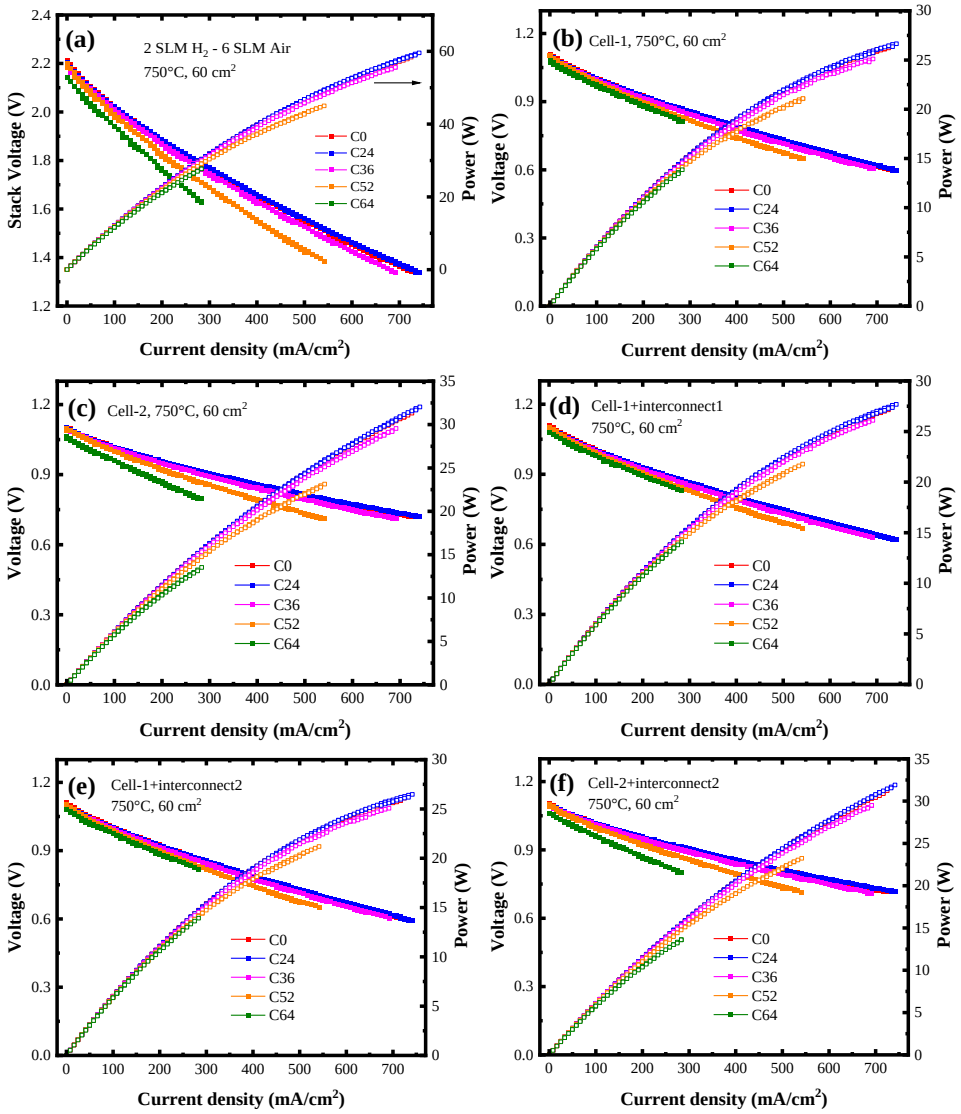

Figure 9.9. Discharge performance changes of the stack during pulse current CO_2 electrolysis testing: (a) Stack; (b) Cell1; (c) Cell2; (d) Cell 1+interconnect1; (e) Cell1+interconnect2; (f) Cell2+interconnect2

9.2.4 Electrochemical impedance and DRT analysis

Figure 9.10 exhibits the AC impedance spectra of two cells and the corresponding stack units during CO_2 electrolysis testing. **Figure 9.10a** and **Figure 9.10d** display the total impedance of Cell1 and Cell2. It was observed that the change of cell impedance mainly derived from ohmic impedance.

After long-term CO_2 electrolysis, ohmic impedance of the two cells in the stack increased by about 0.1 Ω cm^2 and 0.25 Ω cm^2, respectively, which revealed the possibility of the damage of electrolyte or the worse surface contact between stack components.

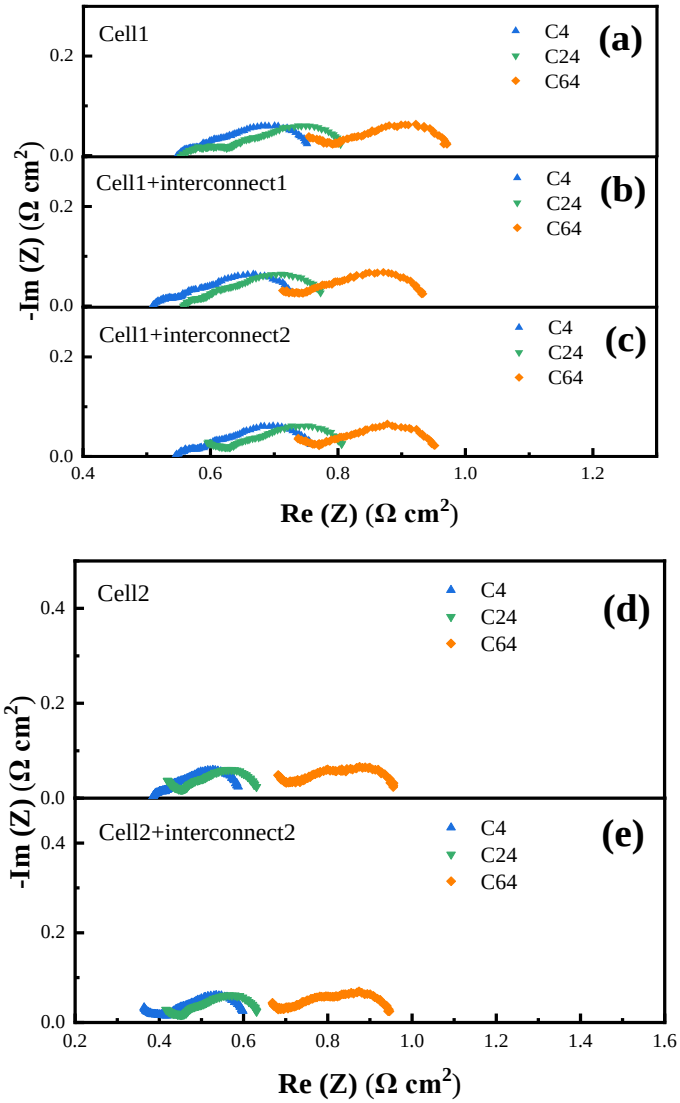

Figure 9.10. EIS impedance analysis during the long-term pulsed current CO_2 electrolysis: (a) Cell1; (b) Cell1+interconnect1; (c) Cell1+interconnect2; (d) Cell2; (e) Cell2+interconnect2

Compared with the three repeating unit (**Figure 9.10b**, **9.10c** and **9.10e**),

the ohmic impedance variation trends were almost the same as that of the cell unit (**Figure 9.10a** and **9.10d**), which proved that the damage was included in all the repeating units, especially in the cell unit. The cell unit contained the functional layers (electrodes and electrolyte) and non-functional layers (supporting layer and current collection layer). The degradation part was analyzed subsequently.

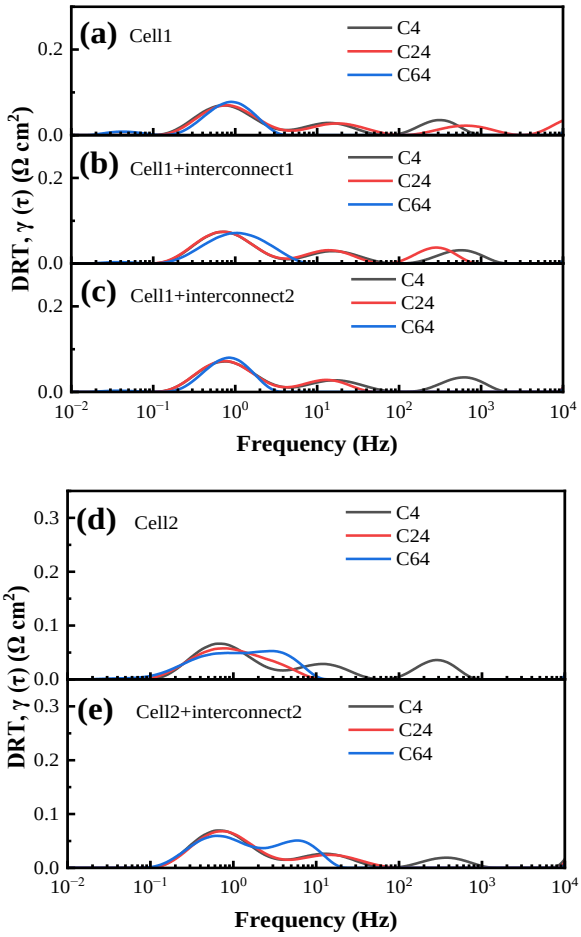

Figure 9.11. DRT of each repeating unit during the long-term testing: (a) Cell1; (b) Cell1+interconnect1; (c) Cell1+interconnect2; (d) Cell2; (e) Cell2+interconnect2

The DRT diagrams of the cells and the repeating units of the stack are

presented in **Figure 9.11**. The results revealed three electrode reaction processes of the cell unit. According to the previous research results, the peaks from low frequency to high frequency represented the gas diffusion polarization impedance (10^{-1}-10^{0} Hz), the LSCF-GDC surface oxygen exchange process (10^{1}-10^{2} Hz), and the fuel electrode charge transfer process (10^{2}-10^{3} Hz) [338, 339]. Polarization impedance of each part of the cell unit in **Figure 9.11** was not significantly attenuated, which implied the intact electron transport channel and preferable catalytic activity in the fuel electrode and the air electrode. Therefore, it could be speculated that the degradation of the cell might be mainly caused by the LSC current collection layer (inactive region) according to previous published research articles [340-342].

9.3 Analysis of degradation mechanisms of SOEC stacks

After long-term testing, the stack was cooled to 350 °C at 1 °C/min, and then naturally cooled to room temperature. After disassembly, the macro morphologies of the cells and interconnects are shown in **Figure 9.12**. The fragmentation of the cells was caused by violent disassembly, and no microcracks caused by high-temperature electrolysis were found, indicating that the cells were in good condition during the test. The main body of the cells not being green (nickel oxide) indicated that the main body was well sealed.

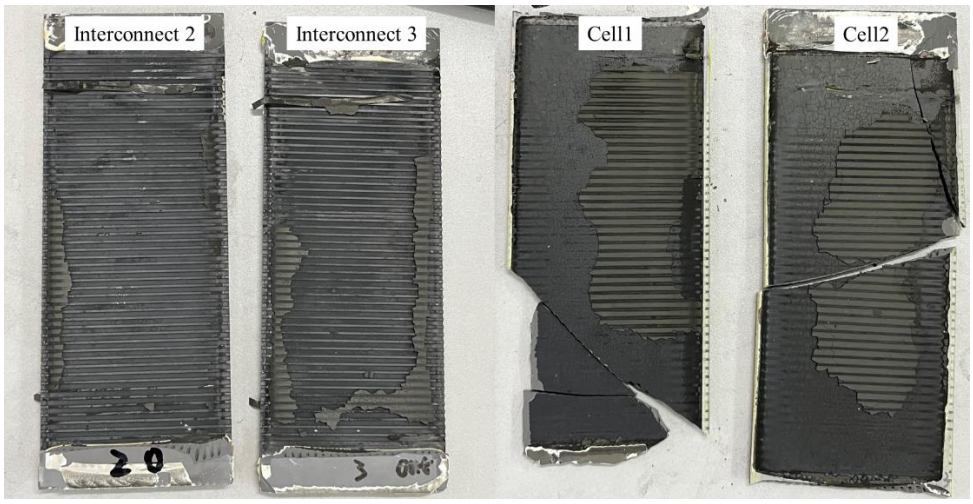

Figure 9.12. Macroscopic view of the disassembly of the SOEC stack after long-term testing of pulse CO_2 electrolysis testing

The SEM photos of the cells in **Figure 9.13** revealed slight particle growth in the air electrode of the cells, which might be related to high-temperature operation. Under 900 h of high-temperature testing, nickel coarsening occurred. To determine the degree of nickel coarsening, the size of nickel particles in the active fuel electrode area (yellow area) of three cells was analyzed through ImageJ software. The percentage contents of nickel particles in different sizes are shown in **Figure 9.13(d)-(f)**. In Cell1, Cell2, and reference cells, the proportions of nickel particles smaller than 0.5 μm^2 were 68.31%, 68.64%, and 65.96%, respectively; the proportions of nickel particles between 0.5-1 μm^2 were 11.27%, 14.79%, and 13.48% respectively. The proportions of small nickel particles within 1 μm^2 in three cells were very close, indicating that the degree of agglomeration was not significant. Therefore, the change of ohmic impedance might be because of the contact

interface of the voltage probes.

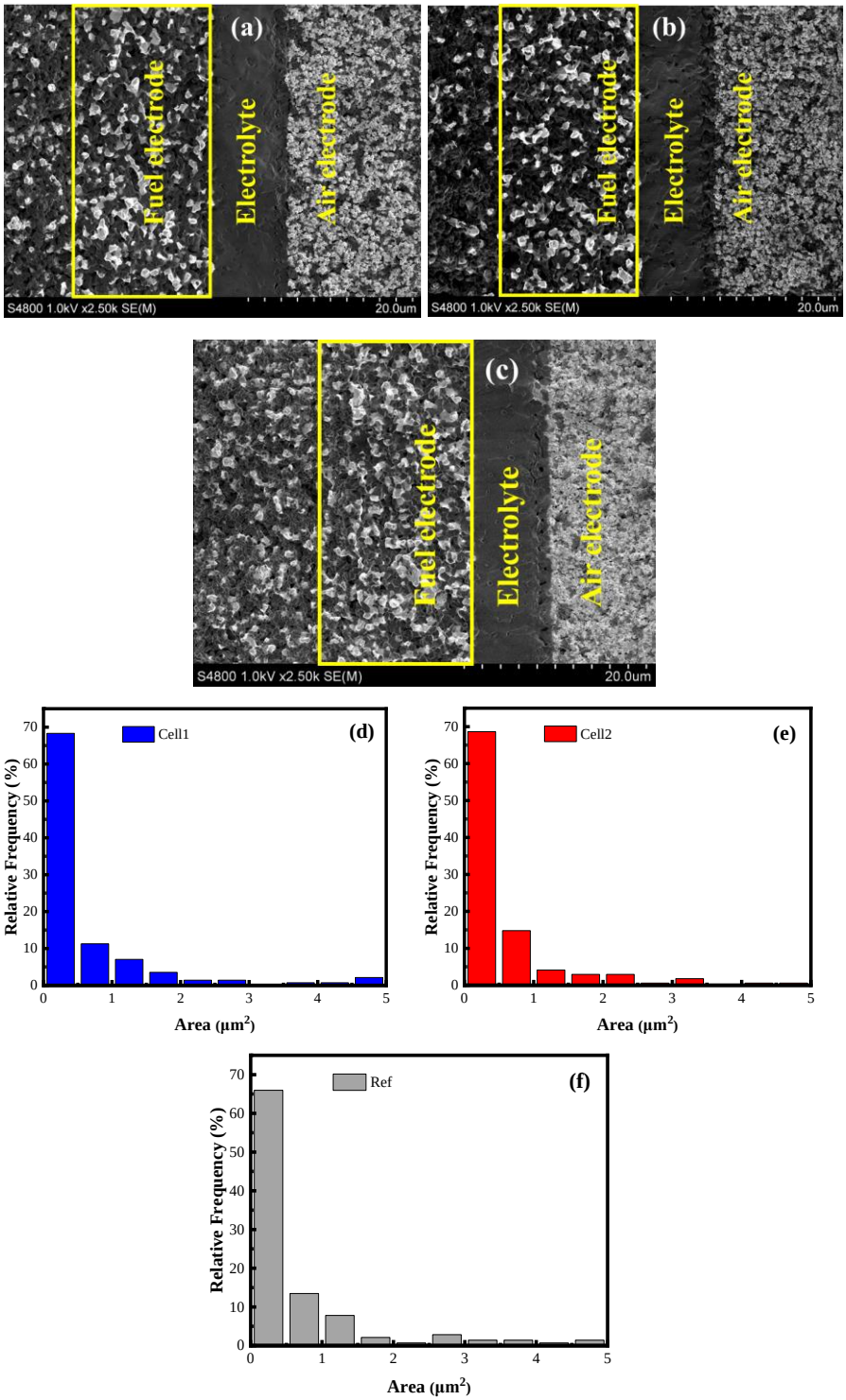

Figure 9.13. SEM after long-term test of pulsed current electrolysis: (a) Cell1; (b) Cell2; (c) Reference cell, nickel particle content of different sizes in Cell1 (d); Cell2 (e) and reference cell (f)

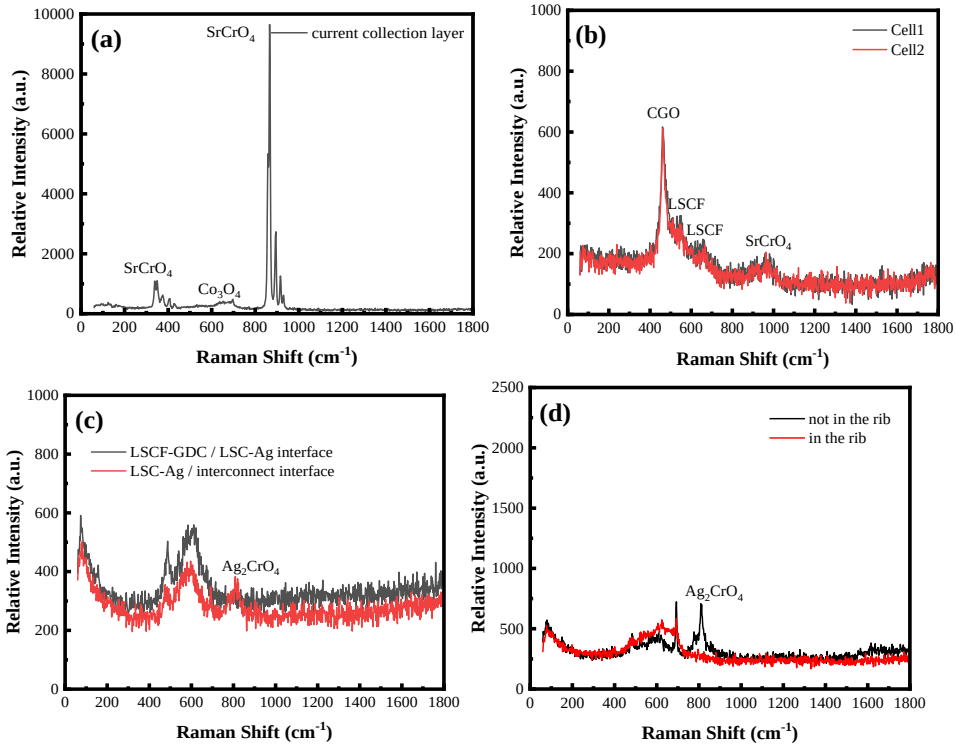

Figure 9.14. Raman spectrum after the long-term test of SOEC stack: (a) Powder sample of the current collection layer; (b) Surface of the air electrode of Cell1 and Cell2 (contains some current collection layer); (c) Air electrode/current collection layer surface and current collection layer/interconnect surface; (d) Detailed interface analysis between the current collection layer and the interconnect

The tested cell samples containing the current collection layer were characterized by Raman spectroscopy, and the results are shown in **Figure 9.14**. The sharp double peaks with Raman shift of 865 cm^{-1} and 895 cm^{-1} and the characteristic peaks with Raman shift of 690 cm^{-1} were observed in the current collection layer powder (**Figure 9.14a**), which belonged to $SrCrO_4$

and Co_3O_4 respectively [333]. However, $SrCrO_4$ phase also appeared on the air electrode surface of the cell sample (**Figure 9.14b**), which might be caused by a small amount of current collection layer remaining on the active surface of the electrode, and the possibility of Cr poisoning in the active air electrode could not be ruled out. In **Figures 9.14a** and **9.14b**, the $SrCrO_4$ signal in the current collection layer powder was the strongest, with the peak intensity exceeding 9000 counts, while the $SrCrO_4$ peak counts on the surface of the air electrode of the cells were lower than 200, indicating the highest $SrCrO_4$ content in the LSC-Ag current collection layer. This phenomenon was attributed to the chemical reaction between the volatilization of Cr element in the metal interconnect and the material of the current collection layer.

Cr element exerts its poisoning effect mainly through gaseous deposition and surface diffusion, in which the gaseous deposition is primarily affected by oxygen partial pressure and water pressure, while surface diffusion requires direct contact surface [305]. To verify the poisoning mechanism of Cr species, the contact surface of the interconnect / current collection layer and the contact surface of the cell / current collection layer were characterized based on the sheet-like current collection layer sample. For the contact surface between the current collection layer and the interconnect, the solid phase contact point (in the “rib”) and the gas phase contact point (not in the “rib”) were characterized respectively, and the

results are shown in **Figure 9.14c** and **9.14d**. The results in **Figure 9.14c** revealed that there existed Ag_2CrO_4 species with Raman shift of about 800 cm^{-1} at the contact surface between the current collection layer and the interconnect, but no Ag_2CrO_4 signal was found between the current collection layer and the functional layer of the air electrode [343]. According to **Figure 9.14d,** there was almost no Ag_2CrO_4 signal on the "rib" (solid phase contact point) where the current collection layer and interconnect remained direct contact, while there was Ag_2CrO_4 signal at the non-"rib" (gas phase contact point). Therefore, it could be judged that: (i) Cr poisoning was dominated by gas diffusion; (ii) after 900 h of operation, Cr element in the metal interconnect did not completely pass through the current collection layer to the active layer of the air electrode.

To sum up, the effect of Cr species on the current collection layer material became the main reason for the increase of ohmic impedance. In other words, the current collection layer caused the effect of delaying the penetration of Cr [305]. The degradation of the current collection layer was mainly due to the formation of $SrCrO_4$ species. For the direct contact between the Fe-Cr interconnect and the cell, the Cr element evaporated from the interconnect and preferentially nucleated with SrO that segregated from the grain surface of the cell electrode, leading to the formation of $SrCrO_4$. The $SrCrO_4$ phase deposited at the non-"rib" of the contact surface between the current collection layer and the air electrode interconnect (**Eq.9.1** and

Eq.9.2) [344- 346]. Generally, $SrCrO_4$ has strong insulation, capable of blocking the active sites of oxygen reduction reaction on the triple phase boundaries, reducing the surface exchange coefficient and increasing the degradation of the cell, which is also the reason for the increase of ohmic impedance [347, 348].

$$2Cr_2O_3(s) + 4H_2O(g) + 3O_2 \rightarrow 4CrO_2(OH)_2(g) \qquad \text{(Eq.9.1)}$$

$$SrO(s) + CrO_2(OH)_2(g) \rightarrow SrCrO_4(s) + H_2O(g) \qquad \text{(Eq.9.2)}$$

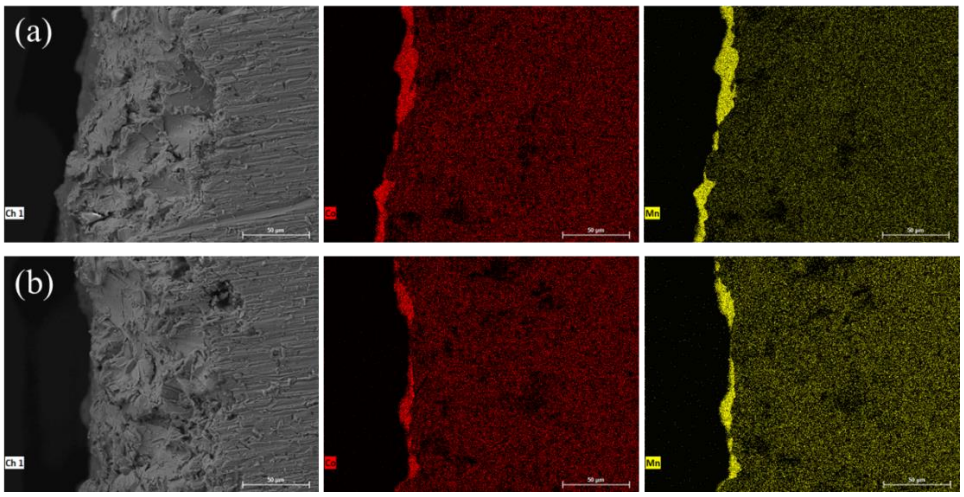

Figure 9.15. EDS of the coating of the interconnect: (a) Interconnect2, non-"rib", (b) Interconnect3, non-"rib"

Figure 9.15 shows the EDS analysis results of the interconnects in the stack after long-term testing with pulsed electrolysis. The EDS results at the non-"ribs" of the interconnects indicated that the $(Mn,Co)_3O_4$ coating began to fracture and peeled off after testing. The cracking of the coating might be caused by high-temperature electrolysis operations, or by the immature

coating technology. Additionally, the non-dense coating was one of the reasons for the release of Cr element from the interconnects.

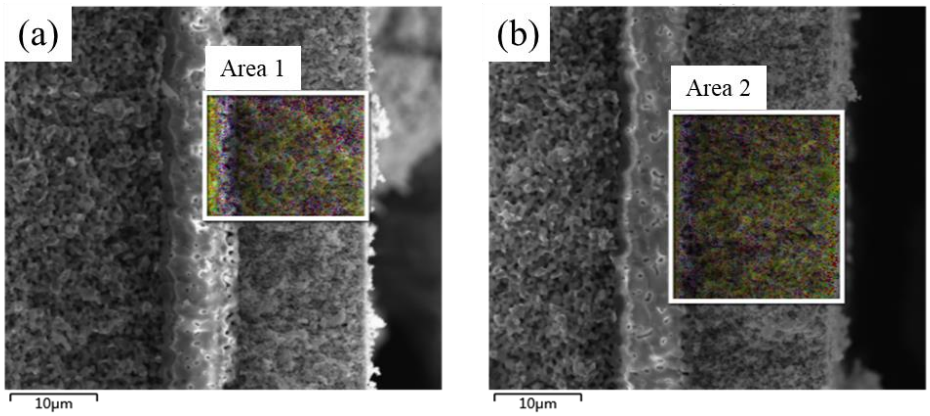

Figure 9.16. EDS of the air electrode functional layer of the cells in the stack after the long-term CO_2 electrolysis testing: (a) Cell1, (b) Cell2

Table 9.4. EDS analysis of the air electrode functional layer after long-term test under pulse current CO_2 electrolysis

Element	**Percentage**	
	Cell1	Cell2
Cr	0.00	0.00
Co	2.03	2.28
Sr	5.94	6.69
La	18.25	19.33

Figure 9.16 and **Table 9.4.** show the EDS analysis of the air electrode functional layer of the cells in the stack after the long-term test of pulse current CO_2 electrolysis. The results manifested that no obvious Cr element was found in the air electrode functional layer, indicating that Cr element did

not penetrate the LSCF-GDC perovskite structure, which was consistent with the results of polarization impedance analysis and Raman characterization. This proved that the substances such as $SrCrO_4$ only existed in the LSC-Ag current collection layer.

9.3 Summary

This study reproduced the intermittent scenario of solar power generation, and carried out research on cyclic CO_2 electrolysis in the flat-tube SOEC stack using -50 mA/cm^2~250 mA/cm^2 pulse current. The results demonstrated that the average degradation rate of the SOEC stack was about 0.018%/cycle during the 64 cycles (900 h), and the lifespan reached 1100 cycles (10000 h) under such working condition. The degradation rate of Cell1 in the stack was about -0.0066%~0.0238%/cycle, and that of Cell2 was between 0%~0.0715%/cycle during 64 pulse electrolysis cycles. The increase of ohmic impedance between the cell cathode and the metal interconnect was the main reason for the voltage degradation.

Moreover, the Cr-containing species volatilized from the metal interconnects reacted with the SrO isolated from the LSC in the current collection layer to generate $SrCrO_4$, which increased the resistance of the electron transfer inside the stack, thus accelerating the performance degradation of the stack. In addition, Raman analysis revealed that the Cr element in the metal interconnect did not penetrate the functional layer of

the air electrode of the cell, but only existed in the material of the current collection layer.

To sum up, the flat-tube SOEC stack exhibited good stability and tolerance in the CO_2 electrolysis environment coupled with renewable energy power, providing a reference for the absorption of intermittent renewable energy and the application of large-scale CO_2 electrolysis systems.

Chapter 10. Conclusions and Outlook

10.1 Conclusions

CO_2 conversion to fuels from SOECs is promising. The objective of this thesis was to study the CO_2 electrolysis performance, electrolysis efficiency and degradation mechanisms of Ni-based flat-tube solid oxide cells and stacks. The thesis involves six research projects, and the main results are as follows:

(i) In **Chapter 4**, through instantaneous performance tests under different conditions and the properties of sealing materials, it was found that 750°C was a suitable working temperature for cells and stacks. By comparing the impedance and DRT analysis measured in H_2-CO_2 and CO-CO_2 fuel electrode atmospheres, it was found that under the same oxygen partial pressure conditions, the polarization resistance in the CO-CO_2 atmosphere tended to be higher, limiting the CO_2 electrolysis performance. According to the instantaneous performance test results, under the same oxygen partial pressure, when the volume fractions of H_2 in the fuel electrode were 25%, 50%, and 75%, the limiting current densities of CO_2 electrolysis were -550 mA/cm^2, -480 mA/cm^2, and -250 mA/cm^2, respectively. When using CO as a reducing gas, the limiting current densities were reduced to -480 mA/cm^2, -415 mA/cm^2, and -220 mA/cm^2, respectively. The corresponding volume contents of CO were 23.8%, 46.7%, and 71.7%.

Through short-term performance testing, it was found that in the 71.7 vol.% CO-28.3 vol.% CO_2 fuel electrode atmosphere, the SOEC underwent irreversible degradation after only one hour of operation at a current density of -200 mA/cm^2, accompanied by cell fragmentation and electrolyte detachment. Under 75% H_2 protection, irreversible degradation only occurred when the current density reached -300 mA/cm^2. The thermodynamic analysis of the reaction system implied that when the CO_2-H_2 ratio was 3:1, methane was not formed above 600 °C, and the CO selectivity of the product reached 100%. Through fuel electrode product analysis and energy efficiency calculation, in the constant current electrolysis of -200 mA/cm^2, if the heat energy consumed by air was not considered (i.e. assuming air electrode heat exchange), the energy efficiency could reach 81.6%.

(ii) In **Chapter 5**, flat-tube solid oxide electrolysis cells were employed to investigate the effects of different fuel electrode atmospheres, air electrode atmospheres, electrolysis current or voltage on the durability of the cells. The degradation mechanism of flat-tube structure SOECs during long-term electrolysis was analyzed using electrochemical impedance, DRT, gas chromatography, SEM, EDS, and Raman spectroscopy. The total electrolytic time of Cell5.1 was 471 h. The results suggested that a large amount of air entering the air electrode was not conducive to the long-term operation of the cell, because the supply of a large amount of cold air increased the local

temperature difference and resulted in a structural damage to the cell. The DRT results reflected the degradation of the fuel electrode with increasing time. The energy conversion efficiency calculated was around 25% when 5 SLM of air was used in the air electrode. The microstructure characterization confirmed that the fuel electrode degradation was caused by the migration and loss of nickel catalysts. Cell5.2 ran stably without supplying air for 1070 h at 200 mA/cm^2, and Cell5.3 ran stably in a no-air atmosphere for 859 h at 218 mA/cm^2, with degradation rates below 10%/kh. The DRT results revealed that the degradation of the air electrode was an important reason of cell degradation. This means that CO_2 electrolysis without air in the air electrode still needs to be further verified. Another discovery was that the energy conversion efficiency could be increased to over 80% without air supply to the air electrode, given the neglect of the heat energy of the air. Through microstructure characterization, it was found that the formation of strontium rich phases between LSCF and YSZ was the main reason of cell degradation. For the situation of the fuel electrode not being protected by a reducing gas, a stable CO_2 electrolysis test was achieved for about 100 h in Cell5.4, but the risk of oxidation of the fuel electrode still existed.

(iii) **Chapter 6** describes simulated intermittent renewable energy power to carry out CO_2 electrolysis based on SOEC. -100-300 mA/cm^2 was selected as the pulsed current for long-term operation, and the test was conducted for 101 cycles (808 h), with voltage degradation mainly

concentrated in the 71-100 cycles. The agglomeration of nickel particles at the fuel electrode was found to be one of the important reasons for voltage degradation. Carbon deposition might be another main cause of cell degradation, but it mainly occurred at the gas outlet pipeline of the fuel electrode. Without considering air heat, the energy conversion efficiency of Cell6.1 could reach over 88%. Compared to the previous experiment using 25 vol.% H_2-75 vol.% CO_2 fuel electrode atmosphere for pulsed current CO_2 electrolysis, the degradation of the SOEC operated in the CO-CO_2 atmosphere was higher.

(iv) In **Chapter 7**, power-to-gas and gas-to-power processes were simulated using CO as an energy storage medium under a CO-CO_2 fuel electrode atmosphere and reversible current. When Cell7.2 served for more than 100 cycles (> 400 h), the maximum discharge power decayed from 637.1 mW/cm^2 to 571.4 mW/cm^2, with a degradation rate of 0.1%/cycle. The results indicated that the flat-tube SOEC achieved stable operation for hundreds of hours under constant current, pulsed current and reversible operating conditions.

(v) In **Chapter 8**, the stack structure, surface contact, airtightness and assembly method for multiple cells were researched. Subsequently, the long-term durability of a three-unit SOEC stack was tested with different constant currents. At -250 mA/cm^2 and -500 mA/cm^2, the stack carried out stable CO_2 electrolysis operation for more than 1000 h. If external factors were not

considered, the durability of the flat-tube SOEC stack might exceed 5000 h. The stack generated 500-700 sccm CO from CO_2 electrolysis, with an energy conversion efficiency of 58.6% -73.9%, which was lower than that in single cells. This might be because some components in the stack exhibited higher internal resistance after high-temperature oxidation. Also, the interface between the cells and the interconnects in the stack may demonstrated poor contact and high interface resistance, affecting electron conduction. The reason for degradation of fuel electrodes in the stack after long-term CO_2 electrolysis was quite similar to that in single cells. Specifically, nickel at the interface of electrolyte and fuel electrode gradually decreased, moved towards the area far away from the electrolyte, and attached itself to large particles of nickel in the form of smaller nanoscale particles. Some parts of the electrolytes changed into Kirkendall voids, hindering the oxygen ion transport process. Notably, unmodified 441 stainless steel was adopted in the stack, in which Cr is prone to evaporate and diffuse. The chemical reaction between elemental Cr and the LSC current collection layer of the air electrode generated $SrCrO_4$ and Ag_2CrO_4 components, resulting in poor contact between the interconnects and the cells.

The mechanical strength analysis of stacks after CO_2 electrolysis testing manifested that the strength of the cell decreased by about 30 N due to the electrolysis operation, while the reduction operation and thermal cycle operation led to a decrease in the cell strength of about 37 N, which was

higher than that of high-temperature CO_2 electrolysis operation.

(vi) Based on the conclusion in **Chapter 6** that the cell decayed the fastest under pulsed current, for improving the stack stability, a layer of (Mn, Co)$_3O_4$ coating was sprayed onto the interconnect by plasma in **Chapter 9**. A -50 mA/cm^2~250 mA/cm^2 pulsed current CO_2 electrolysis test was carried out in the flat-tube SOEC stack. The results implied that the average degradation rate of the SOEC stack was about 0.018%/cycle during the 64 cycles (900 h), and the lifespan reached 1100 cycles (10000 h) under such working condition. The degradation rate of Cell1 in the stack was about -0.0066%~0.0238%/cycle, and that of Cell2 was between 0%~0.0715%/cycle during 64 pulse electrolysis cycles. The increase of ohmic impedance between the cell cathode and the metal interconnect was found to be the main reason for the voltage degradation. Further microscopic characterization of the interconnect and LSC current collection layer showed that the coating cracked during the test and $SrCrO_4$ generated at the surface of LSC current collection layer, enhancing the resistance of the electron transfer between the current collection layer and the air electrode of the cell. Raman analysis also revealed that the element Cr in the metal interconnect did not penetrate the functional layer of the air electrode of the cell, but only existed in the material of the current collection layer.

10.2 Outlook

1. For intensifying the energy conversion efficiency of CO_2 electrolysis reaction in solid oxide electrolysis cells and stacks, great efforts in the gas leakage rate of stacks are necessitated, and more detailed research is needed on the stack structure, sealing material ratio, and solid content.

2. For boosting the electrolytic performance of solid oxide cells and stacks, it is necessary to improve interface contact to reduce the loss of interface contact. The LSC-Ag current collection layer may be optimized or replaced by other materials.

3. To prolong the lifespan of solid oxide electrolysis cells and stacks, it is crucial to improve the fuel electrode nickel-based materials to strengthen their resistance to carbon deposition, such as using impregnation method.

4. To maintain the activity of oxygen exchange reaction in the air electrode, suppressing the Cr toxicity and strontium segregation of the air electrode becomes important. The main approach to suppress the Cr toxic effect of air electrode is to improve the coating of the interconnects. Methods to prevent strontium segregation include improving the high-temperature stability of air electrode materials or developing new materials that do not contain strontium. However, Ni-YSZ and LSCF-GDC materials, as the two most mature solid oxide electrode materials, require more profound research and extensive practice in replacement and modification.

Reference

[1] Song, Y.; Zhang, X.; Xie, K.; Wang, G.; Bao, X. High-Temperature CO_2 Electrolysis in Solid Oxide Electrolysis Cells: Developments, Challenges, and Prospects. *Advanced Materials* **2019,** *31* (50), 1902033.

[2] Walker, A. P.; De Kauwe, M. G.; Bastos, A.; Belmecheri, S.; Georgiou, K.; Keeling, R. F.; McMahon, S. M.; Medlyn, B. E.; Moore, D. J. P.; Norby, R. J.et al. Integrating the evidence for a terrestrial carbon sink caused by increasing atmospheric CO_2. *New Phytologist* **2021,** *229* (5), 2413.

[3] Rogelj, J.; Fricko, O.; Meinshausen, M.; Krey, V.; Zilliacus, J. J. J.; Riahi, K. Understanding the origin of Paris Agreement emission uncertainties. *Nature Communications* **2017,** *8* (1), 15748.

[4] Sikarwar, V. S.; Reichert, A.; Jeremias, M.; Manovic, V. COVID-19 pandemic and global carbon dioxide emissions: A first assessment. *Science of The Total Environment* **2021,** *794*, 148770.

[5] Hanna, R.; Victor, D. G. Marking the decarbonization revolutions. *Nature Energy* **2021,** *6* (6), 568.

[6] Schiffer, Z. J.; Manthiram, K. Electrification and Decarbonization of the Chemical Industry. *Joule* **2017,** *1* (1), 10.

[7] Yekini Suberu, M.; Wazir Mustafa, M.; Bashir, N. Energy storage systems for renewable energy power sector integration and mitigation of intermittency. *Renewable and Sustainable Energy Reviews* **2014,** *35*,

499.

[8] Baños, R.; Manzano-Agugliaro, F.; Montoya, F. G.; Gil, C.; Alcayde, A.; Gómez, J. Optimization methods applied to renewable and sustainable energy: A review. *Renewable and Sustainable Energy Reviews* **2011,** *15* (4), 1753.

[9] Zhang, Y.; Ma, T.; Elia Campana, P.; Yamaguchi, Y.; Dai, Y. A techno-economic sizing method for grid-connected household photovoltaic battery systems. *Applied Energy* **2020,** *269*, 115106.

[10] Jiang, Y.; Xu, J.; Sun, Y.; Wei, C.; Wang, J.; Liao, S.; Ke, D.; Li, X.; Yang, J.; Peng, X. Coordinated operation of gas-electricity integrated distribution system with multi-CCHP and distributed renewable energy sources. *Applied Energy* **2018,** *211*, 237.

[11] Li, J.; Chen, S.; Wu, Y.; Wang, Q.; Liu, X.; Qi, L.; Lu, X.; Gao, L. How to make better use of intermittent and variable energy? A review of wind and photovoltaic power consumption in China. *Renewable and Sustainable Energy Reviews* **2021,** *137*, 110626.

[12] Ellabban, O.; Abu-Rub, H.; Blaabjerg, F. Renewable energy resources: Current status, future prospects and their enabling technology. *Renewable and Sustainable Energy Reviews* **2014,** *39*, 748.

[13] Moriarty, P.; Honnery, D. What is the global potential for renewable energy? *Renewable and Sustainable Energy Reviews* **2012,** *16* (1), 244.

[14] Rehman, S.; Al-Hadhrami, L. M.; Alam, M. M. Pumped hydro energy

storage system: A technological review. *Renewable and Sustainable Energy Reviews* **2015,** *44*, 586.

[15] Son, Y. G.; Choi, S.; Aquah, M. A.; Kim, S. Y. Systematic planning of power-to-gas for improving photovoltaic acceptance rate: Application of the potential RES penetration index. *Applied Energy* **2023,** *349*, 121611.

[16] Vialetto, G.; Noro, M.; Colbertaldo, P.; Rokni, M. Enhancement of energy generation efficiency in industrial facilities by SOFC - SOEC systems with additional hydrogen production. *International Journal of Hydrogen Energy* **2019,** *44* (19), 9608.

[17] Dadak, A.; Mehrpooya, M.; Kasaeian, A. Design and development of an innovative integrated structure for the production and storage of energy and hydrogen utilizing renewable energy. *Sustainable Energy Technologies and Assessments* **2021,** *45*, 101123.

[18] Kamkeng, A. D. N.; Wang, M. Long-term performance prediction of solid oxide electrolysis cell (SOEC) for CO_2/H_2O co-electrolysis considering structural degradation through modelling and simulation. *Chemical Engineering Journal* **2022,** *429*, 132158.

[19] Wang, Y.; Li, W.; Ma, L.; Li, W.; Liu, X. Degradation of solid oxide electrolysis cells: Phenomena, mechanisms, and emerging mitigation strategies-A review. *Journal of Materials Science & Technology* **2020,** *55*, 35.

[20] Hubert, M.; Laurencin, J.; Cloetens, P.; Morel, B.; Montinaro, D.; Lefebvre-Joud, F. Impact of Nickel agglomeration on Solid Oxide Cell operated in fuel cell and electrolysis modes. *Journal of Power Sources* **2018,** *397*, 240.

[21] Papaefthimiou, V.; Niakolas, D. K.; Paloukis, F.; Teschner, D.; Knop-Gericke, A.; Haevecker, M.; Zafeiratos, S. Operando observation of nickel/ceria electrode surfaces during intermediate temperature steam electrolysis. *Journal of Catalysis* **2017,** *352*, 305.

[22] Mewafy, B.; Paloukis, F.; Papazisi, K. M.; Balomenou, S. P.; Luo, W.; Teschner, D.; Joubert, O.; Le Gal La Salle, A.; Niakolas, D. K.; Zafeiratos, S. Influence of Surface State on the Electrochemical Performance of Nickel-Based Cermet Electrodes during Steam Electrolysis. *ACS Applied Energy Materials* **2019,** *2* (10), 7045.

[23] Kukk, F.; Möller, P.; Kanarbik, R.; Nurk, G. Study of Long-Term Stability of Ni-$Zr_{0.92}Y_{0.08}O_{2-\delta}$|$Zr_{0.92}Y_{0.08}O_{2-\delta}$|$Ce_{0.9}Gd_{0.1}O_{2-\delta}$ |$Pr_{0.6}Sr_{0.4}CoO_{3-\delta}$ at SOFC and SOEC Mode. In *Energies*, **2021**, *14*(4), 1.

[24] Koo, B.; Kim, K.; Kim, J. K.; Kwon, H.; Han, J. W.; Jung, W. Sr Segregation in Perovskite Oxides: Why It Happens and How It Exists. *Joule* **2018,** *2* (8), 1476.

[25] Jung, W.; Tuller, H. L. Investigation of surface Sr segregation in model thin film solid oxide fuel cell perovskite electrodes. *Energy & Environmental Science* **2012,** *5* (1), 5370.

[26] Monaco, F.; Ferreira-Sanchez, D.; Hubert, M.; Morel, B.; Montinaro, D.; Grolimund, D.; Laurencin, J. Oxygen electrode degradation in solid oxide cells operating in electrolysis and fuel cell modes: LSCF destabilization and interdiffusion at the electrode/electrolyte interface. *International Journal of Hydrogen Energy* **2021,** *46* (62), 31533.

[27] Chen, Y.; Fan, Y.; Lee, S.; Hackett, G.; Abernathy, H.; Gerdes, K.; Song, X. Interface and grain boundary degradation in LSM-YSZ composite Solid Oxide Fuel Cell cathodes operated in humidified air. *Journal of Power Sources* **2019,** *438*, 227043.

[28] Mehdi, A. M.; Hussain, A.; Song, R. H.; Lim, T.-H.; Kazmi, W. W.; Ishfaq, H. A.; Khan, M. Z.; Qamar, S.; Syed, M. W.; Mehran, M. T. Improving the durability of cobaltite cathode of solid oxide fuel cells - a review. *RSC Advances* **2023,** *13* (36), 25029.

[29] Cheng, K.; Xu, H.; Zhang, L.; Zhou, J.; Wang, X.; Du, Y.; Chen, M. Computational engineering of the oxygen electrode-electrolyte interface in solid oxide fuel cells. *npj Computational Materials* **2021,** *7* (1), 119.

[30] Wang, R.; Sun, Z.; Pal, U. B.; Gopalan, S.; Basu, S. N. Mitigation of chromium poisoning of cathodes in solid oxide fuel cells employing $CuMn_{1.8}O_4$ spinel coating on metallic interconnect. *Journal of Power Sources* **2018,** *376*, 100.

[31] Yang, Z.; Guo, M.; Wang, N.; Ma, C.; Wang, J.; Han, M. A short review of cathode poisoning and corrosion in solid oxide fuel cell. *International*

Journal of Hydrogen Energy **2017,** *42* (39), 24948.

[32] Opila, E. J.; Myers, D. L.; Jacobson, N. S.; Nielsen, I. M. B.; Johnson, D. F.; Olminsky, J. K.; Allendorf, M. D. Theoretical and Experimental Investigation of the Thermochemistry of $CrO_2(OH)_2$(g). *The Journal of Physical Chemistry A* **2007,** *111* (10), 1971.

[33] Tomas, M.; Visibile, A.; Svensson, J. E.; Froitzheim, J. Novel coatings for protecting solid oxide fuel cell interconnects against the dual-atmosphere effect. *International Journal of Hydrogen Energy* **2023,** *48* (48), 18405.

[34] Zhao, M.; Geng, S.; Chen, G.; Wang, F.; Ivey, D. G. Sputtered $Fe_{1.5}CoNi_{0.5}$ coating: An improved protective coating for SOFC interconnect applications. *International Journal of Hydrogen Energy* **2022,** *47* (22), 11658.

[35] Posdziech, O.; Schwarze, K.; Brabandt, J. Efficient hydrogen production for industry and electricity storage via high-temperature electrolysis. *International Journal of Hydrogen Energy* **2019,** *44* (35), 19089.

[36] Liu, Z.; Deng, Z.; He, G.; Wang, H.; Zhang, X.; Lin, J.; Qi, Y.; Liang, X. Challenges and opportunities for carbon neutrality in China. *Nature Reviews Earth & Environment* **2022,** *3* (2), 141.

[37] Zou, C.; Pan, S.; Hao, Q. On the connotation, challenge and significance of China's “energy independence” strategy. *Petroleum Exploration and*

Development **2020,** *47* (2), 449.

[38] Jie, D.; Xu, X.; Guo, F. The future of coal supply in China based on non-fossil energy development and carbon price strategies. *Energy* **2021,** *220*, 119644. IEA World Energy Balances 2022 https://www.iea.org/data-and-statistics/data-product/world-energy-statistics-and-balances

[39] Coal demand by region in the Stated Policies Scenario, 2000-2050. Executive summary – World Energy Outlook 2023 – Analysis - IEA

[40] Hannah Ritchie, Pablo Rosado and Max Roser (2020) - "Energy Production and Consumption" Published online at OurWorldInData.org. Retrieved from: 'https://ourworldindata.org/energy-production-consumption' [Online Resource]

[41] Global Carbon Budget (2023) OurWorldInData.org/co2-and-greenhouse-gas-emissions

[42] Gu, Y.; Wang, D.; Chen, Q.; Tang, Z. Techno-economic analysis of green methanol plant with optimal design of renewable hydrogen production: A case study in China. *International Journal of Hydrogen Energy* **2022,** *47* (8), 5085.

[43] Xu, S. China's climate governance for carbon neutrality: regulatory gaps and the ways forward. *Humanities and Social Sciences Communications* **2023,** *10* (1), 853.

[44] He, M.; Sun, Y.; Han, B. Green carbon science: efficient carbon resource processing, utilization, and recycling towards carbon neutrality.

Angewandte Chemie **2022,** *134* (15), e202112835.

[45] Chen, Y.; Feng, X.; Tian, H.; Wu, X.; Gao, Z.; Feng, Y.; Piao, S.; Lv, N.; Pan, N.; Fu, B. Accelerated increase in vegetation carbon sequestration in China after 2010: A turning point resulting from climate and human interaction. *Global Change Biology* **2021,** *27* (22), 5848.

[46] Rahman, A.; Farrok, O.; Haque, M. M. Environmental impact of renewable energy source based electrical power plants: Solar, wind, hydroelectric, biomass, geothermal, tidal, ocean, and osmotic. *Renewable and Sustainable Energy Reviews* **2022,** *161*, 112279.

[47] Hu, H.; Xue, W.; Jiang, P.; Li, Y. Bibliometric analysis for ocean renewable energy: An comprehensive review for hotspots, frontiers, and emerging trends. *Renewable and Sustainable Energy Reviews* **2022,** *167*, 112739.

[48] Zhao, S.; Li, K.; Yang, Z.; Xu, X.; Zhang, N. A new power system active rescheduling method considering the dispatchable plug-in electric vehicles and intermittent renewable energies. *Applied Energy* **2022,** *314*, 118715.

[49] Xu, T.; Gao, W.; Qian, F.; Li, Y. The implementation limitation of variable renewable energies and its impacts on the public power grid. *Energy* **2022,** *239*, 121992.

[50] León, L. M.; Romero-Quete, D.; Merchán, N.; Cortés, C. A. Optimal design of PV and hybrid storage based microgrids for healthcare and

government facilities connected to highly intermittent utility grids. *Applied Energy* **2023,** *335*, 120709.

[51] W. Jiang, X. Wang, H. Huang, D. Zhang, N. Ghadimi, *Journal of Energy Storage* **2022**, *55*, 105311.

[52] Jiang, W.; Wang, X.; Huang, H.; Zhang, D.; Ghadimi, N. Optimal economic scheduling of microgrids considering renewable energy sources based on energy hub model using demand response and improved water wave optimization algorithm. *Journal of Energy Storage* **2022,** *55*, 105311.

[53] IRENA (2023), Renewable capacity statistics 2023, International Renewable Energy Agency, Abu Dhabi.

[54] National Energy Administration (NEA).

[55] Capurso, T.; Stefanizzi, M.; Torresi, M.; Camporeale, S. M. Perspective of the role of hydrogen in the 21st century energy transition. *Energy Conversion and Management* **2022,** *251*, 114898.

[56] Malaika, A.; Ptaszyńska, K.; Kapska, M.; Kozłowski, M. The role of surface chemistry of carbons in the catalytic production of fuel additives by glycerol etherification. *Fuel* **2024,** *358*, 130147.

[57] Yadav, S.; Mondal, S. S. A review on the progress and prospects of oxy-fuel carbon capture and sequestration (CCS) technology. *Fuel* **2022,** *308*, 122057.

[58] Gao, D.; Li, W.; Wang, H.; Wang, G.; Cai, R. Heterogeneous Catalysis

for CO_2 Conversion into Chemicals and Fuels. *Transactions of Tianjin University* **2022,** *28* (4), 245.

[59] Detz, H.; Butera, V. Insights into the mechanistic CO_2 conversion to methanol on single Ru atom anchored on MoS_2 monolayer. *Molecular Catalysis* **2023,** *535*, 112878.

[60] Zang, Y.; Wei, P.; Li, H.; Gao, D.; Wang, G. Catalyst Design for Electrolytic CO_2 Reduction Toward Low-Carbon Fuels and Chemicals. *Electrochemical Energy Reviews* **2022,** *5* (1), 29.

[61] Ma, D.; Jin, T.; Xie, K.; Huang, H. An overview of flow cell architecture design and optimization for electrochemical CO_2 reduction. *Journal of Materials Chemistry A* **2021,** *9* (37), 20897.

[62] Hui, S.; Yang, D.; Wang, Z.; Yick, S.; Decès-Petit, C.; Qu, W.; Tuck, A.; Maric, R.; Ghosh, D. Metal-supported solid oxide fuel cell operated at 400-600°C. *Journal of Power Sources* **2007,** *167* (2), 336.

[63] del Pozo Gonzalez, H.; Bernadet, L.; Torrell, M.; Bianchi, F. D.; Tarancón, A.; Gomis-Bellmunt, O.; Dominguez-Garcia, J. L. Power transition cycles of reversible solid oxide cells and its impacts on microgrids. *Applied Energy* **2023,** *352*, 121887.

[64] Zhang, X.; Song, Y.; Wang, G.; Bao, X. Co-electrolysis of CO_2 and H_2O in high-temperature solid oxide electrolysis cells: Recent advance in cathodes. *Journal of Energy Chemistry* **2017,** *26* (5), 839.

[65] Ochieng, A. O.; Megahed, T. F.; Ookawara, S.; Hassan, H.

Comprehensive review in waste heat recovery in different thermal energy-consuming processes using thermoelectric generators for electrical power generation. *Process Safety and Environmental Protection* **2022,** *162*, 134.

[66] Wendel, C. H.; Kazempoor, P.; Braun, R. J. A thermodynamic approach for selecting operating conditions in the design of reversible solid oxide cell energy systems. *Journal of Power Sources* **2016,** *301*, 93.

[67] Amores, E.; Rodríguez, J.; Oviedo, J.; de Lucas-Consuegra, A. Development of an operation strategy for hydrogen production using solar PV energy based on fluid dynamic aspects. **2017,** *7* (1), 141.

[68] Li, J.; Yang, L.; Wang, Z.; Sun, H.; Sun, G. Degradation study of high temperature proton exchange membrane fuel cell under start/stop and load cycling conditions. *International Journal of Hydrogen Energy* **2021,** *46* (47), 24353.

[69] Gaikwad, P. S.; Mondal, K.; Shin, Y. K.; van Duin, A. C. T.; Pawar, G. Enhancing the Faradaic efficiency of solid oxide electrolysis cells: progress and perspective. *npj Computational Materials* **2023,** *9* (1), 149.

[70] Lv, H.; Chen, J.; Zhou, W.; Shen, X.; Zhang, C. Mechanism analyses and optimization strategies for performance improvement in low-temperature water electrolysis systems via the perspective of mass transfer: A review. *Renewable and Sustainable Energy Reviews* **2023,** *183*, 113394.

[71] Mohebali Nejadian, M.; Ahmadi, P.; Houshfar, E. Comparative optimization study of three novel integrated hydrogen production systems with SOEC, PEM, and alkaline electrolyzer. *Fuel* **2023,** *336*, 126835.

[72] Salehmin, M. N. I.; Husaini, T.; Goh, J.; Sulong, A. B. High-pressure PEM water electrolyser: A review on challenges and mitigation strategies towards green and low-cost hydrogen production. *Energy Conversion and Management* **2022,** *268*, 115985.

[73] Gul, E.; Baldinelli, G.; Farooqui, A.; Bartocci, P.; Shamim, T. AEM-electrolyzer based hydrogen integrated renewable energy system optimisation model for distributed communities. *Energy Conversion and Management* **2023,** *285*, 117025.

[74] Yu, D.; Hu, J.; Wang, W.; Gu, B. Comprehensive techno-economic investigation of biomass gasification and nanomaterial based SOFC/SOEC hydrogen production system. *Fuel* **2023,** *333*, 126442.

[75] Bianchi, F. R.; Bosio, B. Operating Principles, Performance and Technology Readiness Level of Reversible Solid Oxide Cells. *Sustainability* **2021**, *13* (9), 4777.

[76] Ouyang, Z.; Komatsu, Y.; Sciazko, A.; Onishi, J.; Nishimura, K.; Shikazono, N. Operando observations of active three phase boundary of patterned nickel - Yttria stabilized zirconia electrode in solid oxide cell. *Journal of Power Sources* **2022,** *529*, 231228.

[77] Hassmann, K. SOFC Power Plants, the Siemens-Westinghouse Approach. *Fuel Cells* **2001,** *1* (1), 78.

[78] Huang, K.; Singhal, S. C. Cathode-supported tubular solid oxide fuel cell technology: A critical review. *Journal of Power Sources* **2013,** *237*, 84.

[79] Timurkutluk, B.; Timurkutluk, C.; Mat, M. D.; Kaplan, Y. A review on cell/stack designs for high performance solid oxide fuel cells. *Renewable and Sustainable Energy Reviews* **2016,** *56*, 1101.

[80] Hedayat, N.; Du, Y.; Ilkhani, H. Review on fabrication techniques for porous electrodes of solid oxide fuel cells by sacrificial template methods. *Renewable and Sustainable Energy Reviews* **2017,** *77*, 1221.

[81] Kuterbekov, K. A.; Nikonov, A. V.; Bekmyrza, K. Z.; Pavzderin, N. B.; Kabyshev, A. M.; Kubenova, M. M.; Kabdrakhimova, G. D.; Aidarbekov, N. Classification of Solid Oxide Fuel Cells. *Nanomaterials* **2022**, *12* (7), 1059.

[82] Bove, R. Solid oxide fuel cells: principles, designs and state-of-the-art in industries. *Recent trends in fuel cell science and technology* **2007**, 267.

[83] McPhail, S. J.; Frangini, S.; Laurencin, J.; Effori, E.; Abaza, A.; Padinjarethil, A. K.; Hagen, A.; Léon, A.; Brisse, A.; Vladikova, D.et al. Addressing planar solid oxide cell degradation mechanisms: A critical review of selected components. *Electrochemical Science Advances* **2022,** *2* (5), e2100024.

[84] Patcharavorachot, Y.; Arpornwichanop, A.; Chuachuensuk, A. Electrochemical study of a planar solid oxide fuel cell: Role of support structures. *Journal of Power Sources* **2008,** *177* (2), 254.

[85] Kim, J.-H.; Song, R.-H.; Song, K.-S.; Hyun, S.-H.; Shin, D.-R.; Yokokawa, H. Fabrication and characteristics of anode-supported flat-tube solid oxide fuel cell. *Journal of Power Sources* **2003,** *122* (2), 138.

[86] Mao, X.; Sang, J.; Xi, C.; Liu, Z.; Yang, J.; Guan, W.; Wang, J.; Xia, C.; Singhal, S. C. Performance evaluation of ammonia-fueled flat-tube solid oxide fuel cells with different build-in catalysts. *International Journal of Hydrogen Energy* **2022,** *47* (55), 23324.

[87] Minh, N. Q. Solid oxide fuel cell technology-features and applications. *Solid State Ionics* **2004,** *174* (1), 271.

[88] Hou, M.; Zhu, F.; Liu, Y.; Chen, Y. A high-performance fuel electrode-supported tubular protonic ceramic electrochemical cell. *Journal of the European Ceramic Society* **2023,** *43* (14), 6200.

[89] Zhang, H.; Chen, T.; Huang, Z.; Hu, G.; Zhou, J.; Wang, S. A cathode-supported solid oxide fuel cell prepared by the phase-inversion tape casting and impregnating method. *International Journal of Hydrogen Energy* **2022,** *47* (43), 18810.

[90] Nakayama, S. Characteristics of electrolyte-supported SOFC single cells using hexagonal perovskite $Ba_3MoNbO_{8.5}$ and $Ba_7Nb_4MoO_{20}$ ceramics. *Results in Materials* **2022,** *16*, 100318.

[91] Wang, B.; Li, T.; Xiao, R.; Hartley, U. W.; Ueda, M.; Han, S. J.; Li, K. Study on the 4-channel micro-monolithic design with geometry control for reversible solid oxide cell. *Separation and Purification Technology* **2023,** *315*, 123732.

[92] Kusnezoff, M.; Trofimenko, N.; Müller, M.; Michaelis, A. Influence of Electrode Design and Contacting Layers on Performance of Electrolyte Supported SOFC/SOEC Single Cells. *Materials* **2016**, *9* (11), 906.

[93] Yamaguchi, T.; Shimizu, S.; Suzuki, T.; Fujishiro, Y.; Awano, M. Fabrication and evaluation of a novel cathode-supported honeycomb SOFC stack. *Materials Letters* **2009,** *63* (29), 2577.

[94] Wang, H.; Liu, J. Effect of anode structure on performance of cone-shaped solid oxide fuel cells fabricated by phase inversion. *International Journal of Hydrogen Energy* **2012,** *37* (5), 4339.

[95] Badwal, S. P. S.; Ciacchi, F. T. Oxygen-ion conducting electrolyte materials for solid oxide fuel cells. *Ionics* **2000,** *6* (1), 1.

[96] Xie, D.; Ling, A.; Yan, D.; Jia, L.; Chi, B.; Pu, J.; Li, J. A comparative study on the composite cathodes with proton conductor and oxygen ion conductor for proton-conducting solid oxide fuel cell. *Electrochimica Acta* **2020,** *344*, 136143.

[97] Mojaver, P.; Chitsaz, A.; Sadeghi, M.; Khalilarya, S. Comprehensive comparison of SOFCs with proton-conducting electrolyte and oxygen ion-conducting electrolyte: Thermoeconomic analysis and multi-

objective optimization. *Energy Conversion and Management* **2020,** *205*, 112455.

[98] Goodenough, J. B.; Huang, Y.-H. Alternative anode materials for solid oxide fuel cells. *Journal of Power Sources* **2007,** *173* (1), 1.

[99] Shri Prakash, B.; Senthil Kumar, S.; Aruna, S. T. Properties and development of Ni/YSZ as an anode material in solid oxide fuel cell: A review. *Renewable and Sustainable Energy Reviews* **2014,** *36*, 149.

[100] Khan, M. S.; Lee, S.-B.; Song, R.-H.; Lee, J.-W.; Lim, T.-H.; Park, S.-J. Fundamental mechanisms involved in the degradation of nickel–yttria stabilized zirconia (Ni-YSZ) anode during solid oxide fuel cells operation: A review. *Ceramics International* **2016,** *42* (1, Part A), 35.

[101] Du, Z.; Zhao, H.; Li, S.; Zhang, Y.; Chang, X.; Xia, Q.; Chen, N.; Gu, L.; Świerczek, K.; Li, Y.et al. Exceptionally High Performance Anode Material Based on Lattice Structure Decorated Double Perovskite $Sr_2FeMo_{2/3}Mg_{1/3}O_{6-\delta}$ for Solid Oxide Fuel Cells. *Advanced Energy Materials* **2018,** *8* (18), 1800062.

[102] Mahato, N.; Banerjee, A.; Gupta, A.; Omar, S.; Balani, K. Progress in material selection for solid oxide fuel cell technology: A review. *Progress in Materials Science* **2015,** *72*, 141.

[103] Laurencin, J.; Delette, G.; Morel, B.; Lefebvre-Joud, F.; Dupeux, M. Solid Oxide Fuel Cells damage mechanisms due to Ni-YSZ re-oxidation: Case of the Anode Supported Cell. *Journal of Power Sources* **2009,** *192*

(2), 344.

[104] Zhu, W. Z.; Deevi, S. C. A review on the status of anode materials for solid oxide fuel cells. *Materials Science and Engineering: A* **2003,** *362* (1), 228.

[105] Song, B.; Ruiz-Trejo, E.; Bertei, A.; Brandon, N. P. Quantification of the degradation of Ni-YSZ anodes upon redox cycling. *Journal of Power Sources* **2018,** *374*, 61.

[106] Waldbillig, D.; Wood, A.; Ivey, D. G. Thermal analysis of the cyclic reduction and oxidation behaviour of SOFC anodes. *Solid State Ionics* **2005,** *176* (9), 847.

[107] Lin, Y.-C.; Wei, W.-C. J. Porous Cu–Ni-YSZ cermets using CH_4 fuel for SOFC. *International Journal of Hydrogen Energy* **2020,** *45* (46), 24253.

[108] Wei, B.; Lü, Z.; Jia, D.; Huang, X.; Zhang, Y.; Su, W. Thermal expansion and electrochemical properties of Ni-doped $GdBaCo_2O_{5+\delta}$ double-perovskite type oxides. *International Journal of Hydrogen Energy* **2010,** *35* (8), 3775.

[109] Prasad, D. H.; Park, S. Y.; Oh, E. O.; Ji, H.; Kim, H. R.; Yoon, K. J.; Son, J. W.; Lee, J. H. Synthesis of nano-crystalline $La_{1-x}Sr_xCoO_{3-\delta}$ perovskite oxides by EDTA-citrate complexing process and its catalytic activity for soot oxidation. *Applied Catalysis A: General* **2012,** *447-448*, 100.

[110] Li, N.; Sun, L.; Li, Q.; Xia, T.; Huo, L.; Zhao, H. Novel and high-performance (La,Sr)MnO_3 based composite cathodes for intermediate-temperature solid oxide fuel cells. *Journal of the European Ceramic Society* **2023,** *43* (12), 5279.

[111] Jiang, S. P. Development of lanthanum strontium cobalt ferrite perovskite electrodes of solid oxide fuel cells - A review. *International Journal of Hydrogen Energy* **2019,** *44* (14), 7448.

[112] Huang, Z.; Qi, H.; Zhao, Z.; Shang, L.; Tu, B.; Cheng, M. Efficient CO_2 electroreduction on a solid oxide electrolysis cell with $La_{0.6}Sr_{0.4}Co_{0.2}Fe_{0.8}O_{3-\delta}$-$Gd_{0.2}Ce_{0.8}O_{2-\delta}$ infiltrated electrode. *Journal of Power Sources* **2019,** *434*, 226730.

[113] Carter, S.; Selcuk, A.; Chater, R. J.; Kajda, J.; Kilner, J. A.; Steele, B. C. H. Oxygen transport in selected nonstoichiometric perovskite-structure oxides. *Solid State Ionics* **1992,** *53-56*, 597.

[114] Katsuki, M.; Wang, S.; Dokiya, M.; Hashimoto, T. High temperature properties of $La_{0.6}Sr_{0.4}Co_{0.8}Fe_{0.2}O_{3-\delta}$ oxygen nonstoichiometry and chemical diffusion constant. *Solid State Ionics* **2003,** *156* (3), 453.

[115] Yao, Y.; Wang, C.; Ma, Y.; Ye, H.; Liu, Y.; Liu, J.; Zhao, X.; Tao, T.; Yao, Y.; Lu, S.et al. Preparation and performance of a nano-honeycomb cathode for microtubular solid oxide fuel cells. *International Journal of Hydrogen Energy* **2023,** *48* (13), 5229.

[116] Shen, C.-T.; Lee, K.-R.; Hsieh, Y.-P.; Lee, S.-W.; Chang, J.-K.; Jang, S.-C.; Tseng, C.-J. Effects of TiO_2 and SDC addition on the properties of YSZ electrolyte. *International Journal of Hydrogen Energy* **2019,** *44* (56), 29426.

[117] Xi, X.; Kondo, A.; Kozawa, T.; Naito, M. LSCF–GDC composite particles for solid oxide fuel cells cathodes prepared by facile mechanical method. *Advanced Powder Technology* **2016,** *27* (2), 646.

[118] Hussain, S.; Yangping, L. Review of solid oxide fuel cell materials: cathode, anode, and electrolyte. *Energy Transitions* **2020,** *4* (2), 113.

[119] Vinchhi, P.; Khandla, M.; Chaudhary, K.; Pati, R. Recent advances on electrolyte materials for SOFC: A review. *Inorganic Chemistry Communications* **2023,** *152*, 110724.

[120] Cho, G. Y.; Lee, Y. H.; Yu, W.; An, J.; Cha, S. W. Optimization of Y_2O_3 dopant concentration of yttria stabilized zirconia thin film electrolyte prepared by plasma enhanced atomic layer deposition for high performance thin film solid oxide fuel cells. *Energy* **2019,** *173*, 436.

[121] Arifin, N. A.; Afifi, A. A.; Samreen, A.; Hafriz, R. S. R. M.; Muchtar, A. Characteristic and challenges of scandia stabilized zirconia as solid oxide fuel cell material - In depth review. *Solid State Ionics* **2023,** *399*, 116302.

[122] Nikonov, A. V.; Kaygorodov, A. S.; Kuterbekov, K. A.; Bekmyrza, K. Z. Microhardness and fracture toughness of ZrO_2-Sc_2O_3 solid

electrolyte, doped with rare-earth and transition metals. *Inorganic Materials* **2017,** *53* (9), 937.

[123] Brandon, N. P.; Corcoran, D.; Cummins, D.; Duckett, A.; El-Khoury, K.; Haigh, D.; Leah, R.; Lewis, G.; Maynard, N.; McColm, T.et al. Development of metal supported solid oxide fuel cells for operation at 500-600 °C. *Journal of Materials Engineering and Performance* **2004,** *13* (3), 253.

[124] Szabo, P.; Arnold, J.; Franco, T.; Gindrat, M.; Refke, A.; Zagst, A.; Ansar, A. Progress in the Metal Supported Solid Oxide Fuel Cells and Stacks for APU. *ECS Transactions* **2009,** *25* (2), 175.

[125] Smart, W.; Weissbart, J. "Development of a CO_2-H_2O solid oxide electrolyte electrolysis system Annual report," **1970**.

[126] Shumar, J.; Berger, T. "Advanced solid electrolyte cell for CO_2 and H_2O electrolysis," **1978**.

[127] Isenberg, A. O. Energy conversion via solid oxide electrolyte electrochemical cells at high temperatures. *Solid State Ionics* **1981**, *3-4*, 431.

[128] Hino, R.; Aita, H.; Sekita, K.; Haga, K.; Iwata, T.-o. "Study on hydrogen production by high temperature electrolysis of steam," **1997**.

[129] Stoots, C. M.; O'Brien, J. E.; Condie, K. G.; Hartvigsen, J. J. High-temperature electrolysis for large-scale hydrogen production from nuclear energy – Experimental investigations. *International Journal of*

Hydrogen Energy **2010,** *35* (10), 4861.

[130] Brisse, A.; Schefold, J. High Temperature Electrolysis at EIFER, Main Achievements at Cell and Stack Level. *Energy Procedia* **2012,** *29*, 53.

[131] Ebbesen, S. D.; Mogensen, M. Electrolysis of carbon dioxide in Solid Oxide Electrolysis Cells. *Journal of Power Sources* **2009,** *193* (1), 349.

[132] Anelli, S.; Hernández, E.; Bernadet, L.; Sun, X.; Hagen, A.; Baiutti, F.; Torrell, M.; Tarancón, A. Co-electrolysis of steam and carbon dioxide in large area solid oxide cells based on infiltrated mesoporous oxygen electrodes. *Journal of Power Sources* **2020,** *478*, 228774.

[133] Song, Y.; Zhang, X.; Zhou, Y.; Jiang, Q.; Guan, F.; Lv, H.; Wang, G.; Bao, X. Promoting oxygen evolution reaction by RuO_2 nanoparticles in solid oxide CO_2 electrolyzer. *Energy Storage Materials* **2018,** *13*, 207.

[134] Song, Y.; Zhang, X.; Zhou, Y.; Lv, H.; Liu, Q.; Feng, W.; Wang, G.; Bao, X. Improving the performance of solid oxide electrolysis cell with gold nanoparticles-modified LSM-YSZ anode. *Journal of Energy Chemistry* **2019,** *35*, 181.

[135] Tian, Y.; Zheng, H.; Zhang, L.; Chi, B.; Pu, J.; Li, J. Direct Electrolysis of CO_2 in Symmetrical Solid Oxide Electrolysis Cell Based on $La_{0.6}Sr_{0.4}Fe_{0.8}Ni_{0.2}O_{3-\delta}$ Electrode. *Journal of The Electrochemical Society* **2018,** *165* (2), F17.

[136] Kwon, Y.; Yoo, J. Y.; Jang, Y.-h.; Bae, J. Long-term durability of $La_{0.75}Sr_{0.25}Cr_{0.5}Mn_{0.5}O_{\delta-3}$ as a fuel electrode of solid oxide electrolysis cells for co-electrolysis. *Journal of CO_2 Utilization* **2019,** *31*, 192.

[137] Yue, X.; Irvine, J. T. S. Alternative Cathode Material for CO_2 Reduction by High Temperature Solid Oxide Electrolysis Cells. *Journal of The Electrochemical Society* **2012,** *159* (8), F442.

[138] Duan, N.; Yang, J.; Gao, M.; Zhang, B.; Luo, J.-L.; Du, Y.; Xu, M.; Jia, L.; Chi, B.; Li, J. Multi-functionalities enabled fivefold applications of $LaCo_{0.6}Ni_{0.4}O_{3-\delta}$ in intermediate temperature symmetrical solid oxide fuel/electrolysis cells. *Nano Energy* **2020,** *77*, 105207.

[139] Peng, X.; Tian, Y.; Liu, Y.; Wang, W.; Jia, L.; Pu, J.; Chi, B.; Li, J. An efficient symmetrical solid oxide electrolysis cell with LSFM-based electrodes for direct electrolysis of pure CO_2. *Journal of CO_2 Utilization* **2020,** *36*, 18.

[140] Zheng, Y.; Wang, S.; Pan, Z.; Yin, B. Electrochemical CO_2 reduction to CO using solid oxide electrolysis cells with high-performance Ta-doped bismuth strontium ferrite air electrode. *Energy* **2021,** *228*, 120579.

[141] Tian, Y.; Zhang, L.; Liu, Y.; Jia, L.; Yang, J.; Chi, B.; Pu, J.; Li, J. A self-recovering robust electrode for highly efficient CO_2 electrolysis in symmetrical solid oxide electrolysis cells. *Journal of Materials Chemistry A* **2019,** *7* (11), 6395.

[142] Wang, M.; Wang, J.; Du, J. A symmetrical solid oxide electrolysis cell supported by nanostructured electrodes for highly efficient CO_2 electrolysis. *Journal of Power Sources* **2024,** *610*, 234742.

[143] Lu, L.; Liu, W.; Wang, J.; Wang, Y.; Xia, C.; Zhou, X.-D.; Chen, M.; Guan, W. Long-term stability of carbon dioxide electrolysis in a large-scale flat-tube solid oxide electrolysis cell based on double-sided air electrodes. *Applied Energy* **2020,** *259*, 114130.

[144] Aslam, S.; Rani, S.; Lal, K.; Fatima, M.; Hardwick, T.; Shirinfar, B.; Ahmed, N. Electrochemical hydrogen production: sustainable hydrogen economy. *Green Chemistry* **2023,** *25* (23), 9543.

[145] Zhu, Q.; Zeng, Y.; Zheng, Y. Overview of CO_2 capture and electrolysis technology in molten salts: operational parameters and their effects. *Industrial Chemistry & Materials* **2023,** *1* (4), 595.

[146] Kutz, R. B.; Chen, Q.; Yang, H.; Sajjad, S. D.; Liu, Z.; Masel, I. R. Sustainion Imidazolium-Functionalized Polymers for Carbon Dioxide Electrolysis. *Energy Technology* **2017,** *5* (6), 929.

[147] Hosseini-Benhangi, P.; Gyenge, C. C.; Gyenge, E. L. The carbon dioxide redox flow battery: Bifunctional CO_2 reduction/formate oxidation electrocatalysis on binary and ternary catalysts. *Journal of Power Sources* **2021,** *495*, 229752.

[148] Guo, Y.; Zhang, R.; Zhang, S.; Zhi, C. Recent advances in Zn-CO_2 batteries for the co-production of electricity and carbonaceous fuels.

Nano Materials Science **2022**, DOI:https://doi.org/10.1016/j.nanoms.2022.09.004 https://doi.org/10.1016/j.nanoms.2022.09.004.

[149] Gao, S.; Wei, T.; Sun, J.; Liu, Q.; Ma, D.; Liu, W.; Zhang, S.; Luo, J.; Liu, X. Atomically Dispersed Metal-Based Catalysts for Zn-CO_2 Batteries. *Small Structures* **2022,** *3* (12), 2200086.

[150] Xie, J.; Wang, X.; Lv, J.; Huang, Y.; Wu, M.; Wang, Y.; Yao, J. Reversible Aqueous Zinc-CO_2 Batteries Based on CO_2-HCOOH Interconversion. *Angewandte Chemie International Edition* **2018,** *57* (52), 16996.

[151] Kaur, S.; Kumar, M.; Gupta, D.; Mohanty, P. P.; Das, T.; Chakraborty, S.; Ahuja, R.; Nagaiah, T. C. Efficient CO_2 utilization and sustainable energy conversion via aqueous Zn-CO_2 batteries. *Nano Energy* **2023,** *109*, 108242.

[152] Nevin Kelly, P.; Woodard Trevor, L.; Franks Ashley, E.; Summers Zarath, M.; Lovley Derek, R. Microbial Electrosynthesis: Feeding Microbes Electricity To Convert Carbon Dioxide and Water to Multicarbon Extracellular Organic Compounds. *mBio* **2010,** *1* (2), 10.1128/mbio.00103.

[153] Bajracharya, S.; Srikanth, S.; Mohanakrishna, G.; Zacharia, R.; Strik, D. P.; Pant, D. Biotransformation of carbon dioxide in bioelectrochemical systems: State of the art and future prospects.

Journal of Power Sources **2017,** *356*, 256.

[154] Ayol, A.; Peixoto, L.; Keskin, T.; Abubackar, H. N. Reactor Designs and Configurations for Biological and Bioelectrochemical C1 Gas Conversion: A Review. *International Journal of Environmental Research and Public Health* **2021,** *18* (21), 11683.

[155] Rodríguez-Alegre, R.; Ceballos-Escalera, A.; Molognoni, D.; Bosch-Jimenez, P.; Galí, D.; Licon, E.; Della Pirriera, M.; Garcia-Montaño, J.; Borràs, E. Integration of Membrane Contactors and Bioelectrochemical Systems for CO_2 Conversion to CH_4. *Energies* **2019,** *12* (3), 361.

[156] Xu, H.; Feng, J.-X.; Tong, Y.-X.; Li, G.-R. Cu_2O-Cu Hybrid Foams as High-Performance Electrocatalysts for Oxygen Evolution Reaction in Alkaline Media. *ACS Catalysis* **2017,** *7* (2), 986.

[157] Luo, J.-T.; Zang, G.-L.; Hu, C. An efficient 3D ordered mesoporous Cu sphere array electrocatalyst for carbon dioxide electrochemical reduction. *Journal of Materials Science & Technology* **2020,** *55*, 95.

[158] Reske, R.; Mistry, H.; Behafarid, F.; Roldan Cuenya, B.; Strasser, P. Particle Size Effects in the Catalytic Electroreduction of CO_2 on Cu Nanoparticles. *Journal of the American Chemical Society* **2014,** *136* (19), 6978.

[159] Zheng, T.; Liu, C.; Guo, C.; Zhang, M.; Li, X.; Jiang, Q.; Xue, W.; Li, H.; Li, A.; Pao, C.-W.et al. Copper-catalysed exclusive CO_2 to pure

formic acid conversion via single-atom alloying. *Nature Nanotechnology* **2021,** *16* (12), 1386.

[160] Zeng, J.; Bejtka, K.; Ju, W.; Castellino, M.; Chiodoni, A.; Sacco, A.; Farkhondehfal, M. A.; Hernández, S.; Rentsch, D.; Battaglia, C.et al. Advanced Cu-Sn foam for selectively converting CO_2 to CO in aqueous solution. *Applied Catalysis B: Environmental* **2018,** *236*, 475.

[161] Dai, Y.; Li, H.; Wang, C.; Xue, W.; Zhang, M.; Zhao, D.; Xue, J.; Li, J.; Luo, L.; Liu, C.et al. Manipulating local coordination of copper single atom catalyst enables efficient CO_2-to-CH_4 conversion. *Nature Communications* **2023,** *14* (1), 3382.

[162] Song, H.; Song, J. T.; Kim, B.; Tan, Y. C.; Oh, J. Activation of C_2H_4 reaction pathways in electrochemical CO_2 reduction under low CO_2 partial pressure. *Applied Catalysis B: Environmental* **2020,** *272*, 119049.

[163] Xiang, K.; Liu, Y.; Li, C.; Liu, X.; Yi, H.; Wu, L.; Shen, F.; Liu, M.; Wang, P.; Liu, H. Microenvironmental Feeding and Stabilization of C_2H_4 Intermediates by Iodide-Doped Copper Nanowire Arrays to Boost C_2H_6 Formation. *Energy & Fuels* **2021,** *35* (19), 15987.

[164] Xie, H.; Wang, T.; Liang, J.; Li, Q.; Sun, S. Cu-based nanocatalysts for electrochemical reduction of CO_2. *Nano Today* **2018,** *21*, 41.

[165] Hemminger, J. C.; Carr, R.; Somorjai, G. A. The photoassisted reaction of gaseous water and carbon dioxide adsorbed on the $SrTiO_3$ (111) crystal face to form methane. *Chemical Physics Letters* **1978,** *57*

(1), 100.

[166] Ran, J.; Jaroniec, M.; Qiao, S.-Z. Cocatalysts in Semiconductor-based Photocatalytic CO_2 Reduction: Achievements, Challenges, and Opportunities. *Advanced Materials* **2018,** *30* (7), 1704649.

[167] Wang, Y.; Chen, E.; Tang, J. Insight on Reaction Pathways of Photocatalytic CO_2 Conversion. *ACS Catalysis* **2022,** *12* (12), 7300.

[168] Mei, D.; Zhu, X.; Wu, C.; Ashford, B.; Williams, P. T.; Tu, X. Plasma-photocatalytic conversion of CO_2 at low temperatures: Understanding the synergistic effect of plasma-catalysis. *Applied Catalysis B: Environmental* **2016,** *182*, 525.

[169] Ashford, B.; Wang, Y.; Poh, C.-K.; Chen, L.; Tu, X. Plasma-catalytic conversion of CO_2 to CO over binary metal oxide catalysts at low temperatures. *Applied Catalysis B: Environmental* **2020,** *276*, 119110.

[170] Snoeckx, R.; Bogaerts, A. Plasma technology - a novel solution for CO_2 conversion? *Chemical Society Reviews* **2017,** *46* (19), 5805.

[171] Zha, S.; Cheng, Z.; Liu, M. Sulfur Poisoning and Regeneration of Ni-Based Anodes in Solid Oxide Fuel Cells. *Journal of The Electrochemical Society* **2007,** *154* (2), B201.

[172] Skafte, T. L.; Blennow, P.; Hjelm, J.; Graves, C. Carbon deposition and sulfur poisoning during CO_2 electrolysis in nickel-based solid oxide cell electrodes. *Journal of Power Sources* **2018,** *373*, 54.

[173] Sehested, J.; Gelten, J. A. P.; Helveg, S. Sintering of nickel catalysts: Effects of time, atmosphere, temperature, nickel-carrier interactions, and dopants. *Applied Catalysis A: General* **2006,** *309* (2), 237.

[174] Sun, X.; Chen, M.; Liu, Y.-L.; Hjalmarsson, P.; Ebbesen, S. D.; Jensen, S. H.; Mogensen, M. B.; Hendriksen, P. V. Durability of Solid Oxide Electrolysis Cells for Syngas Production. *Journal of The Electrochemical Society* **2013,** *160* (9), F1074.

[175] Holzer, L.; Iwanschitz, B.; Hocker, T.; Münch, B.; Prestat, M.; Wiedenmann, D.; Vogt, U.; Holtappels, P.; Sfeir, J.; Mai, A.et al. Microstructure degradation of cermet anodes for solid oxide fuel cells: Quantification of nickel grain growth in dry and in humid atmospheres. *Journal of Power Sources* **2011,** *196* (3), 1279.

[176] Mogensen, M. B.; Chen, M.; Frandsen, H. L.; Graves, C.; Hauch, A.; Hendriksen, P. V.; Jacobsen, T.; Jensen, S. H.; Skafte, T. L.; Sun, X. Ni migration in solid oxide cell electrodes: Review and revised hypothesis. *Fuel Cells* **2021,** *21* (5), 415.

[177] Tao, Y.; Ebbesen, S. D.; Mogensen, M. B. Degradation of solid oxide cells during co-electrolysis of steam and carbon dioxide at high current densities. *Journal of Power Sources* **2016,** *328*, 452.

[178] Trini, M.; Hauch, A.; De Angelis, S.; Tong, X.; Hendriksen, P. V.; Chen, M. Comparison of microstructural evolution of fuel electrodes in solid oxide fuel cells and electrolysis cells. *Journal of Power Sources*

2020, *450*, 227599.

[179] Khan, M. S.; Xu, X.; Knibbe, R.; Zhu, Z. Air electrodes and related degradation mechanisms in solid oxide electrolysis and reversible solid oxide cells. *Renewable and Sustainable Energy Reviews* **2021,** *143*, 110918.

[180] Chen, K.; Jiang, S. P. Failure mechanism of (La,Sr)MnO_3 oxygen electrodes of solid oxide electrolysis cells. *International Journal of Hydrogen Energy* **2011,** *36* (17), 10541.

[181] Park, B.-K.; Zhang, Q.; Voorhees, P. W.; Barnett, S. A. Conditions for stable operation of solid oxide electrolysis cells: oxygen electrode effects. *Energy & Environmental Science* **2019,** *12* (10), 3053.

[182] Graves, C.; Ebbesen, S. D.; Jensen, S. H.; Simonsen, S. B.; Mogensen, M. B. Eliminating degradation in solid oxide electrochemical cells by reversible operation. *Nature Materials* **2015,** *14* (2), 239.

[183] Laguna-Bercero, M. A.; Campana, R.; Larrea, A.; Kilner, J. A.; Orera, V. M. Electrolyte degradation in anode supported microtubular yttria stabilized zirconia-based solid oxide steam electrolysis cells at high voltages of operation. *Journal of Power Sources* **2011,** *196* (21), 8942.

[184] Wang, H.; Yakal-Kremski, K. J.; Yeh, T.; Rupp, G. M.; Limbeck, A.; Fleig, J.; Barnett, S. A. Mechanisms of Performance Degradation of

(La,Sr)(Co,Fe)$O_{3-\delta}$ Solid Oxide Fuel Cell Cathodes. *Journal of The Electrochemical Society* **2016,** *163* (6), F581.

[185] Lee, W.; Han, J. W.; Chen, Y.; Cai, Z.; Yildiz, B. Cation Size Mismatch and Charge Interactions Drive Dopant Segregation at the Surfaces of Manganite Perovskites. *Journal of the American Chemical Society* **2013,** *135* (21), 7909.

[186] Jacobsen, T.; Mogensen, M. The Course of Oxygen Partial Pressure and Electric Potentials across an Oxide Electrolyte Cell. *ECS Transactions* **2008,** *13* (26), 259.

[187] Moçoteguy, P.; Brisse, A. A review and comprehensive analysis of degradation mechanisms of solid oxide electrolysis cells. *International Journal of Hydrogen Energy* **2013,** *38* (36), 15887.

[188] Sakai, N.; Horita, T.; Yamaji, K.; Xiong, Y. P.; Kishimoto, H.; Brito, M. E.; Yokokawa, H. Material transport and degradation behavior of SOFC interconnects. *Solid State Ionics* **2006,** *177* (19), 1933.

[189] Larrain, D.; Van herle, J.; Favrat, D. Simulation of SOFC stack and repeat elements including interconnect degradation and anode reoxidation risk. *Journal of Power Sources* **2006,** *161* (1), 392.

[190] Liu, Y. L.; Jiao, C. Microstructure degradation of an anode/electrolyte interface in SOFC studied by transmission electron microscopy. *Solid State Ionics* **2005,** *176* (5), 435.

[191] Yan, D.; Liang, L.; Yang, J.; Zhang, T.; Pu, J.; Chi, B.; Li, J.

Performance degradation and analysis of 10-cell anode-supported SOFC stack with external manifold structure. *Energy* **2017,** *125*, 663.

[192] Nakajo, A.; Mueller, F.; Brouwer, J.; Van herle, J.; Favrat, D. Mechanical reliability and durability of SOFC stacks. Part II: Modelling of mechanical failures during ageing and cycling. *International Journal of Hydrogen Energy* **2012,** *37* (11), 9269.

[193] Zhang, X.; O'Brien, J. E.; O'Brien, R. C.; Hartvigsen, J. J.; Tao, G.; Housley, G. K. Improved durability of SOEC stacks for high temperature electrolysis. *International Journal of Hydrogen Energy* **2013,** *38* (1), 20.

[194] Zhang, X.; O'Brien, J. E.; Tao, G.; Zhou, C.; Housley, G. K. Experimental design, operation, and results of a 4 kW high temperature steam electrolysis experiment. *Journal of Power Sources* **2015,** *297*, 90.

[195] Schefold, J.; Brisse, A.; Poepke, H. 23,000 h steam electrolysis with an electrolyte supported solid oxide cell. *International Journal of Hydrogen Energy* **2017,** *42* (19), 13415.

[196] Ebbesen, S. D.; Høgh, J.; Nielsen, K. A.; Nielsen, J. U.; Mogensen, M. Durable SOC stacks for production of hydrogen and synthesis gas by high temperature electrolysis. *International Journal of Hydrogen Energy* **2011,** *36* (13), 7363.

[197] Wonsyld, K.; Bech, L.; Nielsen, J. U.; Pedersen, C. F. Operational robustness studies of solid oxide electrolysis stacks. *Journal of Energy*

and Power Engineering **2015,** *9*, 128.

[198] Reytier, M.; Di Iorio, S.; Chatroux, A.; Petitjean, M.; Cren, J.; De Saint Jean, M.; Aicart, J.; Mougin, J. Stack performances in high temperature steam electrolysis and co-electrolysis. *International Journal of Hydrogen Energy* **2015,** *40* (35), 11370.

[199] Küngas, R.; Blennow, P.; Heiredal-Clausen, T.; Holt, T.; Rass-Hansen, J.; Primdahl, S. Systematic Lifetime Testing of Stacks in CO_2 Electrolysis. *ECS Transactions* **2017,** *78* (1), 2895.

[200] Li, S.; Yang, Z.; Shen, Q.; Yang, G. A Parametric Study on the Interconnector of Solid Oxide Electrolysis Cells for Co-Electrolysis of Water and Carbon Dioxide. *Journal of Marine Science and Engineering* **2023,** *11* (5), 1066.

[201] Mendonça, C.; Ferreira, A.; Santos, D. M. F. Towards the Commercialization of Solid Oxide Fuel Cells: Recent Advances in Materials and Integration Strategies. *Fuels* **2021,** *2* (4), 393.

[202] Braz, B. A.; Moreira, C. S.; Oliveira, V. B.; Pinto, A. M. F. R. Electrochemical impedance spectroscopy as a diagnostic tool for passive direct methanol fuel cells. *Energy Reports* **2022,** *8*, 7964.

[203] Quattrocchi, E.; Py, B.; Maradesa, A.; Meyer, Q.; Zhao, C.; Ciucci, F. Deconvolution of electrochemical impedance spectroscopy data using the deep-neural-network-enhanced distribution of relaxation times. *Electrochimica Acta* **2023,** *439*, 141499.

[204] Ahmad, Z.; Mishra, A.; Abdulrahim, S. M.; Touati, F. Electrical equivalent circuit (EEC) based impedance spectroscopy analysis of HTM free perovskite solar cells. *Journal of Electroanalytical Chemistry* **2020,** *871*, 114294.

[205] Matsui, T.; Kosaka, T.; Inaba, M.; Mineshige, A.; Ogumi, Z. Effects of mixed conduction on the open-circuit voltage of intermediate-temperature SOFCs based on Sm-doped ceria electrolytes. *Solid State Ionics* **2005,** *176* (7), 663.

[206] Wu, A.; Xiong, M.; Zhang, Y.; Hanson, S.; Wang, J.; Guan, W.; Singhal, S. C. CO_2 utilization by reversible solid oxide cells towards carbon neutralization for long-term energy storage. *Chemical Engineering Journal* **2023,** *466*, 143275.

[207] Alzate-Restrepo, V.; Hill, J. M. Carbon deposition on Ni/YSZ anodes exposed to CO/H_2 feeds. *Journal of Power Sources* **2010,** *195* (5), 1344.

[208] Zhang, Y.; Shen, L.; Wang, Y.; Du, Z.; Zhang, B.; Ciucci, F.; Zhao, H. Enhanced oxygen reduction kinetics of IT-SOFC cathode with $PrBaCo2O_{5+\delta}/Gd_{0.1}Ce_{1.9}O_{2-\delta}$ coherent interface. *Journal of Materials Chemistry A* **2022,** *10* (7), 3495.

[209] Fujimatsu, R.; Oda, T.; Kobayashi, M.; Ohka, H.; Izumi, M. Measurement of Oxygen Partial Pressure in Fuel Electrode of SOFC. *ECS Transactions* **2016,** *71* (1), 113.

[210] Zhan, Z.; Zhao, L. Electrochemical reduction of CO_2 in solid oxide electrolysis cells. *Journal of Power Sources* **2010,** *195* (21), 7250.

[211] Wang, T.; Wang, J.; Yu, L.; Ye, Z.; Hu, X.; Marnellos, G. E.; Dong, D. Effect of NiO/YSZ cathode support pore structure on CO_2 electrolysis via solid oxide electrolysis cells. *Journal of the European Ceramic Society* **2018,** *38* (15), 5051.

[212] Sumi, H.; Shimada, H.; Yamaguchi, Y.; Mizutani, Y.; Okuyama, Y.; Amezawa, K. Comparison of electrochemical impedance spectra for electrolyte-supported solid oxide fuel cells (SOFCs) and protonic ceramic fuel cells (PCFCs). *Scientific Reports* **2021,** *11* (1), 10622.

[213] Singh, V.; Muroyama, H.; Matsui, T.; Eguchi, K. Performance and Stability of Solid Oxide Electrolysis Cell for CO_2 Reduction under Various Operating Conditions. *Electrochemistry* **2014,** *82* (10), 839.

[214] Yue, X.; Irvine, J. T. S. Impedance Studies on LSCM/GDC Cathode for High Temperature CO_2 Electrolysis. *Electrochemical and Solid-State Letters* **2012,** *15* (3), B31.

[215] Graves, C.; Ebbesen, S. D.; Mogensen, M. Co-electrolysis of CO_2 and H_2O in solid oxide cells: Performance and durability. *Solid State Ionics* **2011,** *192* (1), 398.

[216] Kim, J. W.; Virkar, A. V.; Fung, K. Z.; Mehta, K.; Singhal, S. C. Polarization Effects in Intermediate Temperature, Anode-Supported Solid Oxide Fuel Cells. *Journal of The Electrochemical Society* **1999,**

146 (1), 69.

[217] Baker, D. R.; Wieser, C.; Neyerlin, K. C.; Murphy, M. W. The Use of Limiting Current to Determine Transport Resistance in PEM Fuel Cells. *ECS Transactions* **2006,** *3* (1), 989.

[218] Chen, Y.; Lewis, N. S.; Xiang, C. Modeling the Performance of A Flow-Through Gas Diffusion Electrode for Electrochemical Reduction of CO or CO_2. *Journal of The Electrochemical Society* **2020,** *167* (11), 114503.

[219] Hong, J.; Bhardwaj, A.; Bae, H.; Kim, I.-h.; Song, S.-J. Electrochemical Impedance Analysis of SOFC with Transmission Line Model Using Distribution of Relaxation Times (DRT). *Journal of The Electrochemical Society* **2020,** *167* (11), 114504.

[220] Osinkin, D. A. Identification of gas diffusion phenomena on highly active Ni–ceramic anodes using the DRT technique. *Journal of Power Sources* **2023,** *571*, 233085.

[221] Wang, Y.; Marchetti, B.; Zhou, X.-D. Call attention to using DRT and EIS to quantify the contributions of solid oxide cell components to the total impedance. *International Journal of Hydrogen Energy* **2022,** *47* (83), 35437.

[222] Osinkin, D. A. An approach to the analysis of the impedance spectra of solid oxide fuel cell using the DRT technique. *Electrochimica Acta* **2021,** *372*, 137858.

[223] Kullmann, F.; Mueller, M.; Lindner, A.; Dierickx, S.; Mueller, E.; Weber, A. DRT analysis and transmission line modeling of ceria based electrodes for solid oxide cells. *Journal of Power Sources* **2023,** *587*, 233706.

[224] Baldinelli, A.; Staffolani, A.; Bidini, G.; Barelli, L.; Nobili, F. An extensive model for renewable energy electrochemical storage with Solid Oxide Cells based on a comprehensive analysis of impedance deconvolution. *Journal of Energy Storage* **2021,** *33*, 102052.

[225] Caliandro, P.; Nakajo, A.; Diethelm, S.; Van herle, J. Model-assisted identification of solid oxide cell elementary processes by electrochemical impedance spectroscopy measurements. *Journal of Power Sources* **2019,** *436*, 226838.

[226] Osinkin, D. A. Detailed analysis of electrochemical behavior of high–performance solid oxide fuel cell using DRT technique. *Journal of Power Sources* **2022,** *527*, 231120.

[227] Häffelin, A.; Joos, J.; Ender, M.; Weber, A.; Ivers-Tiffée, E. Time-Dependent 3D Impedance Model of Mixed-Conducting Solid Oxide Fuel Cell Cathodes. *Journal of The Electrochemical Society* **2013,** *160* (8), F867.

[228] Yan, J.; Chen, H.; Dogdibegovic, E.; Stevenson, J. W.; Cheng, M.; Zhou, X.-D. High-efficiency intermediate temperature solid oxide electrolyzer cells for the conversion of carbon dioxide to fuels. *Journal*

of Power Sources **2014,** *252*, 79.

[229] Mahmoud, A.; Al Daroukh, M.; Lipinska-Chwalek, M.; Luysberg, M.; Tietz, F.; Hermann, R. P. A Mössbauer spectral study of degradation in $La_{0.58}Sr_{0.4}Fe_{0.5}Co_{0.5}O_{3-x}$ after long-term operation in solid oxide electrolysis cells. *Solid State Ionics* **2017,** *312*, 38.

[230] Laurencin, J.; Hubert, M.; Sanchez, D. F.; Pylypko, S.; Morales, M.; Morata, A.; Morel, B.; Montinaro, D.; Lefebvre-Joud, F.; Siebert, E. Degradation mechanism of $La_{0.6}Sr_{0.4}Co_{0.2}Fe_{0.8}O_{3-\delta}/Gd_{0.1}Ce_{0.9}O_{2-\delta}$ composite electrode operated under solid oxide electrolysis and fuel cell conditions. *Electrochimica Acta* **2017,** *241*, 459.

[231] Chen, K.; Li, N.; Ai, N.; Cheng, Y.; Rickard, W. D. A.; Jiang, S. P. Polarization-Induced Interface and Sr Segregation of in Situ Assembled $La_{0.6}Sr_{0.4}Co_{0.2}Fe_{0.8}O_{3-\delta}$ Electrodes on Y_2O_3-ZrO_2 Electrolyte of Solid Oxide Fuel Cells. *ACS Applied Materials & Interfaces* **2016,** *8* (46), 31729.

[232] Hartvigsen, J.; Elangovan, S.; Elwell, J.; Larsen, D.; Clark, L. M.; Meaders, T. Mechanical, Structural, and Thermal Qualification of Solid Oxide Elextrolysis for Oxygen Production from Mars Atmosphere Carbon Dioxide. *ECS Transactions* **2017,** *78* (1), 3317.

[233] Liu, Z.; Han, B.; Lu, Z.; Guan, W.; Li, Y.; Song, C.; Chen, L.; Singhal, S. C. Efficiency and stability of hydrogen production from seawater using solid oxide electrolysis cells. *Applied Energy* **2021,** *300*,

117439.

[234] Li, Y.; Zhan, Z.; Xia, C. Highly efficient electrolysis of pure CO_2 with symmetrical nanostructured perovskite electrodes. *Catalysis Science & Technology* **2018,** *8* (4), 980.

[235] Kennouche, D.; Fang, Q.; Blum, L.; Stolten, D. Analysis of the Cathode Electrical Contact in SOFC Stacks. *Journal of The Electrochemical Society* **2018,** *165* (9), F677.

[236] Burnat, D.; Nurk, G.; Holzer, L.; Kopecki, M.; Heel, A. Lanthanum doped strontium titanate - ceria anodes: deconvolution of impedance spectra and relationship with composition and microstructure. *Journal of Power Sources* **2018,** *385*, 62.

[237] Jensen, S. H.; Hauch, A.; Hendriksen, P. V.; Mogensen, M.; Bonanos, N.; Jacobsen, T. A Method to Separate Process Contributions in Impedance Spectra by Variation of Test Conditions. *Journal of The Electrochemical Society* **2007,** *154* (12), B1325.

[238] Nuggehalli Sampathkumar, S.; Aubin, P.; Couturier, K.; Sun, X.; Sudireddy, B. R.; Diethelm, S.; Pérez-Fortes, M.; Van herle, J. Degradation study of a reversible solid oxide cell (rSOC) short stack using distribution of relaxation times (DRT) analysis. *International Journal of Hydrogen Energy* **2022,** *47* (18), 10175.

[239] Lee, S.; Kim, M.; Lee, K. T.; Irvine, J. T. S.; Shin, T. H. Enhancing Electrochemical CO_2 Reduction using $Ce(Mn,Fe)O_2$ with

La(Sr)Cr(Mn)O_3 Cathode for High-Temperature Solid Oxide Electrolysis Cells. *Advanced Energy Materials* **2021,** *11* (24), 2100339.

[240] Igathinathane, C.; Pordesimo, L. O.; Columbus, E. P.; Batchelor, W. D.; Methuku, S. R. Shape identification and particles size distribution from basic shape parameters using ImageJ. *Computers and Electronics in Agriculture* **2008,** *63* (2), 168.

[241] Trini, M.; De Angelis, S.; Jørgensen, P. S.; Hendriksen, P. V.; Thornton, K.; Chen, M. Towards the Validation of a Phase Field Model for Ni Coarsening in Solid Oxide Cells. *Acta Materialia* **2021,** *212*, 116887.

[242] Mason, J.; Celik, I.; Lee, S.; Abernathy, H.; Hackett, G. Performance Degradation Predictions Based on Microstructural Evolution Due to Grain Coarsening Effects in Solid Oxide Fuel Cell Electrodes. *Journal of The Electrochemical Society* **2018,** *165* (2), F64.

[243] Yao, Y.; Wang, C.; Ma, Y.; Ye, H.; Liu, Y.; Liu, J.; Zhao, X.; Tao, T.; Yao, Y.; Lu, S.et al. Preparation and performance of a nano-honeycomb cathode for microtubular solid oxide fuel cells. *International Journal of Hydrogen Energy* **2023,** *48* (13), 5229.

[244] Fabbri, E.; Bi, L.; Pergolesi, D.; Traversa, E. Towards the Next Generation of Solid Oxide Fuel Cells Operating Below 600 °C with Chemically Stable Proton-Conducting Electrolytes. *Advanced Materials* **2012,** *24* (2), 195.

[245] Zhang, S.; Wei, J.; Chen, X.; Zhao, Y. China in global wind power development: Role, status and impact. *Renewable and Sustainable Energy Reviews* **2020,** *127*, 109881.

[246] Dong, C.; Qi, Y.; Dong, W.; Lu, X.; Liu, T.; Qian, S. Decomposing driving factors for wind curtailment under economic new normal in China. *Applied Energy* **2018,** *217*, 178.

[247] Carton, J. G.; Olabi, A. G. Wind/hydrogen hybrid systems: Opportunity for Ireland's wind resource to provide consistent sustainable energy supply. *Energy* **2010,** *35* (12), 4536.

[248] Bianchi, F. R.; Bosio, B.; Conte, F.; Massucco, S.; Mosaico, G.; Natrella, G.; Saviozzi, M. Modelling and optimal management of renewable energy communities using reversible solid oxide cells. *Applied Energy* **2023,** *334*, 120657.

[249] Califano, M.; Sorrentino, M.; Rosen, M. A.; Pianese, C. Optimal heat and power management of a reversible solid oxide cell based microgrid for effective technoeconomic hydrogen consumption and storage. *Applied Energy* **2022,** *319*, 119268.

[250] Biswas, S.; Kulkarni, A. P.; Giddey, S.; Bhattacharya, S. A Review on Synthesis of Methane as a Pathway for Renewable Energy Storage With a Focus on Solid Oxide Electrolytic Cell-Based Processes. *Frontiers in Energy Research* **2020,** *8*.

[251] Hauch, A.; Ebbesen, S. D.; Jensen, S. H.; Mogensen, M. Highly

efficient high temperature electrolysis. *Journal of Materials Chemistry* **2008,** *18* (20), 2331.

[252] Li, Q.; Zheng, Y.; Sun, Y.; Li, T.; Xu, C.; Wang, W.; Chan, S. H. Understanding the occurrence of the individual CO_2 electrolysis during H_2O-CO_2 co-electrolysis in classic planar Ni-YSZ/YSZ/LSM-YSZ solid oxide cells. *Electrochimica Acta* **2019,** *318*, 440.

[253] Salomone, F.; Giglio, E.; Ferrero, D.; Santarelli, M.; Pirone, R.; Bensaid, S. Techno-economic modelling of a Power-to-Gas system based on SOEC electrolysis and CO_2 methanation in a RES-based electric grid. *Chemical Engineering Journal* **2019,** *377*, 120233.

[254] Anelli, S.; Baiutti, F.; Hornés, A.; Bernadet, L.; Torrell, M.; Tarancón, A. Improved mesostructured oxygen electrodes for highly performing solid oxide cells for co-electrolysis of steam and carbon dioxide. *Journal of Materials Chemistry A* **2019,** *7* (48), 27458.

[255] Yang, Y.; Tong, X.; Hauch, A.; Sun, X.; Yang, Z.; Peng, S.; Chen, M. Study of solid oxide electrolysis cells operated in potentiostatic mode: Effect of operating temperature on durability. *Chemical Engineering Journal* **2021,** *417*, 129260.

[256] Mehran, M. T.; Khan, M. Z.; Lee, S.-B.; Lim, T.-H.; Park, S.; Song, R.-H. Improving sulfur tolerance of Ni-YSZ anodes of solid oxide fuel cells by optimization of microstructure and operating conditions. *International Journal of Hydrogen Energy* **2018,** *43* (24), 11202.

[257] Li, Z.; Deng, L.; Kinloch, I. A.; Young, R. J. Raman spectroscopy of carbon materials and their composites: Graphene, nanotubes and fibres. *Progress in Materials Science* **2023,** *135*, 101089.

[258] Graves, C.; Villarreal, D.; Myrdal, J. S. G.; Jensen, S. H.; Chen, M.; Hendriksen, P. V.; Mogensen, M. B. (Invited) Reversible Operation of Solid Oxide Cells for Sustainable Fuel Production and Solar/Wind Load-Balancing. *ECS Meeting Abstracts* **2016,** *MA2016-02* (40), 3075.

[259] Sun, Y.; Qian, T.; Zhu, J.; Zheng, N.; Han, Y.; Xiao, G.; Ni, M.; Xu, H. Dynamic simulation of a reversible solid oxide cell system for efficient H_2 production and power generation. *Energy* **2023,** *263*, 125725.

[260] Mogensen, M. B. Materials for reversible solid oxide cells. *Current Opinion in Electrochemistry* **2020,** *21*, 265.

[261] Hutty, T. D.; Dong, S.; Lee, R.; Brown, S. Long term energy storage with reversible solid oxide cells for microgrid applications. *Energy Reports* **2021,** *7*, 24.

[262] Saarinen, V.; Pennanen, J.; Kotisaari, M.; Thomann, O.; Himanen, O.; Iorio, S. D.; Hanoux, P.; Aicart, J.; Couturier, K.; Sun, X.et al. Design, manufacturing, and operation of movable 2 × 10 kW size rSOC system. *Fuel Cells* **2021,** *21* (5), 477.

[263] Yang, C.; Guo, R.; Jing, X.; Li, P.; Yuan, J.; Wu, Y. Degradation mechanism and modeling study on reversible solid oxide cell in dual-

mode - A review. *International Journal of Hydrogen Energy* **2022,** *47* (89), 37895.

[264] Fontana, S.; Chevalier, S.; Caboche, G. Metallic Interconnects for Solid Oxide Fuel Cell: Performance of Reactive Element Oxide Coating During 10, 20 and 30 Months Exposure. *Oxidation of Metals* **2012,** *78* (5), 307.

[265] Chen, K.; Liu, S.-S.; Ai, N.; Koyama, M.; Jiang, S. P. Why solid oxide cells can be reversibly operated in solid oxide electrolysis cell and fuel cell modes? *Physical Chemistry Chemical Physics* **2015,** *17* (46), 31308.

[266] Myung, J.-h.; Neagu, D.; Miller, D. N.; Irvine, J. T. S. Switching on electrocatalytic activity in solid oxide cells. *Nature* **2016,** *537* (7621), 528.

[267] Hauch, A.; Traulsen, M. L.; Küngas, R.; Skafte, T. L. CO_2 electrolysis - Gas impurities and electrode overpotential causing detrimental carbon deposition. *Journal of Power Sources* **2021,** *506*, 230108.

[268] Kwon, J.; Choi, P.; Jo, S.; Oh, H.; Cho, K.-Y.; Lee, Y.-K.; Kim, S.; Eom, K. Identification of electrode degradation by carbon corrosion in polymer electrolyte membrane fuel cells using the distribution of relaxation time analysis. *Electrochimica Acta* **2022,** *414*, 140219.

[269] Li, C.; Wu, A.; Xi, C.; Guan, W.; Chen, L.; Singhal, S. C. High

reversible cycling performance of carbon dioxide electrolysis by flat-tube solid oxide cell. *Applied Energy* **2022,** *314*, 118969.

[270] Bierschenk, D. M.; Wilson, J. R.; Barnett, S. A. High efficiency electrical energy storage using a methane-oxygen solid oxide cell. *Energy & Environmental Science* **2011,** *4* (3), 944.

[271] Cheng, T.-L.; Lei, Y.; Chen, Y.; Fan, Y.; Abernathy, H.; Song, X.; Wen, Y.-H. Oxidation of nickel in solid oxide cells during electrochemical operation: Experimental evidence, theoretical analysis, and an alternative hypothesis on the nickel migration. *Journal of Power Sources* **2023,** *569*, 232991.

[272] Schuepfer, D. B.; Badaczewski, F.; Guerra-Castro, J. M.; Hofmann, D. M.; Heiliger, C.; Smarsly, B.; Klar, P. J. Assessing the structural properties of graphitic and non-graphitic carbons by Raman spectroscopy. *Carbon* **2020,** *161*, 359.

[273] Chen, C.; Sun, K.; Huang, C.; Yang, M.; Fan, M.; Wang, A.; Zhang, G.; Li, B.; Jiang, J.; Xu, W.et al. Investigation on the mechanism of structural reconstruction of biochars derived from lignin and cellulose during graphitization under high temperature. *Biochar* **2023,** *5* (1), 51.

[274] Sciazko, A.; Komatsu, Y.; Nakamura, A.; Ouyang, Z.; Hara, T.; Shikazono, N. 3D microstructures of solid oxide fuel cell Ni-YSZ anodes with carbon deposition. *Chemical Engineering Journal* **2023,** *460*, 141680.

[275] Rahman, M. M.; Oni, A. O.; Gemechu, E.; Kumar, A. Assessment of energy storage technologies: A review. *Energy Conversion and Management* **2020,** *223*, 113295.

[276] Luo, X.; Wang, J.; Dooner, M.; Clarke, J. Overview of current development in electrical energy storage technologies and the application potential in power system operation. *Applied Energy* **2015,** *137*, 511.

[277] Kebede, A. A.; Kalogiannis, T.; Van Mierlo, J.; Berecibar, M. A comprehensive review of stationary energy storage devices for large scale renewable energy sources grid integration. *Renewable and Sustainable Energy Reviews* **2022,** *159*, 112213.

[278] Cruz, M. R. M.; Fitiwi, D. Z.; Santos, S. F.; Catalão, J. P. S. A comprehensive survey of flexibility options for supporting the low-carbon energy future. *Renewable and Sustainable Energy Reviews* **2018,** *97*, 338.

[279] Rohit, A. K.; Rangnekar, S. An overview of energy storage and its importance in Indian renewable energy sector: Part II - energy storage applications, benefits and market potential. *Journal of Energy Storage* **2017,** *13*, 447.

[280] Gür, T. M. Review of electrical energy storage technologies, materials and systems: challenges and prospects for large-scale grid storage. *Energy & Environmental Science* **2018,** *11* (10), 2696.

[281] Asri, L. I. M.; Ariffin, W. N. S. F. W.; Zain, A. S. M.; Nordin, J.; Saad, N. S. Comparative Study of Energy Storage Systems (ESSs). *Journal of Physics: Conference Series* **2021,** *1962* (1), 012035.

[282] Kim, J.; Im, S.; Oh, S. H.; Lee, J. Y.; Yoon, K. J.; Son, J.-W.; Yang, S.; Kim, B.-K.; Lee, J.-H.; Lee, H.-W.et al. Naturally diffused sintering aid for highly conductive bilayer electrolytes in solid oxide cells. *Science Advances 7* (40), eabj8590.

[283] Wang, C.; Liang, J.; Kim, J. T.; Sun, X. Prospects of halide-based all-solid-state batteries: From material design to practical application. *Science Advances 8* (36), eadc9516.

[284] Erdle, E.; Dönitz, W.; Schamm, R.; Koch, A. Reversibility and polarization behaviour of high temperature solid oxide electrochemical cells. *International Journal of Hydrogen Energy* **1992,** *17* (10), 817.

[285] Wang, Y.; Leung, D. Y. C.; Xuan, J.; Wang, H. A review on unitized regenerative fuel cell technologies, part B: Unitized regenerative alkaline fuel cell, solid oxide fuel cell, and microfluidic fuel cell. *Renewable and Sustainable Energy Reviews* **2017,** *75*, 775.

[286] Minh, N. Q.; Mogensen, M. B. Reversible Solid Oxide Fuel Cell Technology for Green Fuel and Power Production. *The Electrochemical Society Interface* **2013,** *22* (4), 55.

[287] Venkataraman, V.; Pérez-Fortes, M.; Wang, L.; Hajimolana, Y. S.; Boigues-Muñoz, C.; Agostini, A.; McPhail, S. J.; Maréchal, F.; Van

Herle, J.; Aravind, P. V. Reversible solid oxide systems for energy and chemical applications - Review & perspectives. *Journal of Energy Storage* **2019,** *24*, 100782.

[288] Murphy, R.; Zhou, Y.; Zhang, L.; Soule, L.; Zhang, W.; Chen, Y.; Liu, M. A New Family of Proton-Conducting Electrolytes for Reversible Solid Oxide Cells: $BaHfxCe_{0.8-x}Y_{0.1}Yb_{0.1}O_{3-\delta}$. *Advanced Functional Materials* **2020,** *30* (35), 2002265.

[289] Jensen, S. H.; Langnickel, H.; Hintzen, N.; Chen, M.; Sun, X.; Hauch, A.; Butera, G.; Clausen, L. R. Reversible operation of a pressurized solid oxide cell stack using carbonaceous gases. *Journal of Energy Storage* **2019,** *22*, 106.

[290] Smolinka, T.; Bergmann, H.; Garche, J.; Kusnezoff, M. Chapter 4 - The history of water electrolysis from its beginnings to the present. *Electrochemical Power Sources* **2022**, https://doi.org/10.1016/B978-0-12-819424-9.00010-0.

[291] Lamagna, M.; Nastasi, B.; Groppi, D.; Rozain, C.; Manfren, M.; Astiaso Garcia, D. Techno-economic assessment of reversible Solid Oxide Cell integration to renewable energy systems at building and district scale. *Energy Conversion and Management* **2021,** *235*, 113993.

[292] Fang, Q.; Blum, L.; Menzler, N. H. Performance and Degradation of Solid Oxide Electrolysis Cells in Stack. *Journal of The Electrochemical Society* **2015,** *162* (8), F907.

[293] Yang, S.; Wang, F.; Che, Q.; Li, J.; Lu, Y.; Shang, S.; Zhang, H. Quantitative characterization of nickel migration in solid oxide fuel cells under redox cycling. *Journal of Alloys and Compounds* **2022,** *921*, 166085.

[294] Sezer, H.; Celik, I. B. Phosphine induced Nickel Migration in SOFC Anodes: A Computational Study. *Electrochimica Acta* **2015,** *155*, 421.

[295] Zekri, A.; Herbrig, K.; Knipper, M.; Parisi, J.; Plaggenborg, T. Nickel Depletion and Agglomeration in SOFC Anodes During Long-Term Operation. *Fuel Cells* **2017,** *17* (3), 359.

[296] Sciazko, A.; Komatsu, Y.; Shimura, T.; Shikazono, N. Multiscale microstructural evolutions of nickel-gadolinium doped ceria in solid oxide fuel cell anode. *Journal of Power Sources* **2020,** *478*, 228710.

[297] Wang, Y.; Wu, C.; Zhao, S.; Guo, Z.; Han, M.; Zhao, T.; Zu, B.; Du, Q.; Ni, M.; Jiao, K. Boosting the performance and durability of heterogeneous electrodes for solid oxide electrochemical cells utilizing a data-driven powder-to-power framework. *Science Bulletin* **2023,** *68* (5), 516.

[298] Kawasaki, T.; Matsuda, J.; Tachikawa, Y.; Lyth, S. M.; Shiratori, Y.; Taniguchi, S.; Sasaki, K. Oxidation-induced degradation and performance fluctuation of solid oxide fuel cell Ni anodes under simulated high fuel utilization conditions. *International Journal of Hydrogen Energy* **2019,** *44* (18), 9386.

[299] Jung, H. Y.; Choi, S. H.; Kim, H.; Son, J. W.; Kim, J.; Lee, H. W.; Lee, J. H. Fabrication and performance evaluation of 3-cell SOFC stack based on planar 10cm×10cm anode-supported cells. *Journal of Power Sources* **2006,** *159* (1), 478.

[300] Comminges, C.; Fu, Q. X.; Zahid, M.; Steiner, N. Y.; Bucheli, O. Monitoring the degradation of a solid oxide fuel cell stack during 10,000h via electrochemical impedance spectroscopy. *Electrochimica Acta* **2012,** *59*, 367.

[301] Bernadet, L.; Segura-Ruiz, J.; Yedra, L.; Estrade, S.; Peiró, F.; Montinaro, D.; Torrell, M.; Morata, A.; Tarancón, A. Enhanced diffusion barrier layers for avoiding degradation in SOFCs aged for 14000 h during 2 years. *Journal of Power Sources* **2023,** *555*, 232400.

[302] Knibbe, R.; Traulsen, M. L.; Hauch, A.; Ebbesen, S. D.; Mogensen, M. Solid Oxide Electrolysis Cells: Degradation at High Current Densities. *Journal of The Electrochemical Society* **2010,** *157* (8), B1209.

[303] Kim, H. H.; Akhtar, A.; Kim, M. J.; Jo, J.; Shin, T. H.; Lim, H.-T. Performance and stability of electrolyte-supported solid oxide fuel cells: from button-sized to 5 × 5 cm^2. *Journal of the Korean Ceramic Society* **2024,** *61* (2), 279.

[304] He, S.; Saunders, M.; Chen, K.; Gao, H.; Suvorova, A.; Rickard, W. D. A.; Quadir, Z.; Cui, C. Q.; Jiang, S. P. A FIB-STEM Study of Strontium Segregation and Interface Formation of Directly Assembled

$La_{0.6}Sr_{0.4}Co_{0.2}Fe_{0.8}O_{3-\delta}$ Cathode on Y_2O_3-ZrO_2 Electrolyte of Solid Oxide Fuel Cells. *Journal of The Electrochemical Society* **2018,** *165* (7), F417.

[305] Chen, K.; Jiang, S. P. Surface Segregation in Solid Oxide Cell Oxygen Electrodes: Phenomena, Mitigation Strategies and Electrochemical Properties. *Electrochemical Energy Reviews* **2020,** *3* (4), 730.

[306] Hu, B.; Krishnan, S.; Liang, C.; Heo, S. J.; Aphale, A. N.; Ramprasad, R.; Singh, P. Experimental and thermodynamic evaluation of $La_{1-x}Sr_xMnO_{3\pm\delta}$ and $La_{1-x}Sr_xCo_{1-y}Fe_yO_{3-\delta}$ cathodes in Cr-containing humidified air. *International Journal of Hydrogen Energy* **2017,** *42* (15), 10208.

[307] Zhang, X.; Jin, Y.; Jiang, Y.; Zong, X.; Li, Y.; Xiong, Y. Enhanced electrochemical performance and operating stability of $La_{0.8}Sr_{0.2}Co_{0.2}Fe_{0.8}O_{3-\delta}$ fiber cathode via $Gd_{0.2}Ce_{0.8}O_{1.9-\delta}$ coating for intermediate temperature solid oxide fuel cells. *Applied Surface Science* **2023,** *630*, 157445.

[308] Schuler, J. A.; Yokokawa, H.; Calderone, C. F.; Jeangros, Q.; Wuillemin, Z.; Hessler-Wyser, A.; Van herle, J. Combined Cr and S poisoning in solid oxide fuel cell cathodes. *Journal of Power Sources* **2012,** *201*, 112.

[309] Motin Seikh, M.; Sudheendra, L.; Narayana, C.; Rao, C. N. R. A

Raman study of the temperature-induced low-to-intermediate-spin state transition in $LaCoO_3$. *Journal of Molecular Structure* **2004,** *706* (1), 121.

[310] Zhou, L.; Mason, J. H.; Li, W.; Liu, X. Comprehensive review of chromium deposition and poisoning of solid oxide fuel cells (SOFCs) cathode materials. *Renewable and Sustainable Energy Reviews* **2020,** *134*, 110320.

[311] Sahadevan, J.; Sivaprakash, P.; Esakki Muthu, S.; Kim, I.; Padmanathan, N.; Eswaramoorthi, V. Influence of Te-Incorporated $LaCoO_3$ on Structural, Morphology and Magnetic Properties for Multifunctional Device Applications. *International Journal of Molecular Sciences* **2023,** *24* (12), 10107.

[312] Amezawa, K.; Shindo, Y.; Fujimaki, Y.; Kimura, Y.; Nakamura, T.; Iguchi, F.; Yashiro, K.; Yugami, H.; Kawada, T. Mechanism of Chromium Poisoning in SOFC Cathode Investigated by Using Pattern Thin Film Model Electrode. *ECS Meeting Abstracts* **2017,** *MA2017-03* (1), 147.

[313] Wang, C. C.; Gholizadeh, M.; Hou, B.; Fan, X. Integrated Cr and S poisoning of a $La_{0.6}Sr_{0.4}Co_{0.2}Fe_{0.8}O_{3-\delta}$ (LSCF) cathode for solid oxide fuel cells. *RSC Advances* **2021,** *11* (1), 7.

[314] Horita, T. Chromium poisoning for prolonged lifetime of electrodes in solid oxide fuel cells - Review. *Ceramics International* **2021,** *47* (6), 7293.

[315] Silva, J. M. P.; Andrade Neto, N. F.; Teodoro, M. D.; Paiva, A. E. M.; Bomio, M. R. D.; Motta, F. V. Fabrication of new Ag_2CrO_4/Ag_2MoO_4 and Ag_2CrO_4/Ag_2WO_4 heterostructures with enhanced degradation of the mixture of dyes by photocatalysis. *Journal of Alloys and Compounds* **2022,** *928*, 167136.

[316] P. S, L.; G. S, S.; R. A, R.; M, A.; R, T.-M.; H, B.-M.; G, M.-V.; E, C.; J, A.; E, L. Laser and electron beam-induced formation of Ag/Cr structures on Ag_2CrO_4. *Physical Chemistry Chemical Physics* **2019,** *21* (11), 6101.

[317] Luo, Y.; Wu, X.-y.; Shi, Y.; Ghoniem, A. F.; Cai, N. Exergy analysis of an integrated solid oxide electrolysis cell-methanation reactor for renewable energy storage. *Applied Energy* **2018,** *215*, 371.

[318] Bartela, Ł. A hybrid energy storage system using compressed air and hydrogen as the energy carrier. *Energy* **2020,** *196*, 117088.

[319] Bhandari, R.; Shah, R. R. Hydrogen as energy carrier: Techno-economic assessment of decentralized hydrogen production in Germany. *Renewable Energy* **2021,** *177*, 915.

[320] Tarhan, C.; Çil, M. A. A study on hydrogen, the clean energy of the future: Hydrogen storage methods. *Journal of Energy Storage* **2021,** *40*, 102676.

[321] Amouroux, J.; Siffert, P.; Pierre Massué, J.; Cavadias, S.; Trujillo, B.; Hashimoto, K.; Rutberg, P.; Dresvin, S.; Wang, X. Carbon dioxide:

A new material for energy storage. *Progress in Natural Science: Materials International* **2014,** *24* (4), 295.

[322] Qiao, Y.; Yi, J.; Wu, S.; Liu, Y.; Yang, S.; He, P.; Zhou, H. Li-CO_2 Electrochemistry: A New Strategy for CO_2 Fixation and Energy Storage. *Joule* **2017,** *1* (2), 359.

[323] Duranti, L.; Luisetto, I.; Casciardi, S.; Gaudio, C. D.; Bartolomeo, E. D. Multi-functional, high-performing fuel electrode for dry methane oxidation and CO_2 electrolysis in reversible solid oxide cells. *Electrochimica Acta* **2021,** *394*, 139163.

[324] Liu, S.; Wu, S.; Hu, Y.; Li, H. Comparative analysis of air and CO_2 as working fluids for compressed and liquefied gas energy storage technologies. *Energy Conversion and Management* **2019,** *181*, 608.

[325] Xu, M.; Zhao, P.; Huo, Y.; Han, J.; Wang, J.; Dai, Y. Thermodynamic analysis of a novel liquid carbon dioxide energy storage system and comparison to a liquid air energy storage system. *Journal of Cleaner Production* **2020,** *242*, 118437.

[326] Santhanam, S.; Heddrich, M. P.; Riedel, M.; Friedrich, K. A. Theoretical and experimental study of Reversible Solid Oxide Cell (r-SOC) systems for energy storage. *Energy* **2017,** *141*, 202.

[327] Thema, M.; Bauer, F.; Sterner, M. Power-to-Gas: Electrolysis and methanation status review. *Renewable and Sustainable Energy Reviews* **2019,** *112*, 775.

[328] Wu, A.; Han, B.; Yao, Y.; Zhang, Y.; Tang, Y.; Hanson, S.; Wang, J.; Guan, W.; Singhal, S. C. Degradation of flat-tube solid oxide electrolytic stack for co-electrolysis of H_2O and CO_2 under pulsed current. *Journal of Power Sources* **2023,** *580*, 233372.

[329] Yang, Z. Recent advances in metallic interconnects for solid oxide fuel cells. *International Materials Reviews* **2008,** *53* (1), 39.

[330] Bianco, M.; Linder, M.; Larring, Y.; Greco, F.; Van herle, J. Chapter 7 - Lifetime Issues for Solid Oxide Fuel Cell Interconnects. *Solid Oxide Fuel Cell Lifetime and Reliability* **2017**, DOI:https://doi.org/10.1016/B978-0-08-101102-7.00007-6 https://doi.org/10.1016/B978-0-08-101102-7.00007-6.

[331] Bucher, E.; Gspan, C.; Hofer, F.; Sitte, W. Post-test analysis of silicon poisoning and phase decomposition in the SOFC cathode material $La_{0.58}Sr_{0.4}Co_{0.2}Fe_{0.8}O_{3-\delta}$ by transmission electron microscopy. *Solid State Ionics* **2013,** *230*, 7.

[332] Schuler, J. A.; Wuillemin, Z.; Hessler-Wyser, A.; Comminges, C.; Steiner, N. Y.; Van herle, J. Cr-poisoning in (La,Sr)(Co,Fe)O_3 cathodes after 10,000h SOFC stack testing. *Journal of Power Sources* **2012,** *211*, 177.

[333] Jiang, S. P.; Chen, X. Chromium deposition and poisoning of cathodes of solid oxide fuel cells - A review. *International Journal of Hydrogen Energy* **2014,** *39* (1), 505.

[334] Chen, D.; Mewafy, B.; Paloukis, F.; Zhong, L.; Papaefthimiou, V.; Dintzer, T.; Papazisi, K. M.; Balomenou, S. P.; Tsiplakides, D.; Teschner, D.et al. Revising the role of chromium on the surface of perovskite electrodes: Poison or promoter for the solid oxide electrolysis cell performance? *Journal of Catalysis* **2020,** *381*, 520.

[335] Chen, Y.; Yoo, S.; Li, X.; Ding, D.; Pei, K.; Chen, D.; Ding, Y.; Zhao, B.; Murphy, R.; deGlee, B.et al. An effective strategy to enhancing tolerance to contaminants poisoning of solid oxide fuel cell cathodes. *Nano Energy* **2018,** *47*, 474.

[336] Wang, K.; Liu, Y.; Fergus, J. W. Interactions Between SOFC Interconnect Coating Materials and Chromia. *Journal of the American Ceramic Society* **2011,** *94* (12), 4490.

[337] Malzbender, J.; Batfalsky, P.; Vaßen, R.; Shemet, V.; Tietz, F. Component interactions after long-term operation of an SOFC stack with LSM cathode. *Journal of Power Sources* **2012,** *201*, 196.

[338] Subotić, V.; Königshofer, B.; Juričić, Đ.; Kusnezoff, M.; Schröttner, H.; Hochenauer, C.; Boškoski, P. Detailed insight into processes of reversible solid oxide cells and stacks using DRT analysis. *Energy Conversion and Management* **2020,** *226*, 113509.

[339] Song, W.; Ma, Z.; Yang, Y.; Zhang, S.; Ou, X.; Ling, Y. Characterization and polarization DRT analysis of direct ethanol solid oxide fuel cells using low fuel partial pressures. *International Journal*

of Hydrogen Energy **2020,** *45* (28), 14480.

[340] Zhao, L.; Zhang, J.; Becker, T.; Jiang, S. P. Raman Spectroscopy Study of Chromium Deposition on $La_{0.6}Sr_{0.4}Co_{0.2}Fe_{0.8}O_{3-\delta}$ Cathode of Solid Oxide Fuel Cells. *Journal of The Electrochemical Society* **2014,** *161* (6), F687.

[341] Li, X.; Blinn, K.; Chen, D.; Liu, M. In Situ and Surface-Enhanced Raman Spectroscopy Study of Electrode Materials in Solid Oxide Fuel Cells. *Electrochemical Energy Reviews* **2018,** *1* (3), 433.

[342] Santamaría-Pérez, D.; Bandiello, E.; Errandonea, D.; Ruiz-Fuertes, J.; Gomis, O.; Sans, J. A.; Manjón, F. J.; Rodríguez-Hernández, P.; Muñoz, A. Phase Behavior of Ag_2CrO_4 under Compression: Structural, Vibrational, and Optical Properties. *The Journal of Physical Chemistry C* **2013,** *117* (23), 12239.

[343] Qiu, P.; Lin, J.; Lei, L.; Yuan, Z.; Jia, L.; Li, J.; Chen, F. Evaluation of Cr-Tolerance of the $Sr_2Fe_{1.5}Mo_{0.5}O_{6-\delta}$ Cathode for Solid Oxide Fuel Cells. *ACS Applied Energy Materials* **2019,** *2* (10), 7619.

[344] Xiong, C.; Qiu, P.; Zhang, W.; Pu, J. Influence of practical operating temperature on the Cr poisoning for LSCF-GDC cathode. *Ceramics International* **2022,** *48* (22), 33999.

[345] Jiang, S. P.; Zhang, J. P.; Zheng, X. G. A comparative investigation of chromium deposition at air electrodes of solid oxide fuel cells. *Journal of the European Ceramic Society* **2002,** *22* (3), 361.

[346] Gupta, S.; Zhong, Y.; Mahapatra, M.; Singh, P. Processing and electrochemical performance of manganese-doped lanthanum-strontium chromite in oxidizing and reducing atmospheres. *International Journal of Hydrogen Energy* **2015,** *40* (39), 13479.

[347] Sha, Z.; Shen, Z.; Calì, E.; Kilner, J. A.; Skinner, S. J. Understanding surface chemical processes in perovskite oxide electrodes. *Journal of Materials Chemistry A* **2023,** *11* (11), 5645.

[348] Wei, B.; Chen, K.; Wang, C. C.; Lü, Z.; Jiang, S. P. Cr deposition on porous $La_{0.6}Sr_{0.4}Co_{0.2}Fe_{0.8}O_{3-\delta}$ electrodes of solid oxide cells under open circuit condition. *Solid State Ionics* **2015,** *281*, 29.